

**3-D Observations of Absolute Humidity
from the Land Surface
to the Lower Troposphere
with
Scanning Differential Absorption Lidar**

Dissertation zur Erlangung des Doktorgrades
der Naturwissenschaften (Dr. rer. nat.)

Fakultät Naturwissenschaften
Universität Hohenheim

Institut für Physik und Meteorologie

vorgelegt von Florian Heiko Späth

aus Esslingen am Neckar

2016

Dekan:	Prof. Dr. rer. nat. Heinz Breer
1. berichtende Person:	Prof. Dr. rer. nat. Volker Wulfmeyer
2. berichtende Person:	Prof. Dr. rer. nat. Christoph Kottmeier
Eingereicht am:	28. April 2016
Mündliche Prüfung am:	20. Juli 2016

Zusammenfassung

Die Wasserdampfverteilung in der atmosphärischen Grenzschicht ist räumlich und zeitlich sehr variabel. Als starkes Treibhausgas ist dessen zuverlässige Vorhersage in Klimamodellen wichtig. Zudem wirkt es bei vielen atmosphärischen Prozessen mit, wie z.B. beim Auslösen von Konvektion oder bei der Entstehung von Wolken. Hochaufgelöste mehrdimensionale Daten von Wasserdampf in der atmosphärischen Grenzschicht sind notwendig, um das Verständnis dieser Prozesse zu verbessern und Modellsimulationen zu validieren.

Zu diesem Zweck entwickelte das Institut für Physik und Meteorologie (IPM) an der Universität Hohenheim (UHOH) ein einzigartiges scannendes differentielles Absorptionslidar (DIAL). Dieses ermöglicht Wasserdampfmessungen mit einer zeitlichen und räumlichen Auflösung von wenigen Sekunden und einigen zehn Metern in einem Bereich von mehreren Kilometern vom Boden bis zur unteren Troposphäre. Die DIAL-Technik nutzt dazu zwei Lidarrückstreusignale, die aufgrund unterschiedlicher emittierter Laserwellenlängen (online und offline Wellenlänge) in der Atmosphäre verschieden stark absorbiert werden. Zur Bestimmung der Wasserdampfanzahldichte werden nur die beiden Lidarsignale und die Absorptionsquerschnitte bei der online- und offline-Wellenlänge benötigt. Daher wird diese Technik auch selbstkalibrierend genannt. Das UHOH DIAL-System erlaubt zudem scannende Messungen, die zum einen Messungen bis an den Boden und zum anderen Messungen der horizontalen Variabilität der Feuchtigkeit ermöglichen.

Für hochaufgelöste DIAL-Messungen müssen vom Lasertransmitter einige Anforderungen erfüllt werden, dazu gehören eine sehr hohe Frequenzstabilität und spektrale Reinheit. Zur Frequenzstabilisierung wird die „Injection Seeding“-Technik eingesetzt, bei der ein Diodenlaser in den Resonator eines Hochleistungslasers eingekoppelt wird. Für das UHOH DIAL werden zwei sehr frequenzstabile Diodenlaser, jeweils einer für die online und die offline Wellenlänge, eingesetzt und abwechselnd in den Resonator eingekoppelt. Die Umschaltung erfolgt mittels eines optischen Schalters, der eine ausreichende Fremdkanalunterdrückung aufweist.

Diese Arbeit behandelt drei Aspekte bezüglich hochaufgelöster Feuchtemessung in der atmosphärischen Grenzschicht mit scannendem DIAL: 1) Die Entwicklung eines neuen Seedersystems für den Lasertransmitter, 2) die Vorstellung verschiedener Scan-Modi und 3) Anwendungen von mit dem DIAL gemessenen 2-D–3-D Wasserdampfdaten.

Das neu entwickelte Seedersystem basiert auf Distributed Feedback (DFB) Laserdioden als Seedlaser und einem elektro-optischen Strahlableiter als optischen Schalter. Der Aufbau und die Spezifikationen werden vorgestellt. Die Frequenzstabilität der DFB-

Laserdioden beträgt 6,3 MHz mit einer Linienbreite von $< 4,7$ MHz. Der neukonzipierte optische Schalter erreicht eine Umschaltzeit von weniger als $10\ \mu\text{s}$ bei einer Fremdkanalunterdrückung von 33 dB, das einer spektralen Reinheit von 99,95 % entspricht. Damit werden nicht nur die Anforderungen für bodengestützte DIAL-Systeme erfüllt, sondern auch die Anforderungen für flugzeug-/satellitengestützte DIAL-Systeme. Die hohe Frequenzstabilität erlaubt zudem die Wahl einer Wellenlänge auf der Flanke einer Absorptionslinie, das eine genaue Einstellung des Absorptionswertes entsprechend der meteorologischen Bedingungen ermöglicht. Darüber hinaus wird gezeigt, dass auf der Flanke der Absorptionslinie der Rayleigh-Dopplereffekt zusätzlich stark verringert ist.

Zur Erfassung der räumlichen Wasserdampfstruktur werden scannende Messungen durchgeführt. Dazu werden folgende 3 Scanverfahren mit Messbeispielen vorgestellt:

- 1) Range-height indicator (RHI) Scans liefern vertikale Schnittbilder der atmosphärischen Feuchteverteilung. Die vorgestellte Serie aus vier Messungen zeigt verschiedene Feuchteschichten mit unterschiedlichem Wasserdampfgehalt und deren Entwicklung. Im Messbeispiel treten im letzten durchgeführten Scan Wolken an der Oberkante der konvektiven Grenzschicht auf.
- 2) Der Volumenscan erfasst die gesamte 3-dimensionale Wasserdampfstruktur mittels mehrerer konischer Scans mit unterschiedlichen Elevationswinkeln. Die horizontalen Unterschiede der Schichtenhöhen können anhand des Geländeprofiles mit einem kleinen Hügel in der Nähe des DIAL-Standorts erklärt werden.
- 3) Bodennahe Scans geben die Wasserdampfverteilung direkt über dem Erdboden wieder. Damit können Beziehungen zwischen der Bodenbeschaffenheit und dem -bewuchs mit der darüber liegenden Atmosphäre untersucht werden. So zeigten sich über einem Maisfeld und über Wald höhere Wasserdampfwerte als über einer Grasfläche.

Für die Analyse der scannenden Messungen wurden neue Auswerte- und Darstellungsroutinen, sowie neue Methoden zur Fehlerabschätzung entwickelt.

Die wissenschaftliche Anwendung von hochaufgelösten Wasserdampfdaten aus DIAL-Messungen werden anhand von drei Veröffentlichungen vorgestellt. Eine Evaluierungsstudie zu Modellsimulationen mit unterschiedlichen Land-Atmosphären-Austauschmodellen verglich Feuchtigkeitsprofile aus den Modellen mit horizontal gemittelten Wasserdampfdaten aus scannenden DIAL-Messungen. Hochaufgelöste Feuchtefluktuationen aus Vertikalmessungen wurden verwendet, um höhere Momente bis zur vierten Ordnung sowie Skewness und Kurtosis zu bestimmen. Weiter wurden solche Feuchteprofile mit Profilen von Temperatur und Vertikalwind kombiniert und genutzt, um neue Turbulenzparametrisierungen zu entwickeln und zu testen.

Abstract

The water vapor (WV) distribution in the atmospheric boundary layer (ABL) is spatially and temporally highly variable. Its prediction in climate models is important because it is a strong greenhouse gas. Furthermore, it is involved in many atmospheric processes like convection initiation or cloud formation. High-resolution multi-dimensional WV data of the ABL are required to improve the knowledge of these processes and to validate model simulations.

For this purpose, the Institute of Physics and Meteorology (IPM) at the University of Hohenheim (UHOH) developed a unique scanning differential absorption lidar (DIAL). This instrument allows for water vapor measurements with high temporal and spatial resolutions of the orders of seconds and tens of meters in the range of several kilometers from the surface up to the lower troposphere. The DIAL technique uses two lidar backscatter signals which are absorbed differently by the atmosphere due to different emitted laser wavelengths (online and offline wavelengths). For the calculation of the water vapor number density only the two lidar signals and the absorption cross-section values at the online and offline wavelengths are necessary. Thus, the DIAL technique is called self-calibrating. Additionally, the UHOH DIAL system can perform scanning measurements which allows for observations down to the surface as well as for observations of the horizontal moisture variability.

For high-resolution DIAL measurements several requirements for the laser transmitter need to be fulfilled which include a very high frequency stability and a very high spectral purity. The frequency stabilization is realized with the injection seeding technique. Therefore, a diode laser is coupled into the resonator of a high-power laser. For the UHOH DIAL two diode lasers with high frequency stability are used – one for the online and one for the offline wavelength – and alternately coupled into the resonator. The laser beams are switched with an optical switch with a very low crosstalk.

Within this thesis, three aspects regarding high-resolution observations of moisture in the ABL with scanning DIAL are demonstrated: 1) the developments of a new seeder system for the laser transmitter, 2) the presentation of three scan modes, and 3) applications of 2-D–3-D WV DIAL data.

The newly developed seeder system is based on distributed feedback (DFB) laser diodes as seed lasers and an electro-optical deflector as optical switch. The setup and its specifications are presented. The frequency stability of the DFB laser diodes are 6.3 MHz with a linewidth of < 4.7 MHz. The new concept of the optical switch allows switching times of less than $10 \mu\text{s}$. The crosstalk measures less than 33 dB which is in accordance of a spectral purity of 99.95 %. With theses specifications the requirements for ground-based systems as well as for airborne/satellite-borne systems are fulfilled. In

addition, the high frequency stability allows for selecting an online wavelength on the slope of an absorption line. This enables for an exact adaptation of the WV absorption cross-section value to the meteorological conditions. Furthermore, it is shown that the Rayleigh-Doppler effect is significantly reduced if a wavelength on the slope of the absorption line is selected.

Scanning measurements were performed to capture the spatial WV structures. For this purpose, three scan modes with measurement examples are presented:

- 1) Range-height indicator (RHI) scans provide vertical cross-section images of the atmospheric humidity distribution. The presented series of four measurements show several humidity layers with different WV content and their evolution. Clouds appear in the last scan.
- 2) A volume scan captures the whole three-dimensional WV structure made out of several conical scans of different elevation angles. The horizontal variation of the layer heights can be related to the terrain profile with a small hill near the DIAL site.
- 3) Low elevation scans observe the WV distribution directly above the surface. Thus, relationships of the ground characteristics and vegetation with the humidity content above can be investigated. It is shown that there was more moisture above a maize field and above a forest than above grassland.

For the analysis of scanning measurements, new analysis and visualization routines as well as new methods for the error estimation were developed.

More scientific applications of high-resolution WV data from DIAL measurements are presented in three publications. A evaluation study compared humidity profiles from model simulations with different land-surface schemes with horizontal mean profiles of scanning DIAL measurements. High-resolution humidity fluctuations from vertical measurements were used to determine higher-order moments up to the fourth-order as well as skewness and kurtosis. Furthermore, such WV profiles were combined with profiles of temperature and vertical wind velocities and used for the development of new turbulence parameterizations and for model validation.

Contents

Zusammenfassung	iii
Abstract	v
Contents	vii
1 Introduction	1
1.1 Motivation	1
1.2 Differential Absorption Lidar	4
1.3 The Rayleigh-Doppler Effect	7
2 UHOH DIAL Setup	13
2.1 High-power Ti:sapphire laser at 820 nm for scanning ground-based water-vapor differential absorption lidar	17
2.2 Online/offline injection seeding system with high frequency-stability and low crosstalk for water vapor DIAL	33
3 Scanning DIAL Measurements	41
3.1 3-D water vapor field in the atmospheric boundary layer observed with scanning differential absorption lidar	43
4 Applications	63
4.1 Investigation of PBL schemes combining the WRF model simulations with scanning water vapor differential absorption lidar measurements . .	65
4.2 Turbulent Humidity Fluctuations in the Convective Boundary Layer: Case Studies Using Water Vapour Differential Absorption Lidar Measurements	91
4.3 Determination of Convective Boundary Layer Entrainment Fluxes, Dissipation Rates, and the Molecular Destruction of Variances: Theoretical Description and a Strategy for Its Confirmation with a Novel Lidar System Synergy	115
5 Summary	141
6 Outlook	142
Abbreviations	143
References	145

1 Introduction

1.1 Motivation

In order to forecast the Earth's weather and to predict the future climate, the human being uses all its achieved knowledge of environmental processes. With climate projections the longtime effect of today's way of living is evaluated. Different scenarios help to understand the anthropogenic influence on the climate change. Discussions and decisions of the United Nations conference on climate change (UNFCCC)¹ are also based on the widely admitted results of the climate reports of IPCC². However, longtime projections of the IPCC reports still show large uncertainties. In December 2015 in Paris (France), the parties of UNFCCC agreed on the goal to keep the global warming below 2 K - preferable below 1.5 K – till the end of the century³. For this purpose and for sustainable adaptations, reliable forecasts and projections are needed. Water vapor (WV) is a strong greenhouse gas and plays an important role in Earth's weather and climate. It is involved in many processes which are not yet fully understood nor represented in the simulations. WV is spatially and temporally highly variable and is involved in many atmospheric processes such as convection initiation, cloud formation and heat distribution.

All these relevant processes take place within the atmospheric boundary layer (ABL). The ABL interacts with the free troposphere at the top and with the land surface at the bottom. These interactions form the feedback processes of the land-atmosphere (LA) system (Seneviratne et al., 2010). To improve the process representation through parameterizations in model simulations, so far model studies (e.g. Findell and Eltahir, 2003; Koster et al., 2006; van Heerwaarden et al., 2009; Santanello et al., 2013) or large eddy simulation (LES) models (e.g. Mellor and Yamada, 1982; Hong et al., 2006; Hong, 2007; Warrach-Sagi et al., 2013; Kotlarski et al., 2014) were mostly used. Model evaluation should better be based on observations but only a few data sets of surface measurements are included so far. Wulfmeyer et al. (2015) reviewed state-of-the-art active and passive remote sensing instruments to observe the humidity in the lower troposphere from the surface through the mixed layer up to the entrainment layer at the top of the ABL. Passive remote sensing instruments only provide integrated water vapor (IWV) data which give no spatial information or provide humidity profiles with low resolution. Infrared (IR) spectrometers or microwave radiometers (MWRs), for example, retrieve WV profiles with temporal resolutions of 5 – 10 min requiring an initial first guess WV profile. The vertical resolutions of these instruments are at the surface

¹<http://www.unfccc.int>

²IPCC – Intergovernmental Panel on Climate Change

³see Paris Agreement under <http://www.cop21.gouv.fr/en>

100 m or several 100 m for IR spectrometers and MWRs, respectively, and increase to approximately 800 m and 2000 m for IR spectrometers and MWRs at the top of the ABL (Löhnert et al., 2009; Blumberg et al., 2015; Wulfmeyer et al., 2015).

Lidar as active remote sensing instrument has the ability to measure WV with high temporal and high spatial resolution as well as with high accuracy. It is a new observing method with the means to resolve the relevant processes in the lower troposphere (Wulfmeyer et al., 2015). To measure atmospheric water vapor, two lidar techniques can be applied: differential absorption lidar (DIAL) (Schotland, 1966; Browell et al., 1979; Bösenberg, 1998; Wulfmeyer, 1998) and Raman lidar (e.g. Melfi, 1969; Whiteman et al., 1992; Behrendt et al., 2002; Hammann et al., 2015). The WV Raman lidar (WVRL) technique uses the inelastic scattering (usually in the ultraviolet (UV)) and detects the Raman shifted signals of WV and nitrogen. The ratio of these two signals is then calibrated to derive the WV mixing ratio. As inelastic backscatter signals are used, the signal intensities are quite low and the maximum range is limited especially in daytime. The water vapor DIAL (WVDIAL) technique uses two elastic backscatter signals at wavelengths with high and low absorption of WV. As the WVDIAL technique does not need further information than the absorption cross-section of water vapor at the used wavelengths, DIAL is a self-calibrating system (Browell et al., 1979). Due to the elastic backscatter signals, the signal-to-noise ratio (SNR) is much higher for the detected signals. This allows to reach larger ranges also during daytime and to keep integration times short.

The largest amount of water vapor in the atmosphere is located in the ABL. The main source is the evapotranspiration from the ground. Horizontal humidity variability results from the heterogeneity of the land surface and its vegetation as well as turbulent mixing. The investigation of the exchange processes between the land surface with different vegetation and the ABL, the moistening of the ABL and the entrainment of the moist air of the ABL with the dry air of the lower free troposphere requires observations over the whole height range from the surface up to the lower free troposphere (Wulfmeyer et al., 2016). To observe the horizontal variations of the humidity fields, scanning lidar can be applied. There were several scanning WVRL which, e.g., observed the WV structures in the ABL (Goldsmith et al., 1998; Eichinger et al., 1999; Whiteman et al., 2006; Froidevaux et al., 2013; Matsuda, 2013) or estimated latent heat fluxes at the surface (Eichinger, 2000). But regarding the low SNR during daytime, WVRL scanning measurements are still challenging to be performed under daylight conditions compared to scanning measurements with a WVDIAL.

To close the gap of ABL observations, the Institute of Physics and Meteorology (IPM) at the University of Hohenheim (UHOH) operates two lidar systems, a scanning Raman lidar for temperature and humidity measurements and a scanning DIAL for

water vapor profiling. Details about the Raman system and its performance are given in publications of Radlach et al. (2008); Pal et al. (2010); Hammann et al. (2015); Behrendt et al. (2015) as well as in the recently completed doctoral thesis of Eva Hammann (2016).

Within this thesis, high-resolution observations of humidity in the ABL with the scanning UHOH DIAL are presented. The UHOH DIAL was designed to observe the water vapor content in the ABL with high temporal and spatial resolutions for turbulence investigations. For this purpose, resolutions in the range of seconds and tens of meters have been achieved. Scanning capabilities are also included to observe the spatial distribution from the surface through the ABL to the lower free troposphere. First vertically pointing measurements were performed during the Convective and Orographically-induced Precipitation Study (COPS)⁴ in 2007 (Wulfmeyer et al., 2008, 2011; Behrendt et al., 2011; Bhawar et al., 2011). The performance of the UHOH DIAL was investigated by Bhawar et al. (2011) in an intercomparison study with six other WV lidar systems operated during COPS. This study resulted in a main bias for the UHOH DIAL of only 1.4%. The scanning capability was successfully tested during the Transregio 32 (TR32) FLUXPAT campaign in western Germany in summer 2009 (Behrendt et al., 2009). In spring 2013, the DIAL instrument was operated in the same region within the HD(CP)² Observational Prototype Experiment (HOPE) of the project High Definition of Clouds and Precipitation for advancing Climate Prediction (HD(CP)²)⁵. Within this project, the observations are used for the investigations of LA interaction, cloud formation, aerosol-cloud-microphysics as well as weather and climate model evaluation at the 100-m scale. Furthermore, WVDIAL measurements were performed within the Surface Atmosphere Boundary Layer Exchange (SABLE)⁶ field campaign in southwestern Germany in summer 2014. During this campaign also new scanning modes with the DIAL instrument were executed to get new insights into the spatial WV distribution and to measure down to the surface.

The thesis is structured as follows: It starts with an introduction to the DIAL technique in Sect. 1.2 with a short discussion of the Rayleigh-Doppler (RD) effect in Sect. 1.3. Section 2 gives an overview about the DIAL setup focusing on the laser transmitter with improvements of the wavelength stabilization shown in two publications. Novel scanning modes for DIAL measurements of the spatial WV distribution are presented within a publication in Sect. 3. Applications for high-resolution WVDIAL measurements are model evaluation and investigations of humidity fluctuations for determining higher-order moments. With these data turbulence parameterizations can

⁴cops.uni-hohenheim.de

⁵www.hdcp2.eu

⁶klimawandel.uni-hohenheim.de

be improved. These are topics of three publications presented in Sect. 4. Finally, a summary of the results and an outlook are given in Sect. 5 and 6, respectively.

1.2 Differential Absorption Lidar

Light Detection And Ranging (lidar) is an optical active remote sensing principle with range resolvable capability. For this purpose, laser pulses are transmitted into the atmosphere which are absorbed and scattered by atoms, molecules, and aerosols. A time-resolved recording of the backscattered signal in combination with the speed of light allows to attribute the range r to the temporal course of the signal by

$$r = \frac{c t}{2} \quad (1)$$

with c the speed of light and t the travel time of the laser pulse from transmission till recording.

The differential absorption lidar (DIAL) technique uses two elastic backscatter signals at two different wavelengths to derive the number density of a trace gas. Throughout this thesis the considered trace gas is water vapor (Schotland, 1966) but the description of the DIAL principle is also valid for other trace gases, e.g., ozone (Browell et al., 1983) or carbon dioxide (CO_2) (Koch et al., 2004). One signal is tuned to a wavelength with high absorption of water vapor ($P_{\text{on}}(r)$: online signal) while the other signal uses a wavelength with low absorption ($P_{\text{off}}(r)$: offline signal). The change of the lidar return signal $P(r)$ with respect to the range r for each of the frequencies ν is described by the lidar equation as

$$P_{\nu_0}(r) = P_0 \eta \delta r \frac{A_{\text{tel}}}{r^2} O(r) \Gamma_{\text{air},\nu_0}^2(r) \cdot \quad (2a)$$

$$\cdot \left\{ \beta_{\text{par},\nu_0}(r) \int_{-\infty}^{+\infty} S_L(\nu - \nu_0, r) \Gamma_{\text{WV}}^2(\nu, r) F_R(\nu) d\nu + \right. \quad (2b)$$

$$+ \beta_{\text{mol},\nu_0}(r) \int_{-\infty}^{+\infty} [\{S_L(\nu - \nu_0, r) \Gamma_{\text{WV}}(\nu, r)\} \times DB(\nu, r)] \Gamma_{\text{WV}}(\nu, r) F_R(\nu) d\nu \Big\} + \quad (2c)$$

$$+ P_{\text{B},\nu_0} \quad (2d)$$

with the transmitted intensity P_0 at the laser frequency ν_0 , the system efficiency η , the range resolution $\delta r = \frac{c \Delta t}{2}$ with the pulse length Δt , the telescope area A_{tel} , the overlap function $O(r)$, the particle and molecular backscatter coefficient $\beta_{\text{par},\nu}(r)$ and $\beta_{\text{mol},\nu}(r)$, the normalized laser spectrum at the ground S_L , the spectral broadening due to Rayleigh scattering DB , the transmission function of the receiver interference

filter F_R , and the background signal P_B . The transmission of the atmosphere $\Gamma(r)$ is separated into the transmission of dry air and of WV as

$$\begin{aligned}\Gamma_\nu(r) &= \Gamma_{\text{air},\nu}(r) \Gamma_{\text{WV}}(\nu, r) \\ &= \exp \left\{ - \int_0^r [\alpha_{\text{par},\nu}(r') + \alpha_{\text{mol},\nu}(r')] dr' \right\} \exp \left\{ - \int_0^r \alpha_{\text{WV}}(\nu, r') dr' \right\}, \quad (3)\end{aligned}$$

with the particle and molecular extinction coefficient $\alpha_{\text{par},\nu}(r)$ and $\alpha_{\text{mol},\nu}(r)$, which are only slightly dependent on the frequency ν , and the extinction coefficient of water vapor (of the trace gas) $\alpha_{\text{WV}}(\nu, r)$.

In Eqs. (2) and (3) and throughout this work, equations are given with respect to the frequency ν which is related to the wavelength λ by $\nu = \frac{c}{\lambda}$ with the speed of light c and considering the vacuum wavelength.

In the here given form, the lidar equation considers only the elastic backscattering at particles (Mie scattering) and at molecules (Rayleigh scattering). The particle backscatter coefficient β_{par} can be derived from the offline backscatter signal applying the method of Fernald (1984). Following the algorithm of Bucholtz (1995) yields the molecular backscatter coefficient β_{mol} . A spectral broadening is introduced to the Rayleigh backscatter signal due to the thermal motion of the molecules (Rayleigh-Doppler broadening). This is described by the Doppler broadening function DB in Eq. (2c).

The laser transmitter of the UHOH DIAL system operates with a very small linewidth (< 150 MHz) compared with the width of WV absorption lines (GHz) and is called a narrow-band lidar (Wulfmeyer et al., 2015). Thus, the following approximations are implemented to simplify the extended lidar equation (Eq. (2)): The incident laser line profile S_L can approximate with a δ -distribution because of the narrow laser linewidth (Wagner et al., 2013; Metzendorf et al., 2015). The approximations of wavelength independence of the particle backscatter coefficient β_{par} , of the overlap functions $O(r)$ and of the dry air transmission Γ_{air} are allowed because the online and offline wavelengths are selected close together. A constant value of the filter function F_R can be assumed due to the width of the interference filter which is of about 1.0 to 1.5 nm around the laser wavelength and is even larger than the broadened backscattered light spectrum.

Due to the different laser frequencies, the two signals are absorbed differently on their path through the atmosphere; the online signal stronger than the offline. Figure 1 shows the absorption spectrum of water vapor in the wavelength region around 818 nm at which the UHOH DIAL is operated. The extinction cross-section of water vapor α_{WV} in Eq. (2) is related to the absorption cross-section σ_{WV} by

$$\alpha_{\text{WV}}(\nu, r) = N_{\text{WV}}(r) \sigma_{\text{WV}}(\nu, r) \quad (4)$$

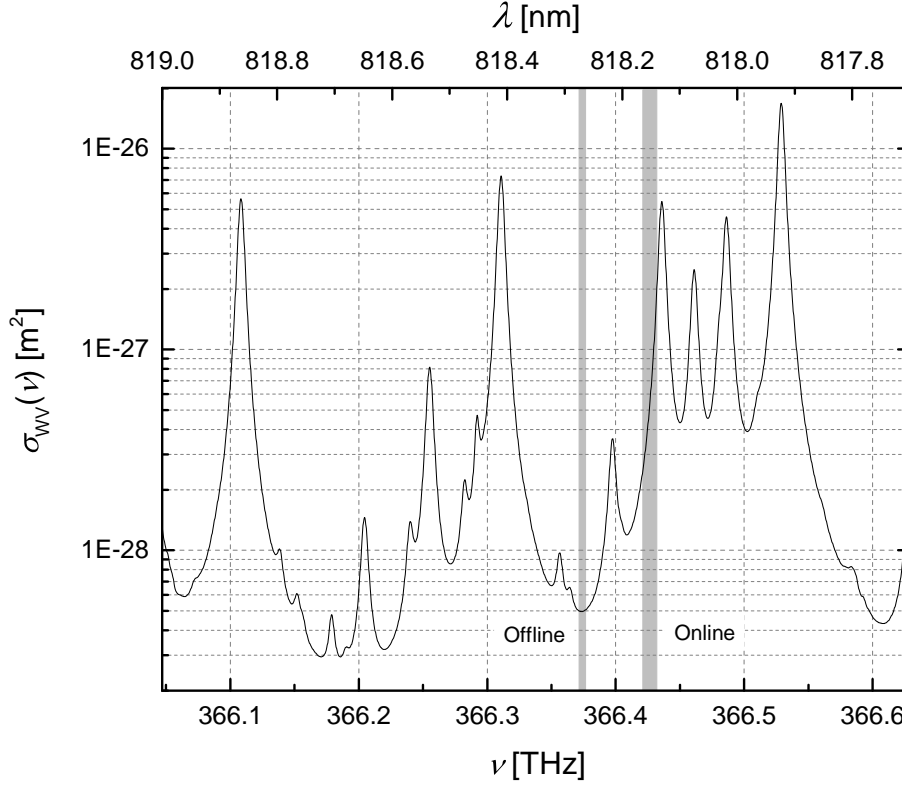


Figure 1: Spectrum of the WV absorption cross-section was plotted in the tuning range of the DFB seed lasers. For the calculation $T = 15^\circ\text{C}$, $p = 1013.25\text{ hPa}$ and $N_{\text{WV}} = 1.7 \times 10^{23}\text{ m}^{-3}$ (ground level of NASA 1976 standard atmosphere (NASA, 1976)) were used as well as spectroscopic parameters from HITRAN 2012 (Rothman et al., 2013). The grey bars indicate the online and offline frequency regions used for the measurements presented in this work below.

with N_{WV} the water vapor number density. Taking the two backscatter signals at the two laser frequencies with different WV absorption, calculating the ratio and solving it for N_{WV} yields the DIAL equation

$$N_{\text{WV}}(r) = \frac{1}{2 \cdot (\sigma_{\text{on}}(r) - \sigma_{\text{off}}(r))} \frac{d}{dr} \ln \left[\frac{P_{\text{off}}(r) - P_{\text{B,off}}}{P_{\text{on}}(r) - P_{\text{B,on}}} \right] - \quad (5a)$$

$$- \frac{1}{2 \cdot (\sigma_{\text{on}}(r) - \sigma_{\text{off}}(r))} \frac{d}{dr} \ln \left[\frac{\beta_{\text{par}}(r) + \beta_{\text{mol,off}}(r) \cdot A(\nu_{\text{off}}, r)}{\beta_{\text{par}}(r) + \beta_{\text{mol,on}}(r) \cdot A(\nu_{\text{on}}, r)} \right] \quad (5b)$$

with

$$A(\nu_i, r) = \frac{\int_{-\infty}^{+\infty} DB(\nu - \nu_i, r) \Gamma_{\text{WV}}(\nu, r) F_{\text{R}}(\nu) d\nu}{\Gamma_{\text{WV}}(\nu_i, r) F_{\text{R}}(\nu_i)} \quad (6)$$

the transmission ratio $A(\nu_i, r)$ with the index i for the online and the offline laser frequency, respectively.

The first term (5a) of the DIAL equation describes the well-known solution of Schotland (1966, 1974). This approximation is valid if $\beta_{\text{par}} \gg \beta_{\text{mol}}$ and the second term can be neglected. The second term (5b) is the so-called Rayleigh-Doppler (RD) correction term which considers the change of the radiation spectrum within the Rayleigh scattering process due to Doppler broadening. More details regarding the RD effect are given in Sect. 1.3.

Considering only the Schotland approximation of the DIAL equation shows that besides the measured two lidar signals only the water vapor absorption cross-section σ_{WV} at the online and offline laser frequencies are required. $\sigma_{\text{WV}}(\nu_i)$ needs to be known very accurately as the relative error of the effective absorption cross-section $\sigma_{\text{eff}} = \sigma_{\text{on}} - \sigma_{\text{off}}$ transfers directly to the relative error of the WV number density N_{WV} according to Wulfmeyer and Walther (2001a,b) with

$$\frac{\Delta N_{\text{WV}}}{N_{\text{WV}}} = \frac{\Delta \sigma_{\text{eff}}}{\sigma_{\text{eff}}} . \quad (7)$$

To keep the error due to the absorption cross-section small, there are two possibilities:

- 1) Calculation of σ_{WV} as accurate as possible. For this the latest compilation of the High-resolution TRANsmission molecular absorption database (HITRAN) is used. A study about the sensitivity of σ_{WV} regarding T , p , and N_{WV} uncertainties within the calculations was performed. According to the study, a pressure uncertainty of 1 % and a temperature uncertainty of 1 K result in a total uncertainty of the WV DIAL data analysis procedure of smaller than 1.4 % up to 3 km and 1.8 % up to 10 km altitude. This is sufficient for most applications and exceeds the development goals of the UHOH DIAL system, which are summarized in Wagner et al. (2013). A detailed publication on this study is planned.

- 2) The laser frequency ν – especially ν_{on} – needs to be tuned very accurate and stabilized as good as possible. A new concept of a seed laser system based on distributed feedback (DFB) lasers for the laser transmitter was developed and is presented in Sect. 2.2.

1.3 The Rayleigh-Doppler Effect

The exact DIAL equation (Eq. (5)) contains the Rayleigh-Doppler correction term to take into account the effect of the changed laser radiation spectrum after Rayleigh scattering. Due to the thermal motion of the atoms and molecules, the laser radiation is Doppler broadened. The Doppler broadening DB of the spectrum depends on the temperature T and follows a Gaussian function with

$$DB(\nu, r) = \frac{1}{b_{\text{mol},i}(r)} \sqrt{\frac{4 \ln 2}{\pi}} \times \exp \left(-4 \ln 2 \left(\frac{\nu - \nu_i}{b_{\text{mol},i}(r)} \right)^2 \right) \quad (8)$$

with a full width at half maximum (FWHM) of

$$b_{\text{mol},i}(r) = \frac{4\nu_i}{c} \sqrt{\frac{2 \ln 2 R T(r)}{M_{\text{air}}}} \quad (9)$$

with ν_i indicating the laser frequency, the speed of light c , the general gas constant R , and the molecular mass of dry air M_{air} . In the discussion throughout this section, the range r written in the equations is equivalent to the height.

Due to the broadening, the radiation is absorbed differently on the return path from the scatterers than on the forward path to the scatterers. In Fig. 2 the absorption cross-section was plotted along with three laser frequencies (dashed lines). To study the frequency sensitivity, three laser frequencies are selected and located as offline in a minimum of absorption and as online at the peak and on the slope of the absorption line. The selected absorption peak is located at a frequency of $\nu_{\text{peak}} = 366.436022$ THz (the corresponding vacuum wavelength is $\lambda_{\text{peak}} = 818.304$ nm). The slope frequency is the online frequency of the DIAL measurements used in the publications of Muppa et al. (2016) and Wulfmeyer et al. (2016). The broadened laser spectrum after Rayleigh scattering is also illustrated in Fig. 2. $\sigma_{\text{WV}}(\nu, r)$ and $DB(\nu, r)$ are calculated for a height of 1200 m. Equation (6) calculates the transmission ratio A of the return and the forward light path. Figure 3 shows vertical profiles of the transmission ratio from the ground up to 1400 m. The profile of the laser frequency at minimum absorption confirms the assumption for the offline signal that the RD effect is not critical and $A(\nu_{\text{off}}, r) = 1$ is valid. The two online frequencies show an increasing effect (increasing deviation from 1) with height but larger for the frequency at the peak than for the one on the slope. Additional, the ratio is greater than one for the peak frequency and lower than one for the frequency on the slope. The reason for this behavior is that at the peak both wings of the broadened spectrum are less absorbed. On the slope one wing is more and the other is less absorbed. For selected frequencies on the slope the more and less absorption along the wings can compensate each other and no RD effect appears at all for these frequencies. These frequencies are located at the turning point on the slope of the absorption line. Figure 4 shows the absorption spectrum for the here considered absorption line with the second derivative and the transmission ratio

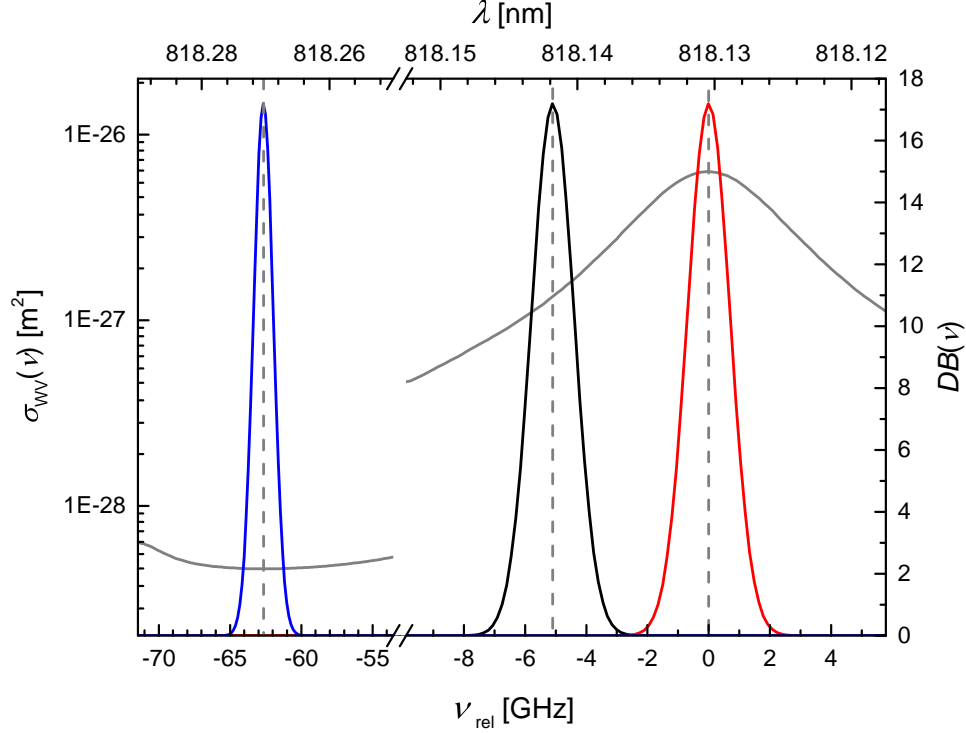


Figure 2: Absorption spectrum of water vapor (grey) with three laser lines (dashed) of the transmitted laser radiation for frequencies in a minimum of absorption as well as at the peak and on the slope of the absorption line. The blue, black, and red curves illustrate the broadened spectrum due to the RD effect. The frequencies ν_{rel} are given relative to the frequency of the absorption peak at $\nu_{\text{peak}} = 366.436022$ THz. σ_{WV} and DB are calculated with respect of a height of 1200 m in a standard atmosphere modified with ground level values of $T = 9.9^\circ\text{C}$, $p = 1017.0$ hPa and $N_{\text{WV}} = 1.7 \times 10^{23} \text{ m}^{-3}$.

A in the panels below. The 1-crossing of A corresponds with the zero-crossing of the second derivative. However, the turning points of the curvature are not fix throughout the atmosphere as the linewidth of the absorption line decreases with increasing height. Nevertheless, whether A is greater or lower than one depends on the balancing effect of the two broadening parts and its maximum is found at the frequency of the peak of the absorption line. The reduction of the RD effect by changing the online frequency from the peak to the slope is for the here shown case of about 90 % and tuning to the slope is recommended to reduce the RD effect.

For reasons of laser stabilization within the DIAL transmitter, online frequencies were recently mostly selected at the peak frequency of absorption lines. Ansmann (1985) and Ansmann and Bösenberg (1987) assessed the RD effect but only for the peak

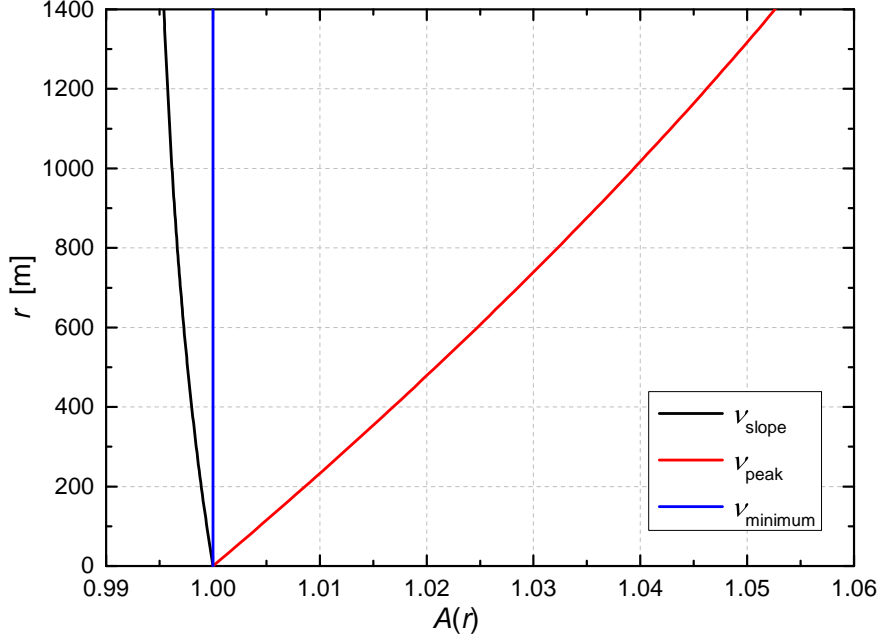


Figure 3: Profiles of the transmission ratio A for the laser frequencies at the peak, on the slope and at the minimum of absorption. For this calculation the range r is equivalent to the height.

frequencies. Here, they investigated that the RD effect needs to be considered where large gradients of the backscatter coefficient and of the temperature occur. However, I could have shown above that tuning the online frequency to the slope of an absorption line reduces the RD effect significantly or that it even vanishes completely for selected frequencies.

A more extended discussion of the RD effect regarding the laser frequency and other sensitivities was presented at the International Laser Radar Conference (ILRC) in New York, USA, in 2015. Based on these results a separate publication is planned.

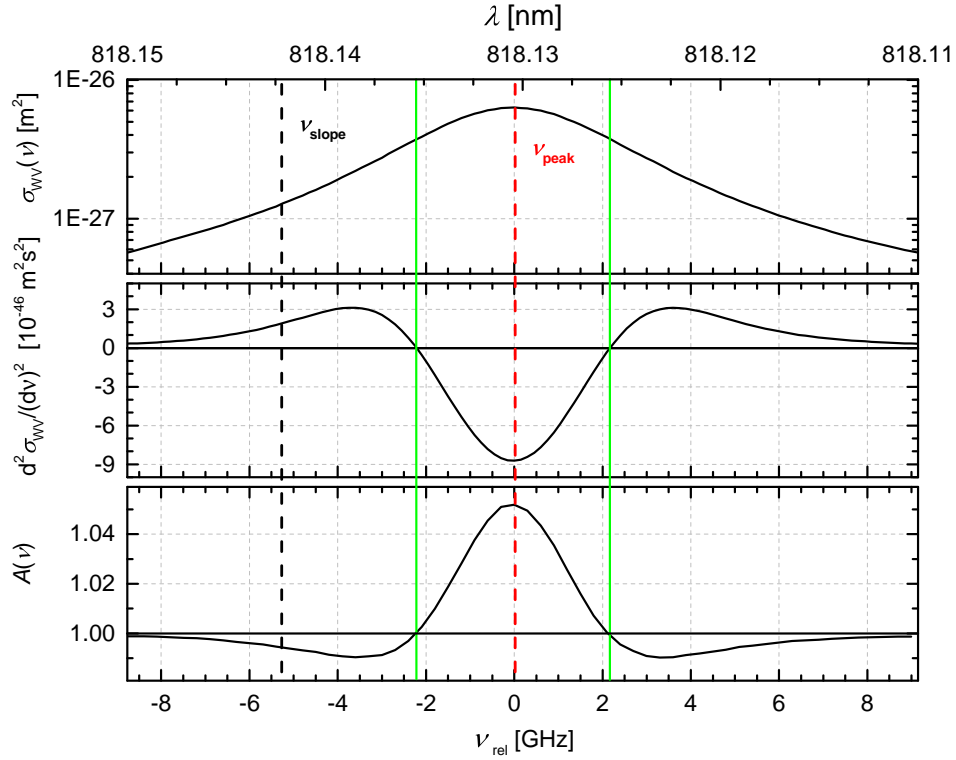


Figure 4: Upper panel: WV absorption spectrum σ_{WV} , middle panel: second derivative of the absorption cross-section, lower panel: transmission ratio A . The curves are calculated for a height of 1200 m standard atmosphere. The frequencies ν_{rel} are given relative to the frequency of the absorption peak at $\nu_{\text{peak}} = 366.436022$ THz. The red and black dashed lines mark the corresponding laser frequencies at the peak and on the slope; the green lines indicate the frequencies where A is equal to 1.

2 UHOH DIAL Setup

The laser transmitter in DIAL systems has to fulfill several requirements regarding the optical specifications of the pulsed laser output to perform DIAL measurements with high accuracy. Critical parameters are, e.g., high frequency stability and high spectral purity. A list of transmitter requirements are in Tab. 2 of Wagner et al. (2013) to be found in Sect. 2.1.

The overall setup of the UHOH DIAL system is depicted in Fig. 5 and consists of three main parts: the laser transmitter, the transmitting-receiving scanner unit, and the data acquisition system. The system can be operated in two configurations: 1) using an optical fiber and a small transmitting telescope with a 20-cm mirror to transmit the laser beam into the atmosphere or 2) using a free-beam path with beam expander and a beam-steering mirror (BSM). A small receiving telescope is optionally installed in addition for vertical measurements. A high-reflection flip mirror (HRFM) is used to switch between the two transmitting configurations. A description of the transmitting-receiving scanner unit and the data acquisition system is given in the publication of Späth et al. (2016) in Sect. 3.1.

The laser transmitter of the UHOH DIAL system consists of four lasers to generate laser pulses at wavelengths around 818 nm with a repetition rate of 250 Hz. The transmitted laser pulses are created in a Ti:sapphire crystal in a ring resonator. The crystal is end-pumped with a frequency-doubled diode-pumped Nd:YAG laser (Ostermeyer et al., 2005). The frequency-control is realized with the injection seeding technique (Wulfmeyer and Bösenberg, 1996; Wulfmeyer, 1998; Barnes and Barnes, 1993; Barnes et al., 1993). The UHOH seed laser system consists of two continuous-wave laser diodes – one for the online wavelength and one for the offline wavelength – which are injected alternately into the Ti:sapphire resonator to control the emitted frequency and to improve the laser specifications. These laser diodes (hereafter called seed lasers) run with superior and precise controllable optical properties, e.g., high frequency stability and narrow linewidth. The injection seeding technique allows to transfer the optical properties of the seed laser to the high-power laser output. The seed beam is toggled between the online and offline seed laser with an optical switch as the online and offline laser pulses are generated in the same Ti:sapphire resonator. The crosstalk of the switch needs to be very low (Späth et al., 2013) because leakage of offline laser light into the Ti:sapphire resonator while online is switched would cause spectral impurity of the Ti:sapphire output. This would distort the measured lidar signals which is very critical especially for the online signal.

With the original design of the DIAL system, a seed laser system with external cavity diode lasers (ECDLs) and a micro-electromechanical fiber switch was developed

by Khalesifard et al. (2009). The laser beams were fiber coupled. Khalesifard et al. (2009) demonstrated that the seeding system fulfilled the requirements. Unfortunately, the performance degraded while operating it in the DIAL system. Particularly, the frequency stability and the seeding power decreased and mode-hops appeared (Schiller, 2008) as well as the optical fiber switch failed regarding the crosstalk specifications. Without functioning optical switch, a DIAL operation only with online seeding was performed which yielded to larger uncertainties.

The design and development of the high-power Ti:sapphire laser transmitter for the UHOH DIAL system is described by Wagner et al. (2013). This publication is inserted in Sect. 2.1. The contribution of the author to this publication was the part about the injection seeders with an upgrade to distributed feedback laser diodes. Furthermore, the author analyzed the presented example measurements of vertical and of the first scanning operation. A more detailed investigation about the performance of the new injection seeding system with DFB laser diodes and an electro-optic deflector (EOD) as fast optical switch is discussed in Späth et al. (2013) in Sect. 2.2.

Since 2010, the Ti:sapphire resonator had undergone a redesign. In 2013, one of the well-performing DFB laser diodes has already been exchanged by a new ECDL. The new ECDL shows a similar satisfying frequency stability but provides in addition higher laser power for injection seeding. Increasing seed laser power becomes more and more important with increasing Ti:sapphire output power. The second DFB seed laser has been replaced in 2014. Also in 2013, a new and suitable optical fiber switch was found and was used in the DIAL system because it is much easier to align in the system. Nevertheless, the DFB laser diodes and the EOD-based optical switch are still available as backup system.

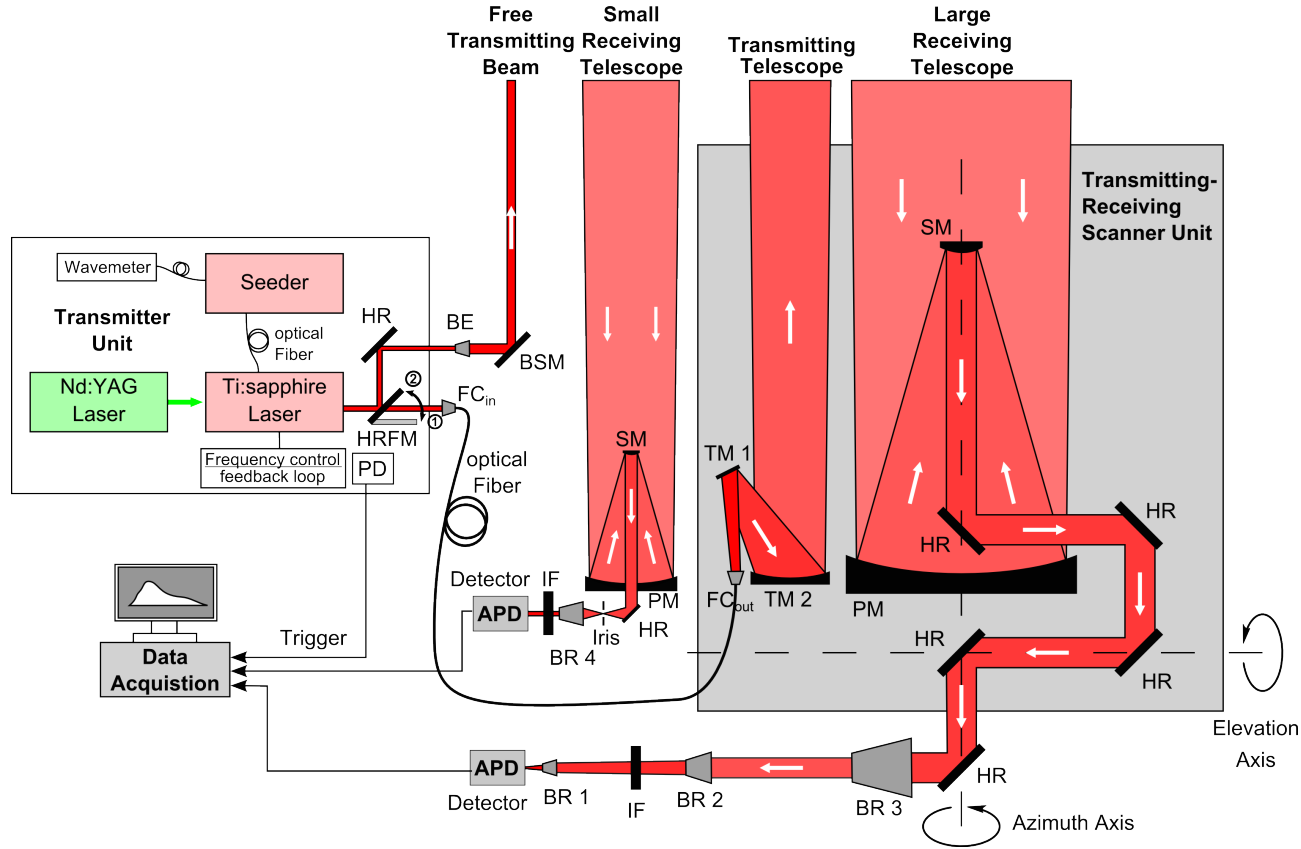


Figure 5: Setup of the UHOH DIAL system for both configurations via optical fiber and via beam steering mirror and free beam path. For vertical measurements an additional small receiving telescope can be used with a second detector. To switch between the two configurations a high-reflexion flip mirror (HRFM) is implemented. Measurements in vertical direction are used in Muppa et al. (2016) and Wulfmeyer et al. (2016). APD – avalanche photo diode, BE – beam expander, BR – beam reducer, BSM – beam-steering mirror, FC – fiber coupler, HR – high-reflection mirror, IF – interference filter, TM – transmitting telescope mirror, PD – photo diode, PM – primary mirror, SM – secondary mirror.

Copyrights

Wagner et al. (2013) shown in Sect. 2.1 on page 17ff:

© 2013 Optical Society of America. One print or electronic copy may be made for personal use only. Systematic reproduction and distribution, duplication of any material in this paper for a fee or for commercial purposes, or modifications of the content of this paper are prohibited ⁷.

Späth et al. (2013) shown in Sect. 2.2 on page 33ff was published under the Creative Common License CC BY-NC-ND 3.0⁸.

This is an open-access article distributed under the terms of the Creative Commons Attribution-NonCommercial-No Derivative Works License, which permits non-commercial use, distribution, and reproduction in any medium, provided the original author and source are credited.

⁷https://www.osapublishing.org/submit/review/copyright_permissions.cfm

⁸<http://creativecommons.org/licenses/by-nc-nd/3.0/>

High-power Ti:sapphire laser at 820 nm for scanning ground-based water–vapor differential absorption lidar

Gerd Wagner,^{1,*} Andreas Behrendt,¹ Volker Wulfmeyer,¹
Florian Späth,¹ and Max Schiller²

¹Institute of Physics and Meteorology (IPM), University of Hohenheim (UHOH), Garbenstrasse 30,
Stuttgart 70599, Germany

²Current affiliation: Fraunhofer-Institute of Optronics, System Technologies and Image Exploitation (IOSB),
Gutleuthausstrasse 1, Ettlingen 76275, Germany

*Corresponding author: Gerd.Wagner@uni-hohenheim.de

Received 18 December 2012; accepted 22 February 2013;
posted 6 March 2013 (Doc. ID 182038); published 10 April 2013

The Ti:sapphire (TISA) laser transmitter of the mobile, three-dimensional-scanning water–vapor differential absorption lidar (DIAL) of the University of Hohenheim is described in detail. The dynamically-stable, unidirectional ring resonator contains a single Brewster-cut TISA crystal, which is pumped from both sides with 250 Hz using a diode-pumped frequency-doubled Nd:YAG laser. The resonator is injection seeded and actively frequency-stabilized using a phase-sensitive technique. The TISA laser is operating near 820 nm, which is optimum for ground-based water–vapor DIAL measurements. An average output power of up to 6.75 W with a beam quality factor of $M^2 < 2$ is reached. The pointing stability is $< 13 \mu\text{rad}$ (rms), the depolarization $< 1\%$. The overall optical–optical conversion efficiency is up to 19%. The pulse length is 40 ns with a pulse linewidth of < 157 MHz. The short- and long-term frequency stabilities are 10 MHz (rms). A spectral purity of 99.9% was determined by pointing to a stratus cloud in low-elevation scanning mode with a cloud bottom height of ≈ 2.4 km. © 2013 Optical Society of America

OCIS codes: (280.1910) DIAL, differential absorption lidar; (140.3580) Lasers, solid-state; (140.3590) Lasers, titanium; (010.3640) Lidar; (120.0280) Remote sensing and sensors.
<http://dx.doi.org/10.1364/AO.52.002454>

1. Introduction

Differential absorption lidar (DIAL) is an active remote sensing technique for measuring trace gases like water vapor or ozone in the atmosphere [1–4]. In contrast to passive remote sensing with Fourier-transform infrared (FTIR) and microwave (MW) spectroscopy, DIAL achieves data with higher spatial and temporal resolution because the signal-to-noise (SNR) ratio can be scaled by transmitter power and receiver aperture. Furthermore, the analysis of

DIAL signals does not contain calibration constants; the required information on absorption cross sections at the online and offline wavelengths can be taken from databases like, e.g., the high-resolution transmission molecular absorption database (HITRAN) [5]. This intrinsic characteristic of the DIAL technique results in high accuracy of the measured data [6–9]. Recent water–vapor DIAL intercomparisons confirmed this advantage [10–12] and led to the acknowledgement of the DIAL technique as one of the water–vapor reference standards of the World Meteorological Organization (WMO) [13].

Remote sensing of water vapor using lidar techniques is very promising for advancing our

1559-128X/13/112454-16\$15.00/0
© 2013 Optical Society of America

understanding of atmospheric processes. Among others, the following main fields of scientific interest have been identified. First, the investigation of land-surface exchange and transport processes, especially in complex terrain, is expected to benefit from the use of water-vapor lidar data; land-surface-vegetation-atmosphere models have still strong deficiencies to simulate fluxes in dependence of the large-scale forcing conditions and of soil and vegetation properties [14–17]. Second, water-vapor lidar will be advantageous for studies of water-vapor turbulence characteristics in the atmospheric boundary layer in dependence of local and large-scale forcing conditions [18–21]. Third, the development and structure of convergence lines leading to convection initiation can be studied in detail with water-vapor lidar [22]. Fourth, data assimilation of water-vapor profiles provided by lidar showed benefits for weather forecasting and regional reanalyses [23–25].

Two independent lidar techniques emerged for these purposes: Besides DIAL, also water-vapor Raman lidar. Water-vapor Raman lidar [19,26–28] is a technique that is based on the detection of the vibrational Raman signal of atmospheric water vapor together with a Raman reference signal of nitrogen and/or oxygen. Water-vapor Raman lidar reached already high maturity with automatic instruments being operated at some sites [29] and even commercial systems being available. The performance of water-vapor Raman lidar, however, is limited due to two effects. First, the Raman backscatter signals are 2–3 orders of magnitude lower than the elastic backscatter signals used in water-vapor DIAL systems. Especially during daytime, this leads to reduced performance with respect to temporal and spatial resolution even though water-vapor Raman lidars use quite powerful commercial laser transmitters—nowadays typically frequency-doubled or tripled Nd:YAG lasers. Second, Raman lidar needs a calibration. Calibration techniques have been developed in combination with, e.g., MW radiometers [27,28], but this approach requires a combination of sensors in order to achieve well-calibrated water-vapor profiles.

In contrast to Raman lidar, water-vapor DIAL requires special laser transmitters in order to fulfill the spectral demands related to water-vapor DIAL. Such lasers are not yet commercially available and have been developed by only a few research institutions. Clearly, the challenge of the water-vapor DIAL technique lies in the development of these transmitters. The set of high requirements that have to be fulfilled include high-average power, high single-shot pulse energy, high spectral purity (SP), high shot-to-shot frequency stability, and a narrow spectral bandwidth of the transmitted laser radiation.

In the following, we introduce a number of present water-vapor DIAL systems and highlight their properties. NASA (National Aeronautic and Space Administration; USA) operates the airborne LASE

system (*Lidar Atmospheric Sensing Experiment*) based on a Ti:sapphire (TISA) laser [6,30,31] with an average output power of 1 W. The laser is injection seeded and actively stabilized. LATMOS (Laboratoire Atmosphères, Milieux, Observations Spatiales; France) uses an Alexandrite laser on the airborne platform LEANDRE II [32–35] (*Lidar pour l'Etude des interactions Aérosols Nuages Dynamique Rayonnement et du cycle de l'Eau*). The transmitter has an average output power of 0.5 W. The resonator contains a Lyot filter and two etalons for frequency selection. DLR (German Aerospace Center) uses optical parametric oscillator (OPO) technology based on KTP (potassium titanyl phosphate) on the airborne platform system WALES [36,37] (*Water-vapor Lidar Experiment in Space*). The OPO has an output power of 4.5–6 W and the resonator is injection seeded. MPI (Max-Planck Institute for Meteorology, Hamburg; Germany) deploys for a ground-based system an Alexandrite-based laser [4,38–41], and more recently a TISA laser [41]. The TISA laser has an output power of 0.93 W and the ring resonator is injection seeded. IMK IFU (Karlsruhe, Germany) exports for a ground-based system OPO technology with a TISA amplifier [42]. An average output power of 5 W is stated. Another category of water-vapor DIAL transmitters use amplified diode lasers. These systems are very compact, but their application is so far limited to the lower troposphere. NOAA (National Oceanic and Atmospheric Administration, USA) applies an amplified distributed feedback (DFB) diode laser in the ground-based CODI (*compact DIAL*) system (average power 0.9–1.5 mW) [43,44]. The University of Adelaide (Australia) developed a ground-based master laser system based on an amplified Fabry–Perot diode laser with an average power of 0.75 mW [45]. Montana State University (USA) incorporates amplified external cavity diode lasers (ECDLs) with an average power of up to 70 mW [46–48]. Table 1 summarizes all systems we are aware of and lists their transmitter and spectral properties, respectively.

At our institute, we decided to build a laser transmitter based on TISA for the use within in a ground-based scanning system. TISA is a well-known laser material with unique optical and mechanical properties [49,50]. It is very flexible due to its broad tuning range (670–1100 nm), and efficient due to using solid-state frequency-doubled Nd:YAG lasers as the pump source. Additionally, manageable resonator concepts and frequency selections methods can be used to achieve high-power, single-mode, and single-frequency operation.

The scope of this paper is to describe the experimental realization of a high-power water-vapor DIAL transmitter based on a TISA laser. We show its setup and characterize the overall system performance in its laboratory configuration and during the COPS (*Convective and Orographically-induced Precipitation Study*) [16,22,51,52] and the FLUXPAT (*integrative characterization of patterns*

Table 1. Comparison of Operated Water-Vapor DIAL Systems^a

System, Transmitter Type	Transmitter Properties	Spectral Narrowing Technique	Spectral Properties
LASE [6,7,30,31] TISA laser	$P = 1$ W $E_p = 100\text{--}150$ mJ $f = 10$ Hz	Injection seeding Active resonator stabilization	$\lambda = 813\text{--}818$ nm $\Delta\omega < 114$ MHz, $\Delta\nu \pm 159$ MHz SP > 99%
LEANDRE [32–35] Alexandrite laser	$P = 0.5$ W $E_p = 50$ mJ $f = 10$ Hz	Intracavity Lyot filter, angle-tuned Etalon, piezo-controlled etalon	$\lambda = 727\text{--}770$ nm $\Delta\omega \approx 738$ MHz, $\Delta\nu \approx 142$ MHz SP > 99.99%
DLR WALES [37] KTP OPO	$P = 4.5\text{--}6$ W $E_p = 45\text{--}60$ mJ $f = 100$ Hz	Injection seeding Active resonator stabilization	$\lambda = 935$ nm $\Delta\omega = 150$ MHz, $\Delta\nu \leq 30$ MHz SP $\geq 99.9\%$
MPI [41] TISA laser	$P = 0.93$ W $E_p = 18.6$ mJ $f = 50$ Hz	Injection seeding Active resonator stabilization	$\lambda = 820$ nm $\Delta\omega = 22.5$ MHz, $\Delta\nu$: n.s. SP $\leq 99.97\%$
IMK IFU [42] OPO with TISA amplifier	$P = 5$ W $E_p = 250$ mJ $f = 20$ Hz	–	$\lambda = 700\text{--}950$ nm $\Delta\omega = 130\text{--}250$ MHz, $\Delta\nu \pm 5$ MHz SP > 99.9%
UHOH DIAL [53,56, this article] TISA laser	$P = 6.75$ W $E_p = 27$ mJ $f = 250$ Hz	Injection seeding Active resonator stabilization	$\lambda = 817\text{--}825$ nm $\Delta\omega < 157$ MHz, $\Delta\nu < 10$ MHz SP = 99.9%
CODI [43,44] Amplified DFB diode laser	$P = 0.9\text{--}1.5$ mW $E_p = 0.15$ μ J $f = 6\text{--}10$ kHz	–	$\lambda = 823$ nm $\Delta\omega \approx 12$ MHz, $\Delta\nu \pm 80$ MHz SP > 99.9%
University of Adelaide [45] Amplified Fabry–Perot diode laser	$P = 0.75$ mW $E_p \approx 500$ nJ $f = 1.5$ kHz	–	$\lambda = 823$ nm $\Delta\omega =$ n.s., $\Delta\nu \pm 1$ MHz SP: n.s.
Montana State University [46–48] Amplified ECDL diode laser	$P = 70$ mW $E_p = 7$ μ J $f = 10$ kHz	–	$\lambda = 828$ nm $\Delta\omega = 0.426$ MHz (seed lasers) $\Delta\nu \pm 55$ MHz, SP $\leq 99.96\%$

^aTransmitter properties: average output power (P), output pulse energy (E_p), pulse repetition rate (f). Spectral properties: wavelength region (λ), linewidth ($\Delta\omega$), frequency stability ($\Delta\nu$), spectral purity (SP). n.s., not specified.

in the atmospheric boundary layer) [53,54] field campaigns in 2007 and 2009, respectively.

The paper is structured as follows: Section 2 introduces the requirements set to a water-vapor DIAL transmitter and the technological challenges for reaching them. Section 3 gives an overview of the water-vapor DIAL system of IPM UHOH. The TISA laser performance is discussed in Section 4. A method to determine the SP by use of an atmospheric cloud measurement and its results are presented in Section 5. DIAL measurement examples are shown in Section 6. The paper closes with a summary in Section 7.

2. Requirements and Laser Transmitter Design Concept

Several important specifications have to be fulfilled for the successful operation of a water-vapor DIAL transmitter. The complete set of requirements is shown in Table 2. The requirements have been derived based on error propagation and performance simulations [55,56].

The selection of the suitable frequency conversion technique starts with the operating wavelength of the transmitter. For ground-based water-vapor DIAL measurements, the wavelength regime around 820 nm can be reached with TISA. This region

provides a large range of suitable absorption lines covering different absorption cross sections which can be selected depending on the humidity present in the atmosphere.

The procedure for designing a TISA laser intended as a water-vapor DIAL transmitter was presented in [57] for stable and unstable resonator configurations. Thus, we will restrict ourselves to a summary here. Our starting point in the laser design was the simulation of thermal effects in the laser crystal, especially for end-pumped configurations. The thermal lensing effect has to be considered in the resonator design [58–63], e.g., the placement of optical components inside the resonator has to be adjusted to avoid optical damages, the radius of the pump beam on the crystal should be adapted to eigenmode radius of the resonator, and the resonator should be dynamically-stable. The next step of the design considerations involves the choice of the optical resonator type.

Using a medium with polarization-dependent gain like TISA, a unidirectional ring must be used for preventing a modulated axial gain distribution (spatial hole burning). Only this setup ensures single-mode operation at high power [39,40,64]. Further spectral narrowing is achieved with a birefringent filter (BF) and injection seeding. Active control of the resonator length is required in order to suppress

Table 2. Transmitter Requirements for Ground-Based Water-Vapor DIAL from Ground to the Upper Troposphere According to [55,56], and Achieved Transmitter Specifications of the UHOH DIAL Transmitter^a

Parameter	Requirement	Achieved
Energy and Efficiency		
Average power	>1 W	6.75 W
Pulse energy	4–10 mJ	27 mJ
Repetition rate	100–250 Hz	250 Hz
Pulse duration	<200 ns	40 ns
Frequency switch	Pulse-to-pulse on- /off-line	Yes
Mode quality		
M^2	<2	<2
Pointing instability	<15 μ rad rms	<13 μ rad rms
Spectral properties of the online frequency		
Wavelength range (wavenumber)	Within 815–825 nm (12270–12121 cm^{-1})	817–825 nm
Spectral purity	>99.5% [40]	99.9%
Bandwidth	<400 MHz	< 157 MHz
Frequency instability	<210 MHz rms	<10 MHz rms
Coarse tuning range	1–3 nm typically for reaching suitable absorption lines under different atmospheric conditions	Yes

^aIf these requirements are met, the relative error in water-vapor measurements due to transmitter performance is <3% over the entire range.

multilongitudinal modes and to meet the desired frequency stability of <210 MHz rms. The expected laser performance can be calculated using a rate equation approach and allowing the output coupler (OC) to be optimized for maximum output power at a given pump power level. The SP of the TISA laser can be modeled using a dual-mode approach. The results of the thermal module, the beam propagation module, the performance module, and the spectral module described in [57] were applied for the TISA laser transmitter development presented here.

3. DIAL Transmitter

The scheme of the DIAL system at UHOH is shown in Fig. 1. A DIAL system mainly consists of three units: (1) the laser frequency converter, (2) telescopes for transmission and receiving, and (3) a data acquisition system. The complete UHOH DIAL

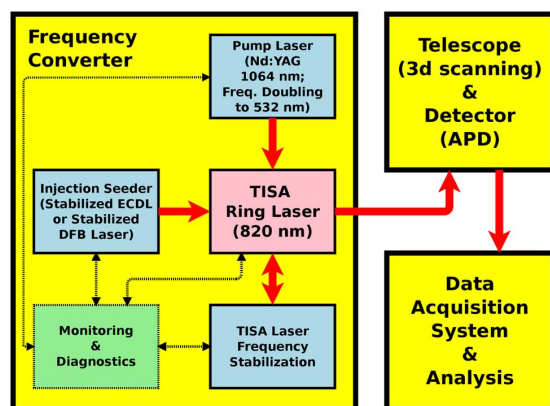


Fig. 1. Scheme of DIAL system. A DIAL system consists of three units: frequency converter, receiver (telescope), and data acquisition system (including data analysis). APD, avalanche photodiode.

system is mounted in a 12 m long trailer. The trailer comprises an energy module with supply units and a laboratory unit [53,65,66]. The air-conditioned laboratory unit contains the transmitter and data acquisition systems. The scanner unit with the transmitting and receiving telescopes is located in a second open-air compartment.

The frequency converter consists of the TISA laser, which is excited by a high-power frequency-doubled, diode-pumped Nd:YAG laser [67,68]. The TISA ring laser is injection seeded and actively stabilized using the technique of Wulfmeyer [69] (U.S. Patent No. 6,633, 596 B1). Each unit is monitored during operation. The pump laser of the TISA laser, the injection seeder (IS) system, the TISA laser breadboard and its frequency stabilization are described in the following.

A. Pump Laser of the TISA Laser

The TISA laser crystal is excited with a diode-pumped, pulsed, frequency-doubled Nd:YAG laser as the pump source. Diode-pumped systems are much more stable than flash-lamp-pumped systems regarding the laser output energy and the energy distribution within the laser profile. Furthermore, they show higher overall wall-plug efficiencies. Maintenance work, cooling efforts, and costs are also significantly reduced.

Our pump laser has undergone two development stages in 2006 and 2011 in collaboration with Innovative Berlin Laser GmbH [70] since its original setup in 2004 [67,68]. The optical setup and the beam profile of the pump laser are depicted in Figs. 2 and 3(a), respectively. In 2006, the laser setup was changed from a bar system to a breadboard for overall stability improvement. Simultaneously, the master oscillator was redesigned to a linear resonator in twisted-mode configuration. The resonator length after the modification was

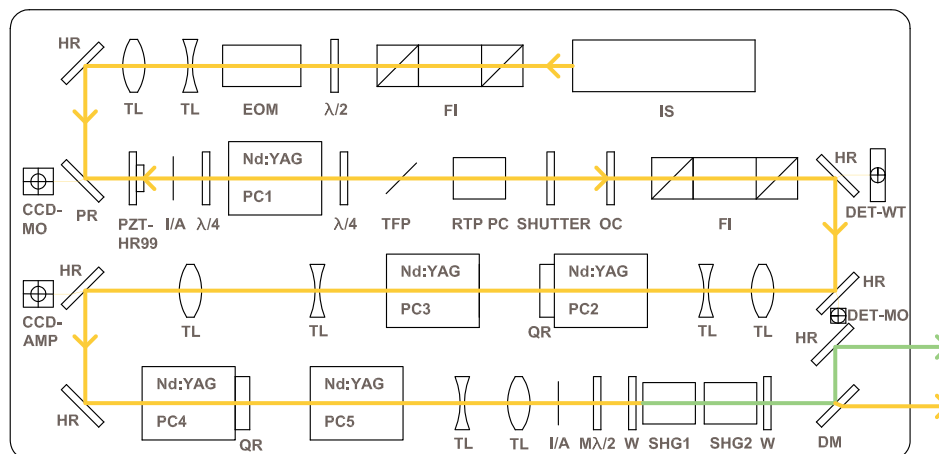


Fig. 2. Pump laser setup on breadboard (dimensions: 120 cm \times 60 cm). Master oscillator power amplifier (MOPA) design. IS, injection seeder; FI, Faraday isolator; $\lambda/2$, half-wave plate; EOM, electro-optical phase modulator; TL, telescope lens; HR, high-reflecting mirror (1064 or 532 nm); PR, partial-reflecting mirror; PZT-HR99, high-reflecting mirror mounted on piezo actuator; I/A, iris/aperture; $\lambda/4$, quarter-wave plate; Nd:YAG PC1, pump chamber of master oscillator; TFP, thin-film polarizer; RTP-PC, RTP Pockels cell; SHUTTER, beam shutter; OC, output coupler (reflectivity $R = 70\%$); Nd:YAG PC2/3, pump chambers of preamplifier stage; QR, quartz rotator (90°); Nd:YAG PC4/5, pump chambers of main amplifier stage; $M\lambda/2$, motorized half-wave plate; W, window; SHG1/2, second-harmonic generation; DM, dichroic mirror; DET-MO, DET-WT, silicon detectors of master oscillator and frequency stabilization; CCD-MO, CCD-AMP, CCD cameras for monitoring beam profiles of master oscillator and preamplifier stage.

77 cm and contained a single pump chamber. The Q-switch was realized with a rubidium titanyl phosphate (RTP) Pockels cell, which can be operated at much lower voltages (850 V) compared to a beta-barium-borate (BBO) Pockels cell (3–5 kV). Optionally, the master laser could be seeded and frequency stabilized using the same phase-sensitive technique of Wulfmeyer [69], as used for the TISA.

In the period of 2006–2010 covering the field campaigns of COPS and FLUXPAT, the master oscillator delivered a maximum power of 1.9 W at 1064 nm at a repetition rate of 250 Hz. After the preamplifier stages (see Fig. 2), a maximum power level of 16.8 W at 1064 nm was reached. The preamplifier stages were operated in a single-pass configuration. Two additional main amplifier stages (single pass) further amplified to 72.5 W. The frequency doubling of the fundamental wavelength was done with two temperature-stabilized BBO crystals and resulted in an average power of >40 W at 532 nm. In addition to the reported specifications [67,68], the polarization of the laser at 1064 nm was specified to be 1.9%–2.9% over the whole power range.

In 2010/2011 the pump laser was redesigned and further system improvements were implemented. The linear master oscillator was replaced by a ring resonator, because a ring resonator has a stability zone that is doubled in width.

B. Injection Seeders of the TISA Laser

For injection seeding, a continuous-wave laser is injected into the TISA resonator. By matching to the TEM_{00} eigenmode, a high seed efficiency can be realized. A single longitudinal resonator mode is favored to build-up and depletes the gain before other

competing modes can reach lasing threshold. As a result, the pulse build-up time and the timing jitter of the pulse are significantly reduced compared to free-running, unseeded operation of the TISA laser. The IS efficiency directly influences the SP of the TISA laser output [41]. The minimum requirements for the seed power can be derived experimentally and by theoretical analyses [57].

We started with the use of commercially available ECDLs (Toptica DL 100 series). A beam profile of the IS is shown in Fig. 3(b). During COPS, the seed laser system of the TISA resonator consisted of two ECDLs, which were frequency-controlled using a He–Ne laser as a reference [71]. One of the ECDLs was tuned to the online wavelength and the other was tuned to the offline wavelength. The seeders were periodically switched using a fast and polarization maintaining optical multiplexer switch. The system showed a frequency stability of ± 20 MHz rms. The output power of a single ECDL was up to 20 mW in the wavelength range of 815–840 nm. A further investigation of the IS system revealed a higher cross talk of the fast multiplexer switch than expected [71]. Therefore, this switch was not used in further experiments. Additionally, the ECDL concept with its grating angle being used to control the frequency showed mechanical stability problems in vibrating environments. During the field experiments COPS and FLUXPAT 2009, the TISA resonator was seeded with only the online seed laser. For the offline-transmitter operation, the online seeder was blocked with a mechanical chopper at a frequency of 125 Hz, and the TISA laser was running freely broadband with a bandwidth of a few nanometers given by the BF and the coatings of the optical components.

After the COPS field campaign, a further IS development was initiated based on DFB lasers [72,73]. The frequency stability of the now used DFB lasers with a standard deviation of only 6.3 MHz is much higher than of ECDLs. As DFB lasers do not contain external cavities, their output performance is much less sensitive to mechanical vibrations and changes in the ambient conditions. DFB lasers are tuned by changing the temperature and laser diode current. A detailed comparison of ECDL and DFB seed lasers can be found in [74]. Although the tuning range of the

DFB lasers of 817.7–819.0 nm is reduced compared to the range of ECDL lasers, it is large enough and covers several suitable water–vapor absorption lines. An IS system using two DFB lasers and an electro-optical deflector instead of an optical multiplexer is currently under investigation [75].

C. Frequency Stabilization of the TISA Laser Resonator

The overall frequency stability of the TISA laser is determined by its passive stability and by the active frequency stabilization. The passive frequency

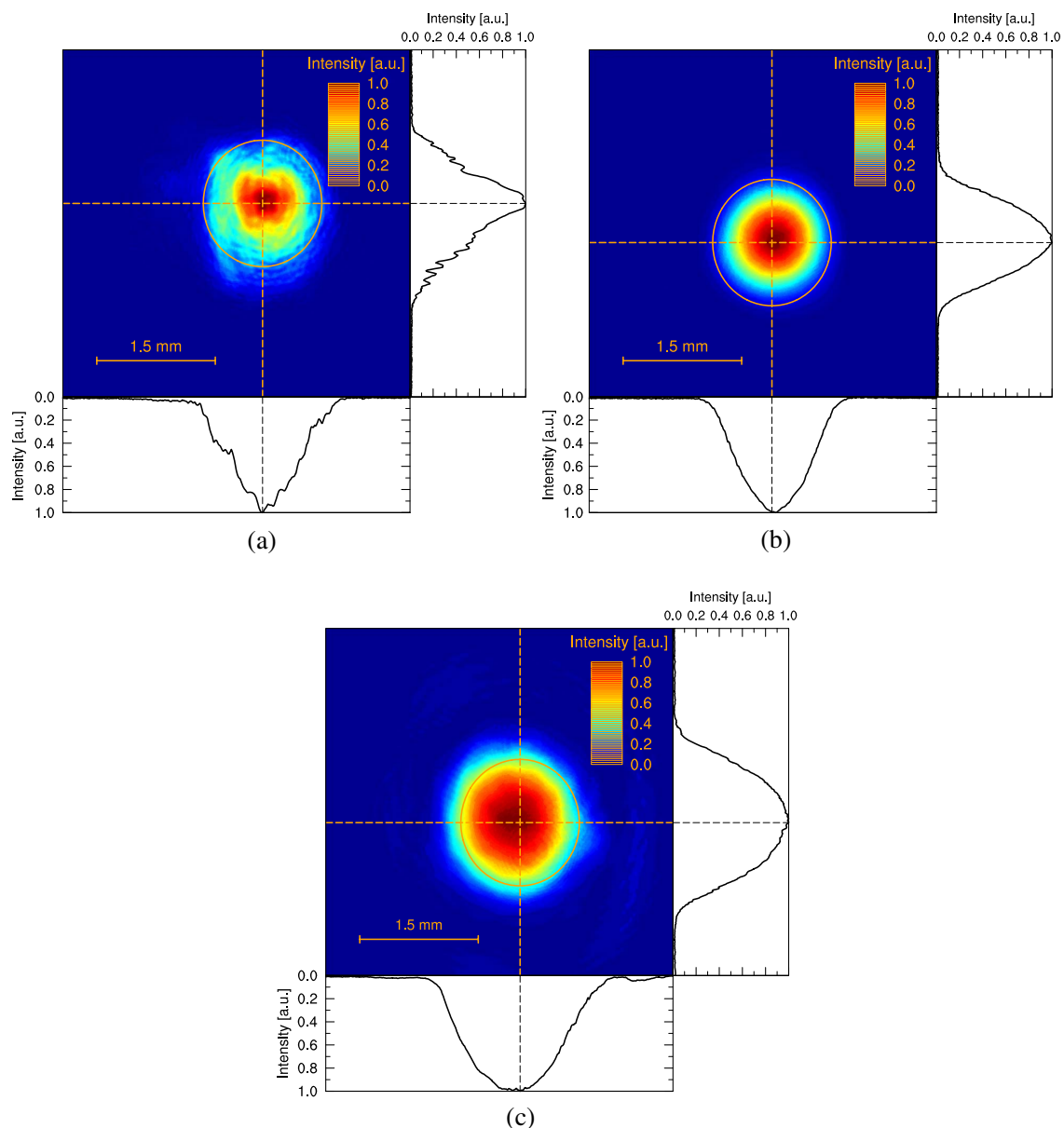


Fig. 3. (a)–(c) Intensity distributions (in arbitrary units) of the pump laser, IS, and TISA laser. (a) Frequency-doubled Nd:YAG pump laser, (b) external cavity diode laser (IS), (c) TISA laser. Circles with diameters of 1.5 mm are shown for comparison.

stability is influenced by the mechanical stability of the laser setup and the environmental changes due to temperature, pressure, and mechanical vibrations. These environmental effects lead to a change in the resonator length. This results in a misaligned resonator and frequency instability or long-term drift, and leads in an extreme case to laser mode hops. Therefore, a stringent requirement for the passive stability is that the TISA laser and any other optical parts should be mounted on a breadboard with a low thermal expansion coefficient. The temperature of the surrounding must be controlled and monitored.

The techniques of stabilizing continuous-wave lasers have been mostly adapted to the application in a pulsed laser. Rahn and Schmitt [76,77] and more recently Schröder *et al.* [78] use the measurement of the pulse build-up time of a *Q*-switched Nd:YAG laser to detect if the slave laser is in resonance with the master laser (IS). A minimization of the pulse build-up time indicates the locking status. If a minimum is not detected, a piezoelectric transducer (PZT) adjusts the resonator length accordingly. This method is also found in commercially available Nd:YAG laser systems.

Another method is to detect an intensity-dependent resonator interference signal, while the PZT is being ramped. The interference signal is given by the IS together with multiple round trips of the seeder inside the resonator. At signal intensity maximum, master and slave cavity are in phase, and the laser *Q*-switch is opened. This technique is called ramp-and-fire [79], and in a modification ramp-hold-fire [80], where the ramp is stopped by a latch signal at resonance. In another variant, the time between each laser pulse is kept constant, but the voltage of the ramp is adjusted according to the resonance signal [41].

It is also possible to use a signed, polarization-dependent error signal to detect the frequency shift of the slave cavity [81]. This technique was introduced by Hänsch and Couillaud [82].

The phase shift between master and slave resonator can be detected by mixing of the phase-modulated reference signal using a phase modulator (PM) or an electro-optical modulator (EOM) with the same signal after a round trip in the slave resonator. By this, a sign-dependent error signal with zero crossing at resonance is obtained. The resonator length can be adjusted accordingly with a PZT. This technique is based on [83] (Pound–Drever–Hall scheme) and was applied for the first time in pulsed lasers by Wulfmeyer *et al.* [69], where a pulsed Tm:LuYAG laser was stabilized to 0.2 MHz rms. Ostermeyer *et al.* [67,68] and Strässer *et al.* [84] incorporated the same technique and achieved a resulting frequency stability of 1.0 MHz rms for the master oscillator of a Nd:YAG laser. An extension using a sample-and-hold circuit resulted in a stability of 0.3 MHz [85]. The stabilization technique according to Wulfmeyer [69] is advantageous, as a phase measurement is used as reference and not the intensity of a resonance. Here,

the resonator is almost always kept at resonance compared to ramp-and-fire methods, and the piezo actuator is less stressed. Additionally, the speed of the stabilization loop is also considerably faster compared to the method of minimizing the pulse build-up time. Fast moving optical elements to detect a resonance are also avoided. The Wulfmeyer technique is therefore considered to be the best method for the frequency stabilization of a pulsed laser under a rough environment.

D. TISA Ring Laser

The TISA laser is based on a dynamically-stable unidirectional ring resonator. The beam propagation inside of the resonator was calculated using the Gaussian beam model and matrix methods [58–63]. The thermal lensing of the Brewster-cut crystal has to be considered in the resonator design process. The finite element analysis (FEA) calculated thermal lensing of the Brewster-cut TISA crystal [57] in comparison with measurements using a probe-beam method is depicted in Fig. 4. The resulting beam propagations and stability zones for tangential and sagittal planes are shown in Fig. 5.

The optical setup of the TISA ring laser on the breadboard is shown in Fig. 6. The Brewster-cut TISA crystal is 20 mm long and has a diameter of 7 mm. It is mounted in a Peltier cooler made of aluminum [57]. Its small-signal absorption coefficient at 514 nm was specified with 1.84 cm^{-1} (Crystal Systems). The crystal is pumped from both sides through dichroic mirrors. The pump beam of the frequency-doubled Nd:YAG laser is adjusted using a telescope (T-L1: +150 mm, T-L2: –75 mm) and divided into two pump branches using a beam splitter (BS). The pump beam radius on the TISA crystal is about 0.9 mm.

The ring resonator consists of five mirrors and has a length of 145 cm. The resonator contains an optical diode ($\lambda/2$ plate, FR: Faraday rotator) to ensure unidirectional counterclockwise propagation. The

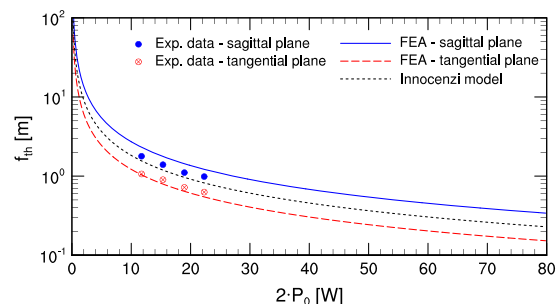


Fig. 4. Focal length of the thermal lens f_{th} of the Brewster-cut TISA crystal for different values of the single-side pump power P_0 at 532 nm. FEA calculated thermal lensing [57] in comparison with experimentally determined values for sagittal and tangential plane, respectively. The thermal lensing was determined from the deflection of a probe beam. Pump-beam radius $\omega_p = 0.75$ mm. Comparison with model of Innocenzi *et al.* [86].

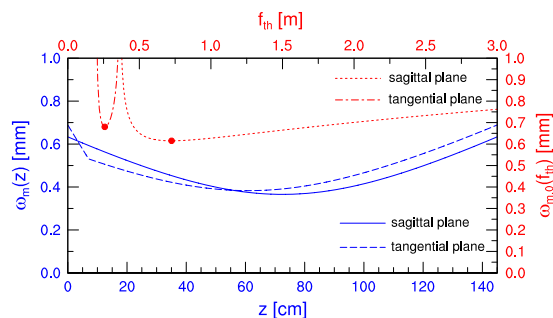


Fig. 5. Beam propagation and stability zone of TISA ring resonator. Mode radius ω_m for resonator position z starting at the first principal plane of TISA crystal. Mode radius $\omega_{m,0}$ on TISA crystal for different values of focal length of thermal lens f_{th} .

propagation direction is indicated by arrows in Fig. 6. Additionally, a four-plate BF is used for coarse frequency selection. The thickness order of the quartz plates is 8-0.5-1-2 mm (manufacturer Bernhard Halle). One of the resonator mirrors (PZT-HR) is mounted on a piezo actuator [Physik Instrumente (PI), piezo model PI010.00H, piezo driver model E507.00X] for the active resonator frequency stabilization. The OC had a reflectivity of 55% or 80%, depending on operating conditions during the two field campaigns. The bandwidth of the TISA resonator mirrors (Laser Components) is about 30 nm (800–830 nm). The TISA laser output is directed

through an additional Faraday isolator (FI) and focused with a lens (L) on an optical fiber, which guides the laser light to the transmission telescope. A thin-film polarizer before the isolator allows to adjust the incident TISA power level on the fiber.

The IS is led through a fiber coupler (FC-SEED) and passes a single lens (L) to adjust the beam radius of the seeder to the eigenmode radius of the resonator. The electronics for the active frequency stabilization according to Wulfmeyer [69] are found on the right-hand side of the breadboard and includes the PM of the IS, the driver of the PM (PM-RF), the detectors for the phase (DET-PM), and the forward resonance detector (WT-DET; located top-left of breadboard). The PM creates two additional sidebands for the active frequency stabilization. The frequency stabilization is implemented as follows in the TISA laser setup (Fig. 6). The IS is phase modulated to create two sidebands with 40 MHz (PM, PM-RF) and is subsequently injected to the laser cavity. The output of the cavity is detected (DET-PM) and mixed with the initial phase signal. The mixed phase signal (WT-PHA) is sent to the electronic circuit. An additional detector is necessary to detect the cavity forward resonance (WT-DET). At cavity resonance, the resulting phase signal after mixing shows a zero crossing at cavity resonance. According to the phase signal and forward resonance detector, the circuit adjusts a piezo driver voltage for the piezo-mounted mirror (PZT-HR).

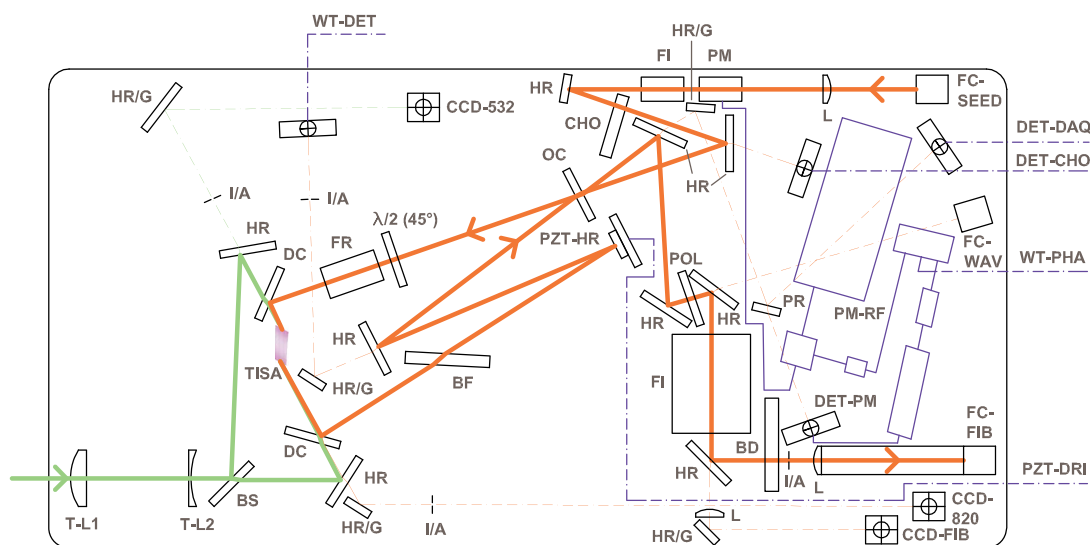


Fig. 6. TISA laser setup on breadboard (dimensions: 120 cm × 60 cm). T-L1, T-L2, pump beam telescope lenses; BS, beam splitter (50:50%); HR, high reflecting mirror (532 or 820 nm); DC, dichroic mirror (shortpass characteristic); TISA, Ti:sapphire crystal; HR/G, high reflecting mirror or gold mirror; I/A, iris/aperture; BF, birefringent filter; FR, Faraday rotator; $\lambda/2(45^\circ)$, half-wave plate aligned to 45° retardation; PZT-HR, high reflecting mirror mounted on piezo actuator; PZT-DRI, piezo actuator driver; OC, output coupler; FI, Faraday isolator; POL, thin-film polarizer; L, lens; BD, beam dump/optical shutter; PM, phase modulator; CHO, optical chopper; PR, partial reflecting mirror; CCD-532, CCD-820, CCD-FIB, CCD cameras for monitoring beam profiles of pump laser, TISA laser (resonator), and TISA laser profile at fiber coupling; FC-SEED, FC-FIB, FC-WAV, fiber couplers of IS, TISA laser fiber, and wavemeter, respectively; DET-PM, silicon detector for phase modulator; PM-RF, phase modulator rf driver; WT-DET, WT-PHA, Wulfmeyer frequency stabilization technique (WT) forward resonance detector and phase signal; DET-CHO, DET-DAQ, silicon detector of optical chopper signal and silicon detector of data acquisition.

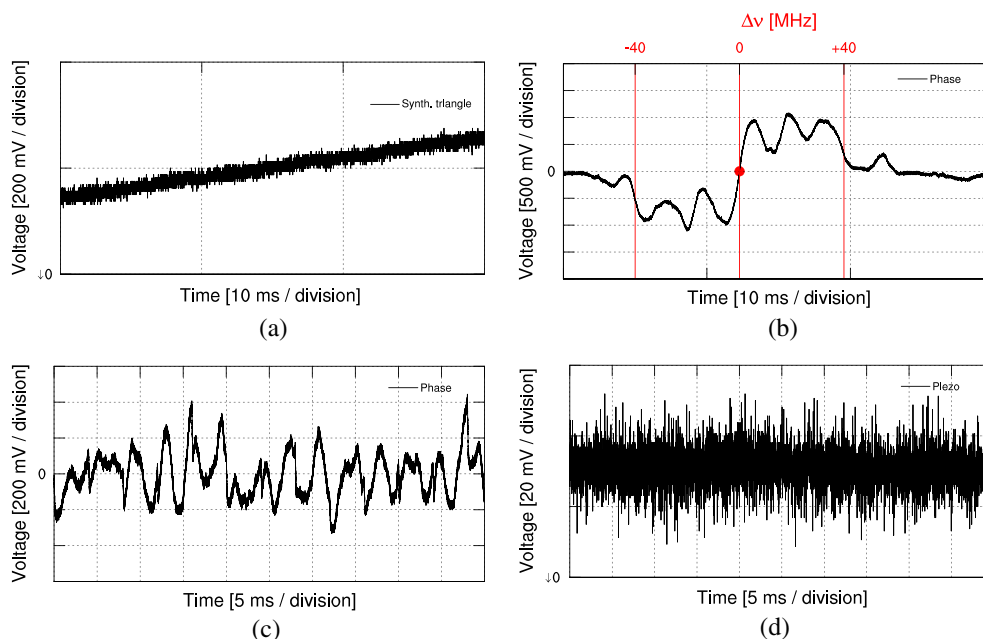


Fig. 7. Active frequency stabilization of resonator. (a) Synthetic triangle signal at piezo voltage driver (zoomed in), (b) resulting phase under triangle signal with zero crossing at cavity resonance with zero frequency shift and frequency shift of ± 40 MHz at location of sidebands, (c) phase signal, and (d) piezo driver signal at closed frequency stabilization loop operation.

For operation of the stabilization loop, it is initially adjusted using a synthetic triangle signal applied to the piezo driver [Fig. 7(a)] and the resulting phase signal is manually shifted to zero crossing at resonance [Fig. 7(b)]. If necessary, the resonator mirrors have to be realigned as the piezo movement usually results in an output power drop of the laser. Therefore, an additional power optimization under the triangle signal applied to the piezo should be performed. After this alignment procedure, the triangle signal is switched off and the feedback loop is closed for operation. Figures 7(c) and 7(d) show the phase signal and the piezo driver signal, respectively.

An FI protects the IS from backreflections from the TISA resonator. The optical chopper (CHO) blocks the seeder for offline (broadband, unseeded) operation. The resonator itself is injection seeded through the OC.

Additional detectors are used to monitor the optical chopper signal (DET-CHO) and the TISA pulse for the data acquisition system (DET-DAQ). CCD cameras (Thorlabs DCC1545M) are used to monitor the positions of the pump beam (CCD-532), the TISA laser or the IS (CCD-820), and the fiber coupling (CCD-FIB). The cameras used the signal leaking through high-reflecting mirrors. The beam direction propagation was fixed using an iris (I/A).

4. Performance of the TISA Laser

The TISA laser has undergone three evolution stages within the years 2005–2009. In the following, we will describe the TISA laser performance in the

laboratory, and during the field campaigns of COPS [16,22,51,52] and FLUXPAT 2009 [53,54].

The initial pump laser in 2005 had an output power of 27 W at 532 nm with 250 Hz [67,68] and a pulse duration of 20 ns FWHM. The beam quality factor was $M^2 = 2.3$. A TISA resonator was built using a Z-shaped (or bow-tie) unidirectional ring configuration with four mirrors. The OC had a reflectivity of 55%. Lasing threshold was at a pump pulse energy of 50 mJ. At a maximum pump pulse energy of 95 mJ, a TISA output pulse energy of 25 mJ with a pulse length of 40 ns was obtained [beam profile shown in Fig. 3(c)]. This corresponds to a TISA laser output power of 6.25 W and an optical–optical conversion efficiency of 26%. The optical overlap η_o is defined as the overlap of the pump beam and the TISA resonator eigenmode at the position of the TISA crystal. Figure 8 shows a comparison of laser performance modeling [57] and experimentally measured laser performance as a function of η_o at a constant dissipative resonator loss of $L = 0.05$. An overlap of $\eta_o \approx 77\%$ was verified in agreement with experimental data.

The pump laser was upgraded in 2006 to achieve a higher output power and a better mechanical stability. The maximum available power was increased to 46 W at 532 nm with 250 Hz at a pulse duration of 19 ns. However, the beam quality factor was decreased from $M^2 = 2.3$ to 4.1. With this new pump configuration, the lasing threshold for the TISA laser significantly increased from 50 to 95 mJ. At a pump pulse energy of 140 mJ, a maximum pulse energy of the TISA laser of 27 mJ was obtained (only 10%

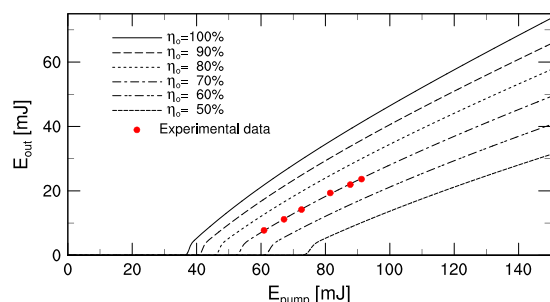


Fig. 8. TISA laser operation: laser performance calculations according to [57] versus experimental results. E_{out} , TISA output pulse energy; E_{pump} , pump pulse energy; η_0 , optical coupling efficiency; L , dissipative resonator loss ($L = 0.05$).

increase compared to the previous setup). This corresponds to a TISA laser output power of 6.75 W and an optical–optical efficiency of 19%. The optical coupling efficiency for this configuration was 50%.

For the COPS field campaign, the pump laser and the TISA were mounted into the trailer. The Z-shaped TISA ring resonator was changed to a configuration using five mirrors (Fig. 6) to obtain a more compact resonator setup. The TISA laser was operated 300 h at a power level of 4–5 W at a pump power of 32 W during the campaign. We recorded the IS and TISA laser transmission through a confocal Fabry–Perot interferometer with a mirror spacing of 10 mm and a free spectral range of 7.5 GHz and a resolution limit of 35 MHz. The fringe patterns of the IS and the TISA laser are shown in Figs. 9(a) and 9(b), respectively. An analysis of the fringe patterns showed that the bandwidth is <157 MHz for the TISA laser. The TISA output wavelength was verified using a wavemeter (HighFinesse Ångström WSU). The frequency stability over a sample period of 120 min of the TISA laser and the IS is depicted in Fig. 10(a). The corresponding histograms are shown in Fig. 10(b). A frequency stability of 10 MHz (rms) was verified, which meets clearly the requirements of <210 MHz.

For the FLUXPAT 2009 campaign, the TISA laser was injection seeded with a DFB laser for the online transmitter operation. The TISA laser operation was reduced to a power level of 2 W at a pump-power level of 22.5 W. The OC reflectivity was increased to 80% to ensure low lasing threshold and reliable operation. The output pulse length was 93.5 ns [Fig. 11(a)], which corresponds to a linewidth of only 8.8 MHz [Fig. 11(b)], which is again much better than the requirement of <400 MHz. Assuming a Gaussian pulse, the theoretical FWHM pulse linewidth is $\Delta\omega_0 = 4.7$ MHz. Figure 11 indicates no mode beating and thus single-mode operation of the TISA laser. Additionally, the working frequency stabilization with zero crossing of the phase signal at resonance (Fig. 7) shows operation at resonance and proves single-frequency operation. Therefore, we can conclude single-mode, single-frequency operation of the TISA laser. An additional and remaining frequency

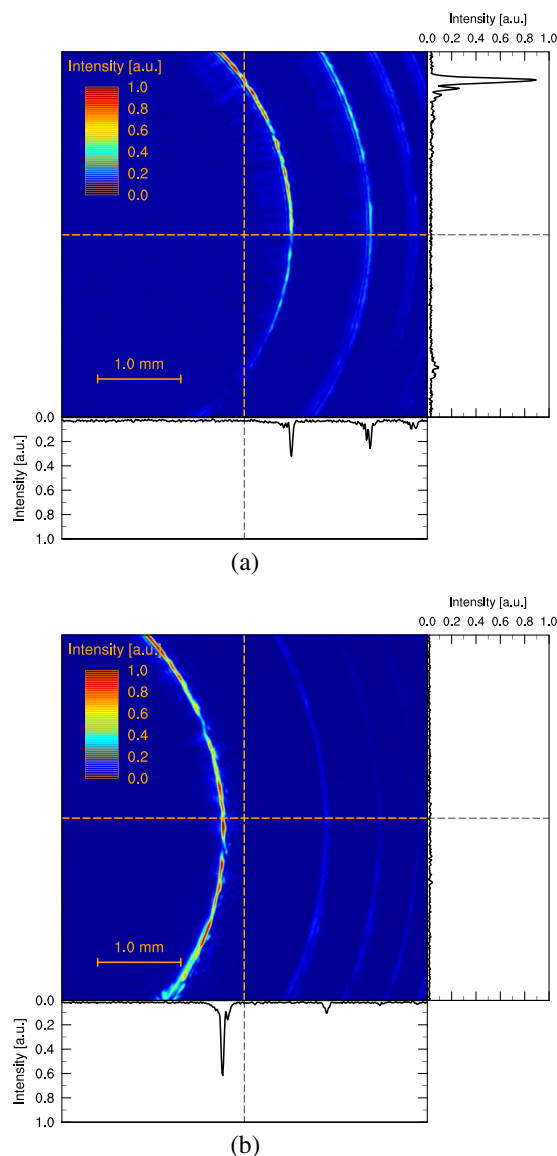


Fig. 9. Fabry–Perot fringe pattern of (a) IS and (b) TISA laser.

chirp contribution to the bandwidth of the laser pulse is attributed due to changes in the refractive index of the TISA laser crystal during the duration of the pump pulse. This contribution cannot be compensated by the frequency stabilization and its general proportion is currently the subject of further investigations.

During FLUXPAT 2009, the output of the TISA laser was coupled using a lens with focal length of +300 mm into a 20 m long optical fiber (Fibertec [87], Berlin, Germany) with a numerical aperture of $NA = 0.2$. The fiber has a diameter of 1000 μm and led the laser radiation to a transmission

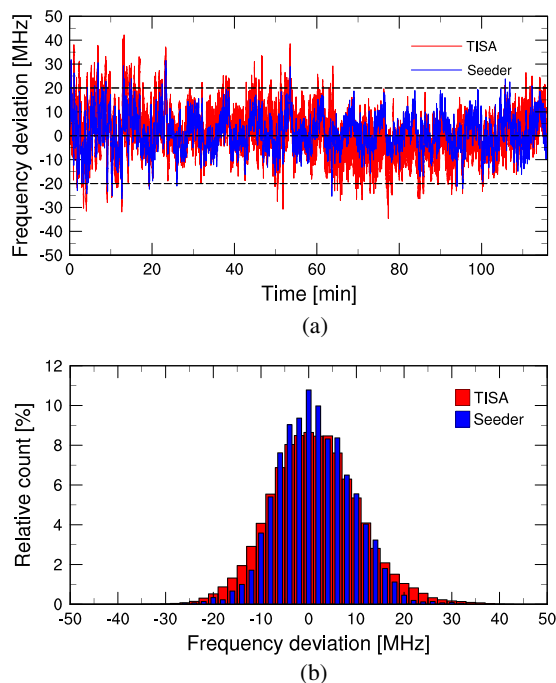


Fig. 10. (a) Frequency stability of TISA laser and IS (standard deviations): $\sigma_{\text{TISA}} = 9.3$ MHz, $\sigma_{\text{seeder}} = 7.8$ MHz; (b) histogram of (a).

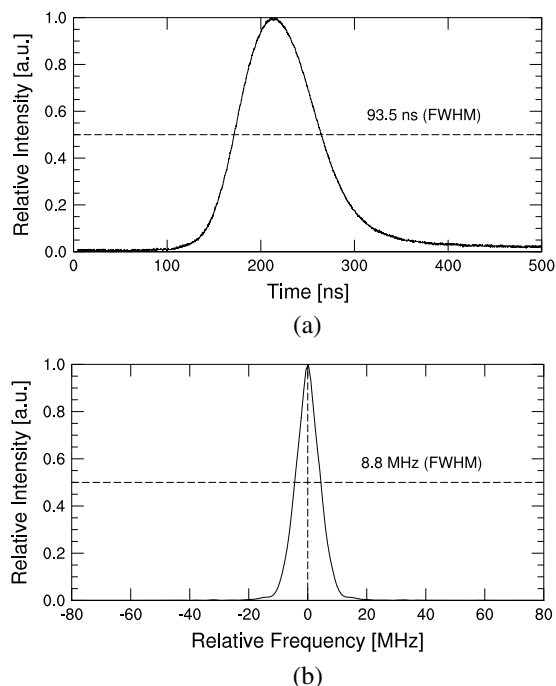


Fig. 11. TISA laser operation at an output power level of ≈ 2 W. (a) Pulse shape and (b) resulting linewidth.

telescope. No nonlinear effects or a limitation in fiber transmission were observed at the power level of 2 W. The transmission of the fiber was 89.5%.

5. Spectral Purity of the Transmitter

The SP of the emitted radiation of the frequency source is one of the most critical parameters of a water-vapor DIAL transmitter. Even small amounts of spectral impurity can lead to significant systematic errors in the water-vapor DIAL data [3,4,6,40]. The SP of a laser (transmitter) is usually determined by measuring the signal intensity on a detector after transmission through an absorption cell filled with water vapor. The remaining transmission in online mode operation is a direct measure for the spectral impurity of the laser. Required is that the laser bandwidth can be neglected with respect to the width of the absorption line, and the selected water-vapor absorption line ensures a (theoretical) total absorption in online mode. Another method to measure SP uses the absolute frequency measurement by a heterodyning technique. The heterodyning can be performed for on- and off-line mode. Additionally, a reference (HeNe laser) can serve as the absolute frequency standard. However, a quantitative analysis on a single-shot basis is yet too demanding.

A method for using the atmospheric transmission is based on a cloud measurement technique. Here, the laser transmitter or scanner is pointing toward an optically dense target (e.g., mountain or cloud) at a low elevation angle in offline and online transmitter operation mode. The target can then be observed at a high signal level in offline mode at the corresponding range (saturation of the detector should be avoided). In contrast, the signal level in online mode should almost vanish at the range of the target if the SP of the transmitter is high. Required is therefore the selection of a suitable strong absorption line to ensure full absorption (high optical depth of ≈ 7) within the range to the target. The remaining detected online signal power $P_{\text{ON,IMP}}$ in relation to the offline signal power P_{OFF} for both at the range r of the hard target is therefore a measure of the spectral impurity of the complete transmitter and receiver unit including data acquisition. The resulting measurement of the spectral purity SP is given by

$$SP = 1 - \frac{P_{\text{ON,IMP}}}{P_{\text{OFF}}}, \quad (1)$$

with $P_{\text{ON,IMP}}$, P_{OFF} at $r = \max(P_{\text{OFF}})$.

Figure 12 shows the online and offline signal intensities for a measurement of a low stratus cloud. The measurement was performed on June 18th, 2010, at 14.45 UTC with a measurement time of 1 min for on-line and offline. The online/offline profiles were measured consecutively. An atmospheric background correction was performed by subtraction of the mean signal value at a range of 18.00–19.95 km. The analysis using Eq. (1) yields an SP of 99.92%, which

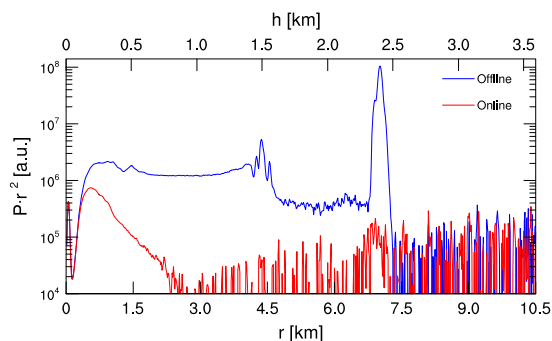


Fig. 12. Cloud measurement to determine SP of the laser transmitter. Offline and online signal (range-corrected signal intensity $P \cdot r^2$); r , range; h , height above ground level; P , signal intensity. Telescope position: elevation -70° . 15,000 laser pulses averaged (60 s averaging).

confirms that the laser transmitter fulfills the requirement of 99.5%.

6. Humidity Measurements with the UHOH DIAL

The UHOH DIAL is mounted onto a mobile trailer and was applied successfully in a number of field campaigns since 2007. The system provides remote sensing data of the atmospheric water-vapor field with previously unachieved resolution allowing for a detailed investigation of the complexity of the humidity field. Intercomparisons with other instruments confirm high accuracy of the measured data and thus that the frequency converter meets the requirements discussed above. By use of a scanning transmitter with an 80 cm receiving telescope, the measurements can be performed in any direction of interest and the three-dimensional structure of the water-vapor field can be observed. Beside humidity, also the backscatter field and thus aerosols and clouds are observed simultaneously.

In the following, we present examples of humidity measurements made with the UHOH DIAL in order

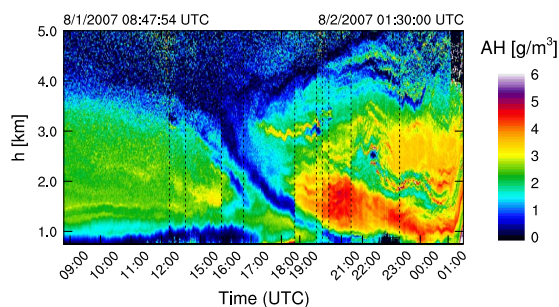


Fig. 13. Example of a 16.5 h long vertically pointed measurement with the UHOH DIAL: absolute humidity (AH) field measured between 8:58 UTC August 1, 2007, and 1:30 UTC August 2, 2007, during the COPS campaign. h is the height above ground level. The temporal resolution of this dataset is 10 s. The range resolution is 15 m. The humidity data were analyzed here using a window width of 150 m for each data point. Dashed lines mark gaps in the data.

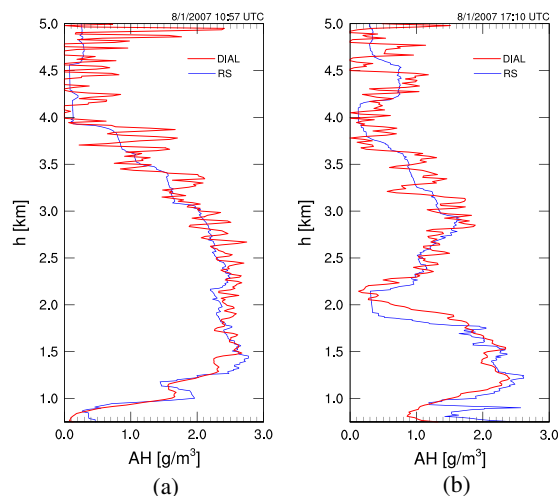


Fig. 14. Comparison of 10 s UHOH DIAL measurements with data of radiosondes launched at the lidar site at (a) 10:57 UTC and (b) 17:10 UTC on August 1, 2007. h , height above ground level; AH, absolute humidity.

to illustrate the performance of the frequency converter during field operation. The data products of the DIAL are profiles of absolute humidity with typical resolutions of 15–300 m with a temporal resolution of 1–10 s and a maximum range of a few kilometers at both day and night. The backscatter profiles are stored for each laser pulse, i.e., with 250 Hz, and a range resolution (distance between two consecutive range bins) of up to 3 m up to 20 km range. Thus, maximum flexibility is possible in post-processing of the data because spatial and temporal resolution can be traded off against each other.

The first field deployment of the UHOH DIAL was during COPS in summer 2007. A measurement

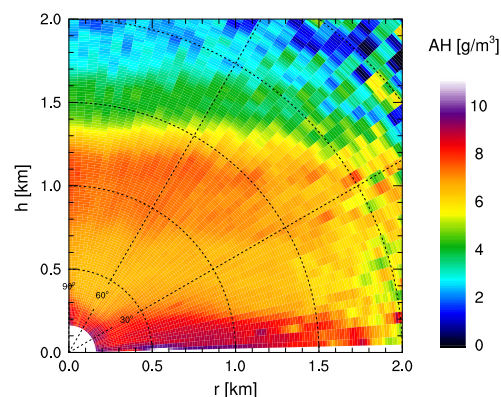


Fig. 15. Example of a scanning measurement with the UHOH DIAL: absolute humidity (AH) field measured at 7:12 UTC on September 9, 2009, during the FLUXPAT campaign. h is the height above ground level, r the horizontal distance to the lidar. The temporal resolution of these data is 10 s while the azimuth angle was changed with $0.1^\circ/\text{s}$ giving an angle resolution of 1° . The range resolution is 15 m. The humidity data were analyzed with a window width of 150 m for each data point.

example collected in vertical pointing mode over a period of 16.5 h during this campaign is shown in Fig. 13. With a resolution of 150 m (window length used for the Savitzky–Golay fit when calculating humidity) and 10 s, the noise of the data is low up to a range of more than 5 km in daytime. On this day, warm moist air was advected from the Mediterranean to South-Western Germany, where the UHOH DIAL was stationed on Hornisgrinde, the highest peak in the northern Black Forest at a height of about 1160 m above sea level. A dry intrusion marks the frontier between the air masses. Especially within the advected dry-warm air, high variability of the water–vapor field with several sharp layers is revealed by the DIAL measurements. Comparisons of the UHOH DIAL measurements with radiosondes launched at the lidar site show close agreement (Fig. 14).

In scanning mode, the UHOH DIAL can be operated with 0.1–10°/s scan speed. By combining range-resolved measurements with scanning capability, different scan patterns can be performed. A scanning measurement example of the campaign FLUXPAT 2009 is presented in Fig. 15. In this range-height indicator (RHI) scan several horizontal layers can be seen in addition to turbulent structures with high moisture values from close to the ground up to a height of 250 m.

7. Summary and Outlook

We have discussed the performance of a high-power TISA laser that serves as the transmitter of the scanning ground-based water–vapor DIAL at UHOH. The transmitter specifications and the spectral properties were demonstrated. The transmitter was successfully operated during two field campaigns.

The TISA ring resonator concept allows for single-mode, single-frequency operation. The pump laser is a frequency-doubled Nd:YAG in MOPA configuration. The pump laser reached an average power level of 46 W at 532 nm with a repetition rate of 250 Hz. Injection seeding of the TISA laser is performed using stabilized DFB lasers. DFB lasers demonstrated a higher frequency stability compared to ECDL lasers. The resonator is further stabilized using a phase-sensitive technique, which shows clear advantages compared to other methods using the intensity of the cavity resonance.

The TISA ring resonator achieved an average output power of up to 6.75 W (19% optical–optical conversion efficiency). We have demonstrated single-mode, single-frequency operation. The resulting bandwidth is < 157 MHz and we found a frequency stability of < 10 MHz, outreaching the requirements of 210 MHz by a factor of > 20. A cloud measurement was performed to determine the SP of the transmitter. We determined a SP of up to 99.9%, which fulfills the requirements of 99.5% for ground-based water–vapor DIAL measurements.

The mobile scanning water–vapor DIAL of UHOH was deployed during field campaigns. The long-term transmitter operation was demonstrated.

A comparison with radiosonde data shows close agreement. The first scanning water–vapor DIAL measurements were performed.

In the future, the DIAL transmitter will be improved to increase the overall efficiency.

The DIAL was built in the frame of a DFG (Deutsche Forschungsgemeinschaft) project [DFG reference number (GZ) WU 356/3-1, WU 356/3-2; cost item (AOBJ) 168889, 516828], which was a joint collaboration of IPM (Institute of Physics and Meteorology, University of Hohenheim: Ti:sapphire laser with frequency stabilization, DFB seeder), DLR (German Aerospace Agency: ECDL seeder system), UP (Institute of Physics and Astronomy, Nonlinear Optics, Potsdam University: pump laser), and IfT (Institute of tropospheric research: trailer and scanner design). The first three-dimensional-scanning water–vapor DIAL measurements were performed during the FLUXPAT 2009 field campaign in Düren (Düren is located about 50 km west of Cologne, Germany) in summer 2009 in the frame of the trans-regional research unit 32 of DFG. The support of Dr. A. Napiwotzki and D. Richter (both Innovative Berlin Laser GmbH [70], Germany) during FLUXPAT 2009 is highly acknowledged.

References

1. R. M. Schotland, "Some observations of the vertical profile of water vapor by means of a ground based optical radar," in *Proceedings of the Fourth Symposium on Remote Sensing of the Environment*, Ann Arbor, Michigan, 12–24 April, Environmental Research Institute of Michigan (University of Michigan, 1966), pp. 273–283.
2. E. V. Browell, T. D. Wilkerson, and T. J. McIlrath, "Water vapor differential absorption lidar development and evaluation," *Appl. Opt.* **18**, 3474–3483 (1979).
3. J. Bösenberg, "Ground-based differential absorption lidar for water-vapor and temperature profiling: methodology," *Appl. Opt.* **37**, 3845–3860 (1998).
4. V. Wulfmeyer and J. Bösenberg, "Ground-based differential absorption lidar for water-vapor profiling: assessment of accuracy, resolution, and meteorological applications," *Appl. Opt.* **37**, 3825–3844 (1998).
5. The HITRAN Database URL, <http://www.cfa.harvard.edu/hitran/>.
6. S. Ismail and E. V. Browell, "Airborne and spaceborne lidar measurements of water vapor profiles: a sensitivity analysis," *Appl. Opt.* **28**, 3603–3615 (1989).
7. E. V. Browell, S. Ismail, and W. B. Grant, "Differential absorption lidar (DIAL) measurements from air and space," *Appl. Phys. B* **67**, 399–410 (1998).
8. É. Gérard, D. G. H. Tan, L. Garand, V. Wulfmeyer, G. Ehret, and P. Di Girolamo, "Major advances foreseen in humidity profiling from the water vapor lidar experiment in space (WALES)," *Bull. Am. Meteorol. Soc.* **85**, 237–251 (2004).
9. V. Wulfmeyer, H. Bauer, P. Di Girolamo, and C. Serio, "Comparison of active and passive remote sensing from space: an analysis based on the simulated performance of IASI and space borne differential absorption lidar," *Remote Sens. Environ.* **95**, 211–230 (2005).
10. A. Behrendt, V. Wulfmeyer, P. Di Girolamo, C. Kiemle, H.-S. Bauer, T. Schaberl, D. Summa, D. N. Whiteman, B. B. Demoz, E. V. Browell, S. Ismail, R. Ferrare, S. Kooi, G. Ehret, and J. Wang, "Intercomparison of water vapor data measured with lidar during IHOP 2002. Part I: airborne to ground-based lidar systems and comparisons with chilled-mirror hygrometer radiosondes," *J. Atmos. Ocean. Technol.* **24**, 3–21 (2007).

11. A. Behrendt, V. Wulfmeyer, C. Kiemle, G. Ehret, C. Flamant, T. Schaberl, H.-S. Bauer, S. Kooi, S. Ismail, R. Ferrare, E. V. Browell, and D. N. Whiteman, "Intercomparison of water vapor data measured with lidar during IHOP 2002. Part II: airborne-to-airborne systems," *J. Atmos. Ocean. Technol.* **24**, 22–39 (2007).
12. R. Bhawar, P. Di Girolamo, D. Summa, C. Flamant, D. Althausen, A. Behrendt, C. Kiemle, P. Bossert, M. Cacciani, C. Champollion, T. Di Iorio, R. Engelmann, C. Herold, S. Pal, A. Riede, M. Wirth, and V. Wulfmeyer, "The water vapour intercomparison effort in the framework of the convective and orographically-induced precipitation study: airborne-to-ground-based and airborne-to-airborne lidar systems," *Q. J. R. Meteorol. Soc.* **137**, 325–348 (2011).
13. "GCOS (Global Climate Observing System) Reference Upper-Air Network (GRUAN)," <http://www.wmo.int/pages/prog/gcos/index.php?name=GRUAN>.
14. W. Eichinger, D. Cooper, J. Kao, L. C. Chen, L. Hipps, and J. Prueger, "Estimation of spatially distributed latent heat flux over complex terrain from a Raman lidar," *Agr. For. Meteorol.* **105**, 145–159 (2000).
15. D. I. Cooper, W. E. Eichinger, J. Archuleta, L. Hipps, C. M. U. Neale, and J. H. Prueger, "An advanced method for deriving latent energy flux from a scanning Raman lidar," *Agron. J.* **99**, 272–284 (2007).
16. V. Wulfmeyer, A. Behrendt, C. Kottmeier, U. Corsmeier, C. Barthlott, G. C. Craig, M. Hagen, D. Althausen, F. Aoshima, M. Apagaus, H.-S. Bauer, L. Bennett, A. Blyth, C. Brandau, C. Champollion, S. Crewell, G. Dick, P. Di Girolamo, M. Dorninger, Y. Dufournet, R. Eigenmann, R. Engelmann, C. Flamant, T. Foken, T. Gorgas, M. Grzeschik, J. Handwerker, C. Hauck, C. H. Höller, W. Junkermann, N. Kalthoff, C. Kiemle, S. Klink, M. König, L. Krauss, C. N. Long, F. Madonna, S. Mobbs, B. Neininger, S. Pal, G. Peters, G. Pigeon, E. Richard, M. W. Rotach, H. Russchenberg, T. Schwitalla, V. Smith, R. Steinacker, J. Trentmann, D. D. Turner, J. van Baelen, S. Vogt, H. Volkert, T. Weckwerth, H. Wernli, A. Wieser, and M. Wirth, "The Convective and Orographically-induced Precipitation Study (COPS): the scientific strategy, the field phase and research highlights," *Q. J. R. Meteorol. Soc.* **137**, 3–30 (2011).
17. C. Hauck, C. Barthlott, L. Krauss, and N. Kalthoff, "Soil moisture variability and its influence on convective precipitation over complex terrain," *Q. J. R. Meteorol. Soc.* **137**, 42–56 (2011).
18. V. Wulfmeyer, "Investigation of turbulent processes in the lower troposphere with water vapor DIAL and Radar-RASS," *J. Atmos. Sci.* **56**, 1055–1076 (1999).
19. V. Wulfmeyer, S. Pal, D. D. Turner, and E. Wagner, "Can water vapour Raman lidar resolve profiles of turbulent variables in the convective boundary layer?," *Boundary-Layer Meteorol.* **136**, 253–284 (2010).
20. C. Kiemle, M. Wirth, A. Fix, S. Rahm, U. Corsmeier, and P. Di Girolamo, "Latent heat flux measurements over complex terrain by airborne water vapour and wind lidars," *Q. J. R. Meteorol. Soc.* **137**, 190–203 (2011).
21. N. Kalthoff, K. Trümner, S. Späth, B. Adler, A. Wieser, J. Handwerker, A. Behrendt, F. Madonna, and V. Wulfmeyer, "Dry and moist convection in the boundary layer over the Black Forest—a combined analysis of in-situ and remote sensing data," *Meteorol. Z.* **22** (2013) (to be published).
22. A. Behrendt, S. Pal, F. Aoshima, M. Bender, A. Blyth, U. Corsmeier, J. Cuesta, G. Dick, M. Dorninger, C. Flamant, P. Di Girolamo, T. Gorgas, Y. Huang, N. Kalthoff, S. Khodayar, H. Mannstein, K. Trümner, A. Wieser, and V. Wulfmeyer, "Observation of convection initiation processes with a suite of state-of-the-art research instruments during COPS IOP 8b," *Q. J. R. Meteorol. Soc.* **137**, 81–100 (2011).
23. R. Kamineni, T. N. Krishnamurti, R. A. Ferrare, S. Ismail, and E. V. Browell, "Impact of high resolution water vapor cross-sectional data on hurricane forecasting," *Geophys. Res. Lett.* **30**, 1234–1237 (2003).
24. V. Wulfmeyer, H.-S. Bauer, M. Grzeschik, A. Behrendt, F. Vandenbergh, E. V. Browell, S. Ismail, and R. Ferrare, "Four-dimensional variational assimilation of water vapor differential absorption lidar data. The first case study within IHOP 2002," *Mon. Weather Rev.* **134**, 209–230 (2006).
25. M. Grzeschik, H.-S. Bauer, V. Wulfmeyer, D. Engelbart, U. Wandinger, I. Mattis, D. Althausen, R. Engelmann, M. Tesche, and A. Riede, "Four-dimensional variational data analysis of water vapor Raman lidar data and their impact on mesoscale forecasts," *J. Atmos. Ocean. Technol.* **25**, 1437–1453 (2008).
26. A. Behrendt, T. Nakamura, M. Onishi, R. Baumgart, and T. Tsuda, "Combined Raman lidar for the measurement of atmospheric temperature, water vapor, particle extinction coefficient, and particle backscatter coefficient," *Appl. Opt.* **41**, 7657–7666 (2002).
27. D. N. Whiteman, B. Demoz, P. Di Girolamo, J. Comer, I. Veselovskii, K. Evans, Z. Wang, D. Sabatino, G. Schwemmer, B. Gentry, R.-F. Lin, A. Behrendt, V. Wulfmeyer, E. Browell, R. Ferrare, S. Ismail, and J. Wang, "Raman water vapor lidar measurements during the international H2O project. II: case studies," *J. Atmos. Ocean. Technol.* **23**, 170–183 (2006).
28. D. N. Whiteman, K. Rush, S. Rabenhorst, W. Welch, M. Cadirola, G. McIntire, F. Russo, M. Adam, D. Venable, R. Connell, I. Veselovskii, R. Forno, B. Mielke, B. Stein, T. Leblanc, S. McDermid, and H. Vömel, "Airborne and ground-based measurements using a high-performance Raman lidar," *J. Atmos. Ocean. Technol.* **27**, 1781–1801 (2010).
29. J. Reichardt, U. Wandinger, V. Klein, I. Mattis, B. Hilber, and R. Begbie, "RAMSES: German Meteorological Service autonomous Raman lidar for water vapor, temperature, aerosol, and cloud measurements," *Appl. Opt.* **51**, 8111–8131 (2012).
30. "LASE Project," <http://asd-www.larc.nasa.gov/lase/ASDLase.html>.
31. R. A. Ferrare, E. V. Browell, S. Ismail, S. A. Kooi, L. H. Brasseur, V. G. Brackett, M. B. Clayton, J. D. W. Barrick, G. S. Diskin, J. E. M. Goldsmith, B. M. Lesht, J. R. Podolske, G. W. Sachse, F. J. Schmidlin, D. D. Turner, D. N. Whiteman, D. Tobin, L. M. Miloshevich, H. E. Revercomb, B. B. Demoz, and P. Di Girolamo, "Characterization of upper-troposphere water vapor measurements during AFWEX using LASE," *J. Atmos. Ocean. Technol.* **21**, 1790–1808 (2004).
32. D. Bruneau, H. Cazeneuve, C. Loth, and J. Pelon, "Double-pulse dual-wavelength alexandrite laser for atmospheric water vapor measurement," *Appl. Opt.* **30**, 3930–3937 (1991).
33. D. Bruneau, T. Arnaud des Lions, P. Quaglia, and J. Pelon, "Injection-seeded pulsed alexandrite laser for differential absorption lidar application," *Appl. Opt.* **33**, 3941–3950 (1994).
34. D. Bruneau, P. Quaglia, C. Flament, M. Meissonnier, and J. Pelon, "Airborne lidar LEANDRE II for water-vapor profiling in the troposphere. I. System description," *Appl. Opt.* **40**, 3450–3461 (2001).
35. D. Bruneau, P. Quaglia, C. Flament, and J. Pelon, "Airborne lidar LEANDRE II for water-vapor profiling in the troposphere. II. First results," *Appl. Opt.* **40**, 3462–3475 (2001).
36. G. Poberaj, A. Fix, A. Assion, M. Wirth, C. Kiemle, and G. Ehret, "Airborne all-solid-state DIAL for water vapour measurements in the tropopause region: system description and assessment of accuracy," *Appl. Phys. B* **75**, 165–172 (2002).
37. M. Wirth, A. Fix, P. Mahnke, H. Schwarzer, F. Schrandt, and G. Ehret, "The airborne multi-wavelength water vapor differential absorption lidar WALES: system design and performance," *Appl. Phys. B* **96**, 201–213 (2009).
38. V. Wulfmeyer, J. Bösenberg, S. Lehmann, C. Senff, and St. Schmitz, "Injection-seeded alexandrite ring laser: performance and application in a water-vapor differential absorption lidar," *Opt. Lett.* **20**, 638–640 (1995).
39. V. Wulfmeyer and J. Bösenberg, "Single-mode operation of an injection-seeded alexandrite ring laser for application in water-vapor and temperature differential absorption lidar," *Opt. Lett.* **21**, 1150–1152 (1996).
40. V. Wulfmeyer, "Ground-based differential absorption lidar for water-vapor and temperature profiling: development and specifications of a high-performance laser transmitter," *Appl. Opt.* **37**, 3804–3824 (1998).
41. K. Ertel, H. Linné, and J. Bösenberg, "Injection-seeded pulsed Ti:sapphire laser with novel stabilization scheme

- and capability of dual-wavelength operation," *Appl. Opt.* **44**, 5120–5126 (2005).
42. H. Vogelmann and T. Trickl, "Wide-range sounding of free-tropospheric water vapor with a differential-absorption lidar (DIAL) at a high-altitude station," *Appl. Opt.* **47**, 2116–2132 (2008).
 43. J. L. Machol, T. Ayers, K. T. Schwenz, K. W. Koenig, R. M. Hardesty, C. J. Senff, M. A. Krainak, J. B. Abshire, H. E. Bravo, and S. P. Sandberg, "Preliminary measurements with an automated compact differential absorption lidar for the profiling of water vapor," *Appl. Opt.* **43**, 3110–3121 (2004).
 44. J. L. Machol, T. Ayers, K. T. Schwenz, K. W. Koenig, R. M. Hardesty, C. J. Senff, M. A. Krainak, J. B. Abshire, H. E. Bravo, and S. P. Sandberg, "Preliminary measurements with an automated compact differential absorption lidar for the profiling of water vapor: errata," *Appl. Opt.* **45**, 3544 (2006).
 45. A. Dinovitser, M. W. Hamilton, and R. A. Vincent, "Stabilized master laser system for differential absorption lidar," *Appl. Opt.* **49**, 3274–3281 (2010).
 46. A. R. Nehrir, K. S. Repasky, J. L. Carlsten, M. D. Obland, and J. A. Shaw, "Water vapor profiling using a widely tunable, amplified diode-laser-based differential absorption lidar (DIAL)," *J. Atmos. Ocean. Technol.* **26**, 733–745 (2009).
 47. M. D. Obland, K. S. Repasky, A. R. Nehrir, J. L. Carlsten, and J. A. Shaw, "Development of a widely tunable amplified diode laser differential absorption lidar for profiling atmospheric water vapor," *J. Appl. Remote Sens.* **4**, 043515 (2010).
 48. A. R. Nehrir, K. S. Repasky, and J. L. Carlsten, "Micropulse water vapor differential absorption lidar: transmitter design performance," *Opt. Express* **20**, 25137–25151 (2012).
 49. P. F. Moulton, "Spectroscopic and laser characteristics of $\text{Ti:Al}_2\text{O}_3$," *J. Opt. Soc. Am. B* **3**, 125–133 (1986).
 50. W. R. Rapoport and C. P. Khatkhat, "Titanium sapphire laser characteristics," *Appl. Opt.* **27**, 2677–2684 (1988).
 51. V. Wulfmeyer, A. Behrendt, H.-S. Bauer, C. Kottmeier, U. Corsmeier, A. Blyth, G. Craig, U. Schumann, M. Hagen, S. Crewell, P. Di Girolamo, C. Flamant, M. Miller, A. Montani, S. Mobbs, E. Richard, M. W. Rotach, M. Arpagaus, H. Russchenberg, P. Schlüssel, M. König, V. Gärtner, R. Steinacker, M. Dörninger, D. D. Turner, T. Weckwerth, A. Hense, and C. Simmer, "RESEARCH CAMPAIGN: the convective and orographically induced precipitation study: a research and development project of the world weather research program for improving quantitative precipitation forecasting in low-mountain regions," *Bull. Am. Meteorol. Soc.* **89**, 1477–1486 (2008).
 52. COPS Field Campaign, "COPS: Convective and Orographically-induced Precipitation Study," <http://www.uni-hohenheim.de/cops>.
 53. A. Behrendt, V. Wulfmeyer, A. Riede, G. Wagner, S. Pal, H. Bauer, M. Radlach, and F. Späth, "3-Dimensional observations of atmospheric humidity with a scanning differential absorption lidar," *Proc. SPIE* **7475**, 74750L (2009).
 54. FLUXPAT 2009 within SFB TR 32, "Transregional Collaborative Research Centre 32," <http://www.tr32.uni-koeln.de>.
 55. V. Wulfmeyer and C. Walther, "Future performance of ground-based and airborne water-vapor differential absorption lidar. I. Overview and theory," *Appl. Opt.* **40**, 5304–5320 (2001).
 56. V. Wulfmeyer and C. Walther, "Future performance of ground-based and airborne water-vapor differential absorption lidar. II. Simulations of the precision of a near-infrared, high-power system," *Appl. Opt.* **40**, 5321–5336 (2001).
 57. G. Wagner, V. Wulfmeyer, and A. Behrendt, "Detailed performance modeling of a pulsed high-power single-frequency Ti:sapphire laser," *Appl. Opt.* **50**, 5921–5937 (2011).
 58. H. Kogelnik, "Imaging of optical modes—resonators with internal lenses," *Bell Syst. Tech. J.* **44**, 455–494 (1965).
 59. H. Kogelnik and T. Li, "Laser beams and resonators," *Appl. Opt.* **5**, 1550–1567 (1966).
 60. J. P. Lörtcher and J. Steffen, "Dynamic stable resonators: a design procedure," *Opt. Quantum Electron.* **7**, 505–514 (1975).
 61. H. P. Körtz, R. Iffländer, and H. Weber, "Stability and beam divergence of multimode lasers with internal variable lenses," *Appl. Opt.* **20**, 4124–4134 (1981).
 62. V. Magni, "Resonators for solid-state lasers with large-volume fundamental mode and high alignment stability," *Appl. Opt.* **25**, 107–117 (1986).
 63. D. Metcalf, P. de Giovanni, J. Zachorowski, and M. Leduc, "Laser resonators containing self-focusing elements," *Appl. Opt.* **26**, 4508–4517 (1987).
 64. W. Koechner, "Longitudinal modes," in *Solid-State Laser Engineering*, T. Tamir and A. L. Schawlow, eds., (Springer-Verlag, 1999), pp. 236–259.
 65. A. Riede, A. Behrendt, V. Wulfmeyer, D. Althausen, U. Wandinger, V. Klein, A. Meister, and M. Schiller, "Transmitter-receiver unit of the UHOH water vapor DIAL with a scanning 800 mm telescope mirror," in Proceedings of the 26th International Laser and Radar Conference (ILRC), Porto Heli, Greece, 25–29 June (International Coordination-group on Laser Atmospheric Studies, 2012), paper S1P-12.
 66. A. Behrendt, V. Wulfmeyer, A. Riede, F. Späth, S. Metzendorf, G. Wagner, S. Pal, and M. Schiller are preparing a manuscript to be called "3D-scanning, water-vapor DIAL of Hohenheim University".
 67. M. Ostermeyer, P. Kappe, R. Menzel, and V. Wulfmeyer, "Diode-pumped Nd:YAG master oscillator power amplifier with high pulse energy, excellent beam quality, and frequency-stabilized master oscillator as a basis for a next-generation lidar system," *Appl. Opt.* **44**, 582–590 (2005).
 68. M. Ostermeyer, P. Kappe, R. Menzel, and V. Wulfmeyer, "Diode-pumped Nd:YAG master oscillator power amplifier with high pulse energy, excellent beam quality, and frequency-stabilized master oscillator as a basis for a next-generation lidar system—erratum," *Appl. Opt.* **44**, 7451 (2005).
 69. V. Wulfmeyer, M. Randall, A. Brewer, and R. M. Hardesty, "2 μm Doppler lidar transmitter with high frequency stability and low chirp," *Opt. Lett.* **25**, 1228–1230 (2000).
 70. "IBL Innovative Berlin Laser GmbH," <http://www.ib-laser.com/>.
 71. H. R. Khalesifard, A. Fix, G. Ehret, M. Schiller, and V. Wulfmeyer, "Fast-switching system for injection seeding of a high-power Ti:sapphire laser," *Rev. Sci. Instrum.* **80**, 073110 (2009).
 72. F. Späth, "Development of injection seeders for water vapor and carbon dioxide DIAL systems based on DFB lasers," Diploma thesis (in German) (University of Stuttgart, 2010).
 73. F. Späth, G. Wagner, H.-D. Wizemann, A. Behrendt, and V. Wulfmeyer, "Injection seeders based on DFB lasers for DIAL of water vapor at 820 nm and CO_2 at 1580 nm," in Proceedings of the 25th International Laser Radar Conference (ILRC), St. Petersburg, Russia, 5–9 July (International Coordination-group on Laser Atmospheric Studies, 2010), pp. 231–234.
 74. R. Matthey, S. Schilt, D. Werner, C. Affolderbach, L. Thévenaz, and G. Milette, "Diode laser frequency stabilisation for water-vapour differential absorption sensing," *Appl. Phys. B* **85**, 477–485 (2006).
 75. F. Späth, S. Metzendorf, A. Behrendt, H.-D. Wizemann, G. Wagner, and V. Wulfmeyer, "Online/offline injection seeding system with high frequency-stability and low crosstalk for water vapor DIAL," *Opt. Commun.* (2012) (in revision).
 76. L. A. Rahn, "Feedback stabilization of an injection-seeded Nd:YAG laser," *Appl. Opt.* **24**, 940–942 (1985).
 77. R. L. Schmitt and L. A. Rahn, "Diode-laser-pumped Nd:YAG laser injection seeding system," *Appl. Opt.* **25**, 629–633 (1986).
 78. T. Schröder, C. Lemmerz, O. Reitebuch, M. Wirth, C. Wührer, and R. Treichel, "Frequency jitter and spectral width of an injection-seeded Q -switched Nd:YAG laser for a Doppler wind lidar," *Appl. Phys. B* **87**, 437–444 (2007).
 79. S. W. Henderson, E. H. Yuen, and E. S. Fry, "Fast resonance-detection technique for single-frequency operation of injection-seeded Nd:YAG lasers," *Opt. Lett.* **11**, 715–717 (1986).
 80. T. Walther, M. P. Larsen, and E. S. Fry, "Generation of Fourier-transform-limited 35 ns pulses with a ramp-hold-fire seeding

- technique in a Ti:sapphire laser," *Appl. Opt.* **40**, 3046–3050 (2001).
81. P. Esherick and A. Owyong, "Polarization feedback stabilization of an injection-seeded Nd:YAG laser for spectroscopic applications," *J. Opt. Soc. Am. B* **4**, 41–47 (1987).
 82. T. W. Hänsch and B. Couillaud, "Laser frequency stabilization by polarization spectroscopy of a reflecting reference cavity," *Opt. Commun.* **35**, 441–444 (1980).
 83. R. W. P. Drever, J. L. Hall, F. V. Kowalski, J. Hough, G. M. Ford, A. J. Munley, and H. Ward, "Laser phase and frequency stabilization using an optical resonator," *Appl. Phys. B* **31**, 97–105 (1983).
 84. A. Strässer, T. Waltinger, and M. Ostermeyer, "Injection seeded frequency stabilized Nd:YAG ring oscillator following a Pound-Drever-Hall scheme," *Appl. Opt.* **46**, 8358–8363 (2007).
 85. M. Ostermeyer, T. Waltinger, and M. Gregor, "Frequency stabilization of a Q-switched Nd:YAG laser oscillator with stability better 300 kHz following an rf-sideband scheme," *Opt. Commun.* **282**, 3302–3307 (2009).
 86. M. E. Innocenzi, H. T. Yura, C. L. Fincher, and R. A. Fields, "Thermal modeling of continuous-wave end-pumped solid-state lasers," *Appl. Phys. Lett.* **56**, 1831–1833 (1990).
 87. Fibertech, LEONI Fiber Optics GmbH, <http://www.fibertech.de/>.



Contents lists available at SciVerse ScienceDirect

Optics Communications

journal homepage: www.elsevier.com/locate/optcom

Online/offline injection seeding system with high frequency-stability and low crosstalk for water vapor DIAL[☆]

Florian Späth^{*}, Simon Metzendorf, Andreas Behrendt, Hans-Dieter Wizemann, Gerd Wagner, Volker Wulfmeyer

University of Hohenheim, Institute of Physics and Meteorology, Garbenstr. 30, 70599 Stuttgart, Germany

ARTICLE INFO

Article history:

Received 24 December 2012

Received in revised form

29 May 2013

Accepted 1 July 2013

Available online 12 July 2013

Keywords:

Laser stabilization

Injection seeding

Distributed-feedback lasers

Water vapor differential absorption lidar

Electro-optic deflector

Fast optical switch

ABSTRACT

A compact and rugged distributed feedback (DFB) laser system has been developed as online–offline injection seeder for the laser transmitter of a ground-based water vapor differential absorption lidar (WV DIAL) near 820 nm. The frequency stability of this injection seeder system shows a standard deviation of only 6.3 MHz and a linewidth of less than 4.6 MHz during continuous operation of more than 14 h. These values by far exceed the requirements for WV DIAL. By use of a novel technique based on an electro-optic deflector (EOD), alternating online–offline wavelength switching is achieved for each shot of the seeded laser with 250 Hz with a response time of less than 10 μ s and very low crosstalk between the channels of only 33 dB. As a result, a spectral purity of 99.95% is reached by the WV DIAL transmitter which again fulfills the requirements for WV DIAL measurements with high accuracy. Because moveable parts are not present in the seeding system, this setup is significantly less sensitive to acoustic vibrations and ambient temperature drifts during field experiments than other seeding systems which use external cavity diode lasers (ECDL) and mechanical switches. By our new seeding system not only the requirements for ground-based water-vapor DIAL are met but also for space-borne WV DIAL applications that pose even higher demands to the frequency stability and spectral purity of the laser transmitters.

© 2013 The Authors. Published by Elsevier B.V. All rights reserved.

1. Introduction

In order to provide measurements with low systematic errors, the transmitter of a ground-based water vapor differential absorption lidar (WV DIAL) system has to fulfill high demands regarding the spectral purity and frequency stability of the pulsed laser radiation [1]. Even higher requirements have to be met for airborne and space-borne WV DIAL [1–7] because the sampled absorption lines are then narrower. Table 1 summarizes the requirements regarding frequency stability, bandwidth, and spectral purity. Injection seeding with stable diode lasers is the technique of choice for spectral narrowing and stabilizing pulsed high-power laser transmitters [8–13].

Depending on the application, these seeding lasers must provide continuous-wave laser radiation at specific wavelengths with preferably high power (several tens of mW) and at least as high frequency stability as what is required for the pulsed laser

that is seeded. For ground-based WV DIAL systems, suitable absorption lines are located, e.g., at wavelengths near 820 nm [14,15]. This wavelength region is reached with high efficiency by Ti:sapphire lasers. Thus, the injection seeded high power Ti:sapphire laser is our choice for the WV DIAL transmitter [5,6]. Alternative concepts use Alexandrite lasers [1,2,12,13] or optical parametric oscillators (OPO) with amplified Ti:sapphire lasers [16] for this purpose. Low power WV DIAL systems near 820 nm have been developed based on amplified diode lasers [17–20].

For airborne and satellite borne WV DIAL systems, absorption lines around the wavelengths of 935 nm are better suited [21,22] because the higher absorption cross-sections in these spectral regions are advantageous. Further wavelength regions suitable for WV DIAL are found around 720 nm [23], 1.5 μ m [24], and 10 μ m [25–27].

DIAL uses alternating laser pulses at two wavelengths in order to determine the number density of a trace gas in the atmosphere. One pulse has to be tuned to a wavelength with high atmospheric absorption of the gas to be detected (online wavelength), and the other pulse at low absorption at a wavelength nearby (offline wavelength). Thus, a DIAL transmitter needs also a device for switching the online and offline wavelengths in short time. For this purpose, one can use two pulsed lasers as transmitters, i.e., one for each wavelength. But it is more cost efficient and technically significantly less complex to use one pulsed laser, the

[☆]This is an open-access article distributed under the terms of the Creative Commons Attribution-NonCommercial-No Derivative Works License, which permits non-commercial use, distribution, and reproduction in any medium, provided the original author and source are credited.

^{*} Corresponding author. Tel.: +49 711 459 22152.

E-mail address: f.spaeth@uni-hohenheim.de (F. Späth).

output of which is switched between the two wavelengths. In principle, seeding only for the online wavelength and letting the pulsed laser run freely without seeding for the offline signal is also possible. This approach, however, has the disadvantage that the output wavelength for the offline signal is not fixed. Multimode operation of the pulsed laser transmitter may result in unwanted modes with a spectrum of uncertain atmospheric absorption characteristics. Hence, a switch between two seeders is advantageous. This switch has to operate not only fast enough for the pulse repetition rate of the seeded laser but also with low crosstalk between the online and offline signals in order to provide online seeding with the required high spectral purity of >99.6% and >99.9% for ground-based and airborne/satellite borne DIAL, respectively [1–4]. Previous approaches for switching between the seed lasers were laser modulators [28], fiber switches [29], and fiber-coupled micro-electromechanical switches (MEMS) [21]. Here we present a new technique based on an electro-optic deflector (EOD). A comparison of the systems is shown in Table 2.

As seed lasers, different kinds of diode lasers have been employed. Ertel et al. [30] are using two external cavity diode lasers (ECDL) to seed a Ti:sapphire resonator. They operate at wavelengths around 820 nm with an output power of 30 mW and a frequency stability of 9 MHz [28]. Wavelengths around 935 nm are used by the airborne system WALES of Wirth et al. [21] which is also intended to serve as a prototype for a space-borne WV DIAL. Four distributed feedback (DFB) lasers are operated as seed lasers for the transmitter, which is here an optical parametric oscillator (OPO). The optical power for seeding of this system is 7 mW with a frequency stability of 14.5 MHz. Two ECDLs in the 820 nm wavelength region were used in the setup of Kholesifard et al. [29]. Their system delivered an optical output power of 20 mW and a frequency stability of 20 MHz in the laboratory. However, during field deployment, it was found that the optical output power changed to <10 mW and the frequency stability changed to 24 MHz with mode jumps [31] severely deteriorating the accuracy of DIAL measurements.

In the following, we present the new injection seeder system of the WV DIAL of the University of Hohenheim (UHOH) and discuss its characteristics. The UHOH DIAL is a ground-based lidar system that is mounted on a mobile platform. It allows for 3-dimensional measurements of the atmospheric water-vapor field with high accuracy and resolution [6,32–35].

This paper is organized as follows: Firstly, the setup and properties of the DFB lasers are described. Secondly, results of the frequency stabilization, linewidth measurements, and performance of the electro-optic switch are presented. Finally, a summary with conclusions is given.

Table 1
Requirements for WV DIAL transmitter [1–7].

	Ground-based WV DIAL	Airborne WV DIAL
Laser frequency stability (MHz)	< 200	< 60
Laser linewidth (FWHM) (MHz)	< 400	< 160
Spectral purity (%)	> 99.6	> 99.9

Table 2
Comparison of recently published seeding systems for WV DIAL.

	Ertel et al. [28,30]	Kholesifard et al. [29]	Wirth et al. [21]	This system
Seed laser	2 × ECDL	2 × ECDL	4 × DFB	2 × DFB
Wavelength (nm)	820	820	935	820
Frequency stability (MHz)	9 (rms)	20 (24 [31]) (rms)	14.5 (stdDev.)	6.3 (HWHM)
Opt. power (mW)	30	20 (< 10 [31])	7	up to 20
Switch	Laser modulator	Fiber switch	Fiber-coupled micro-electromechanical switch	EOD

2. Setup of the injection seeder system

The laser transmitter of the UHOH DIAL is based on a Ti:sapphire laser [5,6] which is end-pumped by the frequency-doubled radiation of a pulsed diode-pumped Nd:YAG laser [36]. The fluorescence spectrum of Ti:sapphire is several hundreds of nm broad [37]. For coarse spectral narrowing, we use an intra-cavity birefringent filter; then the injection seeding technique is employed to stabilize the laser wavelength with high accuracy [1,8,9].

During the first system operation, we used ECDLs as injection seeders of our WV DIAL [29,31]. ECDLs employ a mirror and a grating outside of the laser diode for wavelength selection. By tilting the mirror or grating the emitted wavelength can be changed. Unfortunately, we observed a strong decrease of the frequency stability in the lidar container compared to the measurements in the laboratory. In addition, the wavelength output of the ECDLs was not continuously tunable without mode hops over the desired wavelength range of at least 1 nm. Thus, we decided to replace the ECDLs by two DFB lasers.

DFB lasers have a built-in Bragg grating. The emitted wavelength has to satisfy the Bragg condition and depends on the grating constant, diode current, and temperature. The resonators of DFB lasers are free of movable parts and free-space propagation of eigenmodes like between the laser active material and gratings or mirrors in ECDLs. Thus, DFB lasers are unaffected by mechanical disturbances, which are inevitably present during operation within field campaigns. The two DFB lasers used in our system have mode-hop-free tuning ranges between 817.7 and 819.0 nm encompassing a wide range of water-vapor absorption lines suitable for ground-based WV DIAL (Fig. 1).

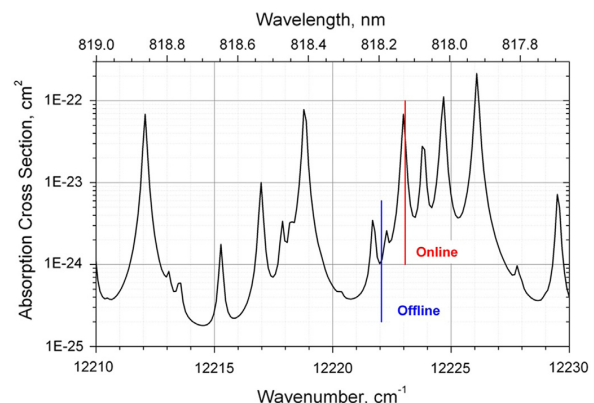


Fig. 1. Absorption spectrum of water vapor within the tuning range of the DFB laser diodes of 12,210–12,230 cm^{-1} (819.0 and 817.7 nm) presenting a range of absorption cross-sections which is well suited for ground-based water-vapor DIAL. Atmospheric constituents other than water vapor do not show absorption in this wavelength region. The spectrum is calculated with the HITRAN 2000 database [46] and Voigt line shape at an altitude of 1000 m in US standard atmosphere [47]. A pair of online and offline wavelengths used by us for measurements in 2012 is marked.

Furthermore, we found that the fiber-based wavelength switch of the system described in Kholesifard et al. [29] operated successfully only for short operation times. It degraded rapidly and did not provide the desired high suppression between the channels during field experiments. Tentatively, we replaced the fiber switch by a chopper and could use the seeder only for stabilizing the online wavelength while the offline laser output of the pulsed Ti:sapphire laser was unseeded [6,32]. However, this led to systematic errors in the DIAL retrieval due to the unknown offline laser spectrum. Therefore, we developed a new online/offline injection seeder system for the UHOH DIAL in order to overcome these limitations. It is based on two DFB lasers and an electro-optic deflector (EOD) as switch.

The DFB lasers (SAR-815 DFB, SRI International, Princeton, USA) were selected from a charge of lasers, which were originally designed for 815 nm, but provide laser output in the wavelength range between 817.7 nm and 819.0 nm due to variations in the manufacturing process. These wavelengths are reached at temperatures T between 10 and 35 °C and at electrical currents I of 90–100 mA. The maximum laser output power is 60 mW at the maximum current of $I_{\max} = 100$ mA. For lower current than 90 mA, there are mode hops to 814 nm and 811 nm. Concerning the lifetime of the DFB lasers our present operation time does not allow a complete performance analysis yet. While we are operating the diodes near the upper

current limit we choose temperatures near the lower temperature limit. We expect that higher temperatures would be more critical than higher currents. In the data sheet, the manufacturer gives a maximum operational current of 100 mA but an absolute maximum current of 150 mA while we are operating the diodes at 95 mA. We will continue to investigate this issue.

The tuning characteristics of the two DFB lasers, i.e., the changes of output wavelength or frequency with temperature and current are the following: $\Delta\lambda/\Delta T = 0.055$ nm/K, $\Delta\lambda/\Delta I = 0.008$ nm/mA, $\Delta\nu/\Delta T = -24.5$ GHz/K, and $\Delta\nu/\Delta I = -3.5$ GHz/mA. Table 3 shows a comparison of the specifications of the DFB lasers and the previously used ECDLs. The specifications of the ECDLs were measured in the environment of a laser laboratory by Kholesifard et al. [29] and during the field campaign COPS (Convective and Orographically-Induced Precipitation Study [33,35,38]) by Schiller [31].

The setup for coupling the DFB laser beam into an optical fiber is shown in Fig. 2. The DFB laser diodes are placed in temperature-controlled homemade housings [39]. The laser diode currents and temperatures are controlled with the drivers PRO800 with ITC 8052 modules of Thorlabs Inc. (USA). In the housing of each DFB laser, a Peltier element was placed underneath the laser diode for temperature controlling. At the front plane of the DFB laser housing, collimation optics ($f = 3.1$ mm, NA = 0.68, Schäfer + Kirchhoff GmbH, Germany) are mounted in a threaded tube.

Table 3
Specifications of DFB lasers vs. ECDLs.

	DFB (used here)	ECDL (used previously)	
		Specified by Kholesifard et al. [29]	Specified by Schiller [31]
Laser linewidth (MHz)	4.57 MHz (FWHM)	Not specified	Not specified
Frequency stability (MHz)	6.3 (HWHM)	20 (rms)	24 (rms)
Optical power (out of the fiber) (mW)	up to 20	20	< 10
Wavelength range (nm)	817.7–819.0	815–840	
Mode-hop-free tuning range (GHz)	581	30	10–15

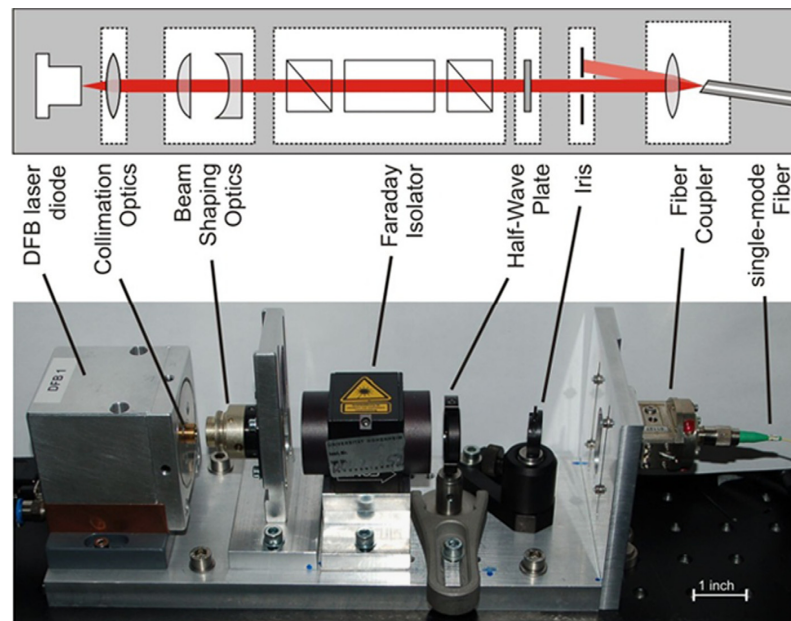


Fig. 2. Fiber coupling of the DFB laser beam. The DFB laser diode is placed in a temperature-controlled housing with integrated collimation optics. The temperature controlling is realized with a Peltier element under the laser diode. The iris blocks back reflections of the fiber end so that these do not disturb the laser diode. The size of the complete setup is 250 mm × 100 mm × 100 mm.

This bi-aspheric lens collimates the divergent laser beam in the vertical direction. In the horizontal plane, the DFB lasers show a larger divergence angle so that additional collimation with a pair of cylindrical lenses is required (denoted with “beam shaping optics” in Fig. 2, Schäfter+Kirchhoff GmbH, Germany). The Faraday isolator (FI-850-5SV, Linos, Germany) protects the laser diode from back reflections. The half-wave plate turns the polarization back to the vertical direction, which is required for coupling into a polarization-maintaining fiber. An iris is implemented in front of the fiber coupler to block the back reflection of the fiber end. This reflection spot is not blocked completely by the Faraday isolator and would disturb the DFB laser diode by inducing mode-hops.

The setup of our injection seeder system is depicted in Fig. 3. It uses some parts of the previous system of Khalesifard et al. [29] like fibers and a wavemeter. The DFB lasers are coupled into cross-coupled polarization-maintaining fibers (XCOF, 954PS, Evanescence Optics Inc., Canada) with transmissions of 99% and 1%. The main fraction of the power within the fiber of both DFB lasers is sent via optical fibers with lengths of 5 m to the breadboard of the Ti:sapphire laser, 1% is used for the frequency control. The high power output of the fibers is collimated and sent to an EOD. The EOD acts as a fast optical switch and deflects either the online or the offline wavelength into the Ti:sapphire resonator while the other seeder beam is blocked (details see Section 5). The power of the DFB lasers behind the EOD is of about 12 mW which are injected in the Ti:sapphire resonator for seeding. According to our simulations of laser performance, an intracavity seed power of 6.7 mW is required to reach a spectral purity of 99.9% [5].

For the active frequency stabilization of the seed lasers, 1% of the power of each DFB laser is coupled over a 4:1-switch (SN1x4-4N, Sercalo Microtechnology Ltd., Switzerland) to a Fizeau wavemeter (Model WS 7, HighFinesse/Angstrom, Germany). The wavemeter measures the laser frequencies of the DFB lasers to determine the deviations of the emitted frequencies compared to the selected online and offline frequencies. Based on the deviations, a program written in LabVIEW (National Instruments Corporation, USA) calculates the corrected laser diode currents I_1 and I_2 . The correction is done alternately for both DFB lasers

(typically all 5 s). Additionally, a frequency-stabilized HeNe laser (SL 03, SIOS Messtechnik GmbH, Germany) as reference laser is coupled by the 4:1-switch to the wavemeter. The fourth input of the 4:1-switch is not used. With the HeNe frequency standard, the wavemeter is stabilized to an absolute accuracy of 20 MHz rms. The temperatures of both DFB lasers T_1 and T_2 are kept constant because the frequency control of the DFB lasers via the electrical currents I_1 and I_2 is much faster.

3. Frequency stability of the DFB lasers

Measurements of the frequency stability of the DFB lasers without active frequency control (so-called passive stability) are shown in Fig. 4. The first experiment presented here was made in the laboratory with constant ambient temperature. Without active frequency control, frequency drifts of several 100 MHz over several hours and short term frequency fluctuations in the range of the digital resolution of the wavemeter of 40 MHz (Fig. 4a) occur already under quite stable ambient conditions in the laboratory. The second experiment (Fig. 4b) was executed in the UHOH DIAL container with less stable conditions concerning ambient temperature and mechanical vibrations. The passive stability degrades to frequency drifts of 1000 MHz over several hours. The short-term frequency fluctuations are ± 80 MHz. Repetitive frequency drifts of about 200–300 MHz are caused by the air condition system. Frequency drifts of the wavemeter are corrected by a HeNe reference laser, so that these data show the drifts of the DFB laser alone. The red lines in Fig. 4 indicate the zero line with the set absolute frequencies of $\nu_{\text{lab}} = 366\,354\,589$ MHz ($\lambda_{\text{lab}} = 818.312$ nm) and $\nu_{\text{DIAL}} = 366\,400\,536$ MHz ($\lambda_{\text{DIAL}} = 818.210$ nm). Clearly, active frequency control is required to meet the stability requirements of water vapor DIAL (see Table 1).

The active frequency stabilization is realized as described in Section 2. For frequency corrections, the laser diode currents I_1 and I_2 are modified. With the frequency deviation and a correction factor, a new diode current is calculated and set to the diode driver. A long-term frequency measurement over 14 h with active frequency stabilization is shown in Fig. 5a. Only single peaks

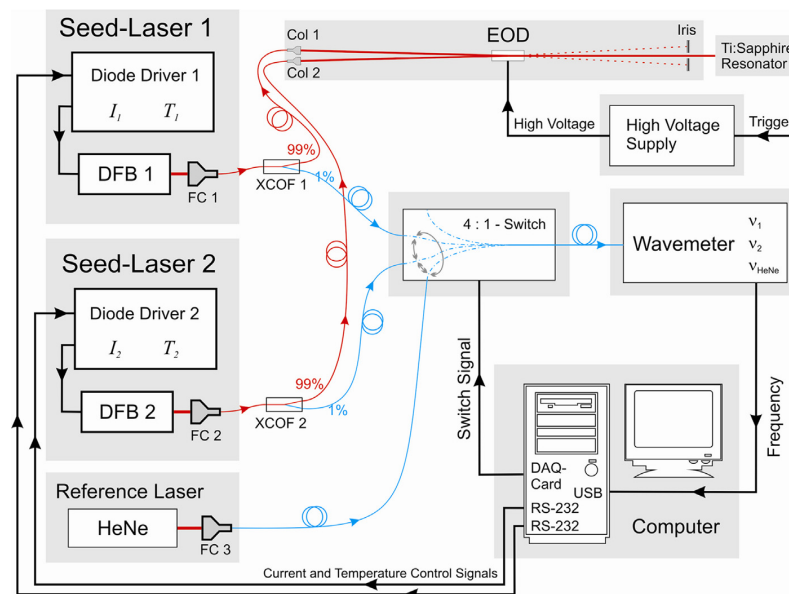


Fig. 3. Setup of the injection seeder system with active frequency stabilization and EOD online-offline switch. FC—fiber coupler, Col—fiber collimator, XCOF—cross-coupled fibers, EOD—electro-optical deflector, USB—Universal Serial Bus, RS-232—Recommended Standard 232 Port, and DAQ—Data Acquisition.

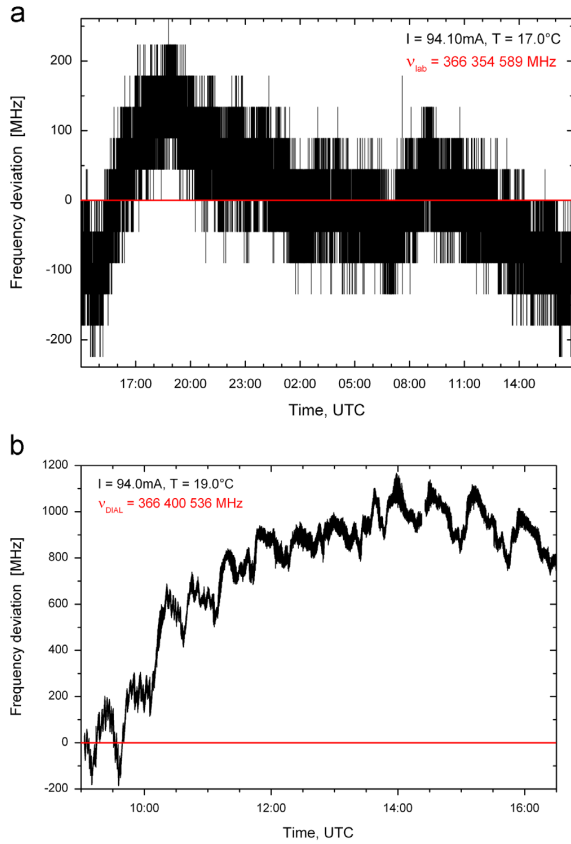


Fig. 4. Passive stability of the DFB laser diode. (a) Measurement in the laboratory with the wavemeter WA-1500 of Burleigh. (b) Measurement in the DIAL container with the wavemeter WS 7 of HighFinesse. (For interpretation of the references to color in this figure, the reader is referred to the web version of this article.)

exceed a deviation of $\pm 30 \text{ MHz}$. With the active stabilization switched on, the standard deviation σ is reduced to 6.3 MHz . Fig. 5b shows the frequency distribution with a Gaussian fit. The half width at half maximum (HWHM) of the fit is nearly the same with 6.7 MHz indicating that the frequency distribution is nearly Gaussian. This measurement was performed during a field measurement campaign in summer 2009 (FLUXPAT 2009 [32]) under real conditions while seeding the Ti:sapphire laser. The frequency stability requirements (Table 1) which are 200 MHz rms for ground-based water-vapor DIAL [1,14,15,38,40] are fulfilled; and even the higher requirements of a frequency stability of at least 60 MHz rms for spaceborne application of WV DIAL [1,14,15,38,40] are met.

Because the DFB lasers have not reached the borders of the mode-hop free wavelength range, there were no frequency instabilities. When using ECDLs as discussed in [31], frequency deviations up to 500 MHz were found. Furthermore, the ECDLs still showed an influence of the air condition system in spite of active frequency stabilization. These problems were eliminated by our new DFB laser seeding system.

4. Linewidth determination with a heterodyne measurement

To determine the linewidth of the DFB laser diodes, a beat note measurement was performed using the heterodyne technique. As the two DFB laser diodes are of the same model, we may assume the

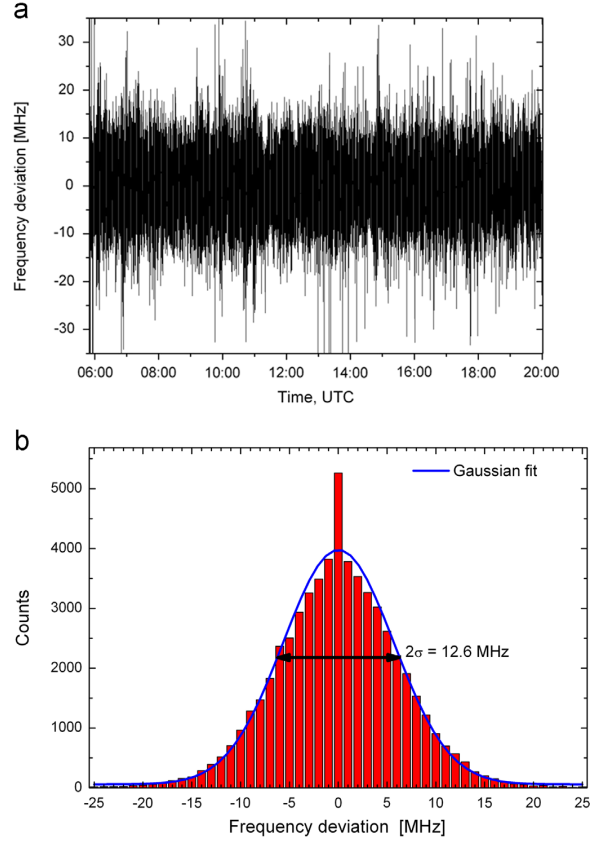


Fig. 5. (a) Frequency stability with active stabilization which removes all frequency drifts successfully. (b) The histogram of (a) shows a nearly Gaussian distribution of the frequency deviation. The measurement period was about 14 h under real operational conditions during a field campaign.

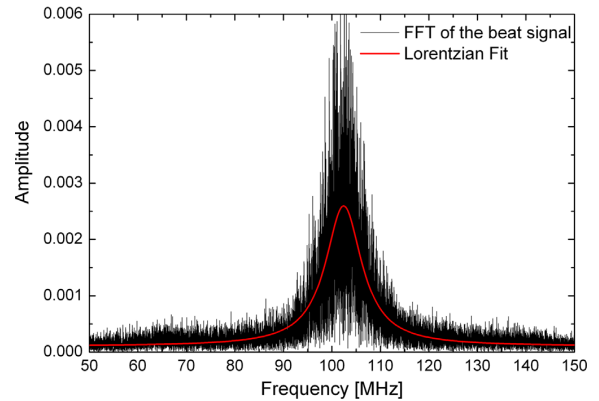


Fig. 6. Fast Fourier transformation of the beat note signal with the Lorentzian fit (red). (For interpretation of the references to color in this figure legend, the reader is referred to the web version of this article.)

same characteristics for both lasers in particular regarding their linewidths. Thus, this experiment is similar to a self-heterodyne measurement of one DFB laser diode with totally uncorrelated partial beams, resulting in a Lorentzian spectrum of the beat signal with a peak width of twice the laser diode linewidth [41–44].

The laser beams were aligned with a beam splitter so that they overlapped in free space. The beat signal was detected in the overlap center with a fast photodiode (818-BB-21A, Newport, USA) which included an integrated lens, and stored with an oscilloscope (LC564DL, LeCroy, USA). The bandwidths of the photodiode and the oscilloscope are 1.2 GHz and 1 GHz, respectively. A fast Fourier transformation (FFT) with an analysis software (Origin 8.6G, OriginLab, USA) delivers the spectral distribution of the beat note signal (Fig. 6). To obtain sufficiently high frequency resolution, the capture time of the oscilloscope was chosen appropriately large. Because too long capture time may cause smearing of the frequency peak in the FFT due to short-term fluctuations of the two laser frequencies, we decided to use a capture time of 100 μ s. The fit of a Lorentzian curve to the frequency distribution gives a peak width of 9.13 ± 0.06 MHz full width at half maximum (FWHM). This results in a linewidth for each of the DFB laser diodes of less than 4.57 ± 0.03 MHz.

We believe that the short-term frequency fluctuations arise from the current noise of the laser diode controller. The manufacturer specified 2 μ A for the capture time scales. Using the tuning characteristics of the DFB lasers (see Section 2), this value corresponds to a frequency variation of 7 MHz Table 3 so that this is obviously responsible for the main portion of the measured linewidth. Thus, it is noteworthy that the linewidth of each laser diode may be reduced furthermore but it is currently limited by the performance of our diode drivers.

5. Fast switching with an electro-optic deflector

The EOD deflects the seed laser beam by changing the refractive index of an electro-optical crystal by an external electrical field [45]. The EOD of our seeder system (ED3-820, Leysop Ltd., England) is controlled with a high voltage supply (5000 series driver, Leysop Ltd., England) and consists of a lithium niobate (LiNbO_3) crystal. The electrodes are aligned as quadrupole so that a linear electric field is generated within the crystal. Its deflection angle is 1.5 mrad/kV. Consequently, a voltage of ± 2.5 kV yields an angle of 7.5 mrad between both beams.

For the characterization of the EOD, measurements with regard to the switching time and the crosstalk have been performed. The laser beam intensity was determined with a photodiode (DET10A/M, Thorlabs, USA) which was positioned behind an iris which transmits one of the beams while the other is blocked (Fig. 3). For the measurements of the switching time, the distance between EOD and iris was 1.2 m and the aperture of the iris is 3 mm. Also, the beam was focused on the detector with a lens because the beam diameter is larger than the active detector area. To measure the short switch process, the detector was coupled to the oscilloscope with 50 Ω to reach high temporal resolution. However, during the measurements of the crosstalk the detector was coupled with 1 M Ω to the oscilloscope in order to reach higher resolution of the measurement of the photodiode voltage. Furthermore, the laser beams were focused into the EOD because of its small aperture. The aperture of the EOD is 3 mm, and the beam diameters at the EOD were 0.7 mm ($4\text{-}\sigma$ beam width).

The switch frequency was half of the repetition rate of the Ti:sapphire laser, i.e. 125 Hz in our case, so that alternative online and offline signals are generated. The temporal characteristics of the EOD switch are shown in Fig. 7a and b, for one of the DFB laser diodes (the characteristics are the same for the other DFB diode). The trigger signal has very short rise and fall times ($\ll 1$ μ s). The monitor signal of the high-voltage supply which drives the EOD cannot follow the trigger immediately which results in rise and fall times of about 8 μ s of the high voltage applied to the EOD. The deflection of the laser beams follows the high voltage applied to the EOD resulting in a time of about 8 μ s between 10% and 90% of the signal intensity. Thus we

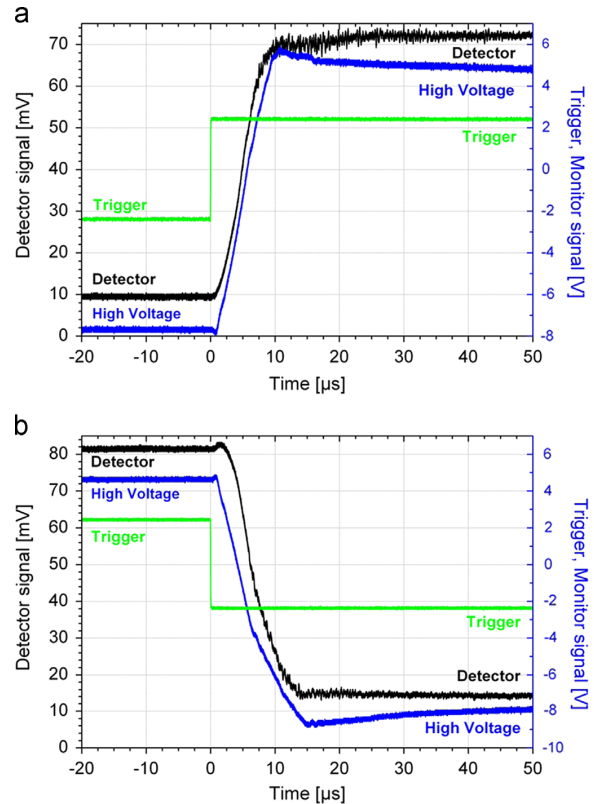


Fig. 7. Temporal behavior of the switching process with EOD: trigger signal (green), monitor signal of the high voltage supply (blue), and signal of the detector of DFB 1 (black). In (a) the switch-on process and in (b) the switch-off process are shown. The switching time of about 8 μ s is limited by the response time of the high-voltage supply. The switching of DFB 2 is the same as for DFB 1 but in the opposite direction and is not shown here. (For interpretation of the references to color in this figure legend, the reader is referred to the web version of this article.)

can state that the switching time for the laser beams is mainly limited by the response time of the high-voltage supply. The monitor signal of the high-voltage supply signal shows small overshoots. These do not disturb the switching process of the laser beams.

In the overall setup of laser transmitter of the UHOH DIAL, some additional optical components are placed in front of the Ti:sapphire resonator for the seeded operation of the laser. The additional components consist among others of a mode-matching lens, an electro-optical modulator and a Faraday isolator [6,31]. Therefore, the crosstalk is measured for two cases: First, in an arrangement focusing on the performance of the EOD-principle. Here the EOD is followed only by the mode-matching lens. This lens is necessary for the compensation of the resulting divergent beam after the prior focusing into the EOD. Second, with all the additional components which are necessary during the operation of Ti:sapphire laser.

To measure the crosstalk of the EOD switch, i.e., how well that seeder laser beam is blocked which is deflected out of the optical path, we switched off one DFB laser and measured the power of the other laser beam for both switch positions of the EOD. In the first configuration, we placed the detector at a distance of 0.85 m behind the EOD. The crosstalk, defined as ratio of both channel intensities, was found to be 32.8 dB for DFB 1 and 33.1 dB for DFB 2 in this configuration. In the second configuration, the detector was placed inside the Ti:sapphire resonator in front of the Ti:sapphire crystal. Thus further optics (the additional components described above and components of the resonator itself) were

present within the seeder beam path. For this configuration, the crosstalk was 35.3 dB for DFB 1 and 27.6 dB for DFB 2. We assume that the small apertures of some of the additional optics caused diffraction and altered the crosstalk. The different values between the two DFB lasers are due to small differences in how well the two beams are aligned to the center of the EOD.

For airborne and space borne water-vapor DIAL, a spectral purity of the online signal of 99.9% is required. The requirements for ground-based water-vapor DIAL are a less stringent with > 99.6%. Thus, if online and offline injection seedings are used, the seeders must be switched with a suppression of the switched-off signal of at least 30 dB and 24 dB for airborne/space-borne and groundbased operation, respectively [1–4]. Both requirements are fulfilled well by the first configuration independent of which seeder is tuned to the online wavelength and which to the offline wavelength. The second configuration fulfills both requirements if DFB 1 is selected as offline seeder because only leaking of the offline signal into the online seeder is critical.

6. Conclusions

We presented an injection seeding system for water-vapor DIAL measurements at around 820 nm consisting of two DFB laser diodes for online and offline wavelength. The DFB laser diodes operate at a high frequency stability of 6.3 MHz (HWHM) and a linewidth of less than 4.57 ± 0.03 MHz (FWHM). The frequency stability requirements of 60 MHz and 200 MHz for airborne and ground-based WV DIAL are by far exceeded. The DFB lasers show a larger mode-hop free wavelength range than ECDLs: we observed no mode-hops within a tuning range of 581 MHz. In contrast, with ECDLs we found critical frequency deviations of up to 500 MHz. Furthermore, the ECDLs still showed an influence of the air condition system even when the active frequency stabilization was switched on. These problems encountered when using ECDLs were overcome by the use of our DFB laser system.

A new optical switch for online/offline switching was installed based on electro-optic deflection. This technique shows a switching time of 8 μ s and a very low crosstalk of more than 30 dB at the position of the Ti:sapphire crystal. This crosstalk ensures a spectral purity of at least 99.9%. We can conclude that the EOD provides sufficient blocking. A further advantage of the EOD switch compared to, e.g., fiber switches, is the short switching time that is mainly limited by the response of the high-voltage supply. Last but not the least, there are no movable parts in the EOD switch that could degrade. Behind the EOD, the power of the DFB lasers for seeding the Ti:Sapphire resonator is of about 12 mW. These parameters fulfill the stringent demands set for water-vapor DIAL measurements with high accuracy.

References

- [1] V. Wulfmeyer, J. Bösenberg, *Applied Optics* 37 (1998) 3804.
- [2] V. Wulfmeyer, H. Bauer, P. Di Girolamo, C. Serio, *Remote Sensing of Environment* 95 (2005) 211.
- [3] P. Di Girolamo, A. Behrendt, C. Kiemle, V. Wulfmeyer, H. Bauer, D. Summa, A. Dörnbrack, G. Ehret, *Remote Sensing of Environment* 112 (2008) 1552.
- [4] S. Ismail, E.V. Browell, *Applied Optics* 28 (1989) 3603.
- [5] G. Wagner, V. Wulfmeyer, A. Behrendt, *Applied Optics* 50 (2011) 5921.
- [6] G. Wagner, A. Behrendt, V. Wulfmeyer, F. Späth, M. Schiller, *Applied Optics* 52 (10) (2013) 2454.
- [7] ESA (European Space Agency), WALES—Water Vapour Lidar Experiment in Space, The Five Candidate Earth Explorer Core Missions, European Space Agency, Report for Assessment, ESA SP-1257, vol. II, 2001.
- [8] N.P. Barnes, J.C. Barnes, *IEEE Journal of Quantum Electronics* 29 (1993) 2670.
- [9] J.C. Barnes, N.P. Barnes, L.G. Wang, W. Edwards, *IEEE Journal of Quantum Electronics* 29 (1993) 2684.
- [10] P. Brockman, C.H. Bair, J.C. Barnes, R.V. Hess, E.V. Browell, *Optics Letters* 11 (11) (1986) 712.
- [11] A. Kasapi, Y. Yin, M. Jain, *Applied Optics* 35 (1996) 1999.
- [12] V. Wulfmeyer, J. Bösenberg, S. Lehmann, C. Senff, St. Schmitz, *Optics Letters* 20 (1995) 638.
- [13] V. Wulfmeyer, J. Bösenberg, *Optics Letters* 21 (1996) 1150.
- [14] V. Wulfmeyer, C. Walther, *Applied Optics* 40 (2001) 5304.
- [15] V. Wulfmeyer, C. Walther, *Applied Optics* 40 (2001) 5321.
- [16] H. Vogelmann, T. Trickl, *Applied Optics* 47 (2008) 2116.
- [17] J.L. Machol, T. Ayers, K.T. Schwenz, K.W. Koenig, R.M. Hardesty, C.J. Senff, M.A. Krainak, J.B. Abshire, H.E. Bravo, S.P. Sandberg, *Applied Optics* 43 (2004) 3110.
- [18] J.L. Machol, T. Ayers, K.T. Schwenz, K.W. Koenig, R.M. Hardesty, C.J. Senff, M.A. Krainak, J.B. Abshire, H.E. Bravo, S.P. Sandberg, *Applied Optics* 45 (2006) 3544.
- [19] A. Dinovits, M.W. Hamilton, R.A. Vincent, *Applied Optics* 49 (17) (2010) 3274.
- [20] A.R. Nehrir, K.S. Repasky, J.L. Carlsten, M.D. Obland, J.A. Shaw, *Journal of Atmospheric and Oceanic Technology* 26 (2009) 733.
- [21] M. Wirth, A. Fix, P. Mahnke, H. Schwarzer, F. Schrandt, G. Ehret, *Applied Physics B* 96 (2009) 201.
- [22] A. Fix, G. Ehret, J. Löhring, D. Hoffmann, M. Alpers, *Applied Physics B* 102 (2011) 905.
- [23] D. Bruneau, P. Quaglia, C. Flamment, M. Meissonnier, J. Pelon, *Applied Optics* 40 (2001) 3450.
- [24] A. Petrova-Mayor, V. Wulfmeyer, P. Weibring, *Applied Optics* 47 (10) (2008) 1522.
- [25] P.W. Baker, *Applied Optics* 22 (15) (1983) 2257.
- [26] W.B. Grant, J.S. Margolis, A.M. Brothers, D.M. Tratt, *Applied Optics* 26 (15) (1987) 3033.
- [27] C. Bellecci, M. Francucci, P. Gaudio, M. Gelfusa, S. Martellucci, M. Ricchetta, T. Lo Feudo, *Applied Physics B* 87 (2007) 373.
- [28] K. Ertel, H. Linné, J. Bösenberg, *Applied Optics* 44 (24) (2005) 5120.
- [29] H.R. Khaledifard, A. Fix, G. Ehret, M. Schiller, V. Wulfmeyer, *Review of Scientific Instruments* 80 (2009) 073110.
- [30] K. Ertel, Application and Development of Water Vapor DIAL Systems, Doctoral thesis, University of Hamburg, 2004.
- [31] M. Schiller, A High-Power Laser Transmitter for Ground-Based and Airborne Water-Vapor Measurements in the Troposphere, Doctoral thesis, University of Hohenheim, 2009.
- [32] A. Behrendt, V. Wulfmeyer, A. Riede, G. Wagner, S. Pal, H. Bauer, M. Radlach, F. Späth, *Proceedings of SPIE* 7475 (2009), <http://dx.doi.org/10.1117/12.835143>.
- [33] A. Behrendt, S. Pal, F. Aoshima, M. Bender, A. Blyth, U. Corsmeier, J. Cuesta, G. Dick, M. Dorninger, C. Flamant, P. Di Girolamo, T. Gorgas, Y. Huang, N. Kalthoff, S. Khodayar, H. Mannstein, K. Trümner, A. Wieser, V. Wulfmeyer, *COPS Special Issue of the Quarterly Journal of the Royal Meteorological Society* 137 (2011) 81.
- [34] R. Bhawar, P. Di Girolamo, D. Summa, C. Flamant, D. Althausen, A. Behrendt, C. Kiemle, P. Bosser, M. Cacciani, C. Champollion, T. Di Iorio, R. Engelmann, C. Herold, S. Pal, A. Riede, M. Wirth, V. Wulfmeyer, *COPS Special Issue of the Quarterly Journal of the Royal Meteorological Society* 137 (2011) 3,325–325.
- [35] V. Wulfmeyer, A. Behrendt, Ch. Kottmeier, U. Corsmeier, C. Barthlott, G.C. Craig, M. Hagen, D. Althausen, F. Aoshima, M. Arpagaus, H.-S. Bauer, L. Bennett, A. Blyth, C. Brandau, C. Champollion, S. Crewell, G. Dick, P. Di Girolamo, M. Dorninger, Y. Dufournet, R. Eigenmann, R. Engelmann, C. Flamant, T. Foken, T. Gorgas, M. Grzeschik, J. Handwerker, C. Hauck, H. Höller, W. Junkermann, N. Kalthoff, C. Kiemle, S. Klink, M. König, L. Krauss, C.N. Long, F. Madonna, S. Mobbs, B. Neininger, S. Pal, G. Peters, G. Pigeon, E. Richard, M.W. Rotach, H. Russchenberg, T. Schwittalla, V. Smith, R. Steinacker, J. Trentmann, D.D. Turner, J. van Baelen, S. Vogt, H. Volkert, T. Weckwerth, H. Wernli, A. Wieser, M. Wirth, *COPS Special Issue of the Quarterly Journal of the Royal Meteorological Society* 137 (2011) 3.
- [36] M. Ostermeyer, P. Kappe, R. Menzel, V. Wulfmeyer, *Applied Optics* 44 (4) (2005) 582.
- [37] P.F. Moulton, *Journal of the Optical Society of America B* 3 (1) (1986) 125.
- [38] V. Wulfmeyer, A. Behrendt, H.-S. Bauer, C. Kottmeier, U. Corsmeier, A. Blyth, G. Craig, U. Schumann, M. Hagen, S. Crewell, P. Di Girolamo, C. Flamant, M. Miller, A. Montani, S. Mobbs, E. Richard, M.W. Rotach, M. Arpagaus, H. Russchenberg, P. Schlüssel, M. König, V. Gärtner, R. Steinacker, M. Dorninger, D.D. Turner, T. Weckwerth, A. Hense, C. Simmer, *Bulletin of the American Meteorological Society* 89 (10) (2008) 1477.
- [39] R. Uhl, Element analysis by spectrometry in direct current and high frequency plasmas by use of diode lasers, Doctoral thesis, University of Hohenheim, 2001, (in German).
- [40] J. Bösenberg, *Applied Optics* 37 (1998) 3845.
- [41] T. Okoshi, K. Kikuchi, A. Nakayama, *Electronics Letters* 16 (1980) 630.
- [42] P.G. Gallion, G. Debarge, *IEEE Journal of Quantum Electronics* QE-20 (1984) 343.
- [43] L.B. Mercer, *Journal of Lightwave Technology* 9 (1991) 485.
- [44] W. Zhou, K.M. Chong, H. Guo, *Physics Letters A* 372 (2008) 4327.
- [45] Y. Chiu, J. Zuo, D.D. Stancil, T.E. Schlesinger, *IEEE Journal of Lightwave Technology* 17 (1999) 108.
- [46] L.S. Rothmann, A. Barbe, D.C. Benner, L.R. Brown, C. Camy-Peyret, M.R. Carleer, K. Chance, C. Clerbaux, V. Dana, V.M. Devi, A. Fayt, J.-M. Flaud, R.R. Gamache, A. Goldman, D. Jacquemart, K.W. Jucks, W.J. Lafferty, J.-Y. Mandin, S.T. Massie, V. Nemtchinov, D.A. Newnham, A. Perrin, C.P. Rinsland, J. Schroeder, K.M. Smith, M.A.H. Smith, K. Tang, R.A. Toth, J.V. Auwera, P. Varanasi, K. Yoshino, *Journal of Quantitative Spectroscopy and Radiative Transfer* 82 (2003) 5.
- [47] U.S. Standard Atmosphere, NASA, 1976.

3 Scanning DIAL Measurements

Performing scanning DIAL measurements are advantageous for two reasons:

- 1) Scanning allows to measure down to the surface and allows to overcome the near-range gap of vertical pointing measurements. This gap is due to no full overlap of the field of view of the receiving telescope and the laser beam.
- 2) Scanning measurements captures not only one full column of the ABL but also the horizontal variability can be observed.

The UHOH DIAL system demonstrated its scanning capability for the first time during the field campaign TR 32 FLUXPAT (funded by the German Science Foundation) near Jülich, western Germany, in summer 2009 (Behrendt et al., 2009; Wagner et al., 2013, see Sect. 2.1). A high temporal resolution in terms of seconds – as it is also required to resolve turbulence processes – allows to perform range-height indicator (RHI) scans within reasonable time and adequate angle resolution. RHI scanning measurements delivered 2-dimensional (2-D) cross-section images of the atmospheric WV field and illustrated layers of different WV content. The resulting 2-D WV fields demonstrated already the potential of multi-dimensional humidity measurements to investigate the spatial humidity distribution in the ABL. A first model evaluation study with data from these scans was performed by Milovac et al. (2016). This study is presented in Sect. 4.1.

The satisfying performance of scanning DIAL measurements in RHI mode led to more sophisticated scan patterns. These were realized during two field experiments in spring 2013 and summer 2014. This also came along with the demand of new analysis tools with error estimations for the different scanning modes as well as new routines of visualization for optimal usage of the new kind of data sets. Both, new scan patterns and new analysis procedures, are presented in the publication of Späth et al. (2016) printed in Sect. 3.1. This publication starts with a brief introduction to the UHOH DIAL setup for scanning measurements and explains the DIAL method and the developed analysis procedure. New approaches of error estimations for the different scan modes are explained as well. With RHI scans in two different directions the WV field was observed during HOPE in spring 2013. The evolution of humidity layers at different height levels are discussed and clouds appeared in the last scan. In 2014 within the SABLE campaign, the first volume scan was performed consisting of several conical scans. Here, the 3-dimensional (3-D) structure of the humidity layers can be related to the surface elevation around the lidar site with a small hill. The observation of humidity fields directly above different kinds of vegetation was realized with low elevation scans. Small variations became visible with averaging over scans from a one hour time period.

This kind of humidity data in combination with temperature and wind velocity will be used in future work to apply the Monin-Obukhov similarity theory (MOST) (Monin and Obukhov, 1954) to estimate heat fluxes.

Copyright

The publication Späth et al. (2016) shown in Sect. 3.1 was published under the Creative Common License CC BY 3.0⁹.

⁹<http://creativecommons.org/licenses/by/3.0/>



3-D water vapor field in the atmospheric boundary layer observed with scanning differential absorption lidar

Florian Späth, Andreas Behrendt, Shravan Kumar Muppa, Simon Metzendorf, Andrea Riede, and Volker Wulfmeyer

University of Hohenheim, Institute of Physics and Meteorology, Garbenstr. 30, 70599 Stuttgart, Germany

Correspondence to: Florian Späth (f.spaeth@uni-hohenheim.de)

Received: 15 December 2015 – Published in Atmos. Meas. Tech. Discuss.: 18 January 2016

Revised: 23 March 2016 – Accepted: 24 March 2016 – Published: 18 April 2016

Abstract. High-resolution three-dimensional (3-D) water vapor data of the atmospheric boundary layer (ABL) are required to improve our understanding of land–atmosphere exchange processes. For this purpose, the scanning differential absorption lidar (DIAL) of the University of Hohenheim (UHOH) was developed as well as new analysis tools and visualization methods. The instrument determines 3-D fields of the atmospheric water vapor number density with a temporal resolution of a few seconds and a spatial resolution of up to a few tens of meters. We present three case studies from two field campaigns. In spring 2013, the UHOH DIAL was operated within the scope of the HD(CP)² Observational Prototype Experiment (HOPE) in western Germany. HD(CP)² stands for High Definition of Clouds and Precipitation for advancing Climate Prediction and is a German research initiative. Range–height indicator (RHI) scans of the UHOH DIAL show the water vapor heterogeneity within a range of a few kilometers up to an altitude of 2 km and its impact on the formation of clouds at the top of the ABL. The uncertainty of the measured data was assessed for the first time by extending a technique to scanning data, which was formerly applied to vertical time series. Typically, the accuracy of the DIAL measurements is between 0.5 and 0.8 g m^{−3} (or < 6 %) within the ABL even during daytime. This allows for performing a RHI scan from the surface to an elevation angle of 90° within 10 min. In summer 2014, the UHOH DIAL participated in the Surface Atmosphere Boundary Layer Exchange (SABLE) campaign in southwestern Germany. Conical volume scans were made which reveal multiple water vapor layers in three dimensions. Differences in their heights in different directions can be attributed to different surface elevation. With low-elevation scans in the surface layer, the humidity profiles and gradients can be related to different land cover

such as maize, grassland, and forest as well as different surface layer stabilities.

1 Introduction

Water vapor (WV) is the most important greenhouse gas and plays a key role in Earth's weather and climate, from the surface to the troposphere to the stratosphere. Particularly important are exchange processes between the land surface and the atmospheric boundary layer (ABL) as well as between the ABL and the lower troposphere. For example, the diurnal cycles of evapotranspiration, the ABL moisture, and entrainment at the top of the ABL are the result of feedback processes in the land–atmosphere (LA) system (Seneviratne et al., 2010). However, generally the understanding of LA interaction has been based on model studies (e.g., Findell et al., 2003; Koster et al., 2006; van Heerwaarden et al., 2009; Santanello et al., 2013) and surface observations but not on suitable data sets including ABL WV fields.

Better parameterizations of land surface and turbulent transport processes in the ABL are essential for improved weather forecasts (e.g., Ek et al., 2003; Niu et al., 2011; Shin and Hong, 2011; Cohen et al., 2015) and regional climate projections (e.g., Warrach-Sagi et al., 2013; Milovac et al., 2016). These parameterizations were mainly derived by large eddy simulation (LES) models (e.g., Mellor and Yamada, 1982; Hong et al., 2006; Hong, 2007; Nakanishi and Niino, 2009; Shin and Hong, 2015) and only to a minor extent by observations. Vertical and horizontal moisture transports via mesoscale circulations and surface heterogeneities can result in convection initiation (CI) as well as the formation of clouds and precipitation (e.g., Behrendt et al., 2011;

Corsmeier et al., 2011), which are very difficult to be observed from space (e.g., Aoshima et al., 2008). All these processes are interacting in a highly nonlinear way; therefore the three-dimensional (3-D) WV content needs to be represented very well in weather forecast models (Crook, 1996; Dierer et al., 2009), reanalyses (Bengtsson et al., 2004), and climate models (e.g., Kotlarski et al., 2014).

Models are only as good as the observations which were used for their parameterization and verification. Advanced observations of WV to study exchange, feedback, and mesoscale circulation processes require the observation of the 3-D WV field with a resolution permitting the simultaneous measurement of vertical gradients in the WV distribution in the surface layer, the mixed layer, and the entrainment layer at the top of the ABL. Only if these gradients are resolved, the corresponding transport processes can be studied and parameterized (Monin and Obukhov, 1954; Wulfmeyer et al., 2016). However, the distribution of ABL WV and its evolution in time is neither fully understood nor sufficiently observed. In consequence, it is not adequately reproduced in weather and climate forecasting models. A detailed overview about these processes and the requirements set to suitable observing systems is given by Wulfmeyer et al. (2015).

For WV measurements passive and active remote sensing instruments as well as in situ sensors are available. In situ sensors only deliver data from one location at one time; thus, remote sensing instruments are preferred for studying the vertical and horizontal WV structure in the ABL. However, many remote sensing systems only provide integrated WV (IWV) data which give no spatial information. Passive instruments like infrared (IR) spectrometers or microwave radiometers (MWRs) are able to retrieve WV profiles based on a first guess with temporal resolutions of 5–10 min. Their vertical range resolutions are 100 m for IR spectrometers or several 100 m for MWRs at the land surface and approximately 800 m for IR spectrometers and 2000 m for MWRs at the top of the ABL (Löhnert et al., 2009; Blumberg et al., 2015; Wulfmeyer et al., 2015). Due to these coarse vertical resolutions, fine structures and gradients cannot be resolved. A combination of several systems may be used to determine horizontal structures with the tomography technique. This was simulated for scanning MWRs (Steinke et al., 2014) but the vertical resolution still remains low due to the coarse resolution of the initial signals and inaccurate knowledge of initial fields. To analyze the aforementioned processes in the ABL, like LA feedback or CI, higher WV resolutions in time and space are needed. The corresponding requirements are summarized in Table 1 in Wulfmeyer et al. (2015).

For WV profiling with lidar, the Raman technique (e.g., Melfi et al., 1969; Whiteman et al., 1992; Behrendt et al., 2002; Hammann et al., 2015; Wulfmeyer et al., 2010) or the WV differential absorption lidar (WVDIAL) technique (Schotland, 1966; Browell et al., 1979; Bösenberg, 1998; Wulfmeyer and Bösenberg, 1998) can be applied. An overview of the performance of these techniques is given

in Behrendt et al. (2007) and Bhawar et al. (2011). It was shown that WVDIAL has a better spatial/temporal resolution in the lower troposphere than WV Raman lidar (WVRL) during daytime (Wulfmeyer and Bösenberg, 1998). The WVDIAL technique uses two elastic backscatter signals at wavelengths with high and low absorption of WV. In contrast to WVRL, the WVDIAL technique is self-calibrating and needs no further information than the absorption cross section at the wavelengths used (Browell et al., 1979). Due to the elastic backscatter signals, the signal-to-noise ratio (SNR) is much higher for the detected signals than using inelastic Raman scattered signals. This also helps to reach a larger range during daytime and allows integration times to be kept short. The horizontal variations of the moisture fields can be detected with scanning lidar. Scanning WVRL measurements were used, for example, to observe the WV structures in the ABL (Goldsmith et al., 1998; Eichinger et al., 1999; Whiteman et al., 2006; Froidevaux et al., 2013; Matsuda, 2013) or to estimate latent heat fluxes at the surface (Eichinger et al., 2000). However, the SNR is still limited during daytime (Turner et al., 2002), making high-resolution scans under daylight conditions more difficult than with WVDIAL; and 3-D measurements of WVRL have not been demonstrated yet.

Therefore, we focused on the WVDIAL technique and developed a scanning system permitting high-resolution scans of the WV field even during daytime. The University of Hohenheim (UHOH) WVDIAL is a ground-based mobile instrument which has already demonstrated vertical measurements in the ABL with high resolution and accuracy (Bhawar et al., 2011; Muppa et al., 2016; Wulfmeyer et al., 2016). Here, we present different types of scanning measurements of this system and discuss the measurement uncertainties. Particularly, we demonstrate the measurement of a 3-D water vapor field, which to our knowledge was achieved for the first time with a lidar.

We focus on three different scan strategies.

1. With range–height indicator (RHI) scanning measurements, the vertical WV structure over a certain horizontal range can be observed. We present a new technique to determine the corresponding 2-D error field and discuss the measurement performance in this configuration. This is essential to find the best compromise between scan speed and temporal and range resolution in order to detect the fine structure of the WV field with high confidence.
2. Conical scans can be performed to study the humidity variations from the mixed layer throughout the top of the ABL. Combining several of such scans with different elevations yields a 3-D image of the ABL moisture field. We discuss a corresponding first measurement and derive the error statistics in order to characterize fine structures in the WV field.

Table 1. Instrument specifications of the UHOH DIAL for scanning WV measurements.

Parameter	
Pump power (532 nm)	14 W
Repetition rate	250 Hz
Ti:sapphire output power (820 nm)	2 W
Pulse energy	8 mJ
Pulse duration	60 ns
Frequency switching	Shot to shot on-/offline 2 × 1 optical fiber switch
Wavelength range	817.7–819.0 nm
Output power sent into the atmosphere	1.6 W
Transmitting telescope diameter	20 cm
Receiving telescope diameter	80 cm
Scan speed	0.1–6.0° s ⁻¹
Sampling rate	10 MHz
Typical time resolutions	1 s–1 min
Typical range resolutions	30–300 m

and fixed azimuth angle) scans and conical scans (varying azimuth angle and fixed elevation angle) as well as different types of volume scans. The signals are detected by an avalanche photodiode (APD) in combination with a highly linear and low-noise transimpedance receiver package from the German Aerospace Center DLR. Further details of the transmitter–receiver unit are presented in Riede et al. (2012).

The 14 bit data acquisition system (transient recorder MI.4032, Spectrum GmbH, Germany) records the atmospheric backscatter signals with typically 10 MHz sampling rate, resulting in a range resolution of the raw signals of 15 m. We store the backscatter signals of each laser shot, which gives us maximum flexibility later when analyzing the data. Together with the lidar signals, elevation and azimuth angles of the telescope are recorded with each pulse. For the WV calculation, the raw data are typically averaged over 1 s to 1 min in time for the online and offline data. Range averaging is applied within the WV derivation (so-called Savitzky–Golay derivation). The system specifications of the UHOH DIAL are summarized in Table 1.

In recent years, the performance of the UHOH DIAL system was investigated within several intercomparison campaigns. Bhawar et al. (2011) performed an extensive comparison study between the UHOH DIAL and six other WV lidar systems during the Convective and Orographically-induced Precipitation Study (COPS) in 2007 (Wulfmeyer et al., 2011; Behrendt et al., 2013). They found a bias of only −1.43 % for the UHOH DIAL relative to the mean of all measurements. In 2013, in Hohenheim, Stuttgart (Germany), a further comparison study with Vaisala RS-92 radiosondes was performed and resulted in a mean bias of −1.0 % ± 2.6 % (Späth et al., 2014). Following the method of Lenschow et al. (2000) and Wulfmeyer et al. (2016), an analysis of the autocovariance function of the WV time series at each height is used to distinguish between instrumental noise and atmospheric vari-

ances. This technique yielded a noise error of < 5 % up to 2 km using a time resolution of 1–10 s (Muppa et al., 2016). Here, we demonstrate for the first time how this technique can be modified and adapted to perform error analysis of 2-D to 3-D scanning measurements.

3 Data processing and derivation of WV profiles

3.1 DIAL methodology

With the DIAL technique the number density of water vapor (or other trace gases like ozone, methane, etc.) can be measured directly with two backscatter lidar signals. One signal is tuned to a wavelength with strong absorption of WV ($P_{\text{on}}(r)$: online signal) and the other signal to a wavelength with weak absorption ($P_{\text{off}}(r)$: offline signal). The range r is measured from the lidar system to the scattering volume along the line of sight. The return signals $P(r)$ for each wavelength can be described with the lidar equation of elastic backscattering as (Wulfmeyer et al., 2015)

$$P_{v_0}(r) = P_0 \eta \frac{c \Delta t}{2} \frac{A_{\text{tel}}}{r^2} O(r) \Gamma_{\text{air}, v_0}^2(r) \times \left\{ \beta_{\text{par}, v_0}(r) \int_{-\infty}^{+\infty} S_L(v - v_0) \Gamma_{\text{WV}}^2(v, r) F_R(v, r) dv + \beta_{\text{mol}, v_0}(r) \int_{-\infty}^{+\infty} [S_L(v - v_0) \Gamma_{\text{WV}}(v, r)] \times \text{DB}(v, r) \Gamma_{\text{WV}}(v, r) F_R(v, r) dv \right\} + P_B, \quad (1)$$

with the transmitted intensity P_0 at the laser frequency v_0 , the system efficiency η , the speed of light c , the sampling resolution of the system Δt , the telescope area A_{tel} , the overlap function $O(r)$, the transmission of the atmosphere $\Gamma(r)$ as

$$\Gamma_v(r) = \Gamma_{\text{air}, v}(r) \Gamma_{\text{WV}}(v, r) = \exp \left\{ - \int_0^r [\alpha_{\text{par}, v}(r') + \alpha_{\text{mol}, v}(r')] dr' \right\} \times \exp \left\{ - \int_0^r \alpha_{\text{WV}}(v, r') dr' \right\}, \quad (2)$$

the particle and molecular extinction coefficient $\alpha_{\text{par}, v}(r)$ and $\alpha_{\text{mol}, v}(r)$, which are only slightly dependent on frequency v , the extinction coefficient of water vapor (of the trace gas) $\alpha_{\text{WV}}(v, r)$, the particle and molecular backscatter coefficient $\beta_{\text{par}, v}(r)$ and $\beta_{\text{mol}, v}(r)$, the normalized laser spectrum at the ground S_L , the spectral broadening due to Doppler-broadened Rayleigh scattering, DB, the transmission function of the receiver interference filter F_R , and P_B the background signal. α_{WV} is related to the absorption cross section

σ_{WV} and the WV number density N_{WV} by

$$\alpha_{\text{WV}}(\nu, r) = N_{\text{WV}}(r) \sigma_{\text{WV}}(\nu, r). \quad (3)$$

Our laser is designed so that the laser spectrum can be considered a delta distribution. In this case, the derivation of the WV profile becomes independent of any laser parameters, which is called narrow-band DIAL. Furthermore, we assume that the overlap function is either the same for online and offline signals or height independent; we also consider the interference filter transmission function to be constant over the frequency range of interest and not dependent on range. Then, calculating the ratio of Eq. (1) for online and offline wavelengths, applying the relation of Eq. (3), and solving for the WV number density N_{WV} leads to the narrow-band DIAL equation

$$N_{\text{WV}}(r) = \frac{1}{2(\sigma_{\text{on}}(r) - \sigma_{\text{off}}(r))} \frac{d}{dr} \ln \left(\frac{P_{\text{off}}(r) - P_{\text{B,off}}}{P_{\text{on}}(r) - P_{\text{B,on}}} \right) + \frac{1}{2(\sigma_{\text{on}}(r) - \sigma_{\text{off}}(r))} \frac{d}{dr} \ln \left(\frac{\beta_{\text{par,on}}(r) + \beta_{\text{mol,on}}(r) \Gamma_{\text{WV, on}}^{-1}(r) \int_{-\infty}^{\infty} \Gamma_{\text{WV}}(\nu, r) \text{DB}(\nu - \nu_{\text{on}}, r) d\nu}{\beta_{\text{par,off}}(r) + \beta_{\text{mol,off}}(r)} \right), \quad (4)$$

where the index “on” and “off” implies that the specific variable is taken at the online or offline wavelength, respectively. Online and offline wavelengths are chosen close to each other because then the particle and molecular extinction and backscatter coefficients for online and offline wavelengths cancel when taking the ratio of the signals in Eq. (4). All system parameters which are constant with range r cancel because of the derivative. Thus, for DIAL measurements no calibration is needed. Only the values of the absorption cross sections at online and offline wavelength σ_{on} and σ_{off} have to be known very accurately.

The second term in Eq. (4) describes the Rayleigh Doppler correction term related to the broadening effect of the laser spectrum by Rayleigh scattering. The particle backscatter coefficient can be calculated from the offline signal (Fernald et al., 1972; Fernald, 1984). Ansmann and Bösenberg (1987) showed that this correction becomes significant when strong particle backscatter gradients are present. However, they only considered that the online laser wavelength is at the peak of the water vapor absorption line.

Within the analyses presented here this effect was not critical, as confirmed not only by comparisons with radiosoundings but also with new sensitivity analyses considering a frequency agile operation of our laser transmitter (Metzendorf et al., 2015). This reduced sensitivity to the Rayleigh Doppler correction was due to two reasons. Firstly, most of the sampled air masses were located within the ABL where no large particle backscatter gradients were present. Secondly, the

Rayleigh Doppler effect is strongly reduced if the online frequency is located on the wing of the absorption line. In this case, the integral in Eq. (4) becomes approximately $\Gamma_{\text{WV, on}}$, so the nominator and the denominator of the term cancel – independent of the aerosol gradient. More details can be found in Späth et al. (2015). For the measurements discussed here, we selected an online frequency away from the peak absorption but still strong enough to produce sufficient differential absorption. This selection allowed us to optimize the sensitivity of the DIAL measurements in the range of interest for the moisture values present (Späth et al., 2014). Thus, the so-called Schotland approximation of the DIAL equation (Schotland, 1966, 1974)

$$N_{\text{WV}}(r) = \frac{1}{2(\sigma_{\text{on}}(r) - \sigma_{\text{off}}(r))} \frac{d}{dr} \ln \left(\frac{P_{\text{off}}(r) - P_{\text{B,off}}}{P_{\text{on}}(r) - P_{\text{B,on}}} \right) \quad (5)$$

was used for all cases presented here. With this approximation no backscatter coefficients were needed for the calculation. In the following, the derived moisture values in number density are transformed in absolute humidity ρ in units of g m^{-3} .

The WV cross section $\sigma_{\text{WV}}(\nu, T, p, N_{\text{WV}})$ depends on N_{WV} by self-broadening, temperature T , and air pressure p at a certain frequency ν . These dependencies have been measured very accurately in the laboratory and collected in databases, e.g., the High-resolution TRANsmission molecular absorption database (HITRAN) (Rothman et al., 2013). Selecting specific absorption lines with low ground-state energy, it was shown that the dependence of the cross sections on the atmospheric temperature, pressure, and WV profiles is weak and that it is sufficient to assume mean hydrostatic and adiabatic conditions merely using surface values. This makes DIAL the most accurate WV remote sensing technique to date.

Suitable wavelength regions for WVDIAL were discussed over a large wavelength range by Wulfmeyer and Walther (2001a, b). Specific DIAL systems were developed, e.g., near 720 nm (Bruneau et al., 2001; Wulfmeyer and Bösenberg, 1998), near 820 nm (Ismail and Browell, 1989; Ertel, 2004; Schiller et al., 2007; Vogelmann et al., 2008; Behrendt et al., 2009; Spuler et al., 2015), near 935 nm (Machol et al., 2004, 2006; Wirth et al., 2009; Fix et al., 2011), and near 1480 nm (Petrova-Mayor et al., 2008). The UHOH DIAL operates at wavelengths near 818 nm because this wavelength region can be reached well with a Ti:sapphire transmitter and offers a sufficiently large range of WV absorption cross sections (Wagner et al., 2011, 2013).

3.2 Data processing

In case of the UHOH DIAL, the atmospheric backscatter data are recorded for each laser shot. Later, these data are averaged in time over typically 1–10 s and background corrected by subtracting the averaged signal between 25 and 30 km. The absorption cross section profiles for the selected online

and offline wavelengths are determined using profiles of temperature $T(z)$ using a surface value in combination with the temperature gradient from the US Standard Atmosphere, a hydrostatic pressure $p(z)$ also initialized with a surface value and an atmospheric mean temperature in the range of interest. An initial guess for the water vapor number density $N_{\text{WV}}(z)$ is taken from the US Standard Atmosphere (NASA, 1976). We take the spectroscopic parameters of water vapor from the latest compilation of HITRAN described by Rothman et al. (2013).

The water vapor profile is then calculated according to Eq. (5) (Schotland approximation). The Savitzky–Golay (SaGo) method is applied for the derivative with respect to range r (Savitzky and Golay, 1964). This method calculates the first derivative using a certain number of data points. The resulting range resolution ΔR is approximately half of the SaGo window length, as the weighting function is parabolic (Ehret et al., 2001). Typically our SaGo window range consists of four data points on each side of a specific range, resulting in a range resolution of $9 \times 15 \text{ m}/2 \cong 67.5 \text{ m}$. The 15 m step size of the data points used for the derivation of the WV profile is kept. Depending on whether Eqs. (4) or (5) must be applied, either an iteration is necessary to derive the WV profiles (Eq. 4) or a direct derivation is sufficient (Eq. 5). However, in both cases the resulting solution is unique and even if an iteration must be applied to find the result it converges very quickly after one to three iterations. The whole chain of data processing is summarized in a flow chart (see Fig. 2).

3.3 Analysis of scanning data

Up to this step, the analysis procedure is similar for vertical and for scanning measurements. After calculating the WV of scanning measurement, the data can be plotted and used for further analysis in polar coordinates (r, Θ, ϕ) . Alternatively, the data can be gridded to a regular horizontally and vertically spaced grid (x, y, z) (see also Fig. 2). We prefer gridded data because atmospheric variations are usually horizontally or vertically oriented. 3-D data sets can be analyzed by extracting slices of different orientation.

To estimate instrumental noise $\Delta\rho$ of vertical measurements, we apply the method of Lenschow et al. (2000) and Wulfmeyer et al. (2016). Here, the autocovariance function (ACF) of the humidity fluctuations for one range bin is determined. The ACF at lag 0 gives the total variance which is the sum of atmospheric variance and noise variance. The atmospheric variance can be separated from the instrumental noise by extrapolating the ACF to lag 0. For conical scanning measurements, this approach can be used without further modification because data points of a certain range are at the same height.

For scanning measurements in RHI mode, the determination of the atmospheric variance is more complicated. When a time series with a large number of fast RHI measurements

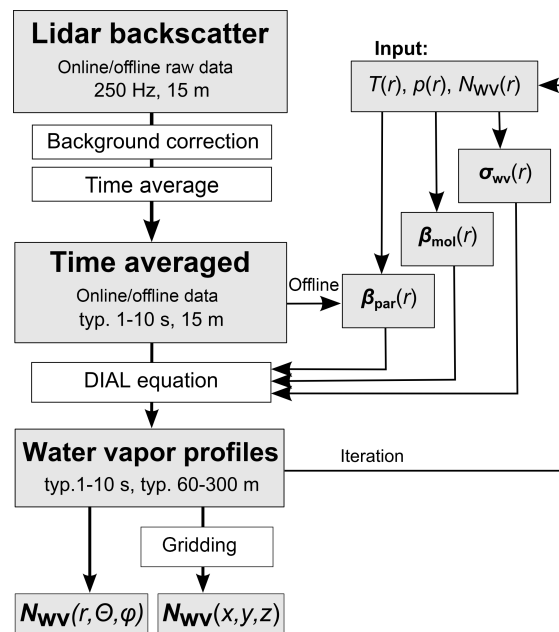


Figure 2. Flow chart of data processing. The backscatter coefficients $\beta_{\text{par}}(r)$ and $\beta_{\text{mol}}(r)$ are only used if the Rayleigh Doppler correction (Eq. 4) is required. For the cases presented here, we used the Schotland approximation (Eq. 5).

with small periods between consecutive scans such as tens of seconds (when scanning fast with 6° s^{-1}) or a few minutes (as for the low-elevation scans with one scan per minute) is available, one can just use the time series of data at one range and elevation. However the noise within single RHI data can also be determined. In contrast to conical scans, rings of constant range cover different heights for RHI data and thus clearly different atmospheric variance values; but even more importantly, the instrumental noise within an RHI scan that covers a large part of the ABL differs for fixed range because the humidity and thus the optical depth show large differences (Wulfmeyer and Walther, 2001b). In consequence, one has to group the measured RHI data then in a more sophisticated way. In the following, we suggest such an approach.

We have tested several different concepts for grouping the data. A simple 1-D approach is to take a number of range bins from one slant profile, but as the required number of independent measurement points is about 10, this still leads to very similar problems as discussed above when selecting measurement points of constant range. Thus, we finally decided to group the measured data set with very high resolution two-dimensionally. We calculate the noise estimation with three independent data points of three profiles giving $3 \times 3 = 9$ data points for each group that is analyzed. The vertical noise profile is then obtained from groups of which the central data points are at a certain horizontal distance to

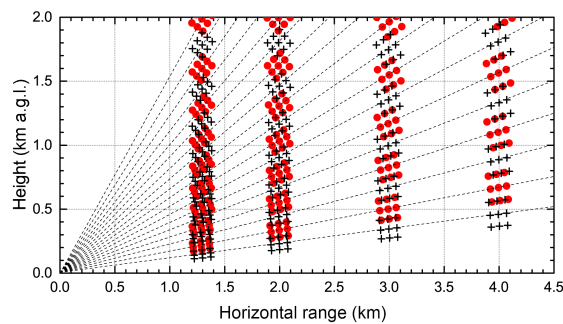


Figure 3. Spatial distribution of the grouping of the measured data used for the noise estimation for a single RHI scan. For each group of nine data points, either black pluses or red dots, the ACF is calculated. Different symbols are used for better understanding when the data points are close to each other. Dashed lines indicate each second profile.

the lidar (Fig. 3). The data set used for the error estimate has the very high resolution over the entire distance range.

When using RHI data sets with very high spatial resolution (in range and elevation), the instrumental noise is much larger than the atmospheric variance. Thus the sequence of the nine data points of each group used for the ACF analysis becomes irrelevant and one can just use lag 0 as the upper limit for the instrumental noise estimation. Finally, the resulting noise values are scaled to the temporal and spatial resolution of the averaged and gridded data according to Ismail and Browell (1989):

$$\frac{\Delta\rho}{\rho} \propto (\Delta t)^{-0.5} (\Delta r)^{-1.5}. \quad (6)$$

In doing so, for the temporal resolution of RHI scans, the scaling results in different angle resolutions.

In the following, we present several examples of 2-D and 3-D scans of the WV fields, analyze the results, and apply our new tools for error analyses.

4 Range–height indicator scans to investigate 2-D turbulence and clouds in the ABL

4.1 Instrumental setup

To capture the horizontal and vertical WV field and its relation to 2-D ABL turbulence statistics and cloud formation, RHI scanning measurements are preferable. With vertical measurements only observations in the so-called Eulerian specification are possible which means that the atmosphere is observed while advecting through the lidar beam. Here, temporal and spatial changes of the measured data are entangled. With RHI scans, this is not the case (or at least much less); therefore both temporal and spatial differences of the moisture field in the ABL can be studied.

The UHOH DIAL was operated in RHI mode within the HD(CP)² Observation Prototype Experiment (HOPE) near Forschungszentrum Jülich, in western Germany (see <http://www.hdcp2.eu/Campaign-HOPE.2306.0.html>). The aim of the experiment was to produce a data set of atmospheric measurements for the investigation of land–atmosphere interaction, cloud formation, aerosol–cloud microphysics as well as weather and climate model evaluation at the 100 m scale. For HOPE, three supersites were set up in a triangular configuration with distances of about 4 km between each other. All these sites were equipped with in situ and remote sensing instruments to measure atmospheric parameters. With the different instruments, the temporal and spatial heterogeneity of the convective boundary layer (CBL) was investigated concerning WV, temperature, and wind fields as well as the distribution of aerosol particles and clouds. The UHOH DIAL was located at the HOPE supersite near Hambach (50°53′50.56″ N, 6°27′50.39″ E; 110 m a.s.l.). At the same site with the UHOH DIAL, the UHOH rotational Raman lidar (RRL) (Radlach et al., 2008; Hammann et al., 2015) measured temperature and the KITcube (Kalthoff et al., 2013) observed – among others – the wind field with scanning Doppler lidar systems (Träumner, 2010) and the surface energy balance (Kalthoff et al., 2006; Krauss et al., 2010). The UHOH DIAL provided measurements of more than 180 h in 18 intensive observation periods (IOPs) in vertical and different scanning modes. The high-resolution fields of the measured thermodynamic variables are also used to derive higher-order moments of turbulent fluctuations (Muppa et al., 2016; Behrendt et al., 2015a) as well as sensible and latent heat fluxes (Wulfmeyer et al., 2014; Behrendt et al., 2015b). This data set will be used for the verification of current approaches of turbulence parameterizations as well as of the development and tests of new turbulence parameterizations. Further details are found in Wulfmeyer et al. (2016).

4.2 Performance and analyses of RHI scans

Our measurements were performed during IOP 4 on 20 April 2013. On this day, the HOPE domain was under the influence of a high pressure system located with its center over the Baltic Sea. The main wind direction was northeast to east as confirmed by the radiosoundings. Figure 4 shows temperature, humidity, and wind velocity profiles of the radiosonde launched at 07:00 UTC at the lidar site. The horizontal wind speed within the ABL was between 8 and 10 m s^{−1} with a minimum of 5.5 m s^{−1} at a height of 1250 m above ground level of the lidar site (a.g.l.). Temperature and absolute humidity were quite low on this day with ground values of only 5 °C and 4.5 g m^{−3}, respectively. Between 06:00 and 07:00 UTC (local time was UTC+2), only thin cirrus clouds were present at heights between 7 and 8 km as found by the offline backscatter signal. The surface temperature profile shows that a very shallow unstable surface layer started to develop by surface heating but it was not deeper than 200 m.

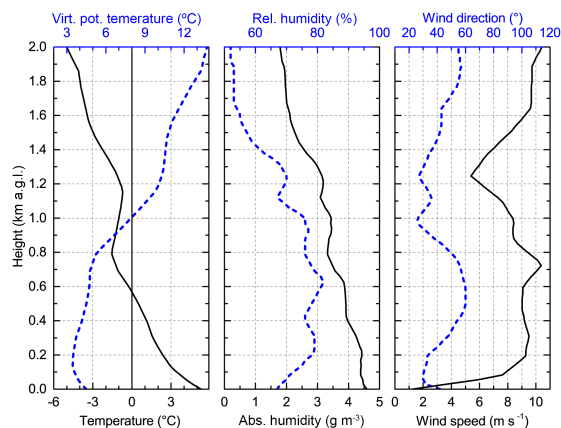


Figure 4. Profiles of temperature, virtual potential temperature, absolute and relative humidity, horizontal wind speed, and wind direction measured with the radiosonde on IOP 5 on 20 April 2013 at 07:00 UTC.

The complex vertical layering is particularly visible in the absolute humidity profile, which shows a series of moisture layers with a thickness of 100 to 200 m, up to 1.4 km a.g.l. However, the virtual potential temperature profile shows that the top of the residual layer was at around 800 m a.g.l., while the top of the developing mixed layer was at 200 m a.g.l. There was another temperature inversion at around 1.6 km a.g.l. that may be related to more synoptic meteorological conditions such as large-scale subsidence.

RHI scanning measurements of the humidity field in the HOPE region were performed on 20 April 2013 between 06:03 and 07:24 UTC. The time resolution for this analysis is 10 s. With a scan speed of $0.15^\circ \text{ s}^{-1}$, this results in an angle resolution of 1.5° . With a covered elevation angle range of 85° each of these RHI scans took around 10 min. Due to the longer path of the laser beam through the aerosol-loaded air in lower elevation and the corresponding higher extinction as well as due to the higher moisture in the boundary layer and the corresponding stronger attenuation of the on-line signal, we averaged the data according to the following procedure. We calculated the absolute humidity with different range resolutions ΔR to keep the angle resolution. Afterwards, the radial data were gridded to a horizontal-vertical grid with a resolution of 50 m. Finally, the data with different resolutions were merged according to the horizontal distance: up to a distance of 1.3 km $\Delta R = 142.5$ m, up to 2.5 km $\Delta R = 307.5$ m, up to 3.0 km $\Delta R = 457.5$ m, and up to 4.2 km $\Delta R = 997.5$ m.

A noise error analysis was carried out as described in Sect. 3 and profiles for the horizontal distances of 1.3, 2, 3, and 4 km are shown in Fig. 5. For all distances, the error profiles show a significant increase above the top of the ABL because there are much fewer aerosol particles present which

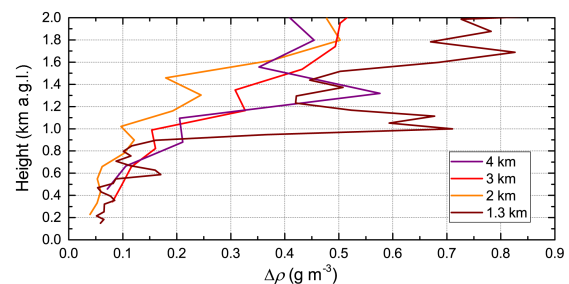


Figure 5. Instrumental noise profiles of the RHI scans shown in Fig. 6 for horizontal distances (range resolution) of 1.3 km ($\Delta R = 142.5$ m), 2 km ($\Delta R = 307.5$ m), 3 km ($\Delta R = 497.5$ m), and 4 km ($\Delta R = 997.5$ m) with a temporal resolution of 10 s.

act as scatterers. The top of the ABL height increases from the near range (1.3 km) to the far range (4 km). At a horizontal distance of 1.3 km the top of the ABL is at 0.9 km a.g.l. while it is 200 m higher (1.1 km a.g.l.) at a distance of 4.0 km. Below the top of the ABL, the noise values are below or around 0.2 g m^{-3} , and above the top of the ABL the noise reaches values between 0.5 and 0.8 g m^{-3} . This results in an upper limit of a relative noise error of $< 6\%$ within the ABL. The noise profile for 1.3 km distance does not show the smallest values but this is maybe due to the assumption of neglecting atmospheric fluctuations which become relatively larger when the instrumental noise decreases.

Figure 6 shows scanning humidity measurements in the HOPE region on 20 April 2013 between 06:03 and 07:24 UTC. The measurements were performed towards the two other experimental sites of the HOPE campaign: towards the Leipzig Aerosol and Cloud Research Observations System (LACROS) southwards and towards the Jülich Observatory for Cloud Evaluation (JOYCE) southwestwards. The plots are geolocated to the Earth surface and cover a horizontal range of 0.7 to 4.2 km up to an altitude of 2 km a.g.l. In the near range of the RHI scans we omitted the data up to 950 m because of no full overlap of the field of view of the transmitting and receiving telescopes.

The WV field in the two scanning directions showed several similarities but also significant differences, revealing the heterogeneities of the ABL in the region. In both directions, three moist layers with drier layers in between can be identified. The altitudes of the layers differ significantly. Towards LACROS, the moist layers were at 500, 1100, and 1500 m a.g.l. while towards JOYCE they were at 300, 1000, and 1400 m a.g.l. for the measurements for the first two scans between 06:03 and 06:27 UTC (Fig. 6a). One hour later (Fig. 6b), the measurements show the same number of layers but the height of the lowest one increased to 600 and 500 m a.g.l. for LACROS and JOYCE directions, respectively.

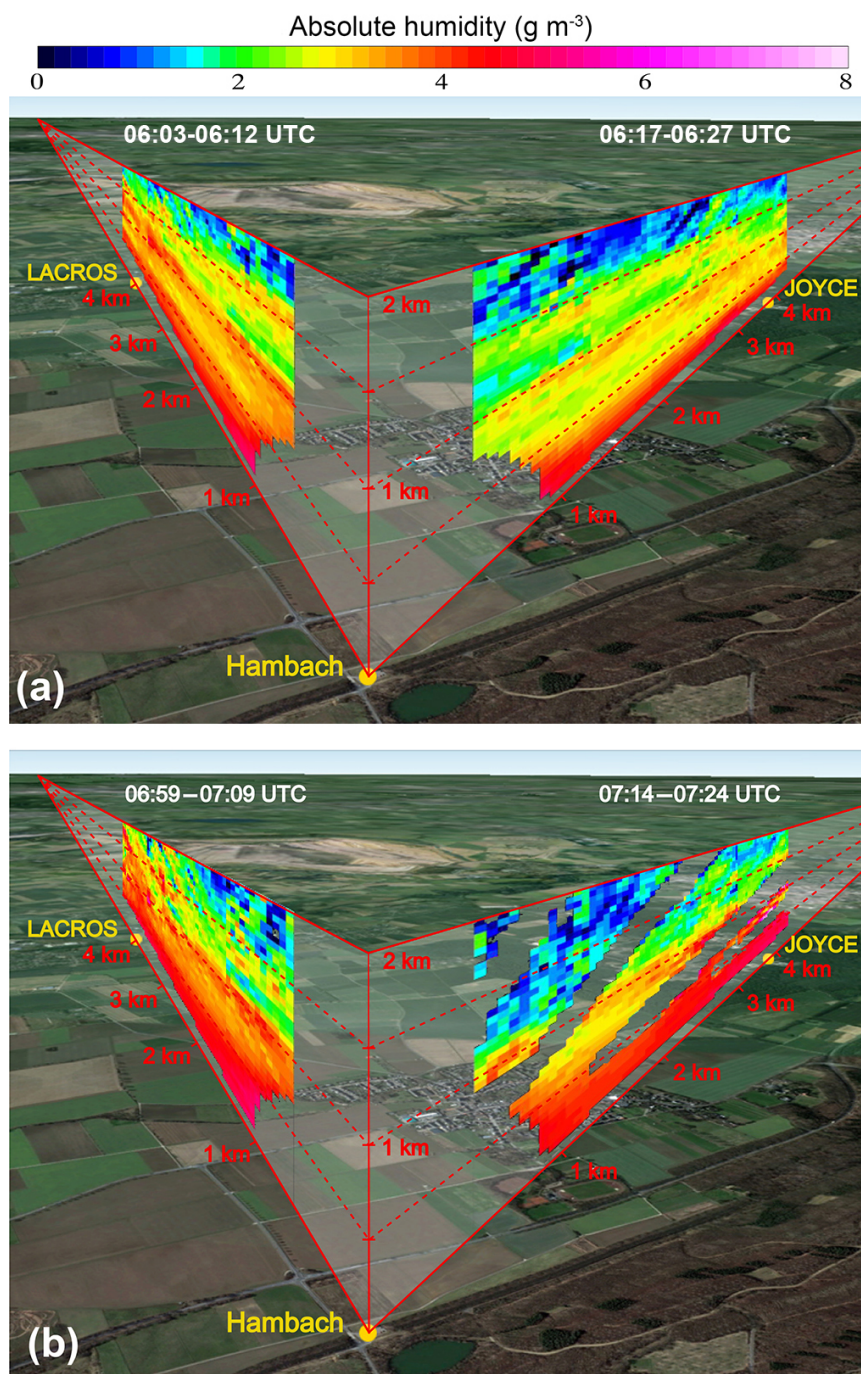


Figure 6. 3-D illustration of the WV field in the HOPE domain. The scanning measurements were performed towards LACROS and JOYCE on IOP 4 on 20 April 2013 between (a) 06:03 and 06:27 UTC and (b) 06:59 and 07:24 UTC. The UHOH DIAL system was located at the Hambach site and scanned towards the other supersites LACROS and JOYCE. The distances to the other sites were around 4 km. In (b) the gaps in the data occur from clouds at the top of the CBL. Background image from Google Earth.

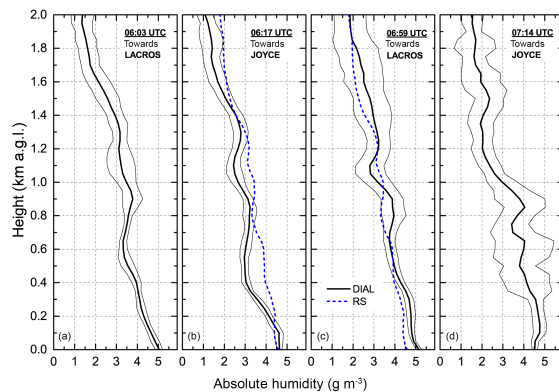


Figure 7. Spatially averaged humidity profiles of the scanning measurements of Fig. 6. The profiles in (a) are of the scans towards LACROS and in (b) towards JOYCE. The thick solid lines show the mean profiles of each scan and the thin lines indicate the horizontal variability of humidity (1σ standard deviation) within the scan range. The radiosonde profile at 07:00 UTC was plotted with a dashed line with the two closest scans (b and c).

In general, we see that the ABL was more moist in the direction of LACROS than in the direction of JOYCE. In order to illustrate this, we have averaged the scanning data horizontally. The averaged vertical humidity profiles of the four RHI measurements of Fig. 6 are shown in Fig. 7. In the profiles, the layer structure discussed above can be identified. The humidity profile of the radiosonde at 07:00 UTC does not fit with an averaged DIAL profile and shows also different structures but the profile stays within the variability of the DIAL measurement towards LACROS. However, different to the DIAL measurements, a radiosonde measures only along its flight path and, thus, can only sample a snapshot of the atmospheric constitution. In this case, northeasterly wind caused a horizontal wind-driven displacement of the radiosonde of about 3 km when it reached an altitude of 2 km a.g.l. The horizontal variability within a certain range can also only be determined with scanning DIAL measurements. For these reasons, horizontally averaged profiles of scanning DIAL measurements are better suited for comparisons with model simulation outputs which also give profiles representative of a whole model grid box (Milovac et al., 2016).

Interestingly, in one of the scans (Fig. 6b towards JOYCE) clouds appear, while all others are cloud-free. Four clouds can be identified in the offline backscatter signals at distances and altitudes of 300 and 700 m a.g.l., of 600 and 600 m a.g.l., of 1.5 km and 500 m a.g.l., and of 3 km and 500 m a.g.l., respectively. The large extinction of the clouds prohibits measurements inside the clouds and beyond, resulting in radial structured gaps in the data (plotted transparently in Fig. 6b). At 560 m a.g.l. the profiles of the radiosonde (Fig. 4) show a zero-crossing in the temperature and a relative humidity

of only about 80 %. The DIAL measurements show values of about 4.5 and 5 g m⁻³ below the clouds at 1.5 and 3 km distance, respectively. As at least 100 % relative humidity is needed for cloud formation, this corresponds to a required absolute humidity of 4.8 g m⁻³ at a temperature of 0 °C. Clearly, the observed clouds are related to locally higher moisture values as revealed by the DIAL scans, which are also seen in Fig. 7d by an upper limit of the 1σ standard deviation above 5 g m⁻³ in heights between 300 and 700 m a.g.l. The measurement 1 h before already showed these humidity values at around 250 m a.g.l. altitude, which was not sufficient to reach saturation but indicate that the humidity came from the ground and reached the condensation level during the last scan.

5 Volume scans for the investigation of the 3-D water vapor field

5.1 Instrumental setup

With volume scans, the relation of the moisture field to surface properties can be investigated more in detail. The observation of 3-D humidity is either possible by a series of fast RHI scans using different azimuth angles or by a series of continuous 360° scans with different elevation angles.

For the first time with the UHOH DIAL, the latter configuration was applied during the Surface Atmosphere Boundary Layer Exchange (SABLE) field campaign in August 2014. The SABLE campaign took place near Pforzheim (48°55′45.85″ N, 8°42′19.57″ E; 320 m a.s.l.) in the Black Forest (southwest Germany) as part of the Research Unit 1695 “Regional Climate Change” of the German Research Foundation (DFG; see <https://klimawandel.uni-hohenheim.de/startseite?&L=1>). The UHOH DIAL was collocated with the UHOH RRL for temperature measurements and with three Doppler lidar systems for measuring the wind velocities as well as with a synergy of surface in situ sensors distributed in the fields, e.g., eddy covariance stations (Wizemann et al., 2015). The results of these campaigns shall contribute to an improved understanding of the relations between surface properties and boundary layer characteristics, shallow cumulus convection, as well as convection initiation.

During the special observations period (SOP) 2 on 22 August 2014, the 3-D WV field was observed with a volume scan. On this day, a low pressure system over Scandinavia and a high pressure system over eastern Europe provoked westerly flow in the SABLE domain. Stratus clouds occurred over the measurement site with a bottom height of about 2.5 km a.g.l. These clouds reduced the surface heating, so no convective boundary layer formed. Consequently, we can assume that the structures of the moisture field were largely advected and modified locally mainly by orography. There was a small hill with a top height of 375 m a.s.l. at 0.6 km distance to the south while the terrain in the near range of

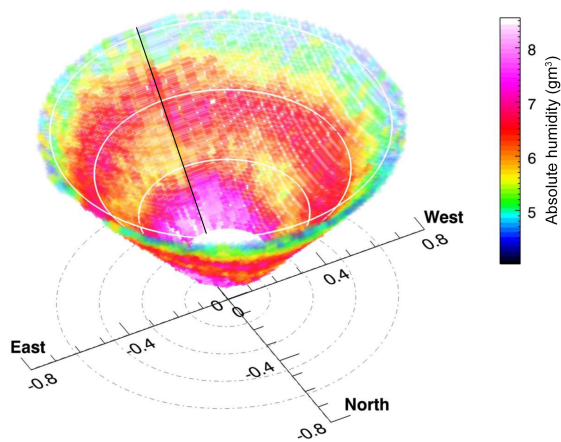


Figure 8. Conical scan of SOP 2 on 22 August 2014 between 08:40 and 08:55 UTC. The cone has an elevation angle of 50° . The data were plotted for a height range from 0.2 up to 0.8 km a.g.l. The white circles indicate the height in 0.2 km steps and the grey dashed-pointed circles show their projection down to the ground. The black solid line marks the start and end direction of the conical scan; the scanner unit moved clockwise. The scales are given in km.

the lidar was mainly flat. The radiosonde from 09:30 UTC showed at the ground a temperature of 16°C and a relative humidity of 60 %. The wind was calm ($<1.5\text{ m s}^{-1}$) at the ground up to 300 m a.g.l. and increased then to 6 m s^{-1} at 600 m a.g.l. in an east–northeast direction.

5.2 Performance and analyses of the volume scan

The area around the DIAL site was observed by performing a series of 360° conical scans around the vertical with elevation angles of 50° , 60° , 70° , 80° , and 90° . Figure 8 shows a 3-D view of the 50° cone of the volume scan between 08:40 and 09:40 UTC. For this measurement, the scan speed was 0.4° s^{-1} , resulting in a total duration of 15 min per cone. Consequently, the full volume with five cones was scanned within 75 min. The start and the end directions were southward-oriented and the scanner moved for the 50° , 70° , and 90° cone clockwise and counter-clockwise for the other scans of 60° and 80° . The WV calculation was performed with 10 s averaged profiles and a 67.5 m range resolution. For plotting, the WV data were transferred from the polar coordinates to Cartesian coordinates and each profile was expanded over an azimuth range of 4° .

The instrumental noise was determined with the method of Lenschow et al. (2000) for each elevation angle separately. Profiles of the absolute and relative noise are shown in Fig. 9. Above 400 m a.g.l., the noise level increases with height. The noise at the same height a.g.l. is higher for lower elevation angles than for higher elevation angles because the range for the same height a.g.l. is larger. The profile of the low-

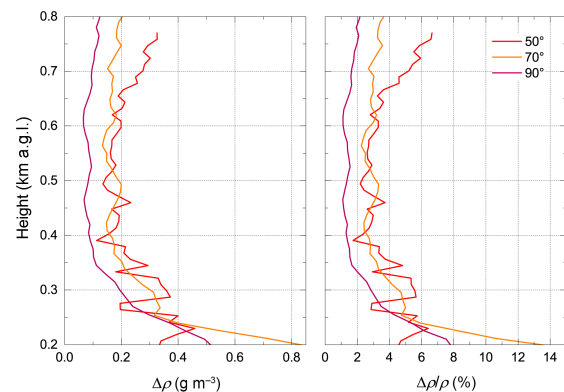


Figure 9. Absolute noise $\Delta\rho$ and relative noise $\Delta\rho/\rho$ profiles of selected parts of the volume scan with the corresponding temporal and spatial resolution of 10 s and 67.5 m, respectively.

est elevation angle shows a maximum noise of $<0.35\text{ g m}^{-3}$ or $<7\%$ at 750 m altitude a.g.l. Below 400 m a.g.l., the noise also increases, but here due to overlap effects. However, this does not occur in the absolute humidity data as the noise is $<0.8\text{ g m}^{-3}$.

The measurement in Fig. 8 shows two moist layers. The lower layer reached altitudes up to between 300 and 400 m a.g.l. with humidity values of $7\text{--}8\text{ g m}^{-3}$. This layer was topped by a drier layer with 5.6 g m^{-3} and a second moist layer at 600 m a.g.l. with a humidity of about 6.5 g m^{-3} .

To get an insight into the whole volume, Fig. 10a shows cross sections and illustrates the whole data set of the volume scan three-dimensionally. In addition and for orientation, the cutting planes are depicted of which the water vapor distribution is then shown in Fig. 10b–i. The figure contains three vertical cross sections in a north–south direction (panel b–d) and three in a west–east direction (panel e–g) as well as horizontal cross section planes at two height levels (panel h–i). The vertical cross section images depict the vertical structure at different distances to the DIAL similar to what was shown above with RHI scans. In Fig. 10b–g the vertical planes are positioned at ± 0.2 and 0.0 km distance with respect to the vertical line above the DIAL location. The horizontal cross section plane can also of course be placed at any height of interest. These plots show the WV distribution with respect to the azimuth angle but in contrast to conical scan plots, the data are not shown along the line of sight but rather at one height the data of all conical scans of different elevation angles of the volume scan are shown. The cross section images depict also the moist layers in the two lower elevation angle scans.

The heights of the layers in Fig. 10 are almost similar for all directions. Because of the full cloud cover on this day, convection was very weak and no large eddies were initiated.

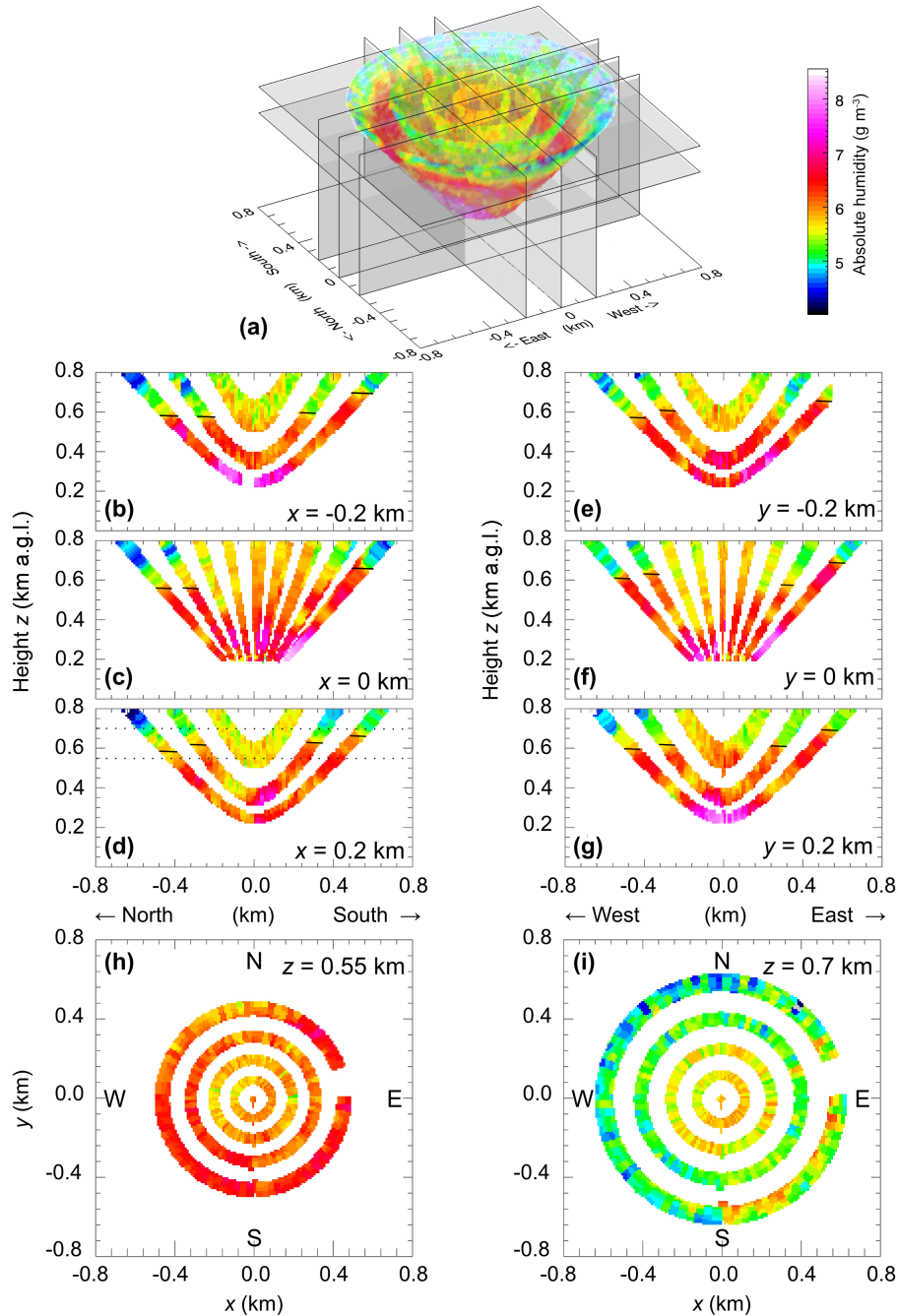


Figure 10. Cutting planes through the 3-D data set provides cross section images. (a) Schematic illustration of the 3-D data set with the cutting planes. (b–i) Horizontal and vertical cross section images of the different cutting planes of (a). The black lines in (b–g) indicate the top of the boundary layer. The dotted lines in (a) illustrate the location of the horizontal planes (h–i).

Thus, the moist layer from the ground grew slowly and varied according to underlying orography. Here, in south direction at a distance of 0.6 km from the DIAL a small hill was located with an increase of the surface elevation of about 55 m. The measurements of the lowest elevation angle in Fig. 10b–d show indeed a higher altitude of the boundary layer of about 50 m at a distance of 0.5 km southwards. Also to the east a small trend to higher altitudes of the top of the boundary layer can be observed. This is also indicated by the horizontal plane image in Fig. 10i for the southeasterly direction and a distance of 0.6 km. This area corresponds in our case to the lee side of the small hill; therefore the higher moisture might be explained by a modification of the moisture field by shifted overflow lifting.

Averaging the volume data horizontally provides the mean humidity profile. The profile was plotted in Fig. 11 up to an altitude of 0.8 km a.g.l. The thin lines mark the horizontal WV variability similar to Fig. 7. The radiosonde profile at 09:30 UTC is given in the diagram as well. Again, there were differences between DIAL and radiosonde measurements but the radiosonde captured similar moisture layers and stayed almost within 1 standard deviation of the DIAL profile.

6 Low-elevation range–height indicator scans for the investigation of the surface layer

6.1 Instrumental setup

On 12 August 2014 the SABLE domain was under westerly flow due to low pressure systems located over the Baltic Sea and Scandinavia, one day before a cold front passed through the measurement area. Vertical DIAL measurements before and after the scanning measurements (not shown here) indicate a CBL height of between 1.0 and 1.5 km a.g.l. and a residual layer up to 2 km a.g.l. The WV content in these two layers was up to 8 g m^{-3} and around 5 g m^{-3} , respectively. During the scanning period, cirrus clouds at 8 km a.g.l. were present and also few low-level clouds at 2–2.5 km a.g.l. at the top of the CBL but these clouds did not inhibit large surface fluxes (sensible heat flux 100 kW m^{-2} and latent heat flux 240 W m^{-2} between 11:00 and 12:00 UTC) and the development of a CBL. The radiosonde profiles from 10:30 UTC measured a temperature of about 18°C and a relative humidity of 60 % at the ground. The relative humidity increased with height and reached 80 % at the top of the CBL. The wind speed was low with $4\text{--}5 \text{ m s}^{-1}$ at the surface and increased linearly with height; the wind direction was west.

In order to observe the surface layer, measurements are needed which reach as close as possible to the land surface or the canopy level. Due to incomplete overlap of the outgoing laser beam and the field of view of the receiver in the near range, vertical measurements of the UHOH DIAL start only a few hundred meters above ground. With low-level RHI scans, these low-level measurements can be realized. Fur-

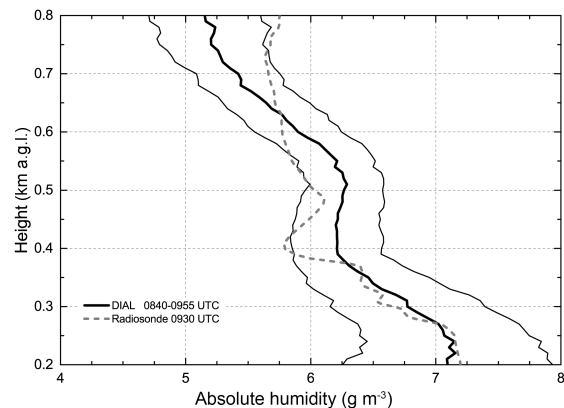


Figure 11. Spatially averaged absolute humidity profiles of the volume scan of Fig. 10 (08:40–09:55 UTC). The thick solid line shows the mean profile of the scanned volume and the thin lines indicate the horizontal WV variability (1σ standard deviation) within the scan range. The radiosonde profile launched at 09:30 UTC was plotted with a dashed line.

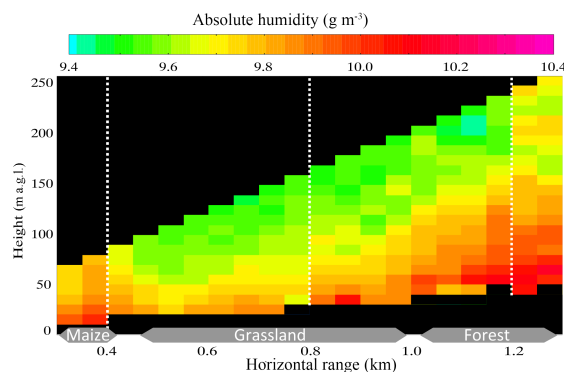


Figure 12. One-hour mean WV field between 11:00 and 12:00 UTC on IOP 4 on 12 August 2014. The covered angle range was 0 to 12° ; the scan speed was 0.2° s^{-1} ; a single scan took 1 min. For the water vapor calculation, 1 s averaged data were used. The land cover along the line of sight is also shown. The dotted lines indicate the location of the vertical profiles shown in Fig. 13.

thermore, the variations in the humidity structures can be related to different types of land use along the line of sight of the low-level scanning measurements.

During the SABLE campaign (see Sect. 5), these low-level scanning measurements were performed to investigate the properties of the atmospheric surface layer. The low-elevation scans covered elevation angles between 0 and 12° . In order to reach a high vertical resolution, the scan speed was 0.2° s^{-1} , which resulted in a time duration of 1 min per scan.

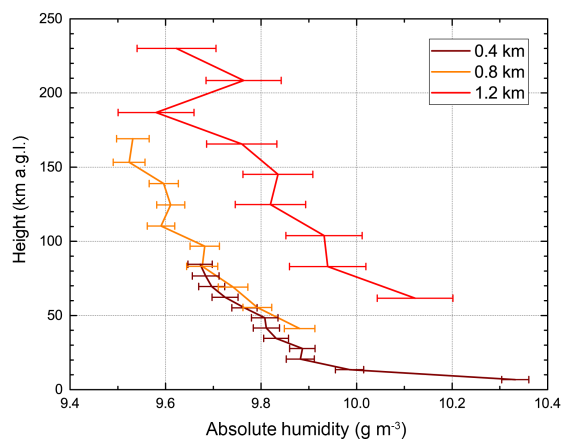


Figure 13. Absolute humidity profiles for the RHI scan of Fig. 12 for the horizontal distances of 0.4, 0.8, and 1.2 km. The noise errors are also shown. The location of the WV and noise profiles are indicated by the dotted white lines in Fig. 12.

6.2 Performance and analyses of the low-level RHI scans

Low-elevation scanning measurements were performed during the SABLE campaign on IOP 4 on 12 August 2014 between 11:00 and 12:00 UTC. The results are presented in Fig. 12. For the WV calculation, 1 s averaged profiles and a SaGo window length of 135 m were used. All scans of the 1 h period (52 scans) were averaged with 1° angle resolution, resulting in a final time resolution of 260 s. Then, the data were gridded to an x - y grid with a resolution of $50 \text{ m} \times 10 \text{ m}$. With the high spatial resolution, small variations in the absolute humidity values (notice color scale 9.4 – 10.4 g m^{-3} in Fig. 12) at different heights and distances can be identified.

The instrumental noise for the low-elevation scan was estimated with the ACF method. The data were used in the initial radial polar coordinates and data points of all scans at a certain range bin covering a 1° angle range were selected for the ACF calculation. The resulting errors were then scaled with Eq. (6) from the 1 s time resolution. In Fig. 13, the noise errors were plotted as error bars with the absolute humidity profiles at the distances of 400, 800, and 1200 m, respectively. All three profiles show a constant noise level for the whole profile which can be expected for the small covered height range because all data points of one profile belong to a similar range bin and as the profile stays within in the boundary layer the optical thickness is constant over the whole height range. Of course, the noise level increases with distance but the noise value stays lower than 0.3 g m^{-3} for 400 m, lower than 0.4 g m^{-3} for 800 m, and lower than 0.9 g m^{-3} for 1200 m. These values translate to relative values of less than 0.3 %, less than 0.4 %, and less than 1 %, respectively.

The humidity values close to the ground are higher than above and at 1200 m distance the humidity was higher than at 800 m distance. Because these measurements are close to the ground, it is possible to relate these changes in horizontal direction to the vegetation at the ground. For the measurement in Fig. 12, the vegetation can be separated into three categories. In the near range up to 450 m there was a maize field, up to 1050 m the ground was covered with grassland, and further away we scanned over forest. The terrain around the DIAL site was mainly flat except for a small hill in a southern direction at a distance of 0.6 km reaching an altitude of 375 m a.s.l. Along the scan direction towards a southwesterly direction; the terrain profile was flat for the maize field and slightly uphill for the grassland, while the forest was located on the small hill at a distance of 1300 m. The measurement in Fig. 12 shows that there was more water vapor in the atmosphere above the maize field and above the forest, which was likely due to higher evapotranspiration than above the grassland.

This 1 h mean profile close to the ground is similar to what was measured by Eichinger et al. (2000) with a scanning Raman lidar. However, with the WVDIAL technique a larger range can be investigated. In the future, such data can be used to estimate the spatial distribution of the latent heat flux over different kinds of land cover (Wulfmeyer et al., 2014). For this purpose, the Monin–Obukhov similarity theory (MOST) (Monin and Obukhov, 1954; Brutsaert, 1982) can be applied using the slope of such a vertical humidity profile and simultaneously obtained friction velocity u^* .

7 Summary and outlook

The measurements of the spatial distribution of water vapor by the UHOH DIAL in three different scanning modes were presented. The UHOH DIAL uses a frequency-stabilized Ti:sapphire resonator as laser transmitter and emits laser pulses at 818 nm. The output power for scanning measurements is currently limited to 1.6 W due to the maximum power which can be transmitted by the optical fiber used. The 20 cm transmitting and 80 cm receiving telescopes form the scanner unit which allows scanning measurements of the whole hemisphere (180° elevation, 360° azimuth) with scan speeds between 0.1 and 6° s^{-1} . For data analyses typical range and temporal resolutions of 50–300 m and 1–10 s, respectively, are used. A new method to determine the noise level of scanning measurements was developed and shows uncertainties of $< 7\%$ within the ABL. With the DIAL technique it is now possible to determine 3-D WV fields with high temporal and spatial resolution including a specific analysis of noise error fields. Therefore, the significance of WV structures in these 2-D and 3-D fields can be studied and specified in great detail.

Scanning measurements in RHI mode were performed in two directions during HOPE with elevation angles from

5 to 90° up to a horizontal distance of 4 km. With these scans the humidity field was investigated regarding turbulent and mesoscale variability as well as cloud formation. Similar layers for both directions but also differences in altitudes of the layers or in the WV content were observed in the WV field. Four scans depict the evolution of the layers within 90 min. In the last measurement of the series, clouds appear at the top of the lowest moist layer where the conditions of 100 % relative humidity for cloud formation were locally fulfilled. Horizontally averaged vertical profiles show also a higher humidity variability for that measurement. The noise at the top of the ABL increases strongly but the noise error remains < 6 % within the ABL.

For the first time, a conical volume scan performed during the SABLE campaign presents the 3-D spatial WV distribution within a distance range of 0.8 km around the DIAL. The data show two moist layers with some variations in height for different directions. These variations can be related to variations in the surface elevation, e.g., in a southeast direction a small hill with a slightly higher elevation was located. The instrumental noise for this case was calculated to be $< 0.5 \text{ g m}^{-3}$ or $< 7 \%$.

Low-elevation scanning measurements revealed the humidity structures close to the ground. The presented data were averaged over 1 h of scanning measurements and cover a height range from 20 to 140 m a.g.l. of the instrument. The horizontal variation of the WV field can be related to the heterogeneity of the vegetation at the ground. The errors for these kinds of measurements were estimated to be $< 0.3 \text{ g m}^{-3}$ or $< 0.3 \%$ at 400 m and $< 0.9 \text{ g m}^{-3}$ or $< 1 \%$ at 1200 m horizontal distance throughout the measured height range.

In conclusion, all scanning modes are applicable to observe the spatial distribution of water vapor in the lower atmosphere. Depending on the focus of the research, the scan pattern can be adapted regarding the covered elevation and azimuth angle ranges.

In future work, these kinds of measurements can be extended to estimate evapotranspiration above different land cover and soil types using the Monin–Obukhov similarity theory. More measurements over different terrains and a larger set of vegetation types as well as under different meteorological conditions will be made. Furthermore, a combination with other instruments (temperature rotational Raman lidar, Doppler lidar, eddy covariance stations, towers, aircraft) will be highly beneficial. In this context, it will be very interesting to perform simultaneous observations of the surface layer and the top of the ABL for heat and WV budget studies. Comparison with LES will allow for validations and improvements of parameterization schemes regarding LA feedback which is essential for further advancements of numerical weather prediction models and climate projections.

Appendix A: Acronyms

3-D	three-dimensional
ABL	atmospheric boundary layer
ACF	autocovariance function
a.g.l.	above ground level of the lidar site
APD	avalanche photodiode
a.s.l.	above sea level
BR	beam reducer
CBL	convective boundary layer
CI	convection initiation
COPS	Convective and Orographically-induced Precipitation Study
DFB	distributed feedback
DIAL	differential absorption lidar
DLR	German Aerospace Center (Deutsches Zentrum für Luft- und Raumfahrt)
ECDL	external cavity diode laser
FC	fiber coupler
HD(CP) ²	High Definition of Clouds and Precipitation for advancing Climate Prediction
HITRAN	High-resolution TRANsmision molecular absorption database
HOPE	HD(CP) ² Observational Prototype Experiment
HR	high-reflection mirror
IOP	intensive observation period
IR	infrared
IWV	integrated water vapor
JOYCE	Jülich ObservatorY for Cloud Evaluation
LA	land-atmosphere
LACROS	Leipzig Aerosol and Cloud Research Observations System
LES	large eddy simulations
MOST	Monin–Obukhov similarity theory
MWR	microwave radiometer
NASA	National Aeronautics and Space Administration
PD	photo diode
PM	primary mirror
RHI	range–height indicator
RRL	rotational Raman lidar
SABLE	Surface Atmosphere Boundary Layer Exchange
SaGo	Savitzky–Golay
SM	secondary mirror
SNR	signal-to-noise ratio
SOP	special observations period
TM	transmitting telescope mirror
UHOH	University of Hohenheim
UV	ultraviolet
WV	water vapor
WVDIAL	WV differential absorption lidar
WVRL	WV Raman lidar

Acknowledgements. The HOPE campaign was funded by the German Research Ministry under the project number 01LK1212A.

The SABLE campaign was included in the Research Unit 1695 “Regional Climate Change” which was funded by the German Research Foundation (DFG) under the DFG Integrated Project PAK 346, project number WU 356-1 AOBJ: 591757.

Edited by: T. von Clarmann

References

- Ansmann, A. and Bösenberg, J.: Correction scheme for spectral broadening by Rayleigh scattering in differential absorption lidar measurements of water vapor in the troposphere, *Appl. Opt.*, 26, 15, 3026–3032, 1987.
- Aoshima, F., Behrendt, A., Bauer, H.-S., and Wulfmeyer, V.: Statistics of convection initiation by use of the Meteosat Rapid Scan Service during the Convective and Orographically-induced Precipitation Study, *Meteorol. Z.*, 17, 921–930, doi:10.1127/0941-2948/2008/0337, 2008.
- Barnes, N. P. and Barnes, J. C.: Injection Seeding I: Theory, *IEEE J. Quantum Electron.*, 29, 2670–2683, 1993a.
- Barnes, J. C., Barnes, N. P., Wang, L. G., and Edwards, W.: Injection Seeding II: $\text{Ti:Al}_2\text{O}_3$ Experiments, *IEEE J. Quantum Electron.*, 29, 2684–2692, 1993b.
- Behrendt, A., Nakamura, T., Onishi, M., Baumgart, R., and Tsuda, T.: Combined Raman lidar for the measurement of atmospheric temperature, water vapor, particle extinction coefficient, and particle backscatter coefficient, *Appl. Opt.*, 41, 7657–7666, 2002.
- Behrendt, A., Wulfmeyer, V., Di Girolamo, P., Kiemle, C., Bauer, H.-S., Schaberl, T., Summa, D., Whiteman, D. N., Demoz, B. B., Browell, E. V., Ismail, S., Ferrare, R., Kooi, S., Ehret, G., Wang, J.: Intercomparison of water vapor data measured with lidar during IHOP_2002 – Part I: Airborne to ground-based lidar systems and comparisons with chilled-mirror hygrometer radiosondes, *J. Atmos. Oceanic Technol.*, 24, 3–21, doi:10.1175/JTECH1924.1, 2007.
- Behrendt, A., Wulfmeyer, V., Riede, A., Wagner, G., Pal, S., Bauer, H., Radlach, M., and Späth, F.: 3-Dimensional observations of atmospheric humidity with a scanning differential absorption lidar, in: *Remote Sensing of Clouds and the Atmosphere XIV*, edited by: Picard, R. H., Schäfer, K., Comeron, A., and van Weele, M., SPIE Conference Proceeding, 7475, 74750L, doi:10.1117/12.835143, 2009.
- Behrendt, A., Pal, S., Aoshima, F., Bender, M., Blyth, A., Corsmeier, U., Cuesta, J., Dick, G., Dorninger, M., Flamant, C., Di Girolamo, P., Gorgas, T., Huang, Y., Kalthoff, N., Khodayar, S., Mannstein, H., Träumner, K., Wieser, A., and Wulfmeyer, V.: Observation of convection initiation processes with a suite of state-of-the-art research instruments during COPS IOP 8b, *Q. J. Roy. Meteor. Soc.*, 137, 81–100, doi:10.1002/qj.758, 2011.
- Behrendt, A., Blyth, A., Dorninger, M., Kalthoff, N., Flamant, C., Di Girolamo, P., and Richard, E.: Convective Precipitation in complex terrain: Results of the COPS campaign, *Meteorol. Z.*, 22, 4, 367–372, doi:10.1127/0941-2948/2013/0541, 2013.
- Behrendt, A., Wulfmeyer, V., Hammann, E., Muppa, S. K., and Pal, S.: Profiles of second- to fourth-order moments of turbulent temperature fluctuations in the convective boundary layer: first measurements with rotational Raman lidar, *Atmos. Chem. Phys.*, 15, 5485–5500, doi:10.5194/acp-15-5485-2015, 2015a.
- Behrendt, A., Wulfmeyer, V., Hammann, E., Muppa, S. K., Späth, F., Metzendorf, S., Riede, A., Karthoff, N., Maurer, V., and Wieser, A.: Atmospheric boundary layer studies with combined temperature rotational Raman lidar, water vapor DIAL, and Doppler lidar, 27th International Laser Radar Conference (ILRC 2015), New York, USA, 5–10 July 2015b.
- Bengtsson, L., Hodges, K. I., and Hagemann, S.: Sensitivity of the ERA40 reanalysis to the observing system: determination of the global atmospheric circulation from reduced observations, *Tellus A*, 56, 456–471, doi:10.1111/j.1600-0870.2004.00079.x, 2004.
- Bhawar, R., Di Girolamo, P., Summa, D., Flamant, C., Althausen, D., Behrendt, A., Kiemle, C., Bosser, P., Cacciani, M., Champollion, C., Di Iorio, T., Engelmann, R., Herold, C., Pal, S., Riede, A., Wirth, M., and Wulfmeyer, V.: The Water Vapour Intercomparison Effort in the Framework of the Convective and Orographically-Induced Precipitation Study: Air-borne-to-Ground-based and airborne-to-airborne Lidar Systems, *Q. J. Roy. Meteor. Soc.*, 137, 325–348, 2011.
- Blumberg, W. G., Turner, D. D., Löhnert, U., and Castleberry, S.: Ground-Based Temperature and Humidity Profiling Using Spectral Infrared and Microwave Observations – Part II: Actual Retrieval Performance in Clear-Sky and Cloudy Conditions, *J. Appl. Meteor. Climatol.*, 54, 2305–2319, doi:10.1175/JAMC-D-15-0005.1, 2015.
- Bösenberg, J.: Ground-based differential absorption lidar for water-vapor and temperature profiling: methodology, *Appl. Opt.*, 37, 3845–3860, 1998.
- Browell, E. V., Wilkerson, T. D., and McIlrath, T. J.: Water vapor differential absorption lidar development and evaluation, *Appl. Opt.*, 18, 3474–3483, 1979.
- Bruneau, D., Quaglia, P., Flamant, C., Meissonnier, M., and Pelon, J.: Airborne lidar LEANDRE II for water-vapor profiling in the troposphere, I. System description, *Appl. Opt.*, 40, 3450–3461, doi:10.1364/AO.40.003450, 2001.
- Brutsaert, W.: *Evaporation into the Atmosphere*, Kluwer Academic Publishers, Dordrecht, the Netherlands, 1982.
- Cohen, A. E., Cavallo, S. M., Coniglio, M. C., and Brooks, H. E.: A Review of Planetary Boundary Layer Parameterization Schemes and Their Sensitivity in Simulating Southeastern U.S. Cold Season Severe Weather, *Weather Forecast.*, 30, 591–612, doi:10.1175/WAF-D-14-00105.1, 2015.
- Corsmeier, U., Kalthoff, N., Barthlott, C., Aoshima, F., Behrendt, A., Di Girolamo, P., Dorninger, M., Handwerker, J., Kottmeier, C., Mahlke, H., Mobbs, S. D., Norton, E. G., Wickert, J., and Wulfmeyer, V.: Processes driving deep convection over complex terrain: a multi-scale analysis of observations from COPS IOP 9b, *Q. J. Roy. Meteor. Soc.*, 137, 137–155, doi:10.1002/qj.754, 2011.
- Crook, N. A.: Sensitivity of moist convection forced by boundary layer processes to low-level thermodynamic fields, *Mon. Weather Rev.*, 124, 1767–1785, 1996.
- Dierer, S., Arpagaus, M., Seifert, A., Avgoustoglou, E., Dumitrache, R., Grazzini, F., Mercogliano, P., Milelli, M., and Starosta, K.: Deficiencies in quantitative precipitation forecasts: Sensitivity studies using the COSMO model, *Meteorol. Z.*, 18, 631–645, doi:10.1127/0941-2948/2009/0420, 2009.

- Ehret, G., Kiemle, C., Wirth, M., Stoffelen, A., Kummer, U., Schulte, H. R., et al.: Evaluation of spaceborne differential absorption lidar for water vapour, Final Report, ESA Study 3654/00/NL/DC, 2001.
- Eichinger, W., Cooper, D., Froman, P. R., Griegos, J., Osborn, M. A. M., Richter, D., Tellier, L. L., and Thronton, R.: The Development of a Scanning Raman Water Vapor Lidar for Boundary Layer and Tropospheric Observations, *J. Atmos. Oceanic Technol.*, 16, 1753–1766, doi:10.1175/1520-0426(1999)016<1753:TDOASR>2.0.CO;2, 1999.
- Eichinger, W., Cooper, D., Kao, J., Chen, L.C., Hipps, L., and Prueger, J.: Estimation of spatially distributed latent heat flux over complex terrain from a Raman lidar, *Agr. Forest Meteorol.*, 105, 145–159, doi:10.1016/S0168-1923(00)00183-0, 2000.
- Ek, M. B., Mitchell, K. E., Y. Lin, Y., Rogers, E., Grunmann, P., Koren, V., Gayno, G., and Tarpley, J. D.: Implementation of Noah land surface model advances in the National Centres for Environmental Prediction operational mesoscale Eta model, *J. Geophys. Res.*, 108, 8851, doi:10.1029/2002JD003296, 2003.
- Ertel, K.: Application and Development of Water Vapor DIAL Systems, Doctoral Thesis, University of Hamburg, Germany, 2004.
- Fernald, F. G.: Analysis of the atmospheric lidar observations: some comments, *Appl. Opt.*, 23, 652–653, 1984.
- Fernald, F. G., Herman, B. M., and Reagan, J. A.: Determination of Aerosol height Distributions by Lidar, *J. Appl. Meteorol.*, 11, 482–489, 1972.
- Findell, K. L. and Eltahir, E. A. B.: Atmospheric Controls on Soil Moisture–Boundary Layer Interactions – Part II: Feedbacks within the Continental United States, *J. Hydrometeor.*, 4, 570–583, doi:10.1175/1525-7541(2003)004<0570:ACOSML>2.0.CO;2, 2003.
- Fix, A., Ehret, G., Löhring, J., Hoffmann, D., and Alpers, M.: Water vapor differential absorption lidar measurements using a diode-pumped all-solid-state laser at 935 nm, *App. Phys. B*, 102, 905–915, doi:10.1007/s00340-010-4310-5, 2011.
- Froidevaux, M., Higgins, C. W., Simeonov, V., Ristori, P., Pardyjak, E., Serikov, I., Calhoun, R., van den Bergh, H., and Parlange, M. B.: A Raman lidar to measure water vapor in the atmospheric boundary layer, *Adv. Water Resour.*, 51, 345–356, doi:10.1016/j.advwatres.2012.04.008, 2013.
- Goldsmith, J. E. M., Blair, F. H., Bisson, S. E., and Turner, D. D.: Turn-key Raman lidar for profiling atmospheric water vapor, clouds, and aerosols, *Appl. Opt.*, 37, 4979–4990, doi:10.1364/AO.37.004979, 1998.
- Hammann, E., Behrendt, A., Le Mounier, F., and Wulfmeyer, V.: Temperature profiling of the atmospheric boundary layer with rotational Raman lidar during the HD(CP)² Observational Prototype Experiment, *Atmos. Chem. Phys.*, 15, 2867–2881, doi:10.5194/acp-15-2867-2015, 2015.
- Hong, S.-Y.: Stable Boundary Layer Mixing in a Vertical Diffusion Scheme, the Korea Meteor. Soc., Fall conference, Seoul, Korea, 25–26 October, 2007.
- Hong, S.-Y., Noh, Y., and Dudhia, J.: A New Vertical Diffusion Package with an Explicit Treatment of Entrainment Processes, *Mon. Weather Rev.*, 134, 2318–2341, doi:10.1175/MWR3199.1, 2006.
- Ismail, S. and Browell, E. V.: Airborne and spaceborne lidar measurements of water vapor profiles: a sensitivity analysis, *Appl. Opt.*, 28, 3603–3615, 1989.
- Kalthoff, N., Fiebig-Wittmaack, M., Meißner, C., Kohler, M., Uriarte, M., Bischoff-Gauß, I., and Gonzales, E.: The energy balance, evapo-transpiration and nocturnal dew deposition of an arid valley in the Andes, *J. Arid Environ.*, 65, 420–443, 2006.
- Kalthoff, N., Adler, B., Wieser, A., Kohler, M., Trümner, K., Handwerker, J., Corsmeier, U., Khodayar, S., Lambert, D., Kopmann, A., Kunka, N., Dick, G., Ramatschi, M., Wickert, J., and Kottmeier, C.: KITcube – a mobile observation platform for convection studies deployed during HyMeX, *Meteorol. Z.*, 22, 633–647, 2013.
- Koster, R. D., Sud, Y. C., Guo, Z., Dirmeyer, P. A., Bonan, G., Oleson, K. W., Chan, E., Verseghy, D., Cox, P., Davies, H., Kowalczyk, E., Gordon, C. T., Kanae, S., Lawrence, D., Liu, P., Mocko, D., Lu, C.-H., Mitchell, K., Malyshev, S., McAvaney, B., Oki, T., Yamada, T., Pitman, A., Taylor, C. M., Vasic, R., and Xue, Y.: GLACE: The Global Land–Atmosphere Coupling Experiment – Part I: Overview, *J. Hydrometeor.*, 7, 590–610, doi:10.1175/JHM510.1, 2006.
- Kotlarski, S., Keuler, K., Christensen, O. B., Colette, A., Déqué, M., Gobiet, A., Goergen, K., Jacob, D., Lüthi, D., van Meijgaard, E., Nikulin, G., Schär, C., Teichmann, C., Vautard, R., Warrach-Sagi, K., and Wulfmeyer, V.: Regional climate modeling on European scales: a joint standard evaluation of the EURO-CORDEX RCM ensemble, *Geosci. Model Dev.*, 7, 1297–1333, doi:10.5194/gmd-7-1297-2014, 2014.
- Krauss, L., Hauck, C., and Kottmeier, C.: Spatio-temporal soil moisture variability in Southwest Germany observed with a new monitoring network within the COPS domain, *Meteorol. Z.*, 19, 523–537, 2010.
- Lenschow, D. H., Wulfmeyer, V., and Senff, C.: Measuring second-through fourth-order moments in noisy data, *J. Atmos. Oceanic Techn.*, 17, 1330–1347, 2000.
- Löhnert, U., Turner, D. D., and Crewell, S.: Ground-based temperature and humidity profiling using spectral infrared and microwave observations – Part I: Simulated retrieval performance in clear-sky conditions, *J. Appl. Meteorol. Climatol.*, 48, 1017–1032, doi:10.1175/2008JAMC2060.1, 2009.
- Machol, J. L., Ayers, T., Schwenz, K. T., Koenig, K. W., Hardesty, R. M., Senff, C. J., Krainak, M. A., Abshire, J. B., Bravo, H. E., and Sandberg, S. P.: Preliminary Measurements with an Automated Compact Differential Absorption Lidar for the Profiling of Water Vapor, *Appl. Opt.*, 43, 3110–3121, doi:10.1364/AO.43.003110, 2004.
- Machol, J. L., Ayers, T., Schwenz, K. T., Koenig, K. W., Hardesty, R. M., Senff, C. J., Krainak, M. A., Abshire, J. B., Bravo, H. E., and Sandberg, S. P.: Preliminary measurements with an automated compact differential absorption lidar for the profiling of water vapor: errata, *Appl. Opt.*, 45, 3544, doi:10.1364/AO.45.003544, 2006.
- Matsuda, M.: Development of a scanning Raman lidar for observing the spatio-temporal distribution of water vapor, Master Thesis, Bulletin of Research Institute for Sustainable Humanosphere Kyoto University, Japan, 9, 42–42, 2013.
- Melfi, S. H., Lawrence, J. D., and McCormick, M. P.: Observation of Raman scattering by water vapor in the atmosphere, *Appl. Phys. Lett.*, 15, 295–297, 1969.
- Mellor, G. L. and Yamada, T.: Development of a turbulence closure model for geophysical fluid problems, *Rev. Geophys. Space Phys.*, 20, 851–875, doi:10.1029/RG020i004p00851, 1982.

- Metzendorf, S., Behrendt, A., Späth, F., and Wulfmeyer, V.: High-Power Laser Transmitter of the UHOH Water Vapor DIAL, in: 26th International Laser Radar Conference (ILRC 2012), Porto Heli, Greece, 25–29 June 2012, 117–120, 2012.
- Metzendorf, S., Wulfmeyer, V., Behrendt, A., Späth, F., and Riede, A.: Frequency-Agile Ti:Sapphire Laser System with High Power and High Pulse Energy for Spectroscopic Applications, Conference on Lasers and Electro-Optics (CLEO/Europe), Munich, Germany, 21–25 June 2015, CA-12.5, 2015.
- Milovac, J., Warrach-Sagi, K., Behrendt, A., Späth, F., Ingwersen, J., and Wulfmeyer, V.: Investigation of PBL schemes combining the WRF model simulations with scanning water vapor DIAL measurements, *J. Geophys. Res. Atmos.*, 121, 624–649, doi:10.1002/2015JD023927, 2016.
- Monin, A. S. and Obukhov, A. M.: Basic laws of turbulent mixing in the surface layer of the atmosphere, *Tr. Akad. Nauk SSSR Geophys. Inst.*, 24, 163–187, 1954.
- Muppa, S. K., Behrendt, A., Späth, F., Wulfmeyer, V., Metzendorf, S., and Riede, A.: Turbulent humidity fluctuations in the convective boundary layer: Case studies using DIAL measurements, *Bound.-Lay. Meteorol.*, 158, 43–66, doi:10.1007/s10546-015-0078-9, 2016.
- Nakanishi, M. and Niino, H.: Development of an Improved Turbulence Closure Model for the Atmospheric Boundary Layer, *J. Meteorol. Soc. Jpn.*, 87, 895–912, doi:10.2151/jmsj.87.895, 2009.
- NASA (National Aeronautics and Space Administration): US Standard Atmosphere, US Government Printing Office, Washington, DC, 1976.
- Niu, G.-Y., Yang, Z.-L., Mitchell, K. E., Chen, F., Ek, M. B., Barlage, M., Kumar, A., Manning, K., Niyogy, D., Rosero, E., Tewari, M., and Xia, Y.: The community Noah land surface model with multiparameterization options (Noah-MP): 1. Model description and evaluation with local-scale measurements, *J. Geophys. Res.*, 116, D12109, doi:10.1029/2010JD015139, 2011.
- Ostermeyer M., Kappe P., Menzel R., and Wulfmeyer V.: Diode-pumped Nd:YAG master oscillator power amplifier with high pulse energy, excellent beam quality, and frequency-stabilized master oscillator as a basic for a next-generation lidar system, *App. Opt.*, 44, 582–590, doi:10.1364/AO.44.000582, 2005.
- Petrova-Mayor, A., Wulfmeyer, V., and Weibring, P.: Development of an eye-safe solid-state tunable laser transmitter in the 1.4–1.5- μm wavelength region based on Cr⁴⁺:YAG crystal for lidar applications, *Appl. Opt.*, 47, 1522–1534, 2008.
- Radlach, M., Behrendt, A., and Wulfmeyer, V.: Scanning rotational Raman lidar at 355 nm for the measurement of tropospheric temperature fields, *Atmos. Chem. Phys.*, 8, 159–169, doi:10.5194/acp-8-159-2008, 2008.
- Riede, A., Behrendt, A., Wulfmeyer, V., Althausen, D., Wandinger, U., Klein, V., Meister, A., and Schiller, M.: Transmitter-Receiver Unit of the UHOH Water Vapor DIAL with a Scanning 800-mm Telescope Mirror, 26th International Laser Radar Conference (ILRC 2012), Porto Heli, Greece, 25–29 June 2012, 121–124, 2012.
- Rothman, L. S., Gordon, I. E., Babikov, Y., Barbe, A., Chris Benner, D., Bernath, P. F., Birk, M., Bizzocchi, L., Boudon, V., Brown, L. R., Campargue, A., Chance, K., Cohen, E. A., Coudert, L. H., Devi, V. M., Drouin, B. J., Fayt, A., Flaud, J.-M., Gamache, R. R., Harrison, J. J., Hartmann, J.-M., Hill, C., Hodges, J. T., Jacquemart, D., Jolly, A., Lamouroux, J., Le Roy, R. J., Li, G., Long, D. A., Lyulin, O. M., Mackie, C. J., Massie, S. T., Mikhailenko, S., Müller, H. S. P., Naumenko, O. V., Nikitin, A. V., Orphal, J., Perevalov, V., Perrin, A., Polovtseva, E. R., Richard, C., Smith, M. A. H., Starikova, E., Sung, K., Tashkun, S., Tennyson, J., Toon, G. C., Tyuterev, V. I. G., and Wagner, G.: The HITRAN 2012 Molecular Spectroscopic Database, *J. Quant. Spectrosc. Ra.*, 130, 4–50, 2013.
- Santanello, J. A., Peters-Lidard, C. D., Kennedy, A., and Kumar, S. V.: Diagnosing the Nature of Land-Atmosphere Coupling: A Case Study of Dry/Wet Extremes in the U.S. Southern Great Plains, *J. Hydrometeorol.*, 14, 3–24, doi:10.1175/JHM-D-12-023.1, 2013.
- Savitzky, A. and Golay, M. J. E.: Smoothing and Differentiation of Data by Simplified Least Squares Procedures, *Anal. Chem.*, 36, 1627–1639, doi:10.1021/ac60214a047, 1964.
- Schiller, M.: A high-power laser transmitter for ground-based and airborne water-vapor measurements in the troposphere, Doctoral Thesis, University of Hohenheim, Germany, 2009.
- Schotland, R. M.: Some Observations of the Vertical Profile of Water Vapor by Means of a Ground Based Optical Radar, 4th Symposium on Remote Sensing of Environment, U. Michigan, Ann Arbor, 12–24 April, 1966.
- Schotland, R. M.: Errors in the Lidar Measurement of Atmospheric Gases by Differential Absorption, *J. Appl. Meteorol.*, 13, 71–77, 1974.
- Schiller, M., Wulfmeyer, V., Riede, A., Behrendt, A., Bauer, H., Wagner, G., Wandinger, U., and Althausen, D.: Scanning Water Vapor DIAL Based on a High-Power Ti:Sapphire Laser: First Experimental Results, Lidar Technologies, Techniques, and Measurements for Atmospheric Remote Sensing, SPIE International Symposium on Remote Sensing, Florence, Italy, 17–21 September, 2007.
- Shin, H. H. and Hong, S.-Y.: Intercomparison of Planetary Boundary-Layer Parameterizations in the WRF Model for a Single Day from CASES-99, *Bound. Lay. Meteorol.*, 139, 261–281, doi:10.1007/s10546-010-9583-z, 2011.
- Seneviratne, S. I., Corti, T., Davin, E. L., Hirschi, M., Jaeger, E. B., Lehner, I., Orlowski, B., and Teuling, A. J.: Investigating soil moisture-climate interactions in a changing climate: A review, *Earth Sci. Rev.*, 99, 125–161, doi:10.1016/j.earscirev.2010.02.004, 2010.
- Shin, H. H. and Hong, S.-Y.: Representation of the Subgrid-Scale Turbulent Transport in Convective Boundary Layers at Gray-Zone Resolutions, *Mon. Weather Rev.*, 143, 250–271, doi:10.1175/MWR-D-14-00116.1, 2015.
- Späth, F., Metzendorf, S., Behrendt, A., Wizemann, H. D., Wagner, G., and Wulfmeyer, V.: Online/Offline injection seeding system with high frequency-stability and low crosstalk for water vapor DIAL, *Opt. Commun.*, 309, 37–43, doi:10.1016/j.optcom.2013.07.003, 2013.
- Späth, F., Behrendt, A., Muppa, S. K., Metzendorf, S., Riede, A., and Wulfmeyer, V.: High-resolution atmospheric water vapor measurements with a scanning differential absorption lidar, *Atmos. Chem. Phys. Discuss.*, 14, 29057–29099, doi:10.5194/acpd-14-29057-2014, 2014.
- Späth, F., Behrendt, A., and Wulfmeyer, V.: Sensitivity of the Rayleigh-Doppler effect with respect to wavelength and

- backscatter coefficient, 27th International Laser Radar Conference (ILRC 2015), New York, USA, 5–10 July, 2015.
- Spuler, S. M., Repasky, K. S., Morley, B., Moen, D., Hayman, M., and Nehrir, A. R.: Field-deployable diode-laser-based differential absorption lidar (DIAL) for profiling water vapor, *Atmos. Meas. Tech.*, 8, 1073–1087, doi:10.5194/amt-8-1073-2015, 2015.
- Steinke, S., Löhnert, U., Crewell, S., and Liu, S.: Water vapor tomography with two microwave radiometers, *IEEE Geosci. Remote Sens. Lett.*, 11, 419–423, doi:10.1109/LGRS.2013.2264354, 2014.
- Trümner, K.: Einmischprozesse am Oberrand der konvektiven atmosphärischen Grenzschicht, Doctoral Thesis, Karlsruhe Institute of Technology, Germany, 2010.
- Turner, D. D., Ferrare, R. A., Heilman Brasseur, L. A., Feltz, W. F., and Tooman, T. P.: Automated Retrievals of Water Vapor and Aerosol Profiles from an Operational Raman Lidar, *J. Atmos. Oceanic Technol.*, 19, 37–50, doi:10.1175/1520-0426(2002)019<0037:AROWVA>2.0.CO;2, 2002.
- van Heerwaarden, C. C., Vilà-Guerau de Arellano, J., Moene, A. F., and Holtslag, A. A. M.: Interactions between dry-air entrainment, surface evaporation and convective boundary-layer development, *Q. J. Roy. Meteor. Soc.*, 135, 1277–1291, doi:10.1002/qj.431, 2009.
- Vogelmann, H. and Trickl, T.: Wide Range Sounding of Free Tropospheric Water Vapor with a Differential Absorption Lidar (DIAL) at a High Altitude Station, *Appl. Opt.*, 47, 2116–2132, doi:10.1364/AO.47.002116, 2008.
- Wagner, G., Wulfmeyer, V., and Behrendt, A.: Detailed performance modeling of a pulsed high-power single-frequency Ti:sapphire laser, *Appl. Opt.*, 50, 5921–5937, 2011.
- Wagner, G., Behrendt, A., Wulfmeyer, V., Späth, F., and Schiller, M.: High-power Ti:sapphire laser at 820 nm for scanning ground-based water-vapor differential absorption lidar, *Appl. Opt.*, 52, 2454–2469, 2013.
- Warrach-Sagi, K., Schmitalla, T., Wulfmeyer, V., and Bauer, H. S.: Evaluation of a climate simulation based on the WRF-NOAH model system: Precipitation in Germany, *Clim. Dynam.*, 41, 755–774, doi:10.1007/s00382-013-1727-7, 2013.
- Whiteman, D. N., Melfi, S. H., and Ferrare, R. A.: Raman lidar system for the measurement of water vapor and aerosols in the Earth's atmosphere, *Appl. Opt.*, 31, 3068–3082, 1992.
- Whiteman, D. N., Demoz, B., Rush, K., Schwemmer, G., Gentry, B., Di Girolamo, P., Comer, J., Veselovskii, I., Evans, K., Melfi, S. H., Wang, Z., Cadirola, M., Mielke, B., Venable, D., and Van Hove, T.: Raman Lidar Measurements during the International H₂O Project – Part I: Instrumentation and Analysis Techniques, *J. Atmos. Oceanic Technol.*, 23, 157–169, doi:10.1175/JTECH1838.1, 2006.
- Wirth, M., Fix, A., Mahnke, P., Schwarzer, H., Schrandt, F., and Ehret, G.: The airborne multi-wavelength water vapor differential absorption lidar WALES: System design and performance, *Appl. Phys. B*, 96, 201–213, doi:10.1007/s00340-009-3365-7, 2009.
- Wizemann, H. D., Ingwersen, J., Högy, P., Warrach-Sagi, K., Streck, T., and Wulfmeyer, V.: Three year observations of water vapor and energy fluxes over agricultural crops in two regional climates of Southwest, Germany, *Meteorol. Z.*, 24, 39–59, doi:10.1127/metz/2014/0618, 2015.
- Wulfmeyer, V. and Bösenberg, J.: Single-mode operation of an injection-seeded alexandrite ring laser for application in water-vapor and temperature differential absorption lidar, *Opt. Lett.*, 21, 1150–1152, doi:10.1364/OL.21.001150, 1996.
- Wulfmeyer, V. and Bösenberg, J.: Ground-based differential absorption lidar for water-vapor profiling: Assessment of accuracy, resolution, and meteorological applications, *Appl. Opt.*, 37, 3825–3844, doi:10.1364/AO.37.003825, 1998.
- Wulfmeyer, V., Randall, M., Brewer, A., and Hardesty, R. M.: 2-μm Doppler lidar transmitter with high frequency stability and low chirp, *Opt. Lett.*, 25, 1228–1230, 2000.
- Wulfmeyer, V. and Walther, C.: Future performance of ground-based and airborne water-vapor differential absorption lidar – I: Overview and Theory, *Appl. Opt.*, 40, 5304–5320, 2001a.
- Wulfmeyer, V. and Walther, C.: Future performance of ground-based and airborne water-vapor differential absorption lidar – II: Simulations of the precision of a near-infrared, high power system, *Appl. Opt.*, 40, 5321–5336, 2001b.
- Wulfmeyer, V., Turner, D. D., Pal, S., and Wagner, E.: Can Water Vapour Raman Lidar Resolve Profiles of Turbulent Variables in the Convective Boundary Layer?, *Bound.-Lay. Meteorol.*, 136, 253–284, doi:10.1007/s10546-010-9494-z, 2010.
- Wulfmeyer, V., Behrendt, A., Kottmeier, C., Corsmeier, U., Barthlott, C., Craig, G. C., Hagen, M., Althausen, D., Aoshima, F., Arpagaus, M., Bauer, H. S., Bennett, L., Blyth, A., Brandau, C., Champollion, C., Crewell, S., Dick, G., Di Girolamo, P., Dorninger, M., Dufournet, Y., Eigenmann, R., Engelmann, R., Flamant, C., Foken, T., Gorgas, T., Grzeschik, M., Handwerker, J., Hauck, C., Höller, H., Junkermann, W., Kalthoff, N., Kiemle, C., Klink, S., König, M., Krauss, L., Long, C. N., Madonna, F., Mobbs, S., Neininger, B., Pal, S., Peters, G., Pigeon, G., Richard, E., Rotach, M. W., Russchenberg, H., Schmitalla, T., Smith, V., Steinacker, R., Trentmann, J., Turner, D. D., van Baelen, J., Vogt, S., Volkert, H., Weckwerth, T., Wernli, H., Wieser, A., and Wirth, M.: The Convective and Orographically Induced Precipitation Study (COPS): The Scientific Strategy, the Field Phase, and First Highlights, *Q. J. Roy. Meteor. Soc.*, 137, 3–30, doi:10.1002/qj.752, 2011.
- Wulfmeyer, V., Warrach-Sagi, K., Schmitalla, T., Bauer, H. S., and Milovac, J.: Towards seamless mesoscale prediction of the land system for Europe, *The World Weather Open Science Conference*, Montreal, Canada, 16–21 August, 2014.
- Wulfmeyer, V., Hardesty, R. M., Turner, D. D., Behrendt, A., Cadeddu, M. P., Di Girolamo, P., Schüssler, P., Van Baelen, J., and Zus, F.: A review of remote sensing of lower tropospheric thermodynamic profiles and its indispensable role for the understanding and simulation of water and energy cycles, *Rev. Geophys.*, 53, 819–895, doi:10.1002/2014RG000476, 2015.
- Wulfmeyer, V., Muppa, S. K., Behrendt, A., Hammann, E., Späth, F., Sorbjan, Z., Turner, D. D., and Hardesty, R. M.: Determination of Convective Boundary Layer Entrainment Fluxes, Dissipation Rates, and the Molecular Destruction of Variances: Theoretical Description and a Strategy for its Confirmation with a Novel Lidar System Synergy, *J. Atmos. Sci.*, 73, 667–692, doi:10.1175/JAS-D-14-0392.1, 2016.

4 Applications

The UHOH DIAL system performed around 280 hours of measurements in vertical and scanning mode during the recent field experiments. The advancements of the transmitter setup lead to improved performance of the DIAL instrument and a more optimal operation regarding the tuning of the online wavelength. So, the development of the system achieved a status which allows to make use of the measured data sets for further research topics as already outlined in the motivation.

The publication of Milovac et al. (2016) presented in Sect. 4.1 contains a model evaluation study which used scanning WVDIAL measurements for the first time. Simulations of different planetary boundary layer (PBL) schemes and different land surface models within the Weather Research and Forecasting (WRF) model are investigated. I contributed averaged humidity profiles and PBL heights (PBLHs) derived from scanning DIAL data of the FLUXPAT campaign from 2009. The observations were used for validation of the humidity profiles and PBLHs of various simulation outputs. This study has proven the benefits of WVDIAL measurements for a detailed analysis of the grid cell-averaged structure of the moisture profiles, PBLH and development of the convective boundary layer (CBL) and the residual layer.

High-resolution vertical DIAL measurements of HOPE (10 s, 67.5 m) were used by Muppa et al. (2016) to investigate turbulent humidity fluctuations in the CBL. For this purpose, profiles of higher-order moments up to the fourth-order as well as profiles of skewness and kurtosis were derived for two cases. For the WV calculation, I applied the new analysis procedure which was presented in Späth et al. (2016) except of the parts for scanning data. Here, the Rayleigh-Doppler effect needed to be considered and corrected for, even while we used an online wavelength on the slope of the absorption line and only small corrections were applied. But it turned out that the RD correction needs to be applied for accurate higher-order moments profiling due to the non-linearity of the correction. The publication is shown in Sect. 4.2.

Wulfmeyer et al. (2016) discussed the synergy of WVDIAL measurements with lidar measurements of temperature and wind velocity to derive relationships from observations for investigating theoretically derived relationships. With these relationships new approaches for turbulence parameterizations in the CBL shall be developed and tested. The publication, which can be found in Sect. 4.3 of this thesis, introduces an advanced set of scaling relationships in the CBL. These contain relationships of momentum, latent heat and sensible heat fluxes as well as higher-order moments to mean wind,

temperature and moisture gradients. Observations from HOPE of simultaneously performed vertical WVDIAL measurements (same case as discussed in Muppa et al. (2016)) and vertical temperature and wind velocity lidar measurements demonstrate the synergy of these lidar measurements. To this publication I provided the WVDIAL data from which example profiles were derived.

Copyrights

Milovac et al. (2016) shown in Sect. 4.1 on page 65ff is an open access article under the terms of the Creative Commons Attribution-NonCommercial-NoDerivs License, which permits use and distribution in any medium, provided the original work is properly cited, the use is non-commercial and no modifications or adaptations are made.

Muppa et al. (2016) shown in Sect. 4.2 on page 91ff is distributed under the terms of the Creative Commons Attribution 4.0 International License¹⁰, which permits unrestricted use, distribution, and reproduction in any medium, provided you give appropriate credit to the original author(s) and the source, provide a link to the Creative Commons license, and indicate if changes were made.

Wulfmeyer et al. (2016) shown in Sect. 4.3 on page 115ff denotes Open Access content. © Copyright 20 October 2015 American Meteorological Society (AMS). Permission to use figures, tables, and brief excerpts from this work in scientific and educational works is hereby granted provided that the source is acknowledged. Any use of material in this work that is determined to be "fair use" under Section 107 of the U.S. Copyright Act September 2010 Page 2 or that satisfies the conditions specified in Section 108 of the U.S. Copyright Act (17 USC §108, as revised by P.L. 94-553) does not require the AMS's permission. Republication, systematic reproduction, posting in electronic form, such as on a web site or in a searchable database, or other uses of this material, except as exempted by the above statement, requires written permission or a license from the AMS. Additional details are provided in the AMS Copyright Policy, available on the AMS Web site located at (<https://www.ametsoc.org/>) or from the AMS at 617-227-2425 or copyrights@ametsoc.org¹¹.

¹⁰<http://creativecommons.org/licenses/by/4.0/>

¹¹<https://www.ametsoc.org/ams/index.cfm/publications/authors/journal-and-bams-authors/author-resources/copyright-information/copyright-policy/>



RESEARCH ARTICLE

10.1002/2015JD023927

Key Points:

- DIAL measurements convenient for the model evaluation and the CBL study
- The convective PBL higher and drier with NOAA-MP
- Soil-vegetation-atmosphere coupling in WRF stronger toward land

Correspondence to:

J. Milovac,
j.milovac@uni-hohenheim.de

Citation:

Milovac, J., K. Warrach-Sagi, A. Behrendt, F. Späth, J. Ingwersen, and V. Wulfmeyer (2016), Investigation of PBL schemes combining the WRF model simulations with scanning water vapor differential absorption lidar measurements, *J. Geophys. Res. Atmos.*, 121, 624–649, doi:10.1002/2015JD023927.

Received 13 JUL 2015

Accepted 11 DEC 2015

Accepted article online 15 DEC 2015

Published online 19 JAN 2016

Corrected 22 JAN 2016

This article was corrected on 22 JAN 2016. See the end of the full text for details.

©2015. The Authors.

This is an open access article under the terms of the Creative Commons Attribution-NonCommercial-NoDerivs License, which permits use and distribution in any medium, provided the original work is properly cited, the use is non-commercial and no modifications or adaptations are made.

Investigation of PBL schemes combining the WRF model simulations with scanning water vapor differential absorption lidar measurements

Josipa Milovac¹, Kirsten Warrach-Sagi¹, Andreas Behrendt¹, Florian Späth¹, Joachim Ingwersen², and Volker Wulfmeyer¹
¹Institute of Physics and Meteorology, University of Hohenheim, Stuttgart, Germany, ²Institute of Soil Science and Land Evaluation, University of Hohenheim, Stuttgart, Germany

Abstract Six simulations with the Weather Research and Forecasting (WRF) model differing in planetary boundary layer (PBL) schemes and land surface models (LSMs) are investigated in a case study in western Germany during clear-sky weather conditions. The simulations were performed at 2 km resolution with two local and two nonlocal PBL schemes, combined with two LSMs (NOAH and NOAA-MP). Resulting convective boundary layer (CBL) features are investigated in combination with high-resolution water vapor differential absorption lidar measurements at an experimental area. Further, the simulated soil-vegetation-atmosphere feedback processes are quantified applying a mixing diagram approach. The investigation shows that the nonlocal PBL schemes simulate a deeper and drier CBL than the local schemes. Furthermore, the application of different LSMs reveals that the entrainment of dry air depends on the energy partitioning at the land surface. The study demonstrates that the impact of processes occurring at the land surface is not constrained to the lower CBL but extends up to the interfacial layer and the lower troposphere. With respect to the choice of the LSM, the discrepancies in simulating a diurnal change of the humidity profiles are even more significant at the interfacial layer than close to the land surface. This indicates that the representation of land surface processes has a significant impact on the simulation of mixing properties within the CBL.

1. Introduction

Processes involved in planetary boundary layer (PBL) evolution, such as mixing of heat and moisture, are key phenomena for cloud development and precipitation. Therefore, understanding and modeling of these processes is fundamental for weather and climate modeling. The structure of the PBL strongly depends on its interaction with the Earth's surface and the free atmosphere. However, a key for the interaction between land surface and atmosphere is the soil-vegetation-atmosphere (SVA) feedback, from local to global scales [Mahmood *et al.*, 2013; Stéfanon *et al.*, 2014]. The term feedback refers to the fact that between most variables in the SVA system a two-way coupling exists, such as between soil moisture and precipitation [Seneviratne *et al.*, 2010]. The strength of SVA feedback varies across seasons and regions [e.g., Findell and Eltahir, 2003; Koster *et al.*, 2006] and is expected to become stronger in a changing climate, especially in locations where SVA feedback plays an important role [Dirmeyer *et al.*, 2012; Taylor *et al.*, 2012]. Therefore, in weather and climate modeling, it is essential to investigate these interactions across all components of the SVA system. Only by carrying out such studies can we understand SVA feedback within a changing climate and improve weather and climate models. Together these are prerequisites for regional climate models (RCMs) to reach the predictive skill in reproducing the current climate variability including extreme events [Lenderink and van Meijgaard, 2008; Zolina *et al.*, 2013] and to project these to the future.

Various research strategies have been proposed to accurately represent the water and energy exchange processes between the soil, vegetation, and the atmosphere [e.g., Ek and Holtslag, 2004; Seneviratne *et al.*, 2010; Santanello *et al.*, 2013]. In the SVA system there are numerous interactions composed of positive and negative feedback loops between the compartments and variables, such as the accumulation of hydrological anomalies in the soil, changes of vegetation properties, the induction and strength of mesoscale circulations, and their subsequent impacts on the surface energy balance. To assess these feedbacks, it is particularly important to consider the structural evolution of the PBL, humidity profiles, moisture advection, mesoscale circulations, and convection initiation [Sherwood *et al.*, 2010], as well as the formation of clouds and precipitation. Numerous modeling studies have been performed at various scales [e.g., Huang *et al.*, 2011; Jaeger and

Seneviratne, 2011; Gentile *et al.*, 2013; Santanello *et al.*, 2013] in order to quantify these feedback processes. However, processes like entrainment and convection were not considered individually within the analyses. Thus, a general approach for characterizing SVA feedbacks based on modeling studies still needs to be developed. Keeping this in mind, e.g., the GEWEX Local Coupled Land-Atmospheric Coupling project was inaugurated [Santanello *et al.*, 2009, 2011, 2013], to include the development of analyses methods and experimental setups in combination with intensive observation modeling.

Offline applications of land surface models (LSMs) which are “forced” with atmospheric variables lead to substantial errors in the simulation of land surface exchange such as evapotranspiration [Rasmussen *et al.*, 2012]. Moreover, “quick fixes” of LSMs, which were introduced to compensate for these errors, amplified the inconsistency of the results, and impeded the understanding and quantification of SVA feedbacks [Dirmeyer, 2014]. Therefore, the study of SVA feedbacks requires the application of coupled land-surface-atmosphere models. Ideally, an LSM which provides a good representation of land surface processes would be coupled with an atmospheric model providing appropriate representation of PBL and tropospheric physical processes [Dirmeyer, 2014]. One coupled model is the Weather Research and Forecasting (WRF) mesoscale numerical model [Skamarock *et al.*, 2008] coupled with an LSM. It offers a wide range of parameterization schemes, including longwave and shortwave radiation, microphysics, convection, surface layer, and PBL schemes. Further, it allows for the choice of LSMs. Special attention needs to be paid to the selection of PBL scheme and LSM, since they are linked via surface mass and energy fluxes. In the model lower boundary conditions for the PBL scheme are provided by the LSM in the form of surface fluxes of heat and moisture. Therefore, simulated processes in the PBL, and consequently, cloud formation and precipitation, depend on the parameterization of the land surface. On the other hand, the PBL characteristics and its evolution also feed back to the land surface and modify the fluxes.

Many studies have focused on the analysis of WRF sensitivity only to PBL schemes [e.g., Hu *et al.*, 2010, 2013; Shin and Hong, 2011; Xie *et al.*, 2012, 2013; Coniglio *et al.*, 2013; García-Díez *et al.*, 2013], but without considering the sensitivity of the model to LSMs and representation of the SVA feedback processes within the model. This was considered by Santanello *et al.* [2009, 2011, 2013]. They proposed a way to study SVA interactions on diurnal time scales by means of so called “mixing diagrams,” which are essentially detailed analyses of energy and water budgets in the PBL. Two case studies in Lamont (Oklahoma, USA) for a clear-sky day and an unstable cloudy day in June 2002 were studied. The study showed that the coupling between soil moisture and PBL features, such as 2 m specific humidity, 2 m temperature, the PBL height (PBLH), and the lifting condensation level (LCL) was strong on diurnal time scales. Furthermore, Misenis and Zhang [2010] in their 5 day simulations found the sensitivity of WRF to LSM type to be higher than that to PBL schemes, for standard meteorological predictions (i.e., 2 m temperature, 2 m relative humidity, wind speed, and wind direction). This was primarily due to large differences in simulated surface fluxes in the three LSMs used in their study. In their comprehensive analysis of the WRF model sensitivity to microphysics, LSMs, radiation and the PBL parameterization options over the Iberian Peninsula, Borge *et al.* [2008] showed that the model representation of PBL features such as PBLH is influenced more by the PBL scheme and the LSM, than by the other parameterizations.

A key observational basis for SVA feedback studies, such as those just mentioned, are measurements of turbulent fluxes of sensible heat, latent heat, and CO₂ using eddy covariance (EC) techniques. The lack of high-resolution temperature and water vapor profiling is currently a strong weakness within observing systems [Wulfmeyer *et al.*, 2014a]. In most sensitivity studies, point measurements of standard meteorological variables are used for model validation at the surface [e.g., Borge *et al.*, 2008], whereas PBL measurements performed by radiosondes (RS) were applied for comparisons of PBL characteristics [e.g., Misenis and Zhang, 2010; Coniglio *et al.*, 2013]. Such measurement techniques only represent a snapshot of the atmosphere and do not provide any information about entrainment processes. Land surface fluxes and the PBL water vapor both interact with the fluxes at the interfacial layer, and if the measurements are constrained to the land surface, feedback studies are strongly limited. Therefore, the entrainment measurements are a prerequisite for the SVA studies. In the past, entrainment fluxes have been measured mainly in situ by aircrafts [Lenschow *et al.*, 1994], which is a rather expensive method. Another method is the turbulence profiling with ground-based lidar systems such as Doppler lidar for wind measurements, temperature rotational Raman lidar (TRRL) [Radlach *et al.*, 2008], and either water vapor differential absorption lidar (WVDIAL) [Wagner *et al.*, 2013] or a water vapor Raman lidar

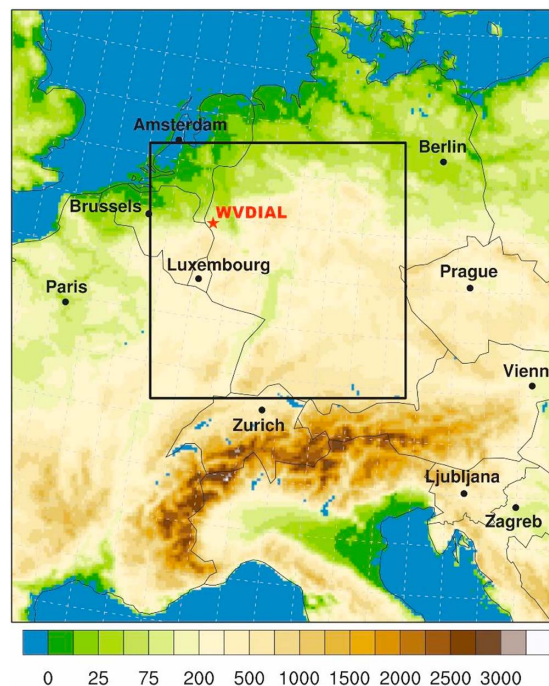


Figure 1. The parent and child domain (black rectangle) in all the six WRF simulations along with the orography field (in m ASL).

[Turner *et al.*, 2002]. These lidar systems are capable of profiling higher-order turbulent moments of vertical wind and turbulent kinetic energy (TKE) dissipation rate [e.g., Wulfmeyer and Janjić, 2005; Tucker *et al.*, 2009; Ansmann *et al.*, 2010; Lenschow *et al.*, 2012], temperature [Behrendt *et al.*, 2015], and water vapor [e.g., Wulfmeyer, 1999a; Wulfmeyer *et al.*, 2010; Turner *et al.*, 2014; Muppa *et al.*, 2015] in the convective PBL (CBL). Furthermore, combinations of these remote sensing systems were applied for profiling of the latent heat flux, as well as stability indices [Wulfmeyer, 1999b; Giez *et al.*, 1999; Corsmeier *et al.*, 2011]. The combination of 3-D scanning WVDIAL and TRRL has the potential to measure fields of surface and entrainment fluxes simultaneously by the application of sophisticated scan strategies [Wulfmeyer *et al.*, 2015]. High-resolution scans in the surface layer allows for studying the two-dimensional structure of the fluxes through application of Monin-Obukhov similarity theory [Cooper *et al.*, 2007; Wulfmeyer *et al.*,

2014b]. In Germany, a corresponding synergy of scanning lidar systems was deployed during field campaigns such as the Convective and Orographically-induced Precipitation Study (COPS) in summer 2007 [Wulfmeyer *et al.*, 2008, 2011; Behrendt *et al.*, 2013], the TransRegio (TR) 32 FLUXPAT campaign in autumn 2009 [Behrendt *et al.*, 2009], the High Definition Clouds and Precipitation (HD(CP)²) Observational Prototype Experiment [Hammann *et al.*, 2015] in spring 2013 and SABLE2014 [Behrendt *et al.*, 2015].

The focus of this study is the analysis of WRF simulations of CBL features and SVA feedback and the sensitivity of the model to state of the art PBL parameterization schemes and LSMs on a diurnal time scale during clear-sky weather conditions. We analyze the WRF model representation of the temperature and humidity profiles in the PBL in comparison with the RS measurements and, for the first time, with high-resolution humidity profile measurements from WVDIAL. We apply the mixing diagram approach to quantify the SVA feedback processes.

In section 2 the experimental design is described including the model setup and measurements. The mixing diagram approach applied for the SVA feedback study is shortly explained in section 3. Section 4 contains the results, which are discussed in section 5. Summary and concluding remarks are given in section 6.

2. Experimental Design

WRF sensitivity to PBL parameterization choices and LSMs in simulating the PBL evolution and its dependence on processes at the land surface and at the interfacial layer are investigated. For this, six WRF simulations are carried out. Crucially, the simulations are verified for the first time with high-quality scanning WVDIAL measurements, performed on 8 September 2009 at clear-sky weather conditions during the field campaign TR 32 FLUXPAT in western Germany. RS measurements are used to verify the simulated temperature profiles.

2.1. Model Description and Experiments

The state and evolution of the SVA system in western Germany were simulated with the WRF model version 3.5.1 [Skamarock *et al.*, 2008]. For this study the resolution of the inner domain was set to 2 km (Figure 1). The

Table 1. A List of the Six Experiments Containing the PBL, the Surface Layer, and the LSM Parameterization Options

Experiment	PBL Scheme	Surface Layer Scheme	LSM
ACM2-NOAH	ACM2	Revised MM5	NOAH
MYJ-NOAH	MYJ	Eta similarity	NOAH
MYNN-NOAH	MYNN 2.5	Revised MM5	NOAH
YSU-NOAH	YSU	Revised MM5	NOAH
MYNN-NOAH-MP	MYNN 2.5	Revised MM5	NOAH-MP
YSU-NOAH-MP	YSU	Revised MM5	NOAH-MP

outer domain, with the 6 km resolution, was chosen as an intermediate step to downscale the coarse European Centre for Medium Range Weather Forecasts (ECMWF) operational analyses data (on a $0.125^\circ \times 0.125^\circ$ grid). It incorporates the whole of Germany and the impact of elevated ranges in the closest neighboring areas. The mountain range of Alps and the Massif Central in southern France were included to capture the major synoptic forcing that influences the local weather in western and southwestern Germany. The inner domain with 270×270 grid cells was nested into this domain covering most of Germany. The model simulations were performed on a vertical grid consisting of 89 full σ levels, with 20 levels within the first 2200 m, and the lowest σ level set to ~ 5 m.

The WRF model was set up with the following physics parameterizations: Morrison 2 moment scheme [Morrison *et al.*, 2005] for microphysics and the rapid radiative transfer model for global circulation models [Iacono *et al.*, 2008] for both the longwave and shortwave radiation. The Kain-Fritsch scheme [Kain, 2004] was selected for convection parameterization in the outer domain. With this configuration, a total of six numerical experiments were conducted with the Asymmetric Convective Model version 2 (ACM2) [Pleim, 2007], the Mellor-Yamada-Janjic (MYJ) [Mellor and Yamada, 1974, 1982; Janjic, 2002], and the Mellor-Yamada-Nakanishi-Niino level 2.5 (MYNN) [Nakanishi and Niino, 2009] PBL schemes and the PBL scheme of Yonsei University (YSU) [Hong *et al.*, 2006; Hong, 2010], in combination with the NOAH [Chen and Dudhia, 2001a, 2001b] and NOAH with multiple physics options (NOAH-MP) [Niu *et al.*, 2011; Yang *et al.*, 2011] LSMs (see Table 1). MYNN and ACM2 have the possibility to be applied with multiple surface layer parameterizations. In order to minimize the impact of the surface layer parameterization in this sensitivity study, the revised MM5 scheme [Jiménez *et al.*, 2012] was selected for all model runs with MYNN, ACM2, and YSU. This was not possible with MYJ, since it can be run only with the Eta similarity scheme [e.g., Janjic, 2002].

The original soil texture data in WRF, which is at the 5' resolution for Europe, is too coarse for studying SVA feedbacks on convection permitting scales [Warrach-Sagi *et al.*, 2008; Sanchez *et al.*, 2009; Guillod *et al.*, 2013]; therefore, it was replaced with new 1 km soil texture maps for Europe [Milovac *et al.*, 2014a] based on the Harmonized World Soil Database, and for Germany based on the German Soil Overview Map (BÜK 1000) [Milovac *et al.*, 2014b].

The ECMWF model since 2007 is coupled to the hydrologically extended multilevel land surface model HTESSEL, which results in a more realistic representation of the soil state [Balsamo *et al.*, 2009]. The ECMWF operational analysis fields are on a $0.125^\circ \times 0.125^\circ$ grid, available on six hourly basis. Tests of initialization and operation of WRF with ECMWF operational analyses (ECMWF analysis) of soil moisture and temperature fields showed that NOAH and NOAH-MP can spin-up within a few weeks for this temperate climate region. Further, the deep soil is weakly coupled to the land surface and therefore its state does not contribute very much to the PBL evolution in short-term simulations [e.g., Angevine *et al.*, 2014]. Therefore, in order to get an equilibrated land surface state, the soil spin-up run was set to run for 82 days, with the soil moisture and soil temperature initialized with ECMWF analysis data obtained from ECMWF Data Server. The initialization was done once at the start of the soil spin-up run on 1 June 2009 at 0 UTC.

All experimental simulations started on 21 August 2009 at 0 UTC and were set to run in cycles of 36 h ("weather forecast mode") [e.g., Williams *et al.*, 2013]. Each successive cycle started every next day from 0 UTC. At the start of each cycle, atmospheric conditions, as well as the lateral boundary conditions for the outer domain (6 km) were initialized by the ECMWF analysis as well. The first 6 h from the each cycle were discarded from the analysis due to the atmospheric spin-up. The soil moisture and soil temperature were once initialized from the soil spin-up run on 21 August 2009, and then evolved freely.

2.1.1. Land Surface Models

LSMs calculate the subgrid scale mass and energy fluxes in the soil-vegetation continuum, and their exchange with the atmosphere. They are developed and applied as stand-alone models (forced with weather

data) or coupled to atmospheric and/or hydrologic models. Coupled with WRF, the LSM interacts with all the other WRF parameterization schemes. The communication linkage to a PBL scheme are water and energy fluxes, which are provided by a LSM directly and/or via a surface layer scheme to the PBL scheme. These fluxes represent the lower boundary conditions for the PBL scheme.

In this study, two LSMs coupled with WRF are analyzed: the extensively used and well-studied NOAH and the more sophisticated and more recent NOAH-MP. The schemes with their major discrepancies are shortly introduced in the following two sections.

2.1.1.1. The NOAH Land Surface Model

The NOAH LSM [Chen and Dudhia, 2001a, 2001b; Ek et al., 2003] is a single column model with four soil layers of thicknesses of 0.1, 0.3, 0.6, and 1 m, a fractional vegetation, and a snow layer. Within the soil column, a diffusive form of the vertical Richard's equation for soil moisture and the thermal diffusion equation are calculated for unfrozen and frozen soils. The fluxes and the skin temperature at the land surface are calculated by solving the energy balance closure formulated as,

$$(1 - \alpha)S_{\downarrow} + L_{\downarrow} - L_{\uparrow} = R_n = H + \lambda E + G \quad (1)$$

with α being the surface albedo, S and L are shortwave and longwave radiation, respectively. The arrows $\downarrow \uparrow$ stand for downward and upward, R_n is the net surface radiation flux, H the sensible heat flux, λE the latent heat flux (the latent heat of vaporization λ multiplied with the actual evapotranspiration E), and G is the ground heat flux. The key for calculating the energy fluxes and closing the energy balance in equation (1) is the surface skin temperature (T_{skin}). The calculation of T_{skin} in NOAH is done by using a simple linearized function of the temperature at some reference height (T) [Chen and Dudhia, 2001a, 2001b; van der Velde et al., 2009]. All fluxes are calculated separately over the vegetation canopy and the bare ground. Therefore, the net flux is a sum of the fluxes over the canopy and bare ground, weighted by the vegetation fraction (F_{veg}).

H is calculated as follows

$$H = \rho C_p C_h u (T_{\text{skin}} - T) \quad (2)$$

where ρ is air density, C_p is specific heat capacity of moist air, C_h the surface exchange coefficient for heat, and u is the wind speed at the reference height. G is related to the temperature gradient between the surface skin (denoted as skin) and midpoint of the first soil layer (denoted as s_1) written as

$$G = \kappa_h(\eta) \frac{T_{\text{skin}} - T_{s_1}}{dz} \quad (3)$$

with κ_h being the thermal conductivity, η soil moisture fraction, T_{s_1} the temperature at the midpoint of the first soil layer, and dz is the soil thickness between the levels skin and s_1 . The calculation of λE is based on the potential evapotranspiration (E_p), following an approach based on Mahrt and Ek [1984], where E_p is a function of R_n , G , and the bulk latent heat flux corrected for the atmospheric stability. The formulation can be written as

$$\lambda E_p = \frac{\Delta(R_n - G) + \rho \lambda C_q u (q_{\text{sat}} - q)}{1 + \Delta} \quad (4)$$

with Δ standing for the saturated vapor pressure curve, C_q for the exchange coefficient for moisture (which is assumed to be equal to that of heat, C_h), q_{sat} and q are the saturated and specific humidity, respectively. The actual evapotranspiration is calculated as the sum of direct evaporation from the bare soil surface, evaporation of water intercepted by vegetation cover, and transpiration of plants. All the three variables are a fraction of the λE_p . The key controlling variable for the canopy transpiration is the stomatal resistance [e.g., van der Velde et al., 2009; Ingwersen et al., 2011], which is calculated using a Jarvis-type formulation [Jarvis, 1976]. The Jarvis approach is dependent on meteorological parameters such as radiation, humidity and temperature.

2.1.1.2. The NOAH-MP Land Surface Model

Since WRF version 3.4 released in 2012, a new LSM, NOAH-MP, can be coupled with WRF. NOAH-MP is an extended version of NOAH, with an internal suite of physics parameterizations and a modified energy balance equation (equation (1)) [Niu et al., 2011; Yang et al., 2011]. The switchable physical parameterizations include an interactive vegetation canopy, dynamic leaf phenology, radiation transfer through the vegetation canopy, the multilayer snowpack topography based runoff, as well as groundwater table calculations. In

Table 2. Complete Configuration of the NOAH-MP LSM Used in This Study^a

NOAH-MP Options	Option	Short Description
Dynamic vegetation model	Off	Leaf area index from table; F_{veg} calculated
Stomatal resistance (SR)	Ball-Berry	Accounts for photosynthesis
Surface layer drag coefficient	Original NOAH	Version used in NOAH [Chen <i>et al.</i> , 1997]
Soil moisture factor for SR	CLM	A function of the matric potential
Runoff and groundwater	Original surface and subsurface runoff	Free drainage
Supercooled liquid water	No iteration	General form of the freezing-point depression equation
Soil permeability	Nonlinear effect, less permeable	Uses only the liquid water volume to calculate hydraulic properties
Radiative transfer	Modified two stream	Probability of gap between canopy equals to $(1-F_{veg})$
Ground surface albedo	BATS	Snow surface albedo accounts for fresh snow, variations in snow age, grain size growth, impurity, etc.
Precipitation–snow or rain	Snow when $T_{sfc} < T_{frz}$	When surface temperature < freezing temperature, snow, and rainfall otherwise.
Soil temperature lower boundary condition	T_{bot} at 8 m from input file	Read T_{bot} at Z_{bot} from wrf input file
Snow/soil temperature time scheme	Fully implicit	Same as used in NOAH

^aCLM is the Community Land Model and BATS is Biosphere–Atmosphere Transfer Scheme. F_{veg} stands for vegetation fraction.

addition, alongside the Jarvis scheme for stomatal resistance included with NOAH, NOAH-MP offers the Ball-Berry scheme [Ball *et al.*, 1987], an approach which links stomatal resistance to leaf photosynthesis.

NOAH-MP applies an advanced method to calculate the energy balance at the land surface (equation (1)). To represent the surface heterogeneity, NOAH-MP uses the “semitile” subgrid method and is one of the major advances compared to the “tile” approach deployed in NOAH. In the semitile approach, shortwave radiation is computed over the entire grid cell, considering gap probabilities, while net longwave radiation and surface turbulent fluxes are calculated separately over a vegetated and bare soil (the tile approach). This semitile approach is designed to avoid overlapping of too many shadows whenever the vegetation is present and the sun is not overhead, which occurs with the conventional tile approach used in NOAH [Niu *et al.*, 2011]. Also there is a modification in the tile approach used in NOAH-MP. Different to NOAH, the fluxes over the vegetated tile are calculated not only over the canopy but also within the canopy (i.e., between the ground and the canopy top). Therefore, the net atmospheric exchange from a whole vegetated grid cell is a weighted sum of all the canopy fluxes (above and underneath the canopy), and the fluxes from the bare ground. Furthermore, the simple linearized method for solving the energy balance in NOAH is replaced with an iterative method in NOAH-MP. The iteration is used to solve the unknown skin temperatures within each tile, and accordingly, the fluxes are updated in each iteration step. The iteration process is stopped when the energy balance is achieved, or when the number of iterations reaches some prescribed value [e.g., Nielsen *et al.*, 2013].

There is also a structural difference in the communication between the LSM, the surface layer scheme, and the PBL scheme, when WRF is coupled with NOAH-MP (WRF-NOAH-MP) and not with NOAH (WRF-NOAH). In WRF-NOAH the exchange coefficients for momentum (C_m) and the scalar variables (C_h , C_q) are calculated within the surface layer scheme, while in WRF-NOAH-MP there is no direct information exchange between NOAH-MP and the surface layer scheme over land surfaces. This means that in WRF-NOAH-MP the exchange coefficients over land are calculated directly in NOAH-MP, while the surface layer scheme calculates fluxes over water surfaces only [e.g., Nielsen *et al.*, 2013].

Table 2 lists the selected settings for NOAH-MP applied for this case study. Aside from calculation of the energy balance closure and the semitile approach, major differences between NOAH-MP and NOAH relate to the Ball-Berry-photosynthesis. The Community Land Model (CLM) is used to calculate soil moisture factor needed for stomatal resistance. Furthermore, the bottom temperature at 8 m from the input file is used as the soil temperature lower boundary condition, and snow/soil temperature time scheme is chosen to be the fully implicit. Rather than applying the NOAH-MP default setting, some switches have been selected to suit the study area according to offline NOAH-MP experiments applied for Germany [Gayler *et al.*, 2014; Ingwersen *et al.*, 2015], and test simulations that were performed prior to the simulations for this study (beyond the scope of this paper and not shown).

2.1.2. Planetary Boundary Layer Parameterizations

In WRF, a PBL parameterization scheme calculates atmospheric tendencies of temperature, moisture with clouds, and horizontal momentum [Skamarock *et al.*, 2008]. The two most common PBL parameterization

Table 3. The Mixing Length Scale (l) Parameterizations as Deployed in MYNN and MYJ^a

MYNN	MYJ
$\frac{1}{l} = \frac{1}{l_s} + \frac{1}{l_t} + \frac{1}{l_b}$	$l = \frac{\kappa z}{1 + \kappa z/\lambda}, z \leq h$
$l_s = \begin{cases} \kappa z/3.7; & z/L \geq 1 \\ \kappa z(1 + 2.7z/L)^{-1}; & 0 \leq z/L < 1 \\ \kappa z(1 - 100z/L)^{0.2}; & z/L < 0 \end{cases}$	$\lambda = 0.25 \frac{\int_0^h qzdz}{\int_0^h qdz}$
$l_t = 0.23 \frac{\int_0^\infty qzdz}{\int_0^\infty qdz}$	$l = 0.23\Delta z; z > h$
$l_b = \begin{cases} q/N; & \partial\theta_v/\partial z > 0, z/L \geq 0 \\ [1 + 5(q_c/l_t N)^{1/2}]q/N; & \partial\theta_v/\partial z > 0, z/L < 0 \\ \infty; & \partial\theta_v/\partial z \leq 0 \end{cases}$	

^aIn MYNN l is controlled by the smallest among: l_s (l in the surface layer), l_t (turbulent length scale), and l_b (l related to the buoyancy force). $q_2 = 2TKE$, κ is the von Karman constant. L represents the Monin-Obukhov length scale and q_c is a velocity scale. N is the Brunt-Väisälä frequency, z is the height of a model level, and h is the diagnosed PBLH.

approaches used in the model are local or nonlocal [e.g., Stull, 1988], which will shortly be explained further in the text.

In this study, we evaluate the dependence of CBL structure and daytime SVA feedback on the two local PBL schemes MYJ and MYNN, and the two nonlocal PBL schemes YSU and ACM2. MYJ and YSU are chosen since they have been most frequently used in sensitivity studies and have been widely evaluated within the WRF community [e.g., Hu et al., 2010; Shin and Hong, 2011; Xie et al., 2013; Hu et al., 2013]. MYNN uses a similar baseline as MYJ, but with considerable modifications of certain parameterizations, e.g., mixing length scale (l), eddy diffusivities, and stability functions in the stable PBL. ACM2 was chosen because it uses a slightly different approach from the other schemes. It combines the nonlocal approach with explicit parameterization of nonlocal mixing by using a transilient matrix, and the typical local eddy diffusivity approach. A short description of the four schemes, and their constraints, deficiencies and advantages are given in the following two subsections.

2.1.2.1. Local Approaches: MYJ and MYNN

MYJ and MYNN are both based on the Mellor-Yamada 1.5 order parameterization scheme [Mellor and Yamada, 1974, 1982], in which the turbulent fluxes of any adiabatically conserved quantity are related to gradients of their mean values at adjacent levels only (therefore local approach). This can be formulated as

$$\overline{w'\psi'} = -K_\psi \frac{\partial \psi}{\partial z}, \quad (5)$$

where w' represents vertical velocity fluctuation, ψ' is fluctuation of an adiabatically conserved variable (momentum m , heat h , or moisture q). Overbars denote averaged values. K_ψ is the eddy diffusivity, which is proportional to l , TKE, and the stability function in both schemes. An additional second-order prognostic equation for TKE is used to diagnose wind variances.

One of the differences between the schemes is the parameterization used for l , which are given in Table 3. In MYJ, l is parameterized with the common formulation suggested by Blackadar [1962], which is valid in the stable and convective PBL, while in MYNN l depends on the PBL stratification. In the higher-order local TKE closure schemes, such as MYNN and MYJ, one of the major obstacles for their improvement is the formulation of l [e.g., Mellor and Yamada, 1974, 1982; Cuijpers and Holtslag, 1998; Weng and Taylor, 2002; Grisogono, 2010].

The PBLH in MYJ is diagnosed using the TKE method [e.g., Janjic, 2002; Mellor and Yamada, 1982]. MYNN uses the TKE method combined with the θ increase method as described in Nakanishi and Niino [2009] and Xie et al. [2013].

2.1.2.2. Nonlocal Approaches: YSU and ACM2

In the YSU scheme the second-order turbulent fluxes are parameterized as

$$\overline{w'\psi'} = -K_{\psi} \left(\frac{\partial \overline{\psi}}{\partial z} - \gamma_{\psi} \right) + \overline{(w'\psi')_h} \left(\frac{z}{h} \right)^3, \quad (6)$$

where γ_{ψ} is the counter gradient correction term, h is the diagnosed PBLH, and z is the model height. By adding γ_{ψ} to the local gradient, YSU accounts for the contribution of large eddies to the total mixing, which makes this scheme nonlocal. The last term on the right-hand side represents the explicit parameterization of the entrainment flux. This was shown to be the most critical step toward an improved representation of the CBL mixing [e.g., Hong *et al.*, 2006].

In ACM2, described by Pleim [2007], total mixing is a weighted sum between local and nonlocal components. The nonlocal part is parameterized using a transilient matrix as described in Pleim [2007], which is a function of the upward convective mixing rate, while the local part is formulated as in equation (5).

The schemes use slightly different approaches to calculate the PBLH, but both are based on the bulk Richardson number method [e.g., Seibert, 2000; LeMone *et al.*, 2013]. A detailed description of the methods used to calculate the PBLH in the schemes can be found in, e.g., Hong [2010], Pleim [2007], and Xie *et al.* [2013]. The major weakness of the nonlocal schemes is their high sensitivity to diagnosed quantities such as PBLH [e.g., Teixeira and Cheinet, 2004], which are often difficult to define precisely and accurately, particularly in numerical weather prediction models and RCMs. Different strategies for calculation of the PBLH may lead to significantly different results.

2.2. Study Area and Weather Conditions

The study site is located in western Germany, near the village of Inden and the Jülich Research Centre (Figure 1). During the field campaign TR 32 FLUXPAT (funded by the German Science Foundation) in September 2009, worldwide the first scanning WVDIAL measurements were taken at the site (50°51'20.55" N, 6°22'4.91"E, 105 m above sea level) [Behrendt *et al.*, 2009]. The measurements were performed over an agriculturally dominated area in a relatively flat terrain within the River Ruhr catchment. However, apart from sugar beet, the fields were harvested in September 2009. An open-pit mine is located in the West and the village of Inden in the North. Soil texture at the study site is primarily silty loam.

On 8 September 2009 during the day the weather in central Europe was controlled by a high-pressure system with its center over Lithuania. During the whole day the weather at the study site was similar across most of Europe, cloudless and dry with weak synoptic forcing. Minimum 2 m temperature measured on 8 September 2009 in the area was about 15°C, while the maximum was between 28 and 30°C. The environmental air was rather dry, with relative humidity at 2 m height between 35 and 55% during the day. The 2 m dew point temperature close to the ground measured with RS at 16 UTC was 12.8°C. Most of the day it was calm with weak winds. Until late afternoon, winds were southerly, southwesterly direction with up to 5 m s⁻¹ speed at elevations ranging from 30 to 360 m. After 17:30 UTC the wind speeds increased up to ~5–9 m s⁻¹. At nighttime the winds turned to an easterly and northeasterly direction. Wind data were obtained from SOnic Detection And Ranging measurements performed at the study site on 8 September 2009 (C. Drüe, personal communication, 2014).

2.3. Measurements With the Water Vapor Differential Absorption Lidar

The WVDIAL is a scanning system, capable of performing three-dimensional observations of humidity with the highest spatial/temporal resolution of all existing water vapor remote sensing systems [Behrendt *et al.*, 2009; Wagner *et al.*, 2011, 2013; Späth *et al.*, 2013, 2014]. Absolute humidity is measured with a spatial and temporal resolution of 15 to 300 m and 0.5 to 10 s, respectively. The maximum range is several kilometers during day and night and can be adapted to the PBL evolution to capture the whole depth of the PBL [Späth *et al.*, 2014]. Validation studies confirmed the high accuracy of the WVDIAL instrument [Bhawar *et al.*, 2011; Muppa *et al.*, 2015]. Combining range-resolved measurements with scanning capability, different scan patterns (e.g., range-height indicator or plane-polar indicator scans) can be performed with the WVDIAL. The instrument allows for different types of volume scan patterns to be realized automatically. These properties allow for studying the temporal and spatial structure of the water vapor field in detail.

Figure 2 shows the range-height indicator scan of the absolute humidity field measured on 8 September 2009 at six time steps between 8:48 and 17:52 UTC. The scan speed was 0.1° s⁻¹. An integration time of

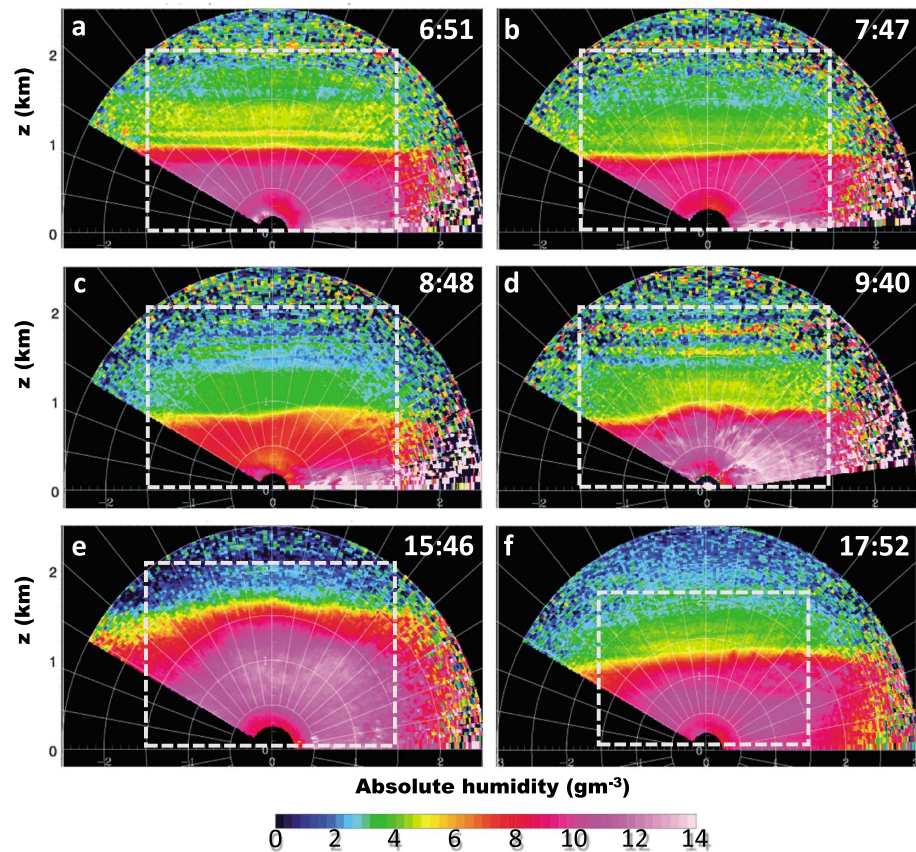


Figure 2. The WVDIAL scans of absolute humidity on 8 September 2009. The starting time of the each scan in UTC is denoted in the lower left corner of the corresponding panel. Each scan lasted approximately 24 min. White rectangles on the scans denote the area (3 km in horizontal and 2.5 km in vertical direction) over which the measured data were averaged to obtain the absolute humidity profiles.

10 s was used for each profile resulting in an angular resolution of 1° . Each of the scans took 24 min to complete. The complex structure of the humidity field and its typical development in the course of the day is revealed: several horizontal layers are seen in addition to turbulent structures close to the ground which extend to the full height of the CBL of ~ 2 km in the afternoon.

In the morning hours (Figures 2a–2c) a CBL started to evolve, which is visible from the strong increase in humidity close to the land surface. High-humidity content above the evolving CBL corresponds to the residual layer from the day before. At about 10 UTC (Figure 2d) the evolving CBL overtook the residual layer. In the afternoon, the CBL was well mixed and about 1.6 km high (Figure 2e), with humidity content lower than on the previous scan which indicates the drying process during the day. Also, the interfacial layer with entrainment of drier air from aloft can be revealed at about 1.6 and up to 2 km. In Figure 2f the CBL collapsed, but the strong residual layer up to 1.2 km from the daytime is clearly apparent from the humidity content, which remained relatively high.

The vertical profiles of absolute humidity used for validation in this study were obtained by averaging the scanning data over a range of 3 km, 1.5 km in each horizontal direction from the WVDIAL site (white dashed rectangle in Figure 2). As humidity within the CBL is highly variable, the averaging scheme of the WVDIAL scans yields data which are more representative for comparisons with the model output and provide lower sampling errors than, e.g., radiosonde profiles, which sample the atmosphere only along its path at certain times.

3. SVA Analysis Method: Mixing Diagram Approach

The mixing diagram approach, introduced by Betts [1992] and extensively used by Santanello *et al.* [2009, 2011, 2013] for the intercomparison of the PBL schemes and LSMs, is applied here to analyze SVA feedbacks. It is a useful technique to diagnose the degree of coupling between the land surface and atmosphere on diurnal time scales. From the diagram it is possible to diagnose total mean flux of heat and moisture within the PBL, as well as the contributions of the surface, advection, and entrainment fluxes to the total mean flux.

To obtain these fluxes, the mixing diagram deploys 2-D vector representation of heat and moisture budgets within the CBL. Changes of heat and moisture in the CBL over some time interval Δt can be considered as vectors in a $(Lq, C_p\theta)$ diagram, with q representing mixing ratio and θ is potential temperature. The surface vector (\mathbf{V}_{sfc}) represents the quantified impact from the surface to the total mean PBL flux (see Figure 7). x component of \mathbf{V}_{sfc} ($C_p\Delta\theta_{\text{sfc}}$) corresponds to the mean H at the land surface and can be calculated as

$$C_p\Delta\theta_{\text{sfc}} = \frac{\overline{H_{\text{sfc}}}\Delta t}{\rho h}, \quad (7)$$

where ρ is the density in the CBL, the subscript sfc denotes the surface, and overbars mark the averaged values over a time interval Δt . The similar principle is valid also for calculating y component of \mathbf{V}_{sfc} ($L\Delta q_{\text{sfc}}$), only with θ being replaced with q , H with λE , and C_p with L .

In the analysis the impact of the advected fluxes was considered as well. The x component of the advection vector (\mathbf{V}_{adv}) can be calculated using:

$$C_p\Delta\theta_{\text{adv}} = C_p\Delta t \left(\left\langle \bar{u} \frac{\partial \theta}{\partial x} \right\rangle + \left\langle \bar{v} \frac{\partial \theta}{\partial y} \right\rangle \right), \quad (8)$$

with u and v being zonal and meridional wind velocities, respectively, angle brackets stand for averaged values within the CBL column. By replacing C_p with L , and θ with q in equation (8), the y component of \mathbf{V}_{adv} can be calculated. \mathbf{V}_{adv} is then added to \mathbf{V}_{sfc} .

The entrainment vector (\mathbf{V}_{entr}) is a residual vector that connects \mathbf{V}_{adv} with the final values of Lq and $C_p\theta$ at t_{end} , and it can be calculated using simple vector algebra. All the vectors are displayed on Figure 7. The x and y components of \mathbf{V}_{entr} correspond to mean H and λE at the interfacial layer, respectively. Negative/positive values of the mean H at the interfacial layer denote mean entrainment of cold/hot air from the free atmosphere, while negative/positive λE stands for the influx of dry/moist air through the interfacial layer. The slope of \mathbf{V}_{sfc} corresponds to the mean Bowen ratio at the surface (β_{sfc}). Using the information obtained from the mixing diagrams, the mean Bowen ratio at the interfacial layer (β_{entr}), which is the slope of \mathbf{V}_{entr} , can be easily calculated as well. More details about vector representation of energy budgets in the form of mixing diagrams are available in Santanello *et al.* [2009, 2011, 2013].

4. Results

Results representing the sensitivity of the WRF model to the PBL schemes are displayed separately from the results showing the model sensitivity to the LSMs. Absolute humidity profiles simulated on 8 September 2009 were compared with the WVDIAL measurements and presented in section 4.1. In section 4.2, the temperature profiles of the six model simulations are compared with the available sounding data to investigate the representation of the CBL in respect to stability. A quantity that describes the ability of a PBL scheme to depict profiles of thermodynamic variables is the PBLH [e.g., Coniglio *et al.*, 2013]. In section 4.3 PBLH calculated from the simulations using two techniques are compared with the measured PBLH, which was estimated from WVDIAL absolute humidity profiles as the height with the highest moisture gradient [e.g., Seibert, 2000; Seidel *et al.*, 2010; Pal *et al.*, 2010]. Furthermore, we examined the sensitivity of the WRF model to the PBL schemes and LSMs in simulating the SVA coupling. In section 4.4, we applied the mixing diagram approach [Santanello *et al.*, 2009, 2011, 2013] to quantify the SVA feedback processes locally on a diurnal time scale.

4.1. Absolute Humidity Profiles

The high-resolution WVDIAL measurements permit a detailed insight into PBL evolution during daytime. On 8 September 2009, measurements were available from 7 to 10 UTC at an hourly scale and in the afternoon at 16 and 18 UTC. The residual layer from the previous day, with a strong inversion layer at ~900 m is visible at 7

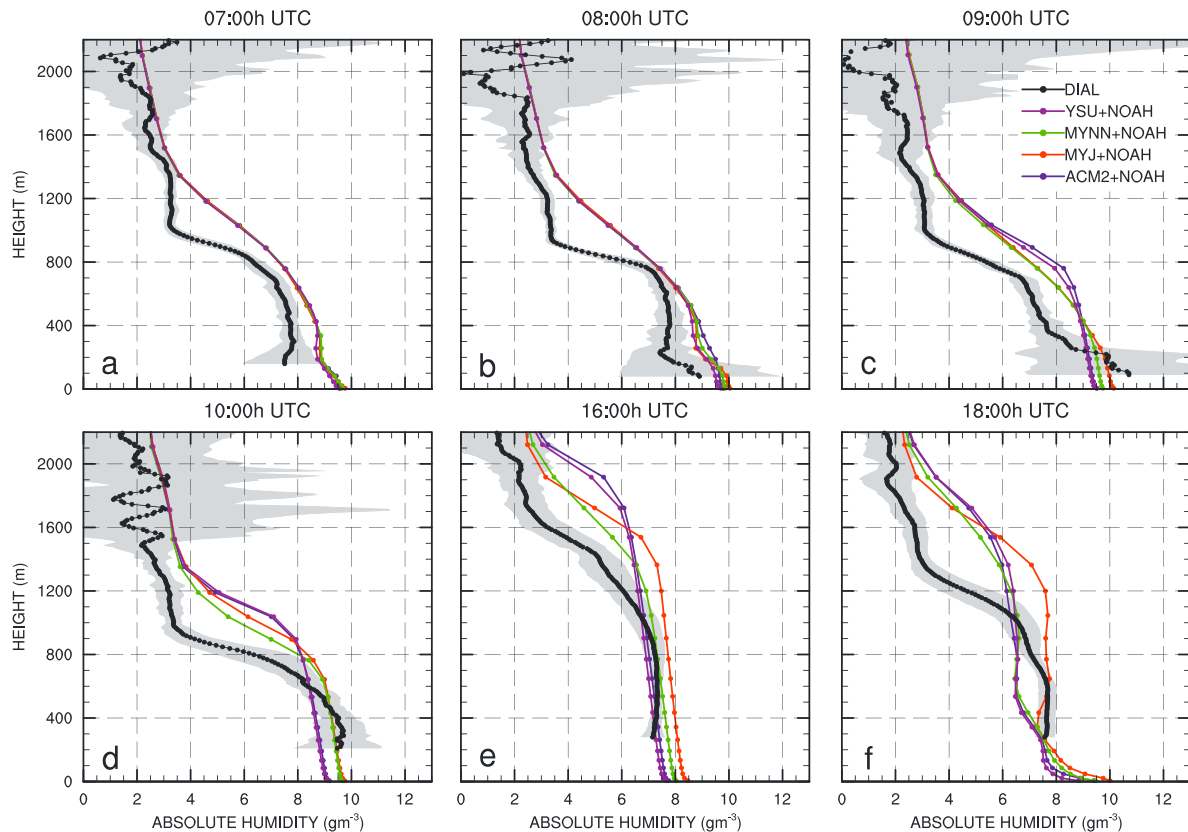


Figure 3. Comparisons of the measured absolute humidity profiles (black dots) with the profiles simulated with WRF configured with the four PBL schemes (ACM2 in blue, MYJ in red, MYNN in green, and YSU in purple) and the NOAH LSM. Shaded grey areas correspond to the standard deviation of the scans due to averaging.

and 8 UTC (black dotted lines on Figures 3 and 4). The PBL started to evolve slowly at the beginning of the day (from 7 to 9 UTC), and at 10 UTC it merged with the residual layer and reached the inversion layer. The PBL was well mixed (almost constant humidity profile) at 16 UTC, but already in the decay phase, while at 18 UTC an abrupt collapse of the PBL was observed. The measurements are compared with the absolute humidity profiles simulated with the six WRF simulations in the following two sections.

4.1.1. Sensitivity to the PBL Parameterizations

Figure 3 displays the sensitivity of WRF to the PBL schemes in simulating the absolute humidity profiles in comparison with the WVDIAL measurements. The LSM selected for this comparison is NOAH.

The discrepancies between the simulations and the measurements are ranging up to 2 g m^{-3} , being the highest at the start of the PBL evolution and at the time of the PBL collapse. The comparisons of the profiles show that all of the schemes fail to reproduce the residual layer and the strong morning inversion observed at $\sim 900 \text{ m}$ (Figures 3a–3c). The PBLH in the CBL can be estimated from vertical humidity profiles as the height where the highest moisture gradient occurs [e.g., Seibert, 2000; Seidel et al., 2010; Pal et al., 2010]. At 7 A.M. the simulated profiles are very similar. They start to diverge from the surface as the CBL evolves and deviate at 8 UTC in the lowest 500 m (Figure 3b). The observed humidity gradient between 100 and 250 m is stronger than the simulated gradients. However, with the two local schemes (MYJ and MYNN) the gradient is closer to the observation than with the nonlocal schemes. From 9 UTC onward, all the PBL schemes result in a higher CBL compared with the measurements. At 9 UTC (Figure 3c) the observed humidity in the lowest 400 m has increased, showing a gradient of 3 g m^{-3} between 100 and 400 m height. This is not simulated

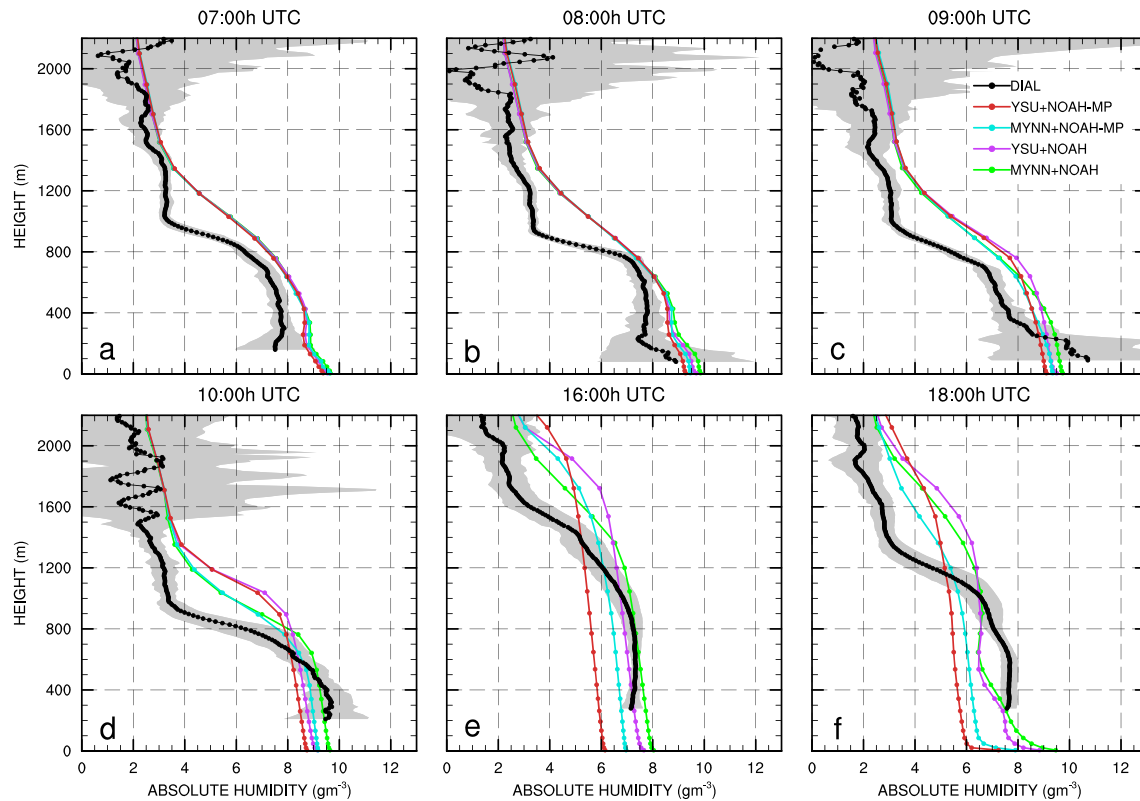


Figure 4. Absolute humidity profiles simulated with the four WRF configurations differed in combinations of the two PBL schemes and the two LSMs compared with the WVDIAL measurements. Turquoise lines denote MYNN with NOAH-MP and brown YSU with NOAH-MP. Other colors and the WVDIAL data the same as on Figure 3.

by the PBL schemes, which only show a decrease of the gradient and an increase in humidity between 400 and 1000 m height. At 10 UTC (Figure 3d) the residual layer vanished and the morning CBL is developed below 800 m. The PBL schemes show a less intense gradient. In the nonlocal schemes the highest gradient is 200 m above the local schemes' gradient. Therefore, the highest CBL is obtained with the nonlocal ACM2 and YSU schemes, which is up to 400 m higher than observed (Figures 3d and 3e). Furthermore, the nonlocal schemes also account for the fastest growth of the PBL in the morning hours (Figures 3b and 3c). Slower evolution and a shallower, but still too high CBL was simulated with the local MYJ and MYNN schemes. At 16 UTC (Figure 3e), when the CBL was fully developed, the shallowest CBL was obtained with the MYNN scheme. However, the humidity gradient of 5 gm^{-3} per 600 m is only simulated by the local MYJ scheme, though the overall humidity is 1 gm^{-3} larger than observed, and the PBLH is for about 250 m higher. Figure 3f shows that the two nonlocal schemes simulate a strong transition, while in MYNN the transition is less pronounced, and MYJ miss to reproduce it completely. However, the simulated reduction of the inversion layer from 16 to 18 UTC is much more gradual for all the PBL schemes than observed, which resulted in a too high residual layer that formed after the PBL collapse (Figure 3f). ACM2, YSU, and MYNN simulate a significant drying in the upper PBL from 16 to 18 UTC, which is not the case with MYJ. Drying of the CBL can be related to advection and entrainment of dry air from the free atmosphere, both parameterized differently in the schemes.

The difference between the profiles obtained with the two nonlocal schemes is almost negligible, while the profiles with the local schemes show significant differences in representing PBL evolution. The largest differences appear when the CBL is well mixed, and during its collapse. MYJ simulates the CBL with higher

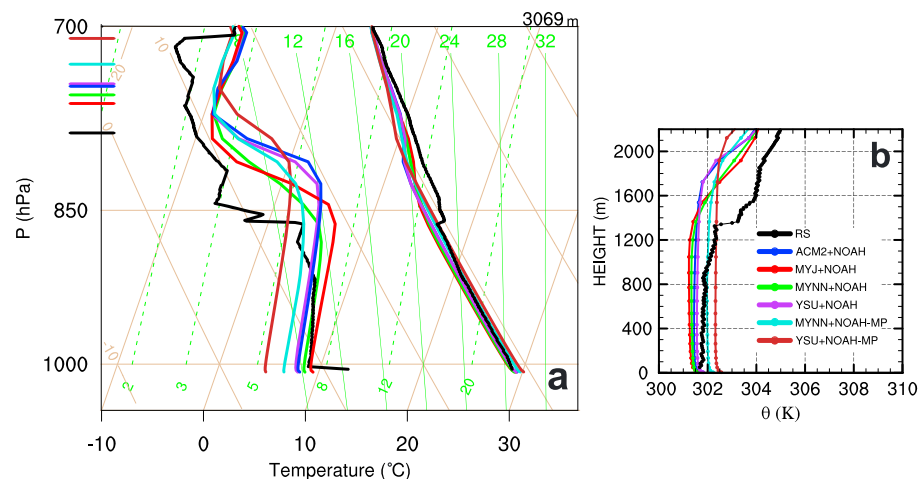


Figure 5. (a) Skew T-logp diagram of 16 UTC 8 September 2009 sounding, as simulated with the six WRF runs along with the RS measurements (the RS launched at 16 UTC). Lines perpendicular to the left vertical axis of the diagram are the LCL values in hPa as calculated from the simulations and the RS measurements. (b) The potential temperature profiles valid at 16 UTC as simulated with the six model simulations and measured with the RS. Colors of the lines on both panels depicted in the legend located in the bottom right corner of Figure 5b.

moisture, stronger inversion, and the thinner interfacial layer than MYNN. The two local schemes are not coupled with the same surface layer parameterization scheme, which can simulate different heat and moisture fluxes at the land surface. This can result in significantly different PBL evolution, since the input variables to the PBL schemes are the fluxes. The latter is discussed in details in section 5.

4.1.2. Sensitivity to the LSMs

Figure 4 shows the WRF sensitivity to LSMs. The WVDIAL measurements of absolute humidity profiles are compared with the NOAH-MP and NOAH simulations, coupled with MYNN and YSU.

The discrepancies between the simulations increase during the morning hours and result in a different CBL evolution (Figures 4a–4c). At 10 UTC (Figure 4d) the CBL is evidently drier with NOAH-MP than with NOAH. In the afternoon, the CBL was well mixed (Figure 4e) and a significant sensitivity of WRF to the coupled LSM is not only apparent close to the ground, but it extends up to the CBL top and the lower free troposphere. In the case of NOAH-MP, the CBL is significantly drier (between ~ 0.5 and $\sim 1.5 \text{ g m}^{-3}$). At 16 UTC the PBLH is slightly higher ($\sim 100 \text{ m}$), and humidity gradients in the interfacial layer are marginally lower with NOAH-MP than with NOAH (Figure 4e). At 18 UTC, just after the CBL collapsing, each profile deviates significantly one from another due to both, different LSMs and different PBL schemes. All in all, the results indicate that a different LSM causes different SVA feedback and that this affects entrainment processes at the interfacial layer and thus impacts on the PBL structure.

4.2. Temperature Profiles

At 16 UTC 8 September 2009 a radiosonde was launched from the study site. The temperature measurements are compared with the six simulations in a form of skew T-logp diagram (Figure 5a) to further investigate the CBL features. This allows for the calculation of the LCL.

Figure 5a shows that the measured capping inversion occurs at approximately 1400 m, which is about 200 lower than in WVDIAL. WRF in all six experiments has a significantly higher inversion layer (more than 400 m higher, depending on model configuration).

Dew point temperature shows a higher dependence on the selected PBL scheme and LSM. The nonlocal PBL schemes and NOAH-MP simulate lower moisture within the CBL than the local PBL schemes and NOAH. Stronger humidity gradients at the inversion are obtained with the nonlocal schemes. This results in a thinner inversion layer than with the local schemes. The most humid CBL and consequently the lowest PBLH is

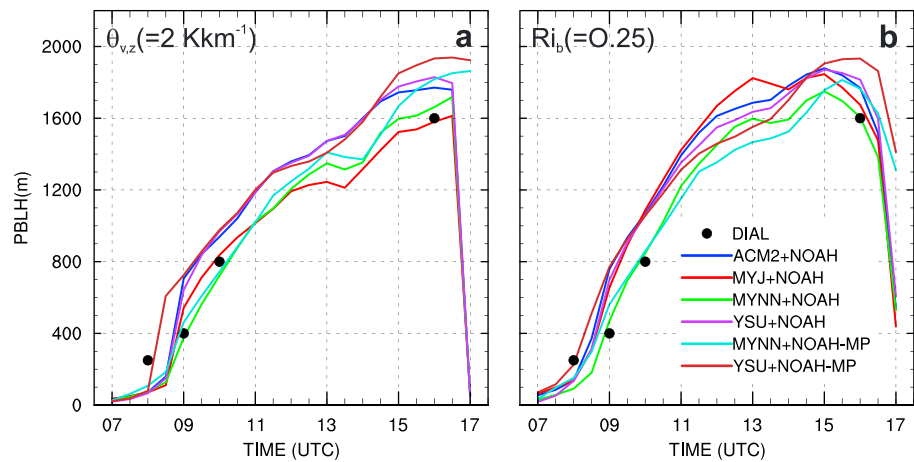


Figure 6. Temporal change of PBLH from WRF compared with the PBLH estimates obtained from the WVDIAL measurements (black dots) on 8 September 2009 between 7 and 17 UTC. The PBLH from the model is calculated using (a) the virtual potential lapse rate method and (b) the bulk Richardson method.

simulated by MYJ, which coincides with the results discussed in section 4.1.1. Within the CBL the model is more sensitive to the LSM choice, while the height and thickness of the inversion layer is more sensitive to the PBL scheme. Comparing to the RS measurements, all the schemes simulated the afternoon overshooting, especially the simulations with nonlocal schemes coupled with NOAH-MP. The inversion layer simulated with the local schemes is too thick, and the inversion is not as sharp as measured. This is especially the case with MYJ simulations. Comparing to the WVDIAL measurements (sections 4.1.1 and 4.1.2), one can see that the RS measured even sharper inversion at 16 UTC (Figure 5a) than the WVDIAL (Figures 3e and 4e).

The observed LCL height of 787 hPa at 16 UTC is overestimated by all simulations as well. The difference between local and nonlocal PBL schemes applied with NOAH becomes evident in the LCL heights, which are lower with the local schemes (MYNN: 756 hPa, MYJ: 763 hPa) than with the nonlocal schemes (YSU: 747 hPa, ACM2: 749 hPa). The height of the LCL was increased by 18 hPa for YSU and 17 hPa for MYNN when applying NOAH-MP.

Potential temperature profiles at 16 UTC depicted on Figure 5b indicate that the profiles simulated with the local PBL schemes are slightly stable, especially with MYJ. The observed unstable profiles are simulated with the nonlocal PBL schemes. The stability of the CBL is not influenced by the LSMs in this case study. The bulk difference between the simulated temperatures within the CBL is less than 1 K, but nevertheless, the profiles show that the CBL was slightly warmer with the local schemes, as well as with the NOAH-MP. NOAH-MP slightly increased the PBLH for both, the local MYNN and nonlocal YSU schemes, but in all the six cases the PBLH is strongly overestimated (>400 m) compared with the RS measurements.

4.3. The Planetary Boundary Layer Height

Each of the PBL schemes deployed uses a different formulation to diagnose the PBLH (see sections 2.1.2.1 and 2.1.2.2), and therefore comparisons of the model diagnostics with the measurements would lead to inconsistent conclusions [e.g., LeMone *et al.*, 2013]. To avoid this, we chose two criteria to calculate the simulated PBLH. A common method to calculate the top of the CBL defines the PBLH as the height where the virtual potential temperature lapse rate exceeds some threshold value [e.g., Seibert, 2000; Liu and Liang, 2010]. We chose the threshold value to be 2 K km^{-1} , as suggested by LeMone *et al.* [2013]. The second criterion applied is the bulk Richardson method as used in YSU, with Ri_{bcr} set to 0.25 [e.g., Hong *et al.*, 2006; Jeričević and Grisogono, 2006]. At 7 and 18 UTC it was not possible to estimate PBLH since the PBL was shallower than the lowest level at which the WVDIAL measurements were performed.

Figure 6a demonstrates the comparisons of the PBLH obtained from the simulations using the virtual potential temperature lapse rate method. The maximum difference between the PBL schemes is $\sim 300 \text{ m}$. The nonlocal

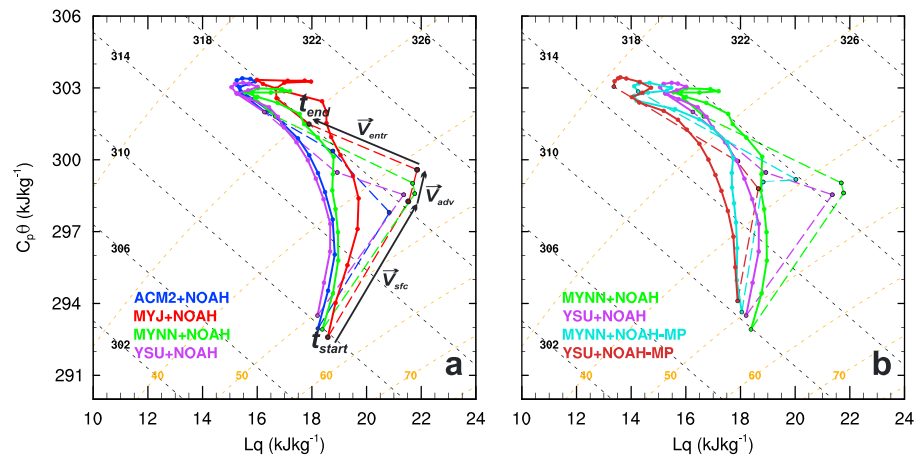


Figure 7. Mixing diagrams for 8 September 2009 between 7 and 17 UTC. Solid lines demonstrate the simulated coevolution of moisture content Lq and heat content $Cp\theta$. Dashed colored lines are vectors which correspond to the surface fluxes (V_{sf}), the advected fluxes (V_{adv}), and the entrainment fluxes (V_{entr}). (a) The simulations with WRF configured with NOAA LSM and the four PBL schemes (ACM2, MYJ, MYNN and YSU). (b) The four WRF simulations configured with combinations of the two PBL schemes (MYNN and YSU) and two LSMs (NOAH and NOAA-MP). Colors of the lines correspond to those on Figures 3 and 4. Overlain are lines of constant θ_e (in K; black dashed) and RH (in %; orange dashed).

schemes exhibit a more rapid evolution of the PBL than the local schemes, which is in agreement with similar studies [e.g., Moeng and Sullivan, 1994; Shin and Hong, 2011; Xie et al., 2013; Coniglio et al., 2013]. There is no significant difference in the results between the two nonlocal schemes, ACM2 and YSU, whereas the PBLH is higher with MYNN than with MYJ most of the day. Only in the morning, the evolution of the PBL is slightly faster with MYJ than with MYNN. From the time when the CBL is fully mixed (i.e., at 11 UTC) the PBLH is higher with MYNN (~100 m) than with MYJ. Comparing the results with the measurements, the PBLH obtained with the local schemes fits better than with the nonlocal schemes, especially in the morning. The PBL evolution as simulated with the both nonlocal schemes is too fast when comparing with the measurements.

The PBLH obtained with NOAA-MP is similar or up to ~100 m higher than with NOAA. Using YSU, the start of the PBL evolution occurs 30 min earlier in NOAA-MP than with NOAA. The highest difference between the two LSMs occurs at the time of the PBL collapse. NOAA-MP postpones the occurrence of the PBL decay for at least 30 min. Furthermore, the increase in the PBLH just before the collapse obtained with MYNN and NOAA-MP is not realistic.

The PBLH maximum occurrence in all cases is in the late afternoon (here at or after 16 UTC). This is not typical for the PBL evolution on clear-sky weather conditions [e.g., Stull, 1988; Seibert, 2000; Zhang et al., 2014]. Therefore, we applied the bulk Richardson method to calculate the PBLH from the model as well. The results are displayed on Figure 6b. The diurnal cycle obtained with this method seems to be more realistic. The highest difference between the two methods is obtained at midday and in the early afternoon, ranging from 300 to 500 m. The most notable difference in the results between the two methods deployed is obtained with MYJ. The PBLH in the CBL is significantly increased with MYJ when the bulk Richardson method was used. This indicates that the impact of wind shear on the PBL evolution, accounted for in the bulk Richardson method, might be higher in the MYJ simulations than in the other simulations. Furthermore, with NOAA-MP the PBL collapse occurs later than with NOAA as well. The delay of the collapse might also be related to wind shear at the top and bottom of the PBL [e.g., Pino et al., 2006; Goulart et al., 2010; Darbieu et al., 2015], but the investigation of wind shear impact on PBL evolution is beyond the scope of this paper. With this method, results obtained with MYNN and NOAA are fitting best with the measurements, which is consistent with the previous results (see section 4.1) and studies such as, e.g., Coniglio et al. [2013] and Huang et al. [2013].

4.4. The Land-Atmosphere Coupling

The results in sections 4.1–4.3 demonstrate the strong influence of the land surface on the PBL evolution. In this section we applied the mixing diagram approach to quantify the simulated influence of land

Table 4. Diagnostics From the Mixing Diagrams^a

Experiment	β_{sfc}	β_{entr}	$A_{\lambda E}$	A_H	$AD_{\lambda E}$	AD_H
ACM2-NOAH	1.86	−1.55	−1.24	0.91	−0.29	0.18
MYJ-NOAH	1.89	−1.18	−1.30	0.72	0.01	0.09
MYNN-NOAH	1.67	−1.09	−1.45	0.84	−0.07	0.04
YSU-NOAH	1.64	−1.54	−1.08	0.90	−0.32	0.07
MYNN-NOAH-MP	6.42	−0.78	−8.48	1.02	0.15	0.02
YSU-NOAH-MP	5.70	−0.86	−7.79	1.15	−0.05	0.08

^aBowen ratio at the land surface (β_{sfc}) is calculated from the model output as the ratio of H to λE , while at the interfacial layer (β_{entr}) are diagnosed from the mixing diagrams. The ratios of the fluxes of latent ($A_{\lambda E}$) and sensible heat (A_H) at the land surface to those at the interfacial layer are also diagnosed from the mixing diagrams. The advected moisture (heat), divided by and the sum of the surface and entrainment flux of latent (sensible) heat is quantified impact $AD_{\lambda E}$ (AD_H) of horizontal advection of moisture (heat). All the variables are mean values averaged over 10 h period (from 7 UTC to 17 UTC) on 8 September 2009 for the six experiments exhibited in this study.

surface processes, advection, and entrainment on PBL evolution. The method is applied on a diurnal time scale at a model grid point closest to the study site. Heat and moisture advection necessary to obtain \mathbf{V}_{adv} (right-hand side of equation (8)) is calculated at the model grid point as well. The values denoted in the diagram represent mean advection of heat (x component of \mathbf{V}_{adv}) and moisture (y component of \mathbf{V}_{adv}) in the CBL over a time period Δt (here 10 h).

The mixing diagram depicted on Figure 7a demonstrates the sensitivity of WRF to the four PBL schemes, all with NOAH, in representing the temporal change of heat and moisture during a 10 h period (from 7 UTC until 17 UTC) on 8 September 2009. Differences between the simulations are evidently small, with low variability of humidity content in the lower PBL during the day. Slightly faster drying of the lower CBL was simulated with ACM2 and YSU than with the local PBL schemes, indicating higher mixing properties with the nonlocal schemes. The highest moisture in the CBL was accounted with MYJ.

Sensitivity of WRF to the LSMs (NOAH and NOAH-MP) together with its sensitivity to the PBL schemes (MYNN and YSU) is shown in Figure 7b. The curves demonstrate the higher sensitivity of the model to the LSMs than to the PBL schemes. The CBL simulated with NOAH-MP is drier and slightly warmer than the one simulated with NOAH. Lines of constant relative humidity (RH) are overlain on the mixing diagrams. There is no significant difference in the RH during the day between the simulations. All configurations simulated the change of about 20% in RH during the 10 h period. However, up to 5% lower values of RH are accounted with the local PBL schemes (Figure 7a) as well as with the NOAH-MP runs (Figure 7b). Moist static energy (MSE), which is defined as a sum of sensible heat, geopotential heat, and latent heat, is proportional to equipotential temperatures (θ_e). Therefore, an increase in θ_e means a buildup in MSE, which implies an increase in potential for a convection occurrence. Therefore, θ_e is a useful measure of the potential for low-level heat and moisture impact on cloud development and precipitation [e.g., Santanello *et al.*, 2011]. Lines of constant θ_e are overlain on the mixing diagrams as well. This allows for simple quantification of the MSE during the day for the each simulation. With ACM2, YSU, and MYNN (Figure 7a) WRF simulated an increase of θ_e by approximately 6 K during the day, while about 8 K was simulated with MYJ. This indicates that slightly higher potential for cloud development was simulated with MYJ. Comparing an impact of the LSM on the θ_e change, NOAH-MP decreases the value for about 2 K, i.e., NOAH-MP reduces the potential for cloud development with both, MYNN and YSU. The overall change of θ_e depends on surface evaporation, the PBL evolution, advection and the processes at the entrainment. These processes can be quantified from the mixing diagrams and the results for this case study are summarized in Table 4. One of the derived variables from the mixing diagram is the mean entrainment Bowen ratio (β_{entr}). The values of β_{entr} indicate that the mean entrainment of warm air is slightly higher than the mean entrainment of dry air for all the PBL schemes deployed, since $\beta_{\text{entr}} < -1$. The values of ratios between the mean latent heat flux at the entrainment and that at the land surface ($A_{\lambda E}$) indicate that the highest mean entrainment of dry air (negative values) was acquired by the nonlocal schemes, while the lowest values were obtained with MYJ scheme.

In case of the local PBL schemes advected fluxes can be neglected due to the low ratios (<0.1) between the mean advected fluxes and the sum of the mean surface and entrainment fluxes ($AD_{\lambda E}$ for latent heat, and AD_H

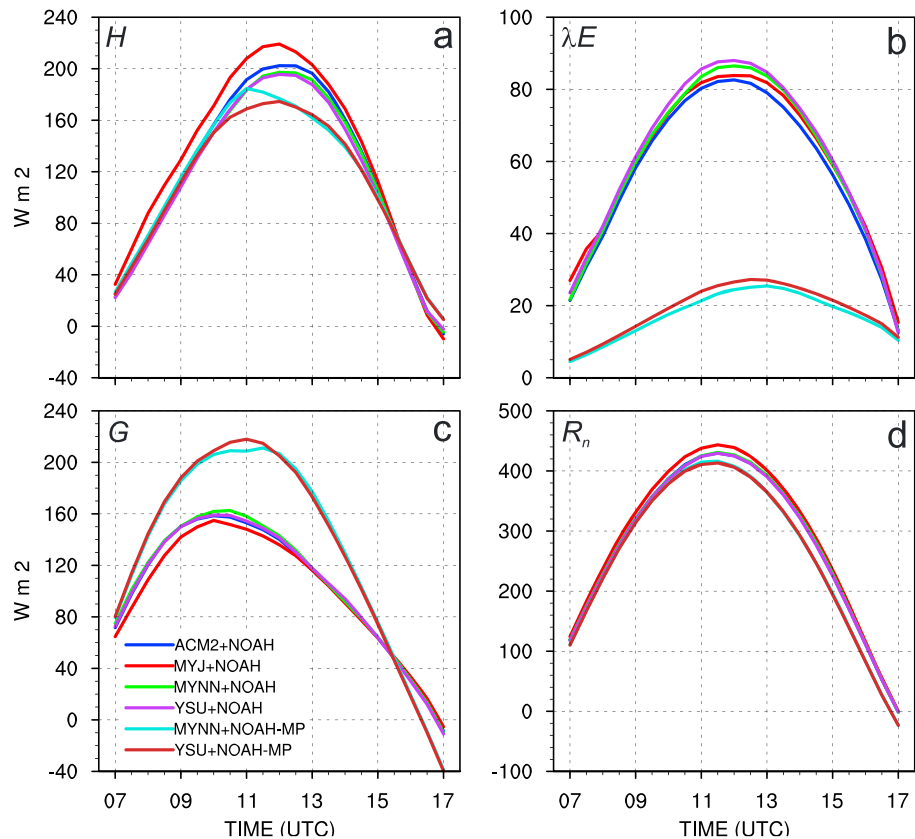


Figure 8. Simulations of the temporal change of (a) sensible heat flux (H), (b) latent heat flux (λE), (c) ground heat flux (G), and (d) radiation flux (R_n) on 8 September 2009 between 7 and 17 UTC.

for sensible heat). Simulations with the nonlocal schemes simulated significant impact of the mean advected fluxes to the mean total fluxes, with the values of around 0.3 for the case of latent heat flux.

The differences between the values derived from the mixing diagrams are significantly higher when comparing the results from the two LSMs to those obtained from the four PBL schemes. The significantly higher Bowen ratio at the land surface (β_{sfc}) calculated with NOAH-MP implies that less energy is partitioned into latent heat compared to NOAH. Since the radiation scheme used in all the simulations is the same, the R_n should not vary significantly between the schemes. Therefore, to close the energy balance at the land surface in equation (1), the residual latent heat flux went to H or/and G . This significant difference in β_{sfc} between the LSMs is due to difference in evaporative physics of the LSMs. In section 5.2 this has been discussed more in detail.

The absolute value of the Bowen ratio at the entrainment ($|\beta_{entr}|$) is < 1 , while from NOAH simulation it is > 1 . Since negative values for $A_{\lambda E}$ indicate a mean influx of dry air from the free atmosphere in the PBL, this suggests that NOAH-MP exhibits a higher entrainment of dry air than NOAH. Since less moisture comes from the land surface and much more dry air is entrained in the PBL ($A_{\lambda E}$ with NOAH-MP is 5 times $A_{\lambda E}$ with NOAH, see Table 4), the PBL is drier in NOAH-MP than in NOAH. This explains the results displayed in section 4.1.2, where the difference obtained in humidity profiles between NOAH and NOAH-MP is up to 20%. Furthermore, comparing only the size and the slope of \mathbf{V}_{entr} versus \mathbf{V}_{sfc} for NOAH-MP and NOAH in the diagram, it can be seen that the drying effect of the free atmosphere (entrainment processes) has a stronger impact on PBL evolution than the moistening from land surface, in all simulations, especially when coupled with NOAH-MP.

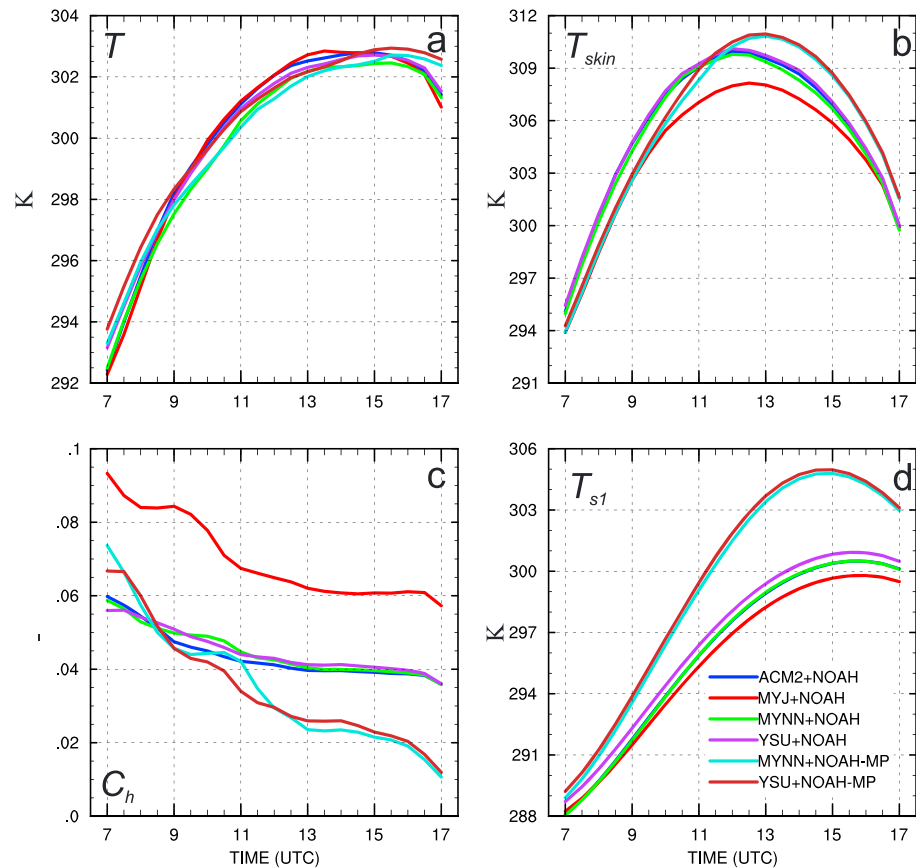


Figure 9. Simulations of the temporal change of (a) the temperature at the first model level (T), (b) the surface temperature (T_{skin}), (c) the surface exchange coefficient for heat and moisture multiplied with the friction velocity (C_h), and (d) the temperature in the first soil layer (T_{s1}) on 8 September 2009 between 7 and 17 UTC.

Quantified impacts of the mean advected fluxes (AD_{iE} and AD_{iH}) in the experiments with NOAH-MP do not exceed 0.1 significantly. Therefore, the impact of horizontal advection to the mean total flux, and subsequently to the PBL evolution at the study site simulated with NOAH-MP is negligible, which can be also confirmed with the size of the \mathbf{V}_{adv} vectors.

5. Discussion

On 8 September 2009 between 7 and 9 UTC the simulated temporal change in absolute humidity within the PBL with the six experiments is not higher than 0.5 g m^{-3} , while the measured changes are ranging up to 3 g m^{-3} . Moistening of the PBL that was measured during the PBL growth can be explained by enhanced evaporation after the sunrise due to evaporation from the bare ground where the WVDIAL was located and transpired water from the surrounding field of sugar beet that was within the 3 km range of the performed measurements (see section 2.2). Higher standard deviation of the measurements within the lower CBL in the morning hours (Figures 3a–3c and 4a–4c) confirms the higher variability in humidity field within the range of averaging (white dashed rectangles on Figure 2). A small change in humidity during the PBL evolution simulated by the model in this study with all the six experiments, indicates that the evaporative fraction simulated by the model is lower than in reality. This can be related to the land surface heterogeneity, which is not captured by the model. The model categorizes the grid cell, which corresponds to the study site,

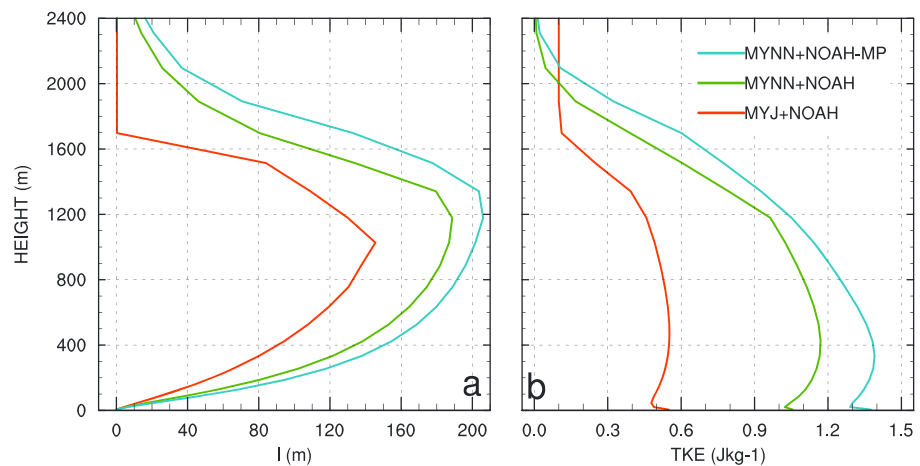


Figure 10. Vertical profiles of the (a) mixing length scale (l) and (b) TKE on 8 September 2009 at 16 UTC as simulated with WRF configured with the local schemes (MYJ with NOAH in red, MYNN with NOAH in green and MYNN with NOAH-MP in turquoise).

as a cropland. In reality this was an open-pit mine surrounded by the agricultural landscapes, where most of the field were harvested apart from the one covered with sugar beet (see section 2.2). Categorization of the landscapes and phenological changes, which are recognized by the WRF model via green vegetation fraction (F_{veg}), determine the vegetation parameters such as leaf area index, albedo, roughness, emissivity, etc. These parameters are read from lookup tables in the LSMs. Therefore, model errors in F_{veg} or in land use will affect the results in the model representation of the fluxes at the land surface significantly [e.g., Nielsen *et al.*, 2013].

5.1. Sensitivity to the PBL Schemes

Results of the simulations differing in the PBL schemes have shown that the highest differences occur between the local and the nonlocal approach.

The behavior of the nonlocal schemes is very similar with respect to humidity and temperature profile evolution. Figure 8 depicts simulations of the daytime temporal change of radiative and surface fluxes over a 10 h period on 8 September 2009. H simulated with ACM2 is up to 10 W m^{-2} higher than with YSU (Figure 8a), and lower λE (Figure 8b) leads to higher β_{sfc} . This implicates therefore greater buoyancy in the CBL. All the aforementioned points lead to the higher mixing associated with ACM2, which support a higher entrainment. This corresponds to the diagnosed values from the mixing diagrams (Table 4) which show that the higher mean entrainment of dry air is simulated with ACM2.

On the other hand, the local schemes demonstrate higher discrepancies in simulating the PBL evolution. One of the reasons is the fact that the WRF configuration with MYJ needs to be coupled to the ETA similarity surface layer scheme, and MYNN with the revised MM5 surface layer scheme. This resulted in significantly higher values of C_h (Figure 9c) with MYJ (also obtained by Xie *et al.* [2013]) and slightly lower T_{skin} . Therefore, up to 35 W m^{-2} higher H is obtained with MYJ, whereas values for λE are similar (Figures 8a and 8b). This results in the higher β_{sfc} with MYJ, which should imply a greater generation of buoyant turbulence and therefore a higher and drier CBL. This is not the case here, however, because of the stronger mixing that occurs with the MYNN scheme. The higher eddy diffusivity for heat and moisture (K_h), which is proportional to l and TKE, the higher the mixing (equation (5)). MYNN accounts for higher values for both l and TKE (Figure 10 depicts an example profile for l and TKE valid at 16 UTC). Furthermore, the mean entrainment of dry and warm air is higher with MYNN, which was derived from the mixing diagrams (Table 4). This leads to the more humid CBL simulated with MYJ than with MYNN scheme. In this case of the local schemes it is evident that the entrainment at the interfacial layer has the highest influence on the PBL evolution.

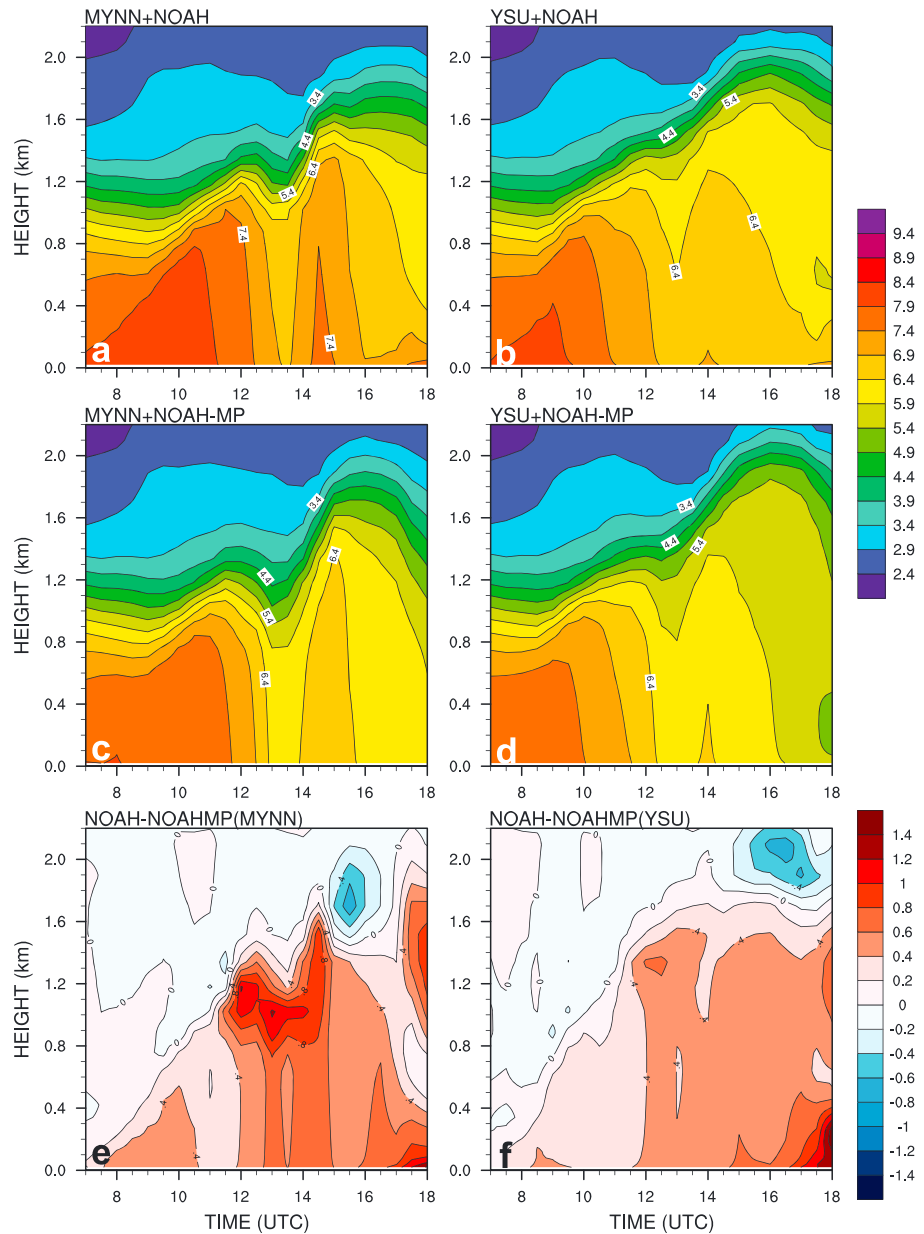


Figure 11. Temporal change of mixing ratio vertical profiles in g kg^{-1} from 7 to 18 UTC on 8 September 2009 at the study site, as simulated with WRF configured with (a) MYNN and NOAH, (b) YSU and NOAH, (c) MYNN and NOAH-MP, and (d) YSU and NOAH-MP. The bottom two panels display the difference between the NOAH and NOAH-MP profiles in g kg^{-1} for the (e) MYNN and (f) YSU PBL schemes.

5.2. Sensitivity to the LSM

This case study shows the high sensitivity of WRF to the LSM choice in representing the PBL features and its evolution. NOAH-MP in its configuration for the model domain accounts for significantly lower λE (Figure 8b) and slightly lower H at the surface (Figure 8a) which corresponds to significantly higher $\beta_{\text{sf}}^{\text{c}}$ in the mixing

diagram when compared to NOAH (see Table 4). The difference in H is related to the lower difference between T (Figure 9a) and T_{skin} (Figure 9b) in equation (2) as well as to the lower C_h obtained with NOAH-MP (Figure 9c). The high difference in λE is partly related also to the lower C_h (since in NOAH and NOAH-MP C_h is equal to C_q) used for the calculation of λE (equation (4)), and partly to the different evaporative physics and the structural changes in NOAH-MP (see section 2.1.1.2). The difference in R_n between NOAH and NOAH-MP is small, up to 20 W m^{-2} (Figure 8d). This is accounted for in the discrepancy in T_{skin} between NOAH and NOAH-MP (Figure 9b), since T_{skin} affects upward longwave radiation from equation (1). Furthermore, the residual energy from the difference in λE goes mostly into the ground as G (Figure 8c). G over vegetated and bare soil in both LSMs is calculated as in equation (3). T_{skin} (Figure 9b) and T_{s1} (Figure 9d) are higher in NOAH-MP than in NOAH, but the difference in T_{skin} between the LSMs is lower than the difference in T_{s1} . Therefore, the temperature gradient between the land surface and the first soil layer in equation (3) is higher with NOAH. This leads to a conclusion that the significantly higher values of G obtained with NOAH-MP are predominantly due to the different methods used for calculating the surface soil thermal conductivity κ_h [Niu et al., 2011]. The difference in the soil moisture η between LSMs has an influence on κ_h as well. At the study site NOAH-MP accounts for $\sim 2\%$ higher η in the top soil layer than NOAH (not shown), which supports the higher κ_h [e.g., Chen and Dudhia, 2001a]. The difference in λE obtained here might also be due to an option in NOAH-MP related to calculation of the soil moisture factor, which is a function of matric potential in NOAH-MP, and of soil moisture η in NOAH. η affects volumetric heat capacity and κ_h in the thermal diffusion equation used for calculation of the soil temperature in NOAH and NOAH-MP [e.g., Chen and Dudhia, 2001a]. Consequently, η affects the soil temperature, T_{skin} , and therefore the fluxes.

The study shows that the higher $\beta_{\text{sf}} c$ also affects the mixing features that are calculated in the PBL schemes. From the humidity profiles represented in section 4.1.2, we can conclude that the spread in the results between the simulations is due to the PBL switches in the morning hours, while in the afternoon the spread is wider and affected more by the land surface exchange, i.e., $\beta_{\text{sf}} c$. Higher mixing was simulated when the schemes were coupled with NOAH-MP. The MYNN scheme, for example, accounts for higher I and TKE when is coupled with NOAH-MP than with NOAH (Figure 10), which results in higher K_r and therefore in higher fluxes.

Figure 11 shows a temporal change of the mixing ratio profiles between 7 and 18 UTC on 8 September 2009 at the study site for MYNN and YSU in combination with NOAH and NOAH-MP. The figure displays that drying in the whole CBL during the afternoon hours is more abrupt with NOAH-MP (Figures 11c and 11d) than with NOAH (Figures 11a and 11b). This can be also seen from the mixing diagram (Figure 7b), especially between 11 and 14 UTC. In the afternoon the $Lq/C_p\theta$ line in the mixing diagram is more sharply curved than in the morning, which indicates that the higher and more abrupt drying with NOAH-MP is related mostly to the entrainment fluxes. In the morning, surface moisture and entrainment are more balanced, since the $Lq/C_p\theta$ line is straighter. Furthermore, the differences in the humidity field between the LSMs range up to 1.4 g kg^{-1} for both MYNN and YSU schemes. The differences are higher in the upper PBL than close to the land surface, especially between 11 and 14 UTC with MYNN (Figure 11e), which is counterintuitive when the LSM is the only difference between the simulations. This is due to the higher entrainment of dry air from the free atmosphere obtained with NOAH-MP, which is also diagnosed as $A_{\lambda E}$ (Table 4) from the mixing diagram (Figure 7b). Due to the higher difference in PBL humidity evolution between NOAH and NOAH-MP, from Figure 11 it can be concluded that WRF coupled with MYNN is more sensitive to the LSM choice than WRF with YSU. All the aforementioned implies that land surface processes are highly influential on mixing properties within the PBL and also processes at the interfacial layer.

6. Summary and Concluding Remarks

This paper has assessed the WRF model sensitivity on PBL parametrization schemes and LSMs in simulating the CBL evolution and its structure during a clear-sky and calm day in Germany. Six simulations have been conducted with two local (MYJ and MYNN) and two nonlocal (ACM2 and YSU) PBL schemes, combined with two LSMs, NOAH, and NOAH-MP (as configured as depicted in Table 2). The focus of the study was on the investigation of WRF representation of the CBL features, such as humidity evolution in the CBL and the PBLH. The SVA feedback analysis has been performed as well, by applying the mixing diagram approach. The model results have been supported with the RS and the high-resolution WVDIAL measurements. The

WVDIAL measurements have been used for the model validation for the first time. They have demonstrated high potential for a detailed analysis of the grid cell-averaged structure of the humidity profiles, PBLH and development of the CBL and the residual moist layer.

All six experiments simulate a too fast CBL evolution, with significant overshooting in the afternoon when comparing the simulated humidity profiles with WVDIAL measurements. Furthermore, the top of the PBL is not as sharp as observed, and none of the schemes has been able to reproduce the strong residual layer as measured. Overshooting in the afternoon is more pronounced with the nonlocal YSU and ACM2 schemes, as well as in the simulations with NOAH-MP. MYJ coupled with NOAH accounts for the highest moisture in the CBL compared to the other five simulations. This is due to the lower mixing properties simulated by MYJ, which is a known disadvantage of the scheme and the local approach in general [e.g., *Holtslag and Boville, 1993; Cuijpers and Holtslag, 1998; Teixeira and Cheinet, 2004*]. The higher humidity obtained with MYJ is also related to the ETA similarity land surface scheme that is coupled with MYJ and is different from the surface layer scheme used in all the other simulations. The exchange coefficient for heat and moisture that is simulated in the ETA scheme is significantly higher than in the other experiments (Figure 9c). The most suitable diurnal evolution of humidity in the PBL in comparison with the WVDIAL measurements has been simulated by MYNN coupled with NOAH. The PBLH estimations from WVDIAL are best fitted to MYNN with NOAH as well.

The budget analysis in a form of the mixing diagram has allowed us to calculate the mean entrainment-to-surface ratios of sensible and latent heat flux in the CBL, the mean heat and moisture advection terms, and the mean Bowen ratio at the interfacial layer. These diagnostics have shown that a significantly higher dry air entrainment is simulated with NOAH-MP than with NOAH. Furthermore, the results indicate that the coupling strength between the local and nonlocal schemes on one hand side and the LSMs on the other hand side is different. An influence of the LSM choice on the simulated CBL features is higher when the model is configured with MYNN than with YSU, which is evident from both the humidity profiles and the mixing diagrams. Due to lack of flux observations at the land surface for this case study, the mixing diagrams could not be supported by the measurements. Nevertheless, this study has demonstrated that the analysis of the simulated mixing diagrams is an effective way of testing the WRF model sensitivity to different parameterization schemes in clear-sky weather conditions via the quantification of SVA feedback processes.

The high impact of the land surface on the PBL, and the height to which this impact extends are distinct findings of this study. The results suggest that the energy partitioning at the land surface strongly influences the CBL evolution and affects also the processes at interfacial layer, such as the entrainment of air from the free atmosphere. From this study it is evident that there is a greater sensitivity of WRF to the LSM than to the PBL schemes on clear-sky days. However, this conclusion might be dependent on the LSM choice itself or to the particular NOAH-MP configuration. Therefore, additional sensitivity studies of WRF to NOAH-MP switches are essential. For a dry case study, particularly important would be the ones regarding the radiative transfer (opt_rad), the calculation of canopy stomatal resistance (opt_crs), the soil moisture factor for stomatal resistance (opt_btr), and surface layer drag coefficient (opt_sfc), since these strongly affect the energy partitioning at the land surface in short time scale simulations, which has been shown here to be the highest difference between NOAH and NOAH-MP.

F_{veg} information used by WRF is based on a 20 year old data set and hence does not reflect changes in agricultural management or modifications imposed by recent climate change [Nielsen *et al.*, 2013]. Neglecting such phenological modifications will subsequently affect the PBL evolution, cloud formation, and precipitation occurrence. Updating the F_{veg} information in WRF and implementation of vegetation growth models within LSMs, which will distinguish summer from winter crops, could improve surface energy and water balance representation in the model. This is increasingly important at finer grid resolutions where field-scale land surface data can be used, as well as in the more sophisticated LSMs such as NOAH-MP.

It is of great relevance to obtain a realistic picture of the sensible and latent heat flux profiles, with emphasis on the fluxes at the interfacial layer. In models, parameterizations of the entrainment fluxes are based mostly on results from large eddy simulation simulations (e.g., in the YSU PBL scheme). Such parameterizations need extensive evaluation and validation using realistic high-resolution measurements, such as WVDIAL. For that, detailed observations of flux profiles are a prerequisite. For improving model accuracy, it is essential to investigate the SVA feedback which varies across seasons and regions, and to identify regions with strong

Acknowledgments

This work is part of the Project PAK 346/RU 1695 funded by DFG and supported by a grant from the Ministry of Science, Research and Arts of Baden-Württemberg (AZ Zu 33–721.3-2). University of Hohenheim DIAL measurements were performed within the Project Transregio 32, also funded by DFG. Model simulations were carried out at the supercomputing center HLRS in Stuttgart. We thank to Alexander Graf for providing us information about agriculture at the study site, as well as to Clemens Drüe for wind information at the DIAL measurement site. All the data for this paper are available from the authors upon request (j.milovac@uni-hohenheim.de). The data are archived at the HLRS storage system (HPSS) in Stuttgart, Germany. We thank the three reviewers for their detailed and helpful reviews.

SVA feedback since this plays a major role in a changing climate. This includes investigation of the interaction between all components of the SVA system, such as the coupling between the soil conditions, convection initiation and precipitation occurrence. Therefore, analyses such as this case study should be carried out in different weather conditions, over various land covers and over different time scales as well, and to validate the results with the measurements.

References

- Angevine, W. M., E. Bazile, D. Legain, and D. Pino (2014), Land surface spinup for episodic modeling, *Atmos. Chem. Phys.*, *14*, 8165–8172, doi:10.5194/acp-14-8165-2014.
- Ansmann, A., J. Fruntke, and R. Engelmann (2010), Updraft and downdraft characterization with Doppler lidar: Cloud-free versus cumuli-topped mixed layer, *Atmos. Chem. Phys.*, *10*, 7845–7858, doi:10.5194/acp-10-7845-2010.
- Ball, J. T., I. Woodrow, and J. Berry (1987), A model predicting stomatal conductance and its contribution to the control of photosynthesis under different environmental conditions, in *Progress in Photosynthesis Research*, edited by J. Biggins, pp. 221–224, doi:10.1007/s00442-007-0951-4, Springer, Netherlands.
- Balsamo, G., P. Viterbo, A. Beljaars, B. van der Hurk, M. Hirschi, A. K. Betts, and K. Scipal (2009), A revised hydrology for the ECMWF model: Verification from field site to terrestrial water storage and impact in the integrated forecast system, *J. Hydrometeorol.*, *10*, 623–643, doi:10.1175/2008JHM1068.1.
- Behrendt, A., V. Wulfmeyer, A. Riede, G. Wagner, S. Pal, H. S. Bauer, M. Radlach, and F. Späth (2009), 3-Dimensional observations of atmospheric humidity with a scanning differential absorption lidar, *Proc. SPIE-Int. Soc. Opt. Eng.*, *7475*, 74750L, doi:10.1117/12.835143.
- Behrendt, A., A. Blyth, M. Dorninger, N. Kalthoff, C. Flamant, P. Di Girolamo, and E. Richard (2013), Convective precipitation in complex terrain: Results of the COPS campaign, *Meteorol. Z.*, *22*, 367–372, doi:10.1127/0941-2948/2013/0541.
- Behrendt, A., V. Wulfmeyer, E. Hammann, S. K. Muppa, and S. Pal (2015), Profiles of second- to fourth-order moments of turbulent temperature fluctuations in the convective boundary layer: First measurements with rotational Raman lidar, *Atmos. Chem. Phys.*, *15*, 5485–5500, doi:10.5194/acp-15-5485-2015.
- Betts, A. K. (1992), FIFE atmospheric boundary-layer budget methods, *J. Geophys. Res.*, *97*(D17), 18,523–18,531, doi:10.1029/91JD03172.
- Bhawar, R., et al. (2011), The water vapor intercomparison effort in the framework of the convective and orographically-induced precipitation study: Airborne-to-ground-based and airborne-to-airborne lidar systems, *Q. J. R. Meteorol. Soc.*, *137*, 325–348, doi:10.1002/qj.697.
- Blackadar, A. K. (1962), The vertical distribution of wind and turbulent exchange in a neutral atmosphere, *J. Geophys. Res.*, *67*, 3095–3102, doi:10.1029/JZ067i008p03095.
- Borge, R., V. Alexandrov, J. J. del Vas, J. Lumbrales, and E. Rodríguez (2008), A comprehensive sensitivity analysis of the WRF model for air quality applications over the Iberian Peninsula, *Atmos. Environ.*, *42*, 8560–8574, doi:10.1016/j.atmosenv.2008.08.032.
- Chen, F., and J. Dudhia (2001a), Coupling an advanced land surface–hydrology model with the Penn State–NCAR MM5 modeling system. Part I: Model implementation and sensitivity, *Mon. Weather Rev.*, *129*, 569–585, doi:10.1175/1520-0493(2001)129<0569:CAALSH>2.0.CO;2.
- Chen, F., and J. Dudhia (2001b), Coupling an advanced land surface–hydrology model with the Penn State–NCAR MM5 modeling system. Part II: Preliminary model validation, *Mon. Weather Rev.*, *129*, 587–604, doi:10.1175/1520-0493(2001)129<0587:CAALSH>2.0.CO;2.
- Chen, F., Z. Janjic, and K. Mitchell (1997), Impact of atmospheric surface layer parameterizations in the new land surface scheme of the NCEP mesoscale Eta model, *Boundary Layer Meteorol.*, *85*, 391–421, doi:10.1023/A:1000531001463.
- Coniglio, M. C., J. Correia, P. T. Marsh, and F. Kong (2013), Verification of convection-allowing WRF model forecasts of the planetary boundary layer using sounding observations, *Weather Forecasting*, *28*, 842–862, doi:10.1175/WAF-D-12-00103.1.
- Cooper, D. I., W. E. Eichinger, J. Archuleta, L. Hipps, C. M. U. Neale, and J. H. Prueger (2007), An advanced method for deriving latent energy flux from a scanning Raman lidar, *Agron. J.*, *99*, 272–284, doi:10.2134/agronj2005.01125.
- Corsmeier, U., et al. (2011), Driving processes for deep convection over complex terrain: A multiscale analysis of observations from COPS-IOP 9c, *Q. J. R. Meteorol. Soc.*, *137*, 137–155, doi:10.1002/qj.754.
- Cuijpers, J. W. M., and A. A. M. Holtslag (1998), Impact of skewness and nonlocal effects on scalar and buoyancy fluxes in convective boundary layers, *J. Atmos. Sci.*, *55*, 151–162, doi:10.1175/1520-0469(1998)055<0151:IOSANE>2.0.CO;2.
- Darbieu, C., et al. (2015), Turbulence vertical structure of the boundary layer during the afternoon transition, *Atmos. Chem. Phys.*, *15*, 10,071–10,086, doi:10.5194/acp-15-10071-2015.
- Dirmeyer, P. A. (2014), The cusp of major progress in predicting land-atmosphere interactions, *GEWEX News*, *24*(1–2), 15–18.
- Dirmeyer, P. A., et al. (2012), Evidence for enhanced land–atmosphere feedback in a warming climate, *J. Hydrometeorol.*, *13*, 981–995, doi:10.1175/JHM-D-11-0104.1.
- Ek, M. B., and A. A. M. Holtslag (2004), Influence of soil moisture on boundary layer cloud development, *J. Hydrometeorol.*, *5*, 86–99, doi:10.1175/1525-7541(2004)005<0086:IOSMOB>2.0.CO;2.
- Ek, M. B., K. E. Mitchell, Y. Lin, E. Rogers, P. Grunmann, V. Koren, G. Gayno, and J. D. Tarpley (2003), Implementation of Noah land surface model advances in the National Centres for Environmental Prediction operational mesoscale Eta model, *J. Geophys. Res.*, *108*(D22), 8851, doi:10.1029/2002JD003296.
- Findell, K. L., and E. A. B. Eltahir (2003), Atmospheric controls on soil moisture–boundary layer interactions. Part II: Feedbacks within the Continental United States, *J. Hydrometeorol.*, *4*, 570–583, doi:10.1175/1525-7541(2003)004<0570:ACOSML>2.0.CO;2.
- García-Díez, M., J. Fernández, L. Fita, and C. Yagüe (2013), Seasonal dependence of WRF model biases and sensitivity to PBL schemes over Europe, *Q. J. R. Meteorol. Soc.*, *139*, 501–514, doi:10.4236/ajcc.2014.35042.
- Gayler, S., T. Wohling, M. Grzeschik, J. Ingwersen, H.-D. Witzmann, K. Warrach-Sagi, P. Hogg, S. Attinger, T. Streck, and V. Wulfmeyer (2014), Incorporating dynamic root growth enhances the performance of Noah-MP at two contrasting winter wheat field sites, *Water Resour. Res.*, *50*, 1337–1356, doi:10.1002/2013WR014634.
- Gentine, P., A. A. M. Holtslag, F. D’Andrea, and M. Ek (2013), Surface and atmospheric controls on the onset of moist convection over land, *J. Hydrometeorol.*, *14*, 1443–1462, doi:10.1175/JHM-D-12-0137.1.
- Giez, A., G. Ehret, R. L. Schwiesow, K. J. Davis, and D. H. Lenschow (1999), Water vapor flux measurements from ground-based vertically pointed water vapor differential absorption and doppler lidars, *J. Atmos. Oceanic Technol.*, *16*, 237–250, doi:10.1175/1520-0426(1999)016<0237:WVFMFG>2.0.CO;2.
- Goulart, A., B. Bodmann, M. Vilhena, P. Soares, and D. Moreira (2010), On the time evolution of the turbulent kinetic energy spectrum for decaying turbulence in the Convective Boundary Layer, *Boundary Layer Meteorol.*, *138*, 61–75, doi:10.1007/s10546-010-9546-4.

- Grisogono, B. (2010), Generalizing "z-less" mixing length for stable boundary layers, *Q. J. R. Meteorol. Soc.*, **136**, 213–221, doi:10.1002/qj.529.
- Guilod, B., E. Davin, C. Kündig, G. Smiatek, and S. Seneviratne (2013), Impact of soil map specifications for European climate simulations, *Clim. Dyn.*, **40**, 123–141, doi:10.1175/JHM-362.1.
- Hammann, E., A. Behrendt, F. Le Mounier, and V. Wulfmeyer (2015), Temperature profiling of the atmospheric boundary layer with rotational Raman lidar during the HD(CP)² Observational Prototype Experiment, *Atmos. Chem. Phys.*, **15**, 2867–2881, doi:10.5194/acp-15-2867-2015.
- Holtslag, A. A. M., and B. A. Boville (1993), Local versus nonlocal boundary-layer diffusion in a global climate model, *J. Clim.*, **6**, 1825–1842, doi:10.1175/1520-0442(1993)006<1825:LVNBLD>2.0.CO;2.
- Hong, S.-Y. (2010), A new stable boundary-layer mixing scheme and its impact on the simulated East Asian summer monsoon, *Q. J. R. Meteorol. Soc.*, **136**, 1481–1496, doi:10.1002/qj.665.
- Hong, S.-Y., Y. Noh, and J. Dudhia (2006), A new vertical diffusion package with an explicit treatment of entrainment processes, *Mon. Weather Rev.*, **134**, 2318–2341, doi:10.1175/MWR3199.1.
- Hu, X.-M., J. W. Nielsen-Gammon, and F. Zhang (2010), Evaluation of three planetary boundary layer schemes in the WRF model, *J. Appl. Meteorol. Climatol.*, **49**, 1831–1844, doi:10.1175/2010JAMC2432.1.
- Hu, X.-M., P. M. Klein, and M. Xue (2013), Evaluation of the updated YSU planetary boundary layer scheme within WRF for wind resource and air quality assessments, *J. Geophys. Res. Atmos.*, **118**, 10,490–10,505, doi:10.1002/jgrd.50823.
- Huang, H.-Y., A. Hall, and J. Teixeira (2013), Evaluation of the WRF PBL parameterizations for marine boundary layer clouds: Cumulus and stratocumulus, *Mon. Weather Rev.*, **141**, 2265–2271, doi:10.1175/MWR-D-12-00292.1.
- Huang, J., X. Lee, and E. G. Patton (2011), Entrainment and budgets of heat, water vapor, and carbon dioxide in a convective boundary layer driven by time-varying forcing, *J. Geophys. Res.*, **116**, D06308, doi:10.1029/2010JD014938.
- Iacono, M. J., J. S. Delamere, E. J. Mlawer, M. W. Shephard, S. A. Clough, and W. D. Collins (2008), Radiative forcing by long-lived greenhouse gases: Calculations with the AER radiative transfer models, *J. Geophys. Res.*, **113**, D13103, doi:10.1029/2008JD009944.
- Ingwersen, J., et al. (2011), Comparison of Noah simulations with eddy covariance and soil water measurements at a winter wheat stand, *Agric. For. Meteorol.*, **151**, 345–355, doi:10.1016/j.agrformet.2010.11.010.
- Ingwersen, J., K. Imkova, P. Högy, and T. Streck (2015), On the use of the post-closure methods uncertainty band to evaluate the performance of land surface models against eddy covariance flux data, *Biogeosciences*, **12**, 2311–2326, doi:10.5194/bg-12-2311-2015.
- Jaeger, E. B., and S. I. Seneviratne (2011), Impact of soil moisture-atmosphere coupling on European climate extremes and trends in a regional climate model, *Clim. Dyn.*, **36**, 1919–1939, doi:10.1002/2013JD020890.
- Janjic, Z. (2002), Nonsingular implementation of the Mellor-Yamada level 2.5 scheme in the NCEP meso model, NCEP Office Note, No. 437, National Centres for Environmental Prediction, 61 p. [Available at <http://www.emc.ncep.noaa.gov/officenotes/newernotes/on437.pdf>].
- Jarvis, P. G. (1976), The interpretation of the variations in leaf water potential and stomatal conductance found in canopies in the field, *Philos. Trans. R. Soc. B*, **273**, 593–610, doi:10.1098/rstb.1976.0035.
- Jeričević, A., and B. Grisogono (2006), The critical bulk Richardson number in urban areas: Verification with application in a numerical weather prediction model, *Tellus*, **58A**, 19–27, doi:10.1111/j.1600-870.2006.00153.x.
- Jiménez, P. A., J. Dudhia, J. F. González-Rouco, J. Navarro, J. P. Montávez, and E. García-Bustamante (2012), A revised scheme for the WRF surface layer formulation, *Mon. Weather Rev.*, **140**, 898–918, doi:10.1175/MWR-D-11-00056.1.
- Kain, J. S. (2004), The Kain-Fritsch convective parameterization: An update, *J. Appl. Meteorol. Climatol.*, **43**, 170–181, doi:10.1175/1520-0450(2004)043<0170:TKCPAU>2.0.CO;2.
- Koster, R. D., et al. (2006), GLACE: The global land-atmosphere coupling experiment. Part I: Overview, *J. Hydrometeorol.*, **7**, 590–610, doi:10.1175/JHM510.1.
- LeMone, M. A., M. Tewari, F. Chen, and J. Dudhia (2013), Objectively determined fair-weather CBL depths in the ARW-WRF model and their comparison to CASES-97 observations, *Mon. Weather Rev.*, **141**, 30–54, doi:10.1175/MWR-D-12-00106.1.
- Lenderink, G., and E. van Meijgaard (2008), Increase in hourly precipitation extremes beyond expectations from temperature changes, *Nat. Geosci.*, **1**, 511–514, doi:10.1038/ngeo262.
- Lenschow, D. H., J. Mann, and L. Kristensen (1994), How long is long enough when measuring fluxes and other turbulence statistics?, *J. Atmos. Oceanic Technol.*, **11**, 661–673, doi:10.1175/1520-0426(1994)011<0661:HLILEW>2.0.CO;2.
- Lenschow, D. H., M. Lothon, S. D. Mayor, P. P. Sullivan, and G. Canut (2012), A comparison of higher-order vertical velocity moments in the convective boundary layer from lidar with in situ measurements and large-eddy simulation, *Boundary Layer Meteorol.*, **143**, 107–123, doi:10.1007/s10546-011-9615-3.
- Liu, S., and X.-Z. Liang (2010), Observed diurnal cycle climatology of planetary boundary layer height, *J. Clim.*, **23**, 5790–5809, doi:10.1175/2010JCLI3552.1.
- Mahmood, R., et al. (2013), Land cover changes and their biogeophysical effects on climate, *Int. J. Climatol.*, **34**, 929–953, doi:10.1002/joc.3736.
- Mahrt, L., and M. Ek (1984), The influence of atmospheric stability on potential evaporation, *J. Climate Appl. Meteorol.*, **23**, 222–234, doi:10.1175/1520-0450(1984)023<0222:TIOASO>2.0.CO;2.
- Mellor, G. L., and T. Yamada (1974), A hierarchy of turbulence closure models for planetary boundary layers, *J. Atmos. Sci.*, **31**, 1791–1806, doi:10.1175/1520-0469(1974)031<1791:AHOTCM>2.0.CO;2.
- Mellor, G. L., and T. Yamada (1982), Development of a turbulence closure model for geophysical fluid problems, *Rev. Geophys. Space Phys.*, **20**, 851–875, doi:10.1029/RG020i004p00851.
- Milovac, J., J. Ingwersen, and K. Warrach-Sagi (2014a), Soil texture forcing data for the whole world for the Weather Research and Forecasting (WRF) Model of the University of Hohenheim (UHOH) based on the Harmonized World Soil Database (HWSD) at 30 arc-second horizontal resolution, World Data Centre for Climate (WDCC), doi:10.1594/WDCC/WRF_NOAH_HWSD_world_TOP_SOILTYP.
- Milovac, J., J. Ingwersen, and K. Warrach-Sagi (2014b), Top soil texture forcing data for the area of Germany for the Weather Research and Forecasting (WRF) model based on the Bodenerhebungs-karte (BUK) at a scale 1:1000000 (BUK1000) and provided by the University of Hohenheim (UHOH), World Data Centre for Climate (WDCC), doi:10.1594/WDCC/WRF_NOAH_BUK_Ger_top_SOILTYP.
- Misenis, C., and Y. Zhang (2010), An examination of sensitivity of WRF/Chem predictions to physical parameterizations, horizontal grid spacing, and nesting options, *Atmos. Res.*, **97**, 315–334, doi:10.1016/j.atmosres.2010.04.005.
- Moeng, C.-H., and P. P. Sullivan (1994), A comparison of shear- and buoyancy-driven planetary boundary layer flows, *J. Atmos. Sci.*, **51**, 999–1022, doi:10.1175/1520-0469(1994)051<0999:ACOSAB>2.0.CO;2.
- Morrison, H., J. A. Curry, and V. I. Khvorostyanov (2005), A new double-moment microphysics parameterization for application in cloud and climate models. Part I: Description, *J. Atmos. Sci.*, **62**, 1665–1677, doi:10.1175/JAS3446.1.
- Muppa, S. K., A. Behrendt, F. Späth, V. Wulfmeyer, S. Metzendorf, and A. Riede (2015), Turbulent humidity fluctuations in the convective boundary layer: Case studies using water vapour differential absorption lidar measurements, *Boundary Layer Meteorol.*, doi:10.1007/s10546-015-0078-9.

- Nakanishi, M., and H. Niino (2009), Development of an improved turbulence closure model for the atmospheric boundary layer, *J. Meteorol. Soc. Jpn.*, **87**, 895–912, doi:10.1029/RG020i004p00851.
- Nielsen, J. R., D. Ebba, A. N. Hahmann, and E. Boegh (2013), Representing vegetation processes in hydrometeorological simulations using the WRF model, DTU Wind Energy, 128 p., (Riso – PhD; No. 0016(EN)).
- Niu, G. Y., et al. (2011), The community Noah land surface model with multiparameterization options (Noah-MP): 1. Model description and evaluation with local-scale measurements, *J. Geophys. Res.*, **116**, D12109, doi:10.1029/2010JD015139.
- Pal, S., A. Behrendt, and V. Wulfmeyer (2010), Elastic-backscatter-lidar-based characterization of the convective boundary layer and investigation of related statistics, *Ann. Geophys.*, **28**, 825–847, doi:10.5194/angeo-28-825-2010.
- Pino, D., H. Jonker, J. Vilà-Guerau De Arellano, and A. Dosio (2006), Role of shear and the inversion strength during sunset turbulence over land: Characteristic length scales, *Boundary Layer Meteorol.*, **121**, 537–556, doi:10.1007/s10546-006-9080-6.
- Pleim, J. E. (2007), A combined local and nonlocal closure model for the atmospheric boundary layer. Part I: Model description and testing, *J. Appl. Meteorol. Climatol.*, **46**, 1383–1395, doi:10.1175/JAM2539.1.
- Radlach, M., A. Behrendt, and V. Wulfmeyer (2008), Scanning rotational Raman lidar at 355 nm for the measurement of tropospheric temperature fields, *Atmos. Chem. Phys.*, **8**, 159–169, doi:10.5194/acp-8-159-2008.
- Rasmussen, S. H., M. B. Butts, S. M. Lerer, and J. C. Refsgaard (2012), Parameterization and scaling of the land surface model for use in a coupled climate-hydrological model, *J. Hydrol.*, **426**–427, 63–78, doi:10.1016/j.jhydrol.2012.01.014.
- Sanchez, P., S. Ahmed, and F. Carré (2009), Digital soil map of the world, *Science*, **325**, 680–681, doi:10.1126/science.1175084.
- Santanello, J. A., C. D. Peters-Lidard, S. V. Kumar, C. Alonge, and W. K. Tao (2009), A modeling and observational framework for diagnosing local land-atmosphere coupling on diurnal time scales, *J. Hydrometeorol.*, **10**, 577–599, doi:10.1175/2009JHM1066.1.
- Santanello, J. A., C. D. Peters-Lidard, and S. V. Kumar (2011), Diagnosing the sensitivity of local land-atmosphere coupling via the soil moisture-boundary layer interaction, *J. Hydrometeorol.*, **12**, 766–786, doi:10.1175/JHM-D-10-05014.1.
- Santanello, J. A., C. D. Peters-Lidard, A. Kennedy, and S. V. Kumar (2013), Diagnosing the nature of land-atmosphere coupling: A case study of dry/wet extremes in the U.S. Southern Great Plains, *J. Hydrometeorol.*, **14**, 3–24, doi:10.1175/JHM-D-12-023.1.
- Seibert, P. (2000), Review and intercomparison of operational methods for the determination of the mixing height, *Atmos. Environ.*, **34**, 1001–1027, doi:10.1016/S1352-2310(99)00349-0.
- Seidel, D. J., C. O. Ao, and K. Li (2010), Estimating climatological planetary boundary layer heights from radiosonde observations: Comparison of methods and uncertainty analysis, *J. Geophys. Res.*, **115**, D16113, doi:10.1029/2009JD013680.
- Seneviratne, S. I., T. Corti, E. L. Davin, M. Hirschi, E. B. Jaeger, I. Lehner, B. Orlowsky, and A. J. Teuling (2010), Investigating soil moisture-climate interactions in a changing climate: A review, *Earth Sci. Rev.*, **99**, 125–161, doi:10.1016/j.earscirev.2010.02.004.
- Sherwood, S. C., R. Roca, T. M. Weckwerth, and N. G. Andronova (2010), Tropospheric water vapor, convection, and climate, *Rev. Geophys.*, **48**, RG2001, doi:10.1029/2009RG000301.
- Shin, H. H., and S. Y. Hong (2011), Intercomparison of planetary boundary layer parameterizations in the WRF model for a single day from CASES-99, *Boundary Layer Meteorol.*, **139**, 261–281, doi:10.1007/s10546-010-9583-z.
- Skamarock, W. C., J. B. Klemp, J. Dudhia, D. O. Gill, D. M. Barker, M. Duda, X. Y. Huang, W. Wang, and J. G. Powers (2008), A description of the advanced research WRF version 3, *NCAR Tech. Note*, doi:10.5065/D6854MVH.
- Späth, F., S. Metzendorf, A. Behrendt, H. D. Wizemann, G. Wagner, and V. Wulfmeyer (2013), Online/offline injection seeding system with high frequency-stability and low crosstalk for water vapor DIAL, *Opt. Commun.*, **309**, 37–43, doi:10.1016/j.optcom.2013.07.003.
- Späth, F., A. Behrendt, S. K. Muppa, S. Metzendorf, A. Riede, and V. Wulfmeyer (2014), High-resolution atmospheric water vapor measurements with a scanning differential absorption lidar, *Atmos. Chem. Phys. Discuss.*, **14**, 29,057–29,099, doi:10.5194/acpd-14-29057-2014.
- Stéfanon, M., P. Drobinski, F. D'Andrea, C. Lebeaupin-Brossier, and S. Bastin (2014), Soil moisture-temperature feedbacks at meso-scale during summer heat waves over Western Europe, *Clim. Dyn.*, **42**, 1309–1324, doi:10.1007/s00382-013-1794-9.
- Stull, R. B. (1988), *An Introduction to Boundary Layer Meteorology*, 666 pp., Kluwer Acad., Dordrecht, doi:10.1017/S0016756800022433.
- Taylor, C. M., R. A. M. de Jeu, F. Guichard, P. P. Harris, and W. A. Dorigo (2012), Afternoon rain more likely over drier soils, *Nature*, **489**(7416), 423–426, doi:10.1038/nature11377.
- Teixeira, J., and S. Cheinet (2004), A simple mixing length formulation for the eddy-diffusivity parameterization of dry convection, *Boundary Layer Meteorol.*, **110**, 435–453, doi:10.1029/2003GL017377.
- Tucker, S. C., C. J. Senff, A. M. Weickmann, W. A. Brewer, R. M. Banta, S. P. Sandberg, D. C. Law, and R. M. Hardisty (2009), Doppler lidar estimation of mixing height using turbulence, shear, and aerosol profiles, *J. Atmos. Oceanic Technol.*, **26**, 673–688, doi:10.1175/2008JTECHA1157.1.
- Turner, D. D., R. A. Ferrare, L. A. Brasseur, W. F. Feltz, and T. P. Tooman (2002), Automated retrievals of water vapor and aerosol profiles from an operational Raman lidar, *J. Atmos. Oceanic Technol.*, **19**, 37–50, doi:10.1175/1520-0426(2002)019<0037:AROWVA>2.0.CO;2.
- Turner, D. D., R. A. Ferrare, V. Wulfmeyer, and A. J. Scarino (2014), Aircraft evaluation of ground-based Raman lidar water vapor turbulence profiles in convective mixed layers, *J. Atmos. Oceanic Technol.*, **31**, 1078–1088, doi:10.1175/JTECH-D-13-00075.1.
- van der Velde, R., Z. Su, M. Ek, M. Rodell, and Y. Ma (2009), Influence of thermodynamic soil and vegetation parameterizations on the simulation of soil temperature states and surface fluxes by the Noah LSM over a Tibetan plateau site, *Hydrol. Earth Syst. Sci.*, **13**, 759–777, doi:10.5194/hess-13-759-2009.
- Wagner, G., V. Wulfmeyer, and A. Behrendt (2011), Detailed performance modeling of a pulsed high-power single-frequency Ti: Sapphire laser, *Appl. Opt.*, **50**, 5921–5937, doi:10.1364/AO.50.005921.
- Wagner, G., A. Behrendt, V. Wulfmeyer, F. Späth, and M. Schiller (2013), High-power Ti: Sapphire laser at 820 nm for scanning ground-based water-vapor differential absorption lidar, *Appl. Opt.*, **52**, 2454–2469, doi:10.1364/AO.52.002454.
- Warrach-Sagi, K., V. Wulfmeyer, R. Grasselt, F. Ament, and C. Simmer (2008), Streamflow simulations reveal the impact of the soil parameterization, *Meteorol. Z.*, **17**, 751–762, doi:10.1127/0941-2948/2008/0343.
- Weng, W., and P. Taylor (2002), On modelling the one-dimensional atmospheric boundary layer, *Boundary Layer Meteorol.*, **107**, 371–400, doi:10.1023/A:1022126511654.
- Williams, K. D., A. Bodas-Salcedo, M. Déqué, S. Fermepin, B. Medeiros, M. Watanabe, C. Jakob, S. A. Klein, C. A. Senior, and D. L. Williamson (2013), The transpose-AMIP II experiment and its application to the understanding of southern ocean cloud biases in climate models, *J. Clim.*, **26**, 3258–3274, doi:10.1175/JCLI-D-12-00429.1.
- Wulfmeyer, V. (1999a), Investigation of turbulent processes in the lower troposphere with water vapor DIAL and Radar-RASS, *J. Atmos. Sci.*, **56**, 1055–1076, doi:10.1175/1520-0469(1999)056<1055:IOTPT>2.0.CO;2.
- Wulfmeyer, V. (1999b), Investigations of humidity skewness and variance profiles in the convective boundary layer and comparison of the latter with large eddy simulation results, *J. Atmos. Sci.*, **56**, 1077–1087, doi:10.1175/1520-0469(1999)056<1077:IOHSAV>2.0.CO;2.

- Wulfmeyer, V., and T. Janjić (2005), Twenty-four-hour observations of the marine boundary layer using shipborne NOAA high-resolution doppler lidar, *J. Appl. Meteorol.*, *44*, 1723–1744, doi:10.1175/JAM2296.1.
- Wulfmeyer, V., et al. (2008), The convective and orographically-induced precipitation study: A research and development project of the world weather research program for improving quantitative precipitation forecasting in low-mountain regions, *Bull. Am. Meteorol. Soc.*, *89*, 1477–1486, doi:10.1175/2008BAMS2367.1.
- Wulfmeyer, V., S. Pal, D. D. Turner, and E. Wagner (2010), Can water vapor Raman lidar resolve profiles of turbulent variables in the convective boundary layer?, *Boundary Layer Meteorol.*, *136*, 253–284, doi:10.1007/s10546-010-9494-z.
- Wulfmeyer, V., et al. (2011), The Convective and Orographically-induced Precipitation Study (COPS): The scientific strategy, the field phase, and research highlights, *Q. J. R. Meteorol. Soc.*, *137*, 3–30, doi:10.1002/qj.752.
- Wulfmeyer, V., M. Hardesty, D. D. Turner, A. Behrendt, M. Cadetdu, P. Di Girolamo, P. Schlüssel, J. van Baelen, and F. Zus (2014a), A review of the remote sensing of lower-tropospheric thermodynamic profiles and its indispensable role for the understanding and the simulation of water and energy cycles, *Rev. Geophys.*, doi:10.1002/2014RG000476.
- Wulfmeyer, V., K. Warrach-Sagi, T. Schmitalla, H. S. Bauer, and J. Milovac (2014b), Towards seamless mesoscale prediction of the land system for Europe, The World Weather Open Science Conference, Montreal, Canada, August 16–21.
- Wulfmeyer, V., et al. (2015), New concepts for studying land-surface-atmosphere feedback based on a new lidar synergy and grey zone simulations, EGU General Assembly, EGU2015-5054, Vienna, Austria, April 12–17.
- Xie, B., J. C. H. Fung, A. Chan, and A. Lau (2012), Evaluation of nonlocal and local planetary boundary layer schemes in the WRF model, *J. Geophys. Res.*, *117*, D12103, doi:10.1029/2011JD017080.
- Xie, B., J. C. R. Hunt, D. J. Carruthers, J. C. H. Fung, and J. F. Barlow (2013), Structure of the planetary boundary layer over Southeast England: Modeling and measurements, *J. Geophys. Res. Atmos.*, *118*, 7799–7818, doi:10.1002/jgrd.50621.
- Yang, Z. L., et al. (2011), The community Noah land surface model with multiparameterization options (Noah-MP): 2. Evaluation over global river basins, *J. Geophys. Res.*, *116*, D12110, doi:10.1029/2010JD015140.
- Zhang, Y., Z. Gao, D. Li, Y. Li, N. Zhang, X. Zhao, and J. Chen (2014), On the computation of planetary boundary layer height using the bulk Richardson number method, *Geosci. Model Dev. Discuss.*, *7*, 4045–4079, doi:10.5194/gmd-7-2599-2014.
- Zolina, O., C. Simmer, K. Belyaev, S. K. Gulev, and P. Koltermann (2013), Changes in the duration of european wet and dry spells during the last 60 years, *J. Clim.*, *26*, 2022–2047, doi:10.1175/JCLI-D-11-00498.1.

Erratum

In the originally published version of this article, the article title incorrectly contained the word “laser” instead of the word “lidar.” The article title has since been corrected and this version may be considered the authoritative version of record.

Turbulent Humidity Fluctuations in the Convective Boundary Layer: Case Studies Using Water Vapour Differential Absorption Lidar Measurements

Shravan Kumar Muppa¹ · Andreas Behrendt¹ · Florian Späth¹ ·
Volker Wulfmeyer¹ · Simon Metzendorf¹ · Andrea Riede¹

Received: 24 October 2014 / Accepted: 26 August 2015 / Published online: 9 September 2015
© The Author(s) 2015. This article is published with open access at Springerlink.com

Abstract Turbulent humidity fluctuations in the convective boundary layer (CBL) under clear-sky conditions were investigated by deriving moments up to fourth-order. High-resolution humidity measurements were collected with a water vapour differential absorption lidar system during the HD(CP)² Observational Prototype Experiment (HOPE). Two cases, both representing a well-developed CBL around local noon, are discussed. While the first case (from the intensive observation period (IOP) 5 on 20 April 2013) compares well with what is considered typical CBL behaviour, the second case (from IOP 6 on 24 April 2013) shows a number of non-typical characteristics. Both cases show similar capping inversions and wind shear across the CBL top. However, a major difference between both cases is the advection of a humid layer above the CBL top during IOP 6. While the variance profile of IOP 5 shows a maximum at the interfacial layer, two variance peaks are observed near the CBL top for IOP 6. A marked difference can also be seen in the third-order moment and skewness profiles: while both are negative (positive) below (above) the CBL top for IOP 5, the structure is more complex for IOP 6. Kurtosis is about three for IOP 5, whereas for IOP 6, the distribution is slightly platykurtic. We believe that the entrainment of an elevated moist layer into the CBL is responsible for the unusual findings for IOP 6, which suggests that it is important to consider the structure of residual humidity layers entrained into the CBL.

Keywords Convective boundary layer · Differential absorption lidar · Skewness · Turbulence · Variance profiles

1 Introduction

Turbulence is responsible for the vertical transport of heat and moisture in the convective boundary layer (CBL). The fluxes of heat and moisture have been investigated quite exten-

✉ Shravan Kumar Muppa
shravan.muppa@uni-hohenheim.de

¹ Institute of Physics and Meteorology, University of Hohenheim, Garbenstrasse 30, 70599 Stuttgart, Germany

sively in the surface layer near the ground (Stull 1988), but remain poorly understood in the upper part of the CBL and especially at the interface of the CBL and the free troposphere, the so-called interfacial layer, where turbulent fluctuations are greatest due to entrainment (Kaimal et al. 1976). An adequate representation of the thermodynamic structure of the CBL in atmospheric models is critical; moisture transport across the CBL influences not only the formation of fair-weather cumuli (Zhu and Albrecht 2002) but also the initiation of deep convection and flash floods (Weckwerth 2000; Behrendt et al. 2011; Corsmeier et al. 2011; Stevens and Bony 2013). Consequently, several large international experiments aimed at a better understanding of the humidity field in the CBL have been carried out, e.g. the Mesoscale Alpine Program for high mountains during the 1990s (Richard et al. 2007); the International H₂O Project (IHOP_2002) in 2002 (Weckwerth et al. 2004), and the Convective and Orographically-induced Precipitation Study (COPS) in 2007 (Wulfmeyer et al. 2011). Recently, the High Definition Clouds and Precipitation for advancing Climate Prediction (HD(CP)²) project was initiated in Germany, which has a goal to investigate whether the simulation of clouds and precipitation can be improved by finer grid increments of the order of 1 km or less (see www.hdcp2.eu). The HD(CP)² Observation Prototype Experiment (HOPE), conducted in spring 2013, was dedicated to providing high resolution datasets of meteorological variables at the subgrid scale that are subject to parametrizations in the high resolution models of HD(CP)².

Studies based on large-eddy simulation (LES) have been widely used to investigate the characteristics of turbulence in the CBL (Deardorff 1974; Deardorff et al. 1980; Wyngaard and Brost 1984; Moeng and Wyngaard 1984; Sorbjan 1996, 1999, 2006; Sullivan et al. 1998). For improved turbulence parametrization schemes, general scaling relationships between the higher-order moments of temperature and humidity fluctuations in the CBL and their vertical gradients in the interfacial layer need to be investigated (Sorbjan 2005; Wulfmeyer et al. 2015). However, present LES studies show a significant uncertainty in their results due to processes at the subgrid scale (Stevens and Lenschow 2001; Zhou et al. 2014). Sullivan and Patton (2011) have shown that turbulent eddies in the middle of the CBL can be resolved with horizontal and vertical grid lengths of 25 m, but there are still significant challenges in modelling the entrainment zone where an even higher resolution is required. This underlines the importance of validating the LES results with corresponding measurements. Vertical motions and their effect on the entrainment in the CBL have been investigated (Hogan et al. 2009; Lenschow et al. 2012), but studies focusing on water vapour exchange at the CBL top are sparse. Recently, Moeng and Arakawa (2012) highlighted the importance of moisture transport at the subgrid scale in the planetary boundary layer (PBL) with respect to cloud-resolving models.

Earlier observations of the humidity structure in the CBL were mainly based on aircraft in situ data and radiosondes. The latter provide a snapshot of the CBL profile and thus do not capture the mean profiles needed for comparisons with models (Weckwerth et al. 1996) nor can they provide information on turbulent fluctuations. The characteristics of humidity fluctuations in the CBL have been studied using in situ measurements (Mahrt 1976, 1991; Lenschow et al. 1994) and active remote sensing techniques, particularly water vapour differential absorption lidar (DIAL) (Kiemle et al. 1997; Wulfmeyer 1999a, b; Giez et al. 1999; Behrendt et al. 2011) and water vapour Raman lidar (Wulfmeyer et al. 2010; Turner et al. 2014). Airborne measurements reveal spatially-averaged properties of the CBL but only at low vertical resolution. Furthermore, the operation of research aircraft is expensive and simultaneous observations at all heights in the CBL are not possible. Remote sensing techniques overcome these limitations and cover larger ranges simultaneously and continuously. Monitoring moisture fluctuations with high resolution for turbulence studies is a challenging

task due to the noise limitation of these instruments; nevertheless, new techniques based on lidar are capable of providing data with sufficient precision and accuracy (Lenschow et al. 2000; Wulfmeyer et al. 2010, 2015).

Couvreur et al. (2005) compared the results of airborne water vapour DIAL measurements from the IHOP campaign with LES for a growing CBL. They found in both observations and LES that dry downdrafts entrained from above the CBL govern the integral scale of moisture variability in the CBL. Later, this study was further extended to the analysis of skewness profiles (Couvreur et al. 2007), showing that dry tongues contribute significantly to the turbulent transport from the top of the CBL into its interior. Wind shear at the interfacial layer also plays an important role in the dynamics and growth of the CBL (Conzemius and Fedorovich 2006; Sorbjan 2006; Fedorovich and Conzemius 2008; Wulfmeyer et al. 2015). However, the role of wind shear on the profile of humidity variance and skewness in the CBL has so far not been investigated in detail. Furthermore, there are only a few studies discussing the influence of elevated dry and moist layers on the turbulent humidity fluctuations and their statistics. Van Heerwaarden et al. (2009) underlined the importance of accurate moisture profiles to properly represent dry air entrainment for understanding cloud formation under moist and dry tropospheric conditions. Recently, Bennett et al. (2010) investigated the vertical and horizontal distributions of humidity in the nocturnal boundary layer (NBL), as well as the evolution and growth of the CBL during the formation of open-cell convection. They found that the advection of drier air into the region resulted in a humidity minimum in the middle and a peak at the top of the residual layer. Grossman and Gamage (1995) observed similar drying in the lower part of the mixed layer and moistening at the top, when an elevated mixed layer was entrained into the CBL. In the current study, we use high-resolution observations to investigate the role of turbulent processes in the CBL humidity structure during such cases.

We present results obtained with recent data from our ground-based, scanning water vapour DIAL system (Wagner et al. 2013). Whereas it is also possible to derive higher-order moments with water vapour Raman lidar, Wulfmeyer et al. (2010) and Turner et al. (2014) demonstrated that the noise level in daytime turbulence profiles is much larger than for water vapour DIAL. Therefore, water vapour Raman lidar turbulence profiles are strongly limited to measurements of third- and fourth-order moments. Our water vapour DIAL uses a high power laser and a very efficient receiver that yields high-resolution data with low noise in the CBL including the interfacial layer. For the two CBL cases presented, turbulent moments were derived from water vapour DIAL data, including reliable skewness, fourth-order, and kurtosis profiles. We further discuss the effect of boundary-layer height, entrainment zone thickness, humidity gradient across the CBL top, and surface latent heat fluxes on the humidity variance profile in the CBL.

This paper is structured as follows. In Sect. 2, we provide a short description of the measurement campaign HOPE, with details of the DIAL system used for the measurements and the properties important for the retrieval of absolute humidity from DIAL given in Sect. 3. A detailed overview of meteorological conditions during the two intensive observation periods (IOPs) selected is given in Sect. 4. The case studies presented here focus on a well-developed CBL under different forcing conditions. Section 5 describes the methodology for deriving the higher-order moments and in Sect. 6, higher-order moments such as the variance, skewness, and kurtosis are presented for both cases. Our findings are compared with previous studies based on observations and LES and are discussed in Sect. 7. Finally, the results are summarized in Sect. 8.

2 The HOPE Campaign

A new model for high-resolution weather forecasts will be developed and verified in the HD(CP)² project. The main aim of the HOPE campaign was to collect high-resolution datasets that will be used for the HD(CP)² model initialization and output evaluation. The Institute of Physics and Meteorology (IPM) of University of Hohenheim (UHOH) operated its water vapour DIAL system at a site close to the village of Hambach near the research centre Jülich, Germany, at 50°53′50.56″N, 6°27′50.39″E, 110 m above sea level. In addition to the DIAL, IPM used a rotational Raman lidar for temperature measurements (Hammann et al. 2015; Behrendt et al. 2015) and the Karlsruhe Institute of Technology (KIT) operated its KITcube (Kalthoff et al. 2013), a suite of instruments including a Doppler lidar (Trümner et al. 2014), at the same site. Radiosondes were launched at this site regularly at 1100 and 2300 UTC during the HOPE campaign and more often during IOPs. In addition to the so-called supersite near Hambach, there were two more supersites in the HOPE area forming a triangle of about 4-km side length, but none of the other sites was equipped with a water vapour DIAL.

3 The UHOH Water Vapour DIAL System

The water vapour DIAL system is a unique remote sensing tool for deriving absolute humidity profiles with high temporal and spatial resolution in the lower troposphere (Wulfmeyer and Bösenberg 1998). During the HOPE campaign, the DIAL system was operated in the vertical steering mode during clear sky conditions and in scanning mode during cloudy periods. In total, the instrument collected 180 h of data during 18 IOP days with the focus on water vapour in the CBL. A detailed description of the UHOH DIAL system set-up during HOPE and the derivation of water vapour profiles is given in Späth et al. (2015). The operational wavelength of the UHOH DIAL is around 818 nm, and the backscatter signals were recorded for each laser shot (250 Hz) with a range resolution of 15 m up to a range of 30 km. The laser transmitter was switched in each shot between the online and offline frequencies. The measured absolute humidity has typical temporal and spatial resolutions of 1 s to 1 min and 15 to 300 m, respectively, depending on the range of interest. Due to the instrument's high laser power (about 2 W) in combination with a very efficient receiver (0.8-m telescope), the data have low noise errors up to the CBL top.

For the derivation of absolute humidity profiles, the following DIAL system and atmospheric properties are important: (1) the laser spectral properties with respect to frequency stability, bandwidth, and spectral purity, (2) the profile of the water vapour absorption cross-section, (3) the temporal variability of the aerosol backscatter coefficient between the online and offline laser pulses, and (4) the Rayleigh–Doppler effect (Ansmann 1985).

All these issues have been taken into account in our system design and methodology to derive accurate humidity profiles including a detailed error analysis. Concerning (1), the laser transmitter is based on an injection-seeding technology. Wagner et al. (2013) demonstrated that the UHOH DIAL transmitter has excellent spectral properties so that remaining systematic errors are <3 % throughout the troposphere. With respect to (2), detailed sensitivity analyses of systematic errors in the derivation of the absorption cross-section profile led to an error <1.3 % (with uncertainties of 1 K in temperature and 1 hPa in pressure, respectively) for measurements in the lower troposphere. Tackling issue (3), the delay between the online and the offline laser pulses was 4 ms, which leads to an air volume displacement of only 40 mm at a horizontal wind speed of 10 m s^{−1}. Thus, considering the typical size of an eddy of several tens of m and a beam radius of 0.35 m at a height of 500 m above ground level, the

10-s averages of online and offline backscatter coefficients are virtually the same. Therefore, systematic errors in the derivation of absolute humidity profiles due to (3) are negligible. The backscatter profiles were used to determine the instantaneous CBL top height with the Haar wavelet technique (Davis et al. 2000; Pal et al. 2010). Its average over the measurement period is an excellent approximation for the mean CBL top height (z_i), which was used for normalizing the height of the turbulence profiles.

With respect to (4), great care has to be taken in the analysis of water vapour DIAL measurements due to Rayleigh–Doppler broadening of the backscattered signal. This effect needs to be considered at height levels where strong gradients in the aerosol backscatter data may be present such as the CBL top or aerosol layers in the free troposphere (Ansmann and Bösenberg 1987; Ismail and Browell 1989). The Rayleigh–Doppler effect can be investigated and corrected with a derived particle backscatter coefficient profile (Fernald 1984) and by determining the Rayleigh–Doppler term in the DIAL equation. With our system set-up, where the online frequency of the water vapour DIAL laser transmitter was tuned at the wing of the water vapour line, the evaluation of the Rayleigh–Doppler term shows a negative correction with a backscatter gradient on the order of 0.4 g m^{-3} (corresponding to a relative correction of about 7 %). At first glance, this may lead to the conclusion that the Rayleigh–Doppler correction is negligible. However, it was found that this correction needs to be applied for accurate profiling of higher-order moments, particularly in the interfacial layer, due to the non-linearity of the correction in the region of the backscatter gradient. Thus, we applied the Rayleigh–Doppler correction to all derivations of water vapour profiles and performed a thorough sensitivity analysis with respect to remaining errors due to the Rayleigh–Doppler correction. For this purpose, we varied the parameters used for deriving the particle backscatter profiles between 20 and 40 sr for the lidar ratio and $0\text{--}10^{-8} \text{ m}^{-1} \text{ sr}^{-1}$ for the initialization of the inversion at a height of 2700 m. We found that the effect of these variations is negligible, e.g. the difference in the derivation of the absolute humidity profiles was $<0.01 \text{ g m}^{-3}$.

A window length of 135 m was used for the Savitzky–Golay (SaGo) algorithm (Savitzky and Golay 1964) when deriving absolute humidity from the UHOH DIAL data. For all turbulence analyses, we used a temporal resolution of 10 s, corresponding to 1250 online and offline laser shots, respectively. The high accuracy of our measurements was also confirmed by several intercomparison campaigns. An extensive comparison between the UHOH water vapour DIAL and six other water vapour lidar systems was performed by Bhawar et al. 2011 during the COPS project, who found a mean bias of 1.4 % for the UHOH water vapour DIAL.

4 Meteorological Conditions

4.1 Case 1: IOP 5, 20 April 2013

For IOP 5, the HOPE domain was in the transition region between an anticyclone with its centre located over the Baltic Sea along the coast of the Netherlands to the south-west and a cold front over the Alps to the south-east. An upper-air warm front was observed to the north. Figure 1 shows the European Centre for Medium-Range Weather Forecasting (ECMWF) reanalysis data at 850 hPa for specific humidity and the horizontal wind vector during both IOPs. For IOP 5, specific humidity at 850 hPa over the measurement site was relatively low and very dry air was advected into the region. Figure 2a shows the particle backscatter coefficient profiles measured with DIAL between 1130 and 1330 UTC for IOP 5. The free troposphere was mainly clear with only very weak aerosol layers; higher aerosol content was

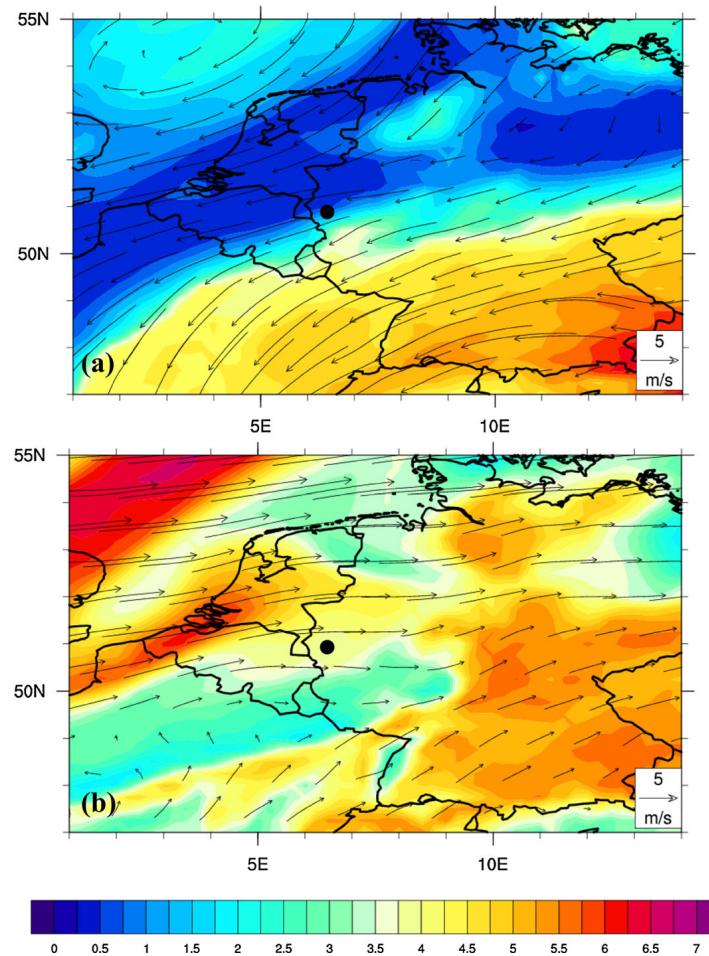


Fig. 1 Meteorological conditions based on ECMWF 850-hPa analysis on **a** 20 April 2013 1200 UTC, **b** 24 April 2013 1200 UTC. Colour scale indicates specific humidity (g kg^{-1}); black arrows represent horizontal wind speed (m s^{-1}). Black dot shows the measurement site

found in the CBL. The period from 1130 to 1330 UTC was selected for the analysis of the higher-order moments and includes local noon at 1134 UTC. The CBL was well developed and became quasi-stationary. Absolute humidity along with the instantaneous CBL top height during the selected period are shown in Fig. 2b. Absolute humidity was around 3.5 g m^{-3} in the CBL at 1130 UTC and then decreased to about 3 g m^{-3} by 1330 UTC. This drying was due to a combination of entrainment of drier air into the CBL and vertical transport of moisture by thermals. The mean of the instantaneous CBL top heights over the selected period, z_i , was 1295 m with a standard deviation of 86 m; the smallest and largest values of the instantaneous CBL heights were 1110 and 1470 m, respectively. We later used the z_i for normalizing the height scales. The mean entrainment zone thickness (EZT) is estimated using the cumulative frequency distribution of the instantaneous CBL top height (Pal et al. 2010). The mean EZT during the period was 73 m. Latent and sensible heat fluxes at the surface were 100 and 255 W m^{-2} during the period selected for the higher-order moment analysis.

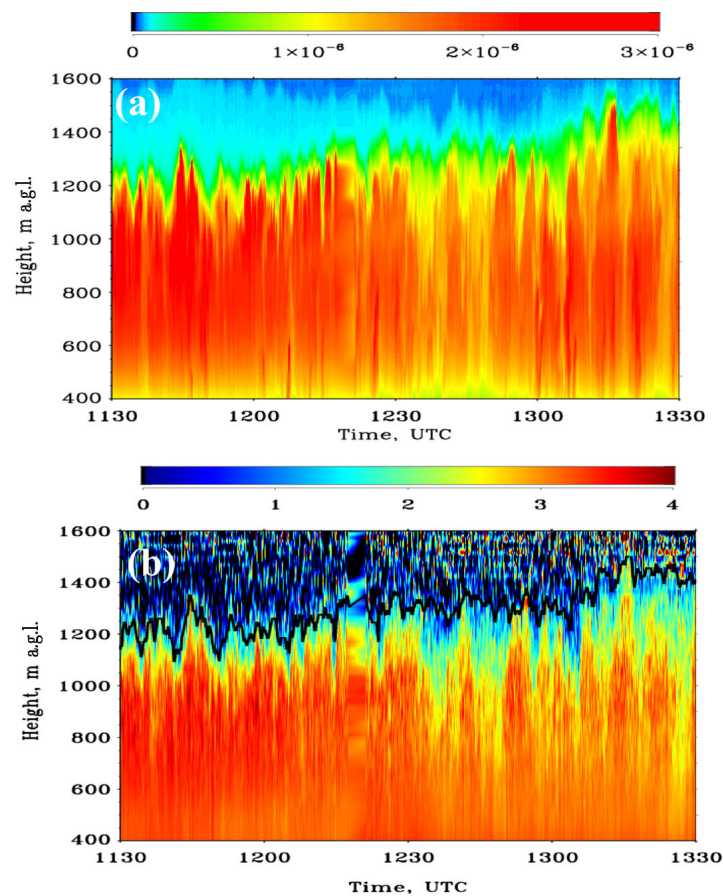


Fig. 2 **a** Particle backscatter coefficient in $\text{m}^{-1}\text{sr}^{-1}$ of the UHOH WVDIAL with resolutions of 10 s and 15 m for IOP 5 on 20 April 2013, 1130–1330 UTC. **b** Absolute humidity measurements in g m^{-3} of the UHOH DIAL (10-s and 67.5-m resolution) for the same period with instantaneous CBL heights shown as a *black solid line*

4.2 Case 2: IOP 6, 24 April 2013

The HOPE domain was under the influence of an anticyclone located over central Europe during IOP 6. The ECMWF 850-hPa specific humidity indicates that moist air was advected from the south-west towards the measurement site (Fig. 1b). Figure 3a shows the UHOH DIAL particle backscatter coefficient for the period from 1100 to 1200 UTC for IOP 6 (same resolutions as Fig. 2a). The CBL was well developed by 1000 UTC, with an elevated aerosol layer found above the CBL top around 1400 m. We selected the period from 1100 to 1200 UTC around local noon for the analysis of higher-order moments. Figure 3b shows the UHOH DIAL absolute humidity during this period, with values in the CBL around 7 g m^{-3} , almost twice as high as for IOP 5. The absolute humidity in the lower free troposphere was around 3.5 g m^{-3} , i.e. much higher than for IOP 5. A dry layer was present at 1100–1200 m around 0900 UTC, with a moist layer above it (1200–1400 m). As the CBL developed, these layers were entrained into the CBL by 1100 UTC. A humidity minimum was found below the CBL top, with humidity increasing above it, similar to observations of

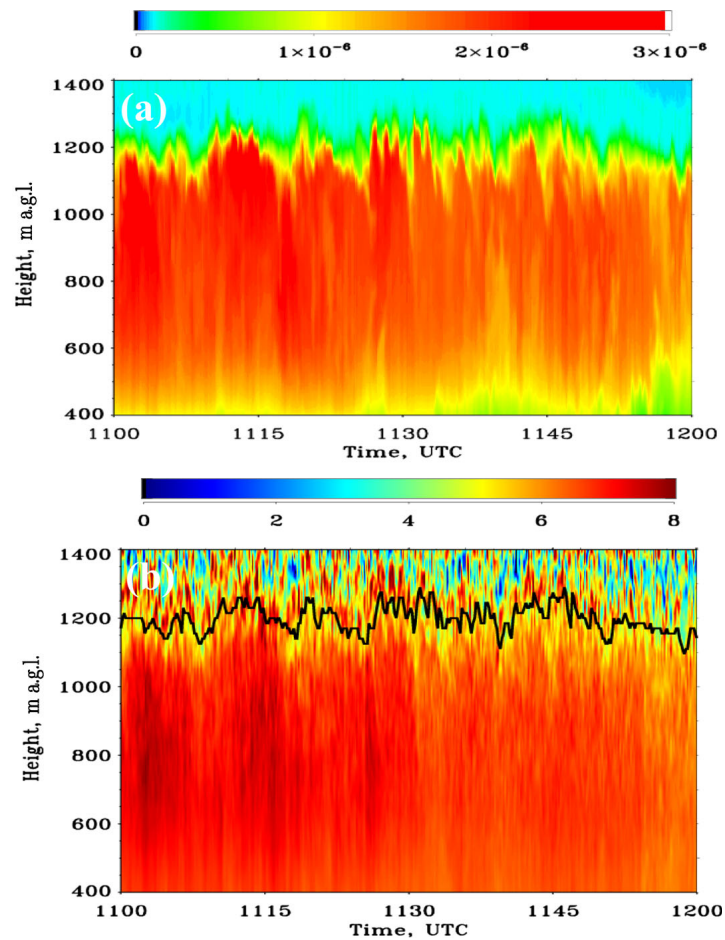


Fig. 3 Same as Fig. 2 but for IOP 6 on 24 April 2013, 1100–1200 UTC

Bennett et al. (2010) where an elevated mixed layer was entrained into the growing CBL during the morning transition period. The mean height of the mixed layer during the selected period was 1200 m with a standard deviation of 39 m and minimum and maximum values of 1125 and 1275 m, respectively. The mean EZT during this period was 36 m. Accordingly, the CBL top was about 100 m lower than for IOP 5 and the spread of the instantaneous CBL top heights was reduced by a factor of two. Sensible heat flux (192 W m^{-2}) was lower and latent heat flux (255 W m^{-2}) was higher for IOP 6 when compared to IOP 5.

4.3 Radiosoundings

Figure 4 shows profiles of various meteorological parameters from radiosoundings launched at the measurement site for IOP 5 at 1300 UTC and for IOP 6 at 1100 UTC. The heights of occurrence of large gradients in the potential temperature and humidity profiles from the radiosondes agree roughly with the z_i values. It should be noted that the radiosonde profiles were measured at specific times while the lidar-derived z_i values are averages over our analysis periods. The characteristics of the two IOP days are summarized in Table 1. The

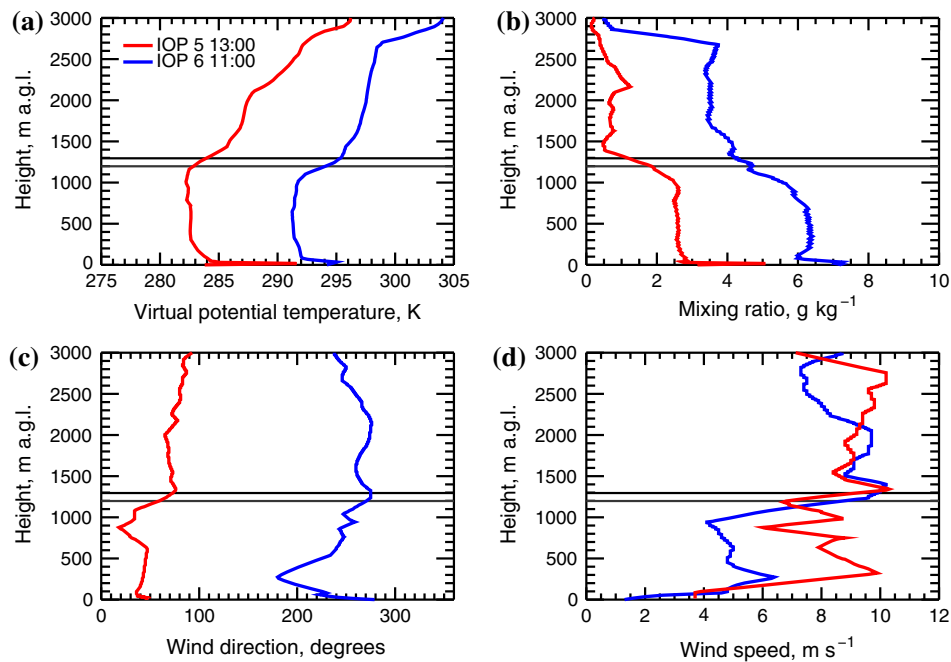


Fig. 4 Profiles of **a** potential temperature, **b** mixing ratio, **c** wind direction, and **d** wind speed from radiosoundings during IOP 5 (1300 UTC, red line) and IOP 6 (1100 UTC, blue line). Black and grey horizontal lines indicate the mean CBL height determined from DIAL data for the turbulence analysis periods of IOP 5 and 6, respectively

Table 1 Main characteristics of the IOPs used in this study—IOP 5 on 20 April 2013 and IOP 6 on 24 April 2013

Parameter	IOP 5 1130–1330 UTC	IOP 6 1100–1200 UTC
Mean CBL top height, z_i (m)	1295 ± 86	1198 ± 39
Convective velocity scale (m s^{-1})	2.1	1.9
Virtual potential temperature, $0.5z_i$ (K)	282	291
Virtual potential temperature, $1.2z_i$ (K)	286	296
Inversion strength (K)	4	5
Mixing ratio, $0.5z_i$ (g kg^{-1})	2.6	6.3
Mixing ratio, $1.2z_i$ (g kg^{-1})	0.5	3.5
Mixing ratio diff across z_i (g kg^{-1})	2.1	2.8
Wind speed, $0.5z_i$ (m s^{-1})	7.0	4.5
Wind speed, $1.2z_i$ (m s^{-1})	10.1	10.3
Wind direction $0.5z_i$ ($^\circ$)	20	250
Wind direction $1.2z_i$ ($^\circ$)	76	270
Shift in wind speed across z_i	3.1	6
Shift in wind direction across z_i	50	20

Units are given in brackets

θ_v profiles of both IOPs show a similar strong capping inversion at z_i of around 4 and 5 K for IOP 5 and 6, respectively. Mixing ratio in the CBL was higher for IOP 6 (6.3 g kg^{-1}) than for IOP 5 (2.6 g kg^{-1}). For IOP 6, a small peak was observed in the mixing ratio profile in the interfacial layer by the radiosonde. The prevailing flow was mainly from the north-east at the surface and veered to the east at the CBL top for IOP 5. At z_i , an increase of 4 m s^{-1} in wind speed and a 50° shift in wind direction was found. For IOP 6, the wind speed was lower ($4 - 6 \text{ m s}^{-1}$) in the CBL and a sharp increase to about 10 m s^{-1} was observed at z_i .

5 Methodology: Turbulence Analyses

Higher-order moments of remote sensing water vapour fluctuation data are an important characteristic of the turbulent structure of the CBL (Wulfmeyer 1999a, b; Kiemle et al. 1997). Lenschow et al. (2000) introduced a procedure for the estimation of higher-order moments that accounts for random instrumental noise. This method was successfully used not only to investigate higher-order moments of water vapour DIAL (Lenschow et al. 2000) but also with water vapour Raman lidar data (Wulfmeyer et al. 2010; Turner et al. 2014), and with Doppler lidar data for vertical velocity (Lenschow et al. 2000; Hogan et al. 2009; Lenschow et al. 2012; Wulfmeyer et al. 2015). More recently, temperature higher-order moments were estimated using rotational Raman lidar data (Behrendt et al. 2015). We follow Lenschow et al. (2000) for resolving the turbulent moments of humidity and for estimating instrument noise errors. A detailed description of this procedure is given in the above reference.

First, humidity data were detrended using a linear fit at each height level to remove influences of large-scale advection, synoptic processes, and the diurnal cycle and to focus on turbulent fluctuations. Time series of humidity observations q were then averaged over the selected periods to obtain mean profiles $\bar{q}(z)$. Mean values were subtracted from the instantaneous humidity values q' at each height to obtain the humidity fluctuations,

$$q'(z, t) = q(z, t) - \bar{q}(z, t), \quad (1)$$

which include the uncorrelated system noise $\varepsilon(z, t)$. It is important to remove the noise for accurate atmospheric measurements. The atmospheric variance σ_a^2 was obtained from the total variance σ_t^2 by determining and then subtracting the noise variance σ_n^2 according to

$$\sigma_a^2 = \sigma_t^2 - \sigma_n^2. \quad (2)$$

The water vapour DIAL instrumental noise variance was estimated by autocovariance analyses of the high-resolution humidity time series data. The autocovariance at zero lag gives the sum of the atmospheric and noise variances. The random instrumental noise is uncorrelated with the atmospheric variance and, by extrapolating a fit to the autocovariance function at non-zero lags to lag zero, the atmospheric variance was obtained,

$$\sigma_n^2 = M_{11}(0) - M_{11}(\tau \rightarrow 0) \equiv M_{11}(0) - \sigma_a^2, \quad (3)$$

where τ is the time lag. According to Monin and Yaglom (1971), the autocovariance function can be approximated by means of the structure function

$$M_{11}(\tau) \approx \sigma_a^2 - C\tau^{2/3} \quad (4)$$

if atmospheric turbulence is sufficiently resolved (Lenschow et al. 2000; Wulfmeyer et al. 2010). Here, C is a scaling parameter, which is related to the turbulent kinetic energy dissipation rate and the rate of the molecular destruction of humidity variance (Wulfmeyer et al. 2015). Using both Eqs. 3 and 4, the variance and noise profiles can be derived simultaneously.

Following the notation that angular brackets denote time averaging and using q'_a for the atmospheric humidity fluctuation, we thus obtained the atmospheric humidity variance,

$$\langle q'_a(z)^2 \rangle = \sigma_a^2(z). \quad (5)$$

The extrapolation of M_{11} to lag zero using the structure function provides a reasonable estimation of the noise variance. It is important to determine the effective number of data points needed for the extrapolation, because too many data points cause a systematic underestimation of the atmospheric variance and vice versa. In our study, a 20-point extrapolation was used for the linear extrapolation and fit of the structure function. This is a reasonable approach because the first zero crossing of the autocovariance function $\tau_0 = 2.5\Pi$, where Π is the integral scale (Behrendt et al. 2015; Wulfmeyer et al. 2015),

$$\Pi = \frac{1}{\langle q_a'^2 \rangle} \int_{\tau \rightarrow 0}^{\tau_0} M_{11}(\tau) d\tau. \quad (6)$$

The integral scale is a measure of the typical energy-containing eddy size in the temporal domain. Thus, by comparing the temporal resolution of the water vapour DIAL measurements with the profile of the integral scale, we can determine whether the temporal resolution is high enough to resolve the major part of the turbulent fluctuations. This was the case during both IOPs (see Sects. 5 and 6). Furthermore, we can determine whether the number of lags is reasonable for the fit of the structure function because this number should not exceed 2.5Π , which was also confirmed in our analyses. The determination of Π is also essential to quantify the uncertainty due to limited sampling of the ensemble of turbulent fluctuations (Lenschow et al. 1994). Relationships between Π and sampling errors of higher-order moments can be found in Lenschow et al. (1994, 2000) with further refinements by Wulfmeyer et al. (2015) and were routinely applied in our data analysis tools as well.

Similarly, the third-order moment (*TOM*) and the fourth-order moment (*FOM*) and their noise errors were computed following Lenschow et al. (2000) and Wulfmeyer et al. (2010) as,

$$TOM = \langle q'_a(z)^3 \rangle, \quad (7)$$

and

$$FOM = \langle q'_a(z)^4 \rangle. \quad (8)$$

The same number of lags was used for the extrapolations; however, due to the unknown shape of higher-order structure functions, a linear fit was used.

Skewness and kurtosis were calculated by normalizing the *TOM* and *FOM* by the variance according to

$$S(z) = \langle q'_a(z)^3 \rangle / (\langle q'_a(z)^2 \rangle)^{3/2}, \quad (9)$$

and

$$K(z) = \langle q'_a(z)^4 \rangle / (\langle q'_a(z)^2 \rangle)^2. \quad (10)$$

The noise error for the accurate determination of atmospheric variance profiles is given by,

$$\Delta \overline{(q'_a)^2} \approx \overline{(q'_a)^2} \sqrt{\frac{4}{N} \frac{\sigma_n^2}{(\overline{(q'_a)^2})^2}}, \quad (11)$$

where N is the number of data points during the observational period (Lenschow et al. 2000). As can be seen from Eq. 11, the relative noise error for the atmospheric variance is proportional to the square root of the ratio of instrumental noise and atmospheric variances. This becomes important for the estimation of the higher-order moments such as the fourth-order moment where the instrument noise levels must be even lower for accurate kurtosis profiles.

6 Results

Comparisons of the averaged absolute humidity measured with the UHOH DIAL during the selected periods and the radiosonde data are shown in Fig. 5. For IOP 5, both DIAL and radiosonde data show similar profile structures and magnitudes for absolute humidity. Good agreement is found up to the CBL top with differences smaller than 0.3 g m^{-3} at each altitude (Fig. 5a). In addition, in the lower free troposphere above, the differences are smaller than 0.5 g m^{-3} . Such close agreements are not necessarily expected, mainly because the radiosonde profile is a line measurement, whereas the DIAL is a spatio-temporal average. For IOP 6 at 1100 UTC, a difference of 0.5 g m^{-3} is observed between DIAL and radiosonde data in the lower CBL (400–600 m). The differences were small in the middle of the CBL (600–1000 m) and increased up to 0.7 g m^{-3} in the interfacial layer. In the lower free troposphere above the CBL top, differences between DIAL and radiosonde data were up to 1.0 g m^{-3} . However, the structure of the absolute humidity profile is similar for both measurements.

The absolute humidity profile of the radiosonde at 0900 UTC for IOP 6 is also shown in Fig. 5b. An elevated humid layer was present between 1200 m and 1400 m above ground level (a.g.l.) approximately 2 h before the period selected for the case study (Fig. 2). Between this elevated humid layer and the moist CBL below, a dry layer was found with a minimum humidity of 3.6 g m^{-3} at 1170 m AGL. By 1100 UTC, this dry layer and the elevated moist layer above had been entrained into the CBL. The mean DIAL profile at 1100 UTC shows that absolute humidity decreased from 7 to 6 g m^{-3} between 400 and 950 m. A sharp decrease by 1 g m^{-3} was observed from 950 to 1100 m. Around 1100–1200 m (near z_i), absolute humidity was found to be constant. Above z_i , another decrease by 2 g m^{-3} was observed between 1200 and 1400 m. At the same-time, a maximum in the humidity profile was observed in the radiosonde data around 1200 m AGL. We believe that this absolute humidity structure influenced the higher-order moment profiles in the interfacial layer during IOP 6 (see Sect. 6). The absolute humidity gradient shows a minimum near the CBL top, as well as two maxima, one below and the other above the CBL top around 1100 and 1300 m, respectively.

6.1 Integral Scale

Integral time scale (Π) profiles were calculated using Eq. 6 and are shown for both IOPs in Fig. 6a together with their statistical uncertainty. For IOP 5, the Π values in the CBL range between 60 s and 130 s. The Π values are larger at about 130 s in the lower CBL ($0.3z_i$), and decrease to 70 s at $0.5z_i$. An increase in Π from 70 s to 100 s up to $0.7z_i$ can be seen. Another decrease to 50 s is found at the CBL top. Similar to IOP 5, Π values range between 60 s and 100 s for IOP 6 in the CBL. In the middle of the CBL, Π is around 100 s and a gradual decrease to 60 s with height up to the CBL top is observed. For both IOPs, an increase of Π can be seen in the interfacial layer. According to Taylor's hypothesis of frozen turbulence

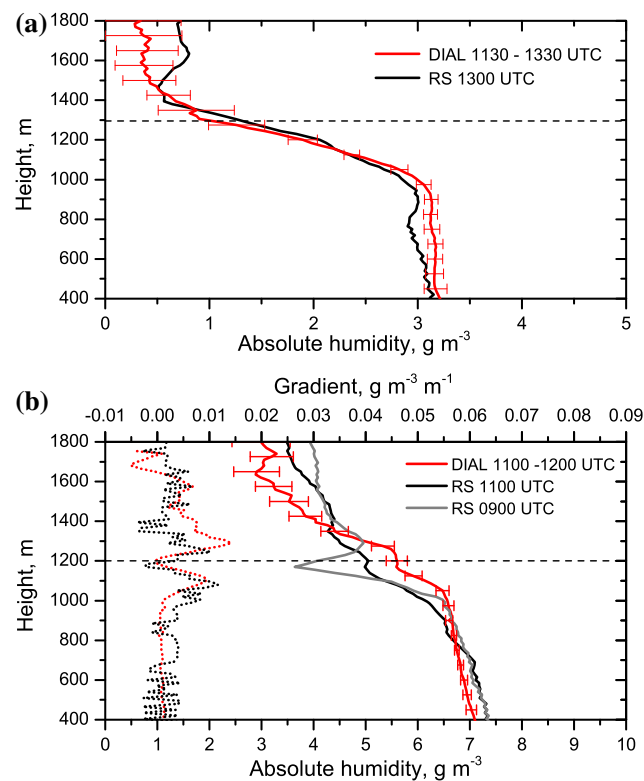


Fig. 5 Averaged DIAL absolute humidity profiles with noise errors and radiosondes during the case study periods IOP 5 (a) and IOP 6 (b), respectively. Gradients of absolute humidity profiles measured with DIAL and radiosonde at 1100 UTC for IOP 6 are also shown. Mean CBL top heights are shown as horizontal dashed lines

(Taylor 1938), the integral length scale of the eddies can be estimated by multiplying Π with the corresponding horizontal wind speed at each height. This is valid if the mean CBL wind speed is large enough to advect the air mass through the laser beam at a time scale smaller than the eddy turnover time. The eddy turnover time for IOP 5 and IOP 6 was 1280 s and 805 s, respectively. Horizontal wind profiles from the radiosondes (Fig. 3d) confirm the validity of Taylor's hypothesis for our case and are used here to estimate the integral length scale. The integral length scales normalized by the CBL depth for both IOPs are shown in Fig. 6b; both profiles roughly show a decrease in eddy size from $0.3z_i$ to $0.8z_i$ and an increase in the interfacial layer. For IOP 5, integral length scale for the eddy size is around $1.0z_i$ in the lower CBL and decreases to $0.3z_i$ at the CBL top, whereas for IOP 6, it decreases from $0.4z_i$ to $0.3z_i$. The integral length scale profiles show slightly larger values around $1.0 - 0.6z_i$ in the middle of the CBL ($0.3 - 0.5z_i$) for IOP 5, compared to previous results of less than $0.4z_i$ in the mid-CBL (Couvreur et al. 2005). The decrease of integral length scale with height is similar to previous observations (Kiemle et al. 1997; Wulfmeyer et al. 2010; Turner et al. 2014) and LES results (de Roode et al. 2004). Eddy size decreases with height mainly due to the entrainment of dry tropospheric air into the CBL (Couvreur et al. 2005). The values for the integral time scale are indeed several times larger than the 10-s temporal resolution of the data used, which again confirms that the resolution is high enough to resolve the inertial subrange.

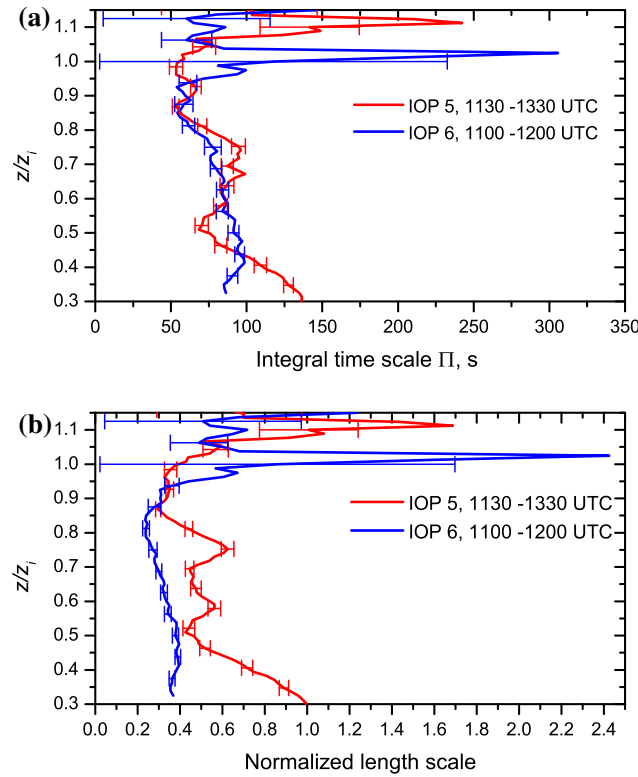


Fig. 6 **a** Integral time scale and **b** normalized length scale, which was obtained by dividing the integral length scale by the mean CBL top height of absolute humidity fluctuations with noise errors for the analysis periods of IOP 5 and IOP 6, respectively

6.2 Variance

The vertical profiles of humidity variance with noise and sampling errors for both IOPs are shown in Fig. 7. In the middle of the CBL, between $0.3z_i$ and $0.8z_i$, the variance is low for both IOPs with values $<0.1 \text{ g}^2 \text{ m}^{-6}$. An increase with height can be seen in the variance profiles for both IOPs in the CBL with a maximum in the interfacial layer. For IOP 5, the variance increases near z_i to a maximum of about $0.39 \pm 0.03 \pm 0.05 \text{ g}^2 \text{ m}^{-6}$. The first and the second error values here and in subsequent sections denote the sampling error and noise error, respectively (see Lenschow et al. 2000). Interestingly, two peaks are observed in the interfacial layer for IOP 6: a small and broad peak of $0.18 \pm 0.03 \pm 0.01 \text{ g}^2 \text{ m}^{-6}$ around $0.95z_i$ and a larger peak of $0.54 \pm 0.10 \pm 0.09 \text{ g}^2 \text{ m}^{-6}$ at $1.1z_i$. Variance in the lower CBL is larger for IOP 6 than for IOP 5. The increase of humidity variance in the CBL with a maximum in the interfacial layer found for IOP 5 can be considered as a typical profile, because it is similar to most cases found in the literature (e.g. Moeng and Wyngaard 1989). However, the variance profile for IOP 6, with its two distinct peaks in the interfacial layer, is unusual.

6.3 Third-order Moment and Skewness

The third-order moment (*TOM*) profile measures the asymmetry in the eddy structure. The *TOM* profiles for IOP 5 and IOP 6 are shown in Fig. 8. For IOP 5, the *TOM* profile shows val-

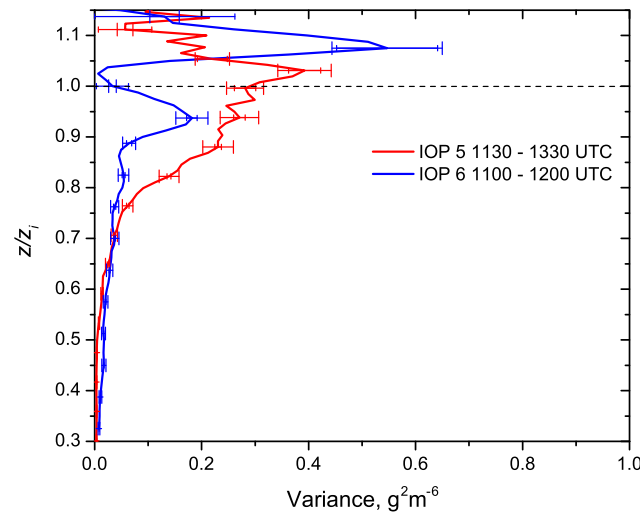


Fig. 7 Vertical profiles of absolute humidity variance with noise (*small*) and sampling (*large*) errors for the analysis periods of IOP 5 and IOP 6

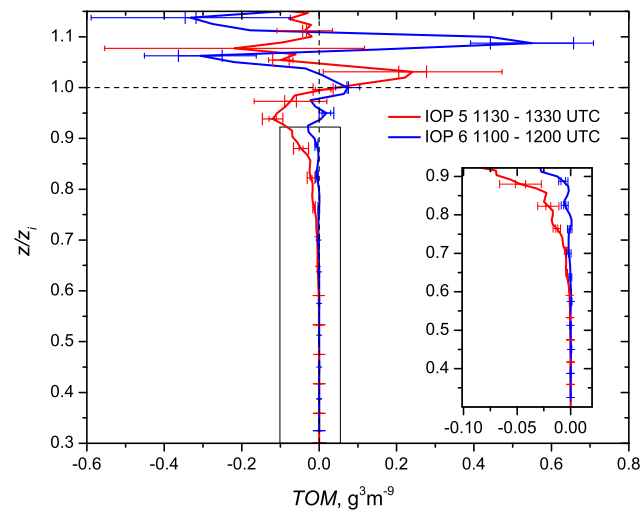


Fig. 8 Vertical profiles of third-order moment (*TOM*). *Inset* shows detail for heights of $0.3 - 0.9z_i$

ues near zero up to $0.5z_i$ and a minimum near $0.9z_i$ down to $-0.12 \pm 0.02 \pm 0.01 \text{ g}^3 \text{ m}^{-9}$. Near z_i , a change to positive values with a maximum *TOM* value of $0.24 \pm 0.03 \pm 0.02 \text{ g}^3 \text{ m}^{-9}$ can be seen. In the lower free troposphere, the noise errors increase and *TOM* is not significantly different from zero. For IOP 6, the *TOM* profile shows values close to zero up to $0.8z_i$ and a few slightly negative data points between $0.8z_i$ and $0.95z_i$. Near z_i , a positive peak similar to IOP 5 is found, but with much lower *TOM* values of only $0.07 \pm 0.002 \pm 0.02 \text{ g}^3 \text{ m}^{-9}$. A steep decrease is observed at $1.05z_i$, with *TOM* around $-0.30 \pm 0.10 \pm 0.01 \text{ g}^3 \text{ m}^{-9}$, followed by a sharp increase with a maximum of $0.54 \pm 0.12 \pm 0.10 \text{ g}^3 \text{ m}^{-9}$ at $1.1z_i$. Entrainment of dry downdrafts into the CBL is deeper for IOP 5 than for IOP 6 (Figs. 2, 3). In summary, the differences between the two IOPs found in the variance profiles correspond to the character-

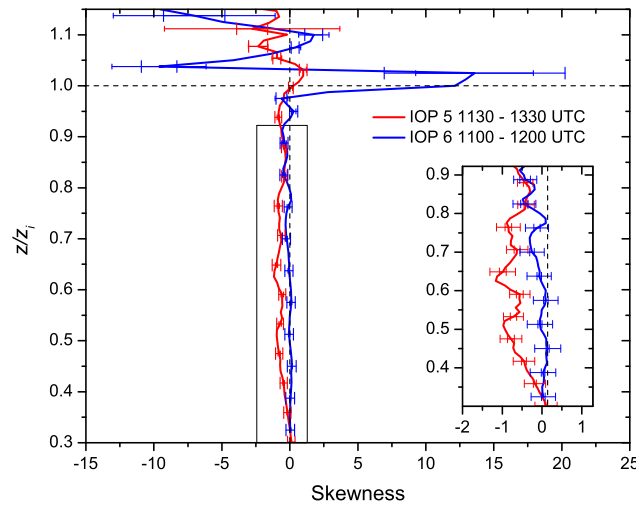


Fig. 9 Same as Fig. 8, but for skewness. *Inset* shows detail for heights of $0.3 - 1.0z_i$

istics of the *TOM* profiles: the variance peak of IOP 5 corresponds to a *TOM* minimum below and a *TOM* maximum above, while the two peaks of IOP 6 correspond to two minima and maxima. Furthermore, the maximum variance of each peak seems to be related to the value of the corresponding *TOM* peaks.

Figure 9 shows the profile of skewness S for IOP 5 and IOP 6, respectively. For IOP 5, the skewness profile shows negative values with a minimum of $-1.16 \pm 0.15 \pm 0.08$ between $0.5z_i$ and $0.8z_i$. At $1.1z_i$, the skewness profile becomes positive with a maximum S of $0.98 \pm 0.25 \pm 0.18$. For IOP 6, the humidity skewness profile shows values close to zero in the CBL up to $0.6z_i$, decreasing to $-0.56 \pm 0.13 \pm 0.15$ at $0.9z_i$, and then changing their sign to positive near z_i . Strongly positive values of up to $13.5 \pm 4.3 \pm 5.2$ are observed in the interfacial layer. The transition of S from negative to positive is found close to z_i for IOP 5, whereas it occurs at $0.93z_i$ for IOP 6. A difference in absolute humidity of 2.3 and 2.8 g m^{-3} between the CBL and the lower free troposphere was found for IOP 5 and IOP 6, respectively. As the error of the variance adds to the error of *TOM* when computing S (see Eq. 9), the errors of the S profiles are larger than the errors in the *TOM* profiles, which makes it more difficult to identify positive and negative peaks. Figure 10 illustrates the findings described above with the distributions of the turbulent fluctuations at three selected heights during the two observation periods. The three height levels were chosen as follows: the first in the middle of the CBL, the second at the maximum negative value in the *TOM* profile below z_i , and the third above z_i , where the *TOM* profile has a positive peak. As expected, the distributions for both IOPs show clear differences between these three heights. In the middle of the CBL at $0.5z_i$, a strong and narrow peak is observed for both IOPs, corresponding to lower variance than at the heights above. In contrast, large variances are observed just below the CBL top at around $0.9z_i$. Furthermore, the distributions here are left-skewed (negative *TOM*) with fewer, but stronger, negative fluctuations and more, but weaker, positive fluctuations. One can identify, however, that S is much smaller for IOP 5 (negative peak; thus larger in terms of absolute value) than for IOP 6, where it is close to zero. Above the CBL top, where positive *TOM* values are present, right-skewed distributions are observed.

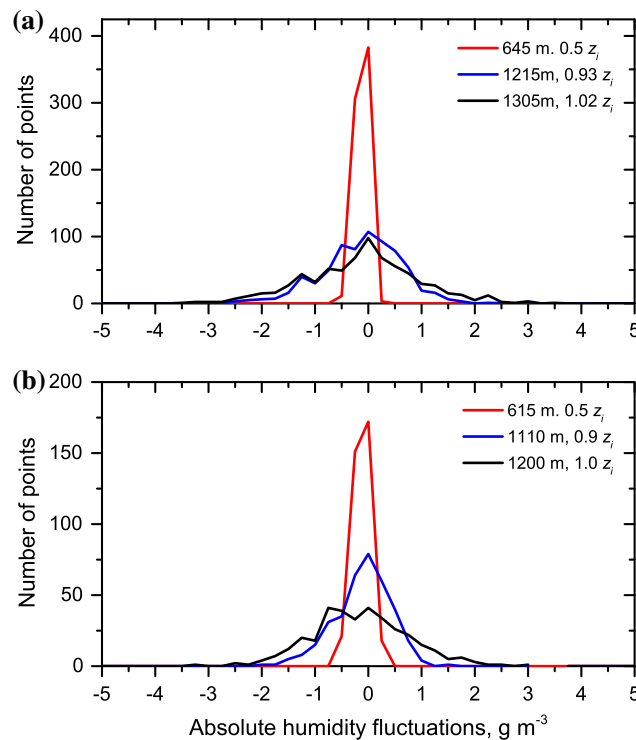


Fig. 10 Histogram of humidity turbulence fluctuations at three height levels for **a** IOP 5 1130–1330 UTC and **b** IOP 6 1100–1200 UTC

6.4 Fourth-order Moment and Kurtosis

Analyses of the fourth-order moment (*FOM*) are only possible if the system noise level is very low. The *FOM* profiles for both IOPs are shown in Fig. 11. Results show that *FOM* increases with height in the CBL and maximum values are found in the interfacial layer. In case of IOP 5, a maximum *FOM* of $2.1 \pm 0.86 \pm 0.13 \text{ g}^4 \text{ m}^{-12}$ at $1.03z_i$ was observed, whereas for IOP 6, there were two maxima at $1.01z_i$ and $1.06z_i$ with $1.07 \pm 0.30 \pm 0.01 \text{ g}^4 \text{ m}^{-12}$ and $2.12 \pm 0.90 \pm 0.01 \text{ g}^4 \text{ m}^{-12}$, respectively. Again, these features correspond to the structures of the variance profiles.

Kurtosis (*K*) is a measure of the peakedness of the distribution, with a *K* value of three representing a Gaussian distribution. In addition, for turbulence studies, *K* values of less than three indicate that turbulence is frequent and the degree of mixing is large. Vertical profiles for *K* are shown in Fig. 12. For IOP 5, *K* values in the CBL are around three, which is the kurtosis value of a mesokurtic (Gaussian) distribution. For IOP 6, *K* values in the CBL are smaller than for IOP 5, with values of about two. Thus, the distributions are slightly platykurtic ($K < 3$) for IOP 6 and show broader peaks but fewer large fluctuations. In the interfacial layer, *K* values increase for both IOPs, which shows that the distributions of the turbulent humidity fluctuations are leptokurtic ($K > 3$). Above $1.0z_i$, the noise of the *K* profiles increases, because humidity is much lower in the free troposphere than in the CBL. Hence, no reliable estimates of kurtosis are possible above z_i . Similar to *TOM* and *S* values, the noise of the variance profile increases the noise for the *K* values compared to *FOM* values, so that the height dependence is better seen in the *FOM* profile than in the *K* profile.

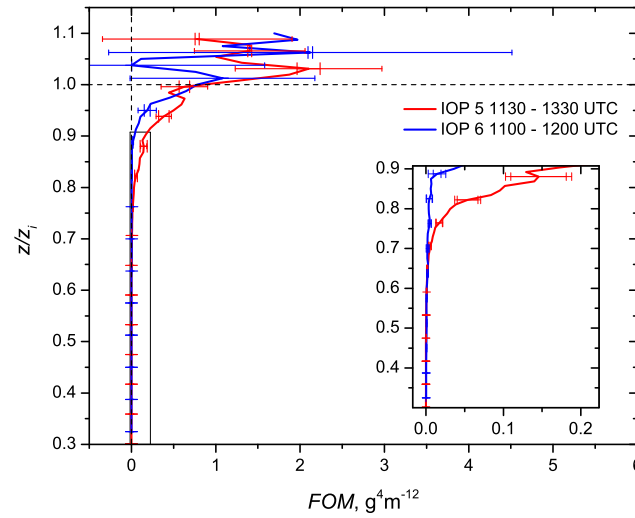


Fig. 11 Same as Fig. 8, but for fourth-order moment (FOM)

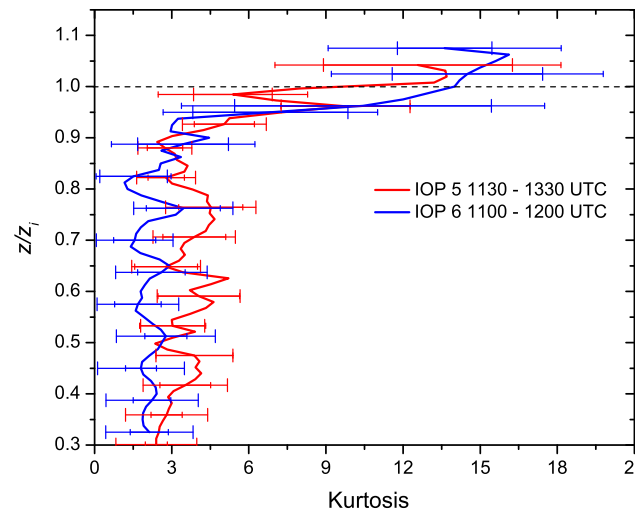


Fig. 12 Same as Fig. 6, but for kurtosis

7 Discussion

As we chose clear-sky days for our analyses, surface forcing was significant during both IOPs. Due to differences in soil moisture, flux partitioning was different for both cases. The mean surface sensible heat flux during the observation period was 36 % higher during IOP 5 (250 W m^{-2}) than during IOP 6 (184 W m^{-2}). The latent heat flux at the ground showed the opposite behaviour and was 2.3 times larger during IOP 6 (210 W m^{-2}) than during IOP 5 (90 W m^{-2}). Related to the differences in sensible heat flux, the mean CBL height during local noon was about 100 m higher during IOP 5 (1295 m) than during IOP 6 (1200 m). At the CBL top, similar decreases of 2.3 and 2.8 g m^{-3} (corresponding to a 22 % difference) were found in the absolute humidity profiles for IOP 5 and 6, respectively. In the following

paragraphs, we discuss whether these differences in the characteristics of the boundary layer influence the results of the turbulence analysis of the moisture fluctuations.

Because the detailed values of the integral length scale depend on the horizontal wind, these scales cannot be readily compared between different studies; however, the profile shapes can be compared. The integral time scales (Π) show similar values for both cases. The profiles for both IOPs show a decreasing trend from $0.4z_i$ up to $0.9z_i$. Such a decrease has already been described in previous studies based on observations (Kiemle et al. 1997; Lenschow et al. 2000; Wulfmeyer et al. 2010) and on LES (Couvreur et al. 2005). The reason for the existence of this structure is that eddy size decreases with height from the middle CBL towards the CBL top due to a loss of buoyancy and entrainment of dry air.

Variance is found to be at a maximum in the interfacial layer for both cases discussed here. Similar to the integral time scale profile, the increase of humidity variance in the CBL with a maximum in the interfacial layer has already been discussed in previous studies, either based on LES (Deardorff 1974; Moeng and Wyngaard 1984; Sullivan et al. 1998; Moene et al. 2006; Couvreur et al. 2007) or on observations (Kiemle et al. 1997; Lenschow et al. 2000; Wulfmeyer et al. 2010). However, with our instruments, the increase of variance can be measured with unprecedented accuracy for a remote sensing system (see Fig. 7). The reason for the variance maximum in the interfacial layer is that the dry air from the lower free troposphere is mixed here most dominantly with the moist CBL air. Wind shear can also contribute to the variance production at z_i (Jiang et al. 2010). Wind shear was present at z_i for both our cases, and thus we believe that this effect was similar for both IOPs.

For IOP 6, however, we found two variance peaks at the CBL top. As revealed by the radiosonde profiles of 0900 UTC and 1100 UTC and by the DIAL measurements, an elevated moist layer above a dry layer was entrained into the CBL during this IOP. This process seems to be responsible for the differences found in the higher-order-moment profiles. The double-layer humidity profile present during IOP 6 resulted in two gradients, one of $0.0091 \text{ g m}^{-3} \text{ m}^{-1}$ at $0.95z_i$ and the other of $0.014 \text{ g m}^{-3} \text{ m}^{-1}$ at $1.0z_i$. A smaller variance peak of $0.18 \pm 0.03 \pm 0.01 \text{ g}^2 \text{ m}^{-6}$ was found for the small gradient at $0.95z_i$, while a larger variance peak of $0.54 \pm 0.10 \pm 0.09 \text{ g}^2 \text{ m}^{-6}$ was found at $1.1z_i$, where the larger gradient was present (Fig. 5).

Previously, a secondary maximum in the variance profile was discussed based on LES of trapped waves in the inversion layer (Deardorff 1974; Moeng and Wyngaard 1984). Moderate to strong wind shear could result in wave activity at the CBL top, but we see no indication of waves for either of our cases, neither in the time–height cross-sections of humidity nor in the range-corrected offline backscatter signals (figures not shown). Thus, we conclude that the entrainment of an elevated moist layer into the CBL explains the unusual variance profile of IOP 6.

The profiles of third-order moment and skewness S are related to the structures found in the variance profiles. The third-order moment profile for IOP 5 shows a negative and a positive peak below and above the CBL top, respectively. This is due to the asymmetry in the fluctuations, namely a few very dry but many slightly moist fluctuations in the upper CBL due to dry air entrainment. At the same time, there is an opposite asymmetry in the lower free troposphere above with a few very moist but many slightly dry fluctuations due to overshooting thermals. Some previous studies have reported on this typical humidity skewness profile in the CBL (Mahrt 1991; Weckwerth et al. 1996; Couvreur et al. 2005, 2007; Turner et al. 2014).

Mahrt (1991) highlighted the fact that the signs of TOM and skewness (which are the same) are positive when the surface moisture flux is larger than the flux generated at the CBL top (in the opposite case, both are negative). Thus, the mean moisture tendency in the

boundary layer, namely moistening or entrainment-drying, is related to the signs of skewness and *TOM*. Furthermore, the strength of this tendency can be related to the absolute skewness values.

For IOP 5, a negative skewness of about -1 was found inside the CBL, which reflects an entrainment drying boundary layer. For IOP 6, lower skewness values were found (zero in the middle of the CBL and about -0.5 in the upper CBL). Thus, the moisture tendency for IOP was weaker. Indeed, the latent heat flux at the surface was much higher for IOP 6 than for IOP 5. Furthermore, the entrainment fluxes at the CBL top were either similar for both cases (as the moisture gradients at the CBL top were similar) or larger for IOP 5. The latter interpretation is supported by the difference in the variance profiles of both cases in the upper CBL. Here, the variances are significantly larger for IOP 5 than for IOP 6, related to a likely larger transport of moisture variance deeper downward into the CBL and thus larger upward latent heat flux. In summary, IOP 5 presents a case for an entrainment-drying boundary layer, while IOP 6 is a case for a CBL without much moisture tendency that is neither drying nor moistening but for which the latent heat flux generated at the surface is transported upward and balanced by the entrainment of dry air at the interfacial layer.

Precise low-noise measurements in the CBL are needed for reliable estimates of the fourth-order moment and kurtosis (Lenschow et al. 2000; Wulfmeyer et al. 2010). Here, as shown in our case study, high power ground-based DIAL offers such humidity data up to the interfacial layer. Fourth-order moment values near zero were observed up to the mid-CBL, but a steep increase is found in the interfacial layer for both cases. To the best of our knowledge, previous results on humidity fourth-order moment were only shown by Lenschow et al. (2000) over a marine CBL. A similar profile was reported by these authors with an increase in the interfacial layer. The sub-structure of the *FOM* profiles followed the variance profiles found in both cases: the distributions become leptokurtic at the heights of variance peaks. In the middle CBL, Lenschow et al. (2000) found a mesokurtic distribution; we found the same for IOP 5, whereas for IOP 6, a slightly platykurtic distribution was found. This confirms that a mesokurtic distribution can be considered typical for an entrainment-drying CBL. Furthermore, it seems that the slightly platykurtic distribution of IOP 6 represents a CBL without moisture tendency.

8 Conclusions

Turbulent humidity fluctuations in the CBL including the interfacial layer were investigated by deriving the higher-order moments from UHOH DIAL data collected during the HOPE campaign. Two periods around noon under clear-sky conditions were identified and reliable profiles of up to the fourth-order moment were obtained for humidity with unprecedented precision. This permitted a very accurate measurement of the variance profile gradient from the mixed layer to the interfacial layer.

The integral-time-scale profiles show a decrease towards the top of the CBL, with values between 60 and 130 s in both cases. Variance was found to be at a maximum in the interfacial layer for both cases but, while one peak is present for IOP 5, two maxima can be observed for IOP 6. We believe that the presence of two maxima for IOP 6 is due to the presence of an elevated humid layer in the lower troposphere that was entrained into the CBL. Larger variance was found in the interfacial layer, when a larger humidity gradient at the CBL top existed. Similarity relationships suggest a dependence on other CBL characteristics and we suggest that future validation studies include these additional variables (Wulfmeyer et al. 2015).

These relationships, if validated with new observations, will be very important components of improved turbulent parametrization schemes and for advanced comparisons with LES.

Significant differences are present in the *TOM* and *S* profiles for both cases. The *TOM* profiles show a negative and a positive peak below and above each variance maximum. For IOP 5, negative *S* values occur in the middle of the CBL, which indicates that the CBL is drying by entrainment. Near-zero *S* was found in the middle of the CBL for IOP 6. Thus, we conclude that, in this case, the CBL humidity budget was in balance between the latent heat flux at the surface and the entrainment flux at the interfacial layer. For both cases, nearly zero *FOM* was observed in the CBL but a steep increase was found in the interfacial layer. The sub-structure of the *FOM* profiles again follows the variance profiles. The distributions become leptokurtic in the heights of variance peaks. The mesokurtic distribution found for IOP 5 may be typical of an entrainment-drying CBL, while the slightly platykurtic distribution of IOP 6 may be representative of a CBL where strong surface evaporation is balanced by entrainment.

These results demonstrate that high-resolution humidity data obtained with the UHOH DIAL provide new insights into the turbulence structure in the CBL and interfacial layer. The importance of subgrid-scale variability of humidity transport between the CBL and cloud layers for improving cloud-resolving model outputs was recently discussed by Moeng and Arakawa (2012).

Acknowledgments The HOPE campaign was funded by the German Research Ministry under the project number 01LK1212A. We thank KIT and the University of Cologne for performing the radiosonde launches during HOPE. We also thank Norbert Kalthoff, Martin Kohler, and all KITCube team members for providing the energy balance station data at the measurement site. We thank ECMWF for providing the analysis data during the measurement period and Thomas Schwitalla for kindly providing the figures of the ECMWF analyses. We would like to thank the three anonymous reviewers for their constructive comments.

Open Access This article is distributed under the terms of the Creative Commons Attribution 4.0 International License (<http://creativecommons.org/licenses/by/4.0/>), which permits unrestricted use, distribution, and reproduction in any medium, provided you give appropriate credit to the original author(s) and the source, provide a link to the Creative Commons license, and indicate if changes were made.

References

- Ansmann A (1985) Errors in ground-based water-vapor DIAL measurements due to Doppler-broadened Rayleigh backscattering. *Appl Opt* 24:3476–3480
- Ansmann A, Bösenberg J (1987) Correction scheme for spectral broadening by Rayleigh scattering in differential absorption lidar measurements of water vapor in the troposphere. *Appl Opt* 26:3026–3032
- Behrendt A, Pal S, Aoshima F, Bender M, Blyth A, Corsmeier U, Cuesta J, Dick G, Dörninger M, Flamant C, Di Girolamo P, Gorgas T, Huang Y, Kalthoff N, Khodayar S, Mannstein H, Träumner K, Wieser A, Wulfmeyer V (2011) Observation of convection initiation processes with a suite of state-of-the-art research instruments during COPS IOP8b. *Q J R Meteorol Soc* 137(S1):81–100
- Behrendt A, Wulfmeyer V, Hammann E, Muppa SK, Pal S (2015) Profiles of second to fourth-order moments of turbulent temperature fluctuations in the convective boundary layer: First measurements with rotational Raman lidar. *Atmos Chem Phys* 15:5485–5500
- Bennett LJ, Weckwerth TM, Blyth AM, Geerts B, Miao Q, Richardson YP (2010) Observations of the evolution of the nocturnal and convective boundary layers and the structure of the open-celled convection on 14 June 2002. *Mon Weather Rev* 138:2589–2607
- Bhawar R, Di Girolamo P, Summa D, Flamant C, Althausen D, Behrendt A, Kiemle C, Bosser P, Cacciani M, Champollion C, Di Iorio T, Engelmann R, Herold C, Pal S, Riede A, Wirth M, Wulfmeyer V (2011) The water vapour intercomparison effort in the framework of the convective and orographically-induced precipitation study: air-borne-to-ground-based and airborne-to-airborne lidar systems. *COPS Special Issue Q J R Meteorol Soc* 137:325–348

- Conzemius RJ, Fedorovich E (2006) Dynamics of sheared convective boundary layer entrainment. Part I: Methodological background and large eddy simulations. *J Atmos Sci* 63:1151–1178
- Corsmeier U, Kalthoff N, Barthlott Ch, Behrendt A, Di Girolamo P, Dorninger M, Aoshima F, Handwerker J, Kottmeier Ch, Mahlke H, St Mobbs, Vaughan G, Wickert J, Wulfmeyer V (2011) Processes driving deep convection over complex terrain: a multi-scale analysis of observations from COPS IOP 9c. *Q J R Meteorol Soc* 137:137–155
- Couvreur F, Guichard F, Redelsperger JL, Kiemle C, Masson V, Lafore JP, Flamant C (2005) Water vapour variability within a convective boundary layer assessed by Large Eddy Simulations and IHOP_2002 observations. *Q J R Meteorol Soc* 131:2665–2693
- Couvreur F, Guichard F, Masson V, Redelsperger JL (2007) Negative water vapour skewness and dry tongues in the convective boundary layer: observations and large-eddy simulation budget analysis. *Bound-Layer Meteorol* 123(2):269–294
- Davis KJ, Gamage N, Hagelberg CR, Kiemle C, Lenschow DH, Sullivan PP (2000) An objective method for deriving atmospheric structure from airborne lidar observations. *J Atmos Ocean Technol* 17:1455–1468
- Deardorff JW (1974) Three-dimensional numerical study of turbulence in an entraining mixed layer. *Bound-Layer Meteorol* 7:199–226
- Deardorff JW, Willis GE, Stockton BH (1980) Laboratory studies of the entrainment zone of a convectively mixed layer. *J Fluid Mech* 100:41–64
- de Roode SR, Duynkerke PG, Jonker HJJ (2004) Large-eddy simulation: how large is large enough? *J Atmos Sci* 61:403–421
- Fedorovich E, Conzemius R (2008) Effects of wind shear on the atmospheric convective boundary-layer structure and evolution. *Acta Geophys* 56:114–141
- Fernald FG (1984) Analysis of atmospheric lidar observations: some comments. *Appl Opt* 23:652–653
- Grossman RL, Gamage N (1995) Moisture flux and mixing processes in the daytime continental convective boundary layer. *J Geophys Res* 100:25665–25674
- Giez A, Ehret G, Schwiesow RL, Davis KJ, Lenschow DH (1999) Water vapor flux measurements from ground-based vertically pointed water vapor differential absorption and doppler lidars. *J Atmos Ocean Technol* 16:237–250
- Hammann E, Behrendt A, Le Mounier F, Wulfmeyer V (2015) Temperature profiling of the atmospheric boundary layer with rotational Raman Lidar during the HD(CP)2 observational prototype experiment. *Atmos Chem Phys* 15:2867–2881
- Hogan RJ, Grant ALM, Illingworth AJ, Pearson GN, O’Conner EJ (2009) Vertical velocity variance and skewness in clear and cloud-topped boundary layers as revealed by Doppler lidars. *Q J R Meteorol Soc* 135:635–643
- Ismail S, Browell EV (1989) Airborne and spaceborne lidar measurements of water vapor profiles: a sensitivity analysis. *Appl Opt* 28:3603–3615
- Jiang Q, Doyle JD, Grubisic V, Smith RB (2010) Turbulence characteristics in an elevated shear layer over Owens valley. *J Atmos Sci* 67:2355–2371
- Kaimal JC, Wyngaard JC, Haugen DA, Cote OR, Izumi Y, Caughey SJ, Readings CJ (1976) Turbulence structure in the CBL. *J Atmos Sci* 33:2152–2169
- Kalthoff N, Adler B, Wieser A, Kohler M, Träumner K, Handwerker J, Corsmeier U, Khodayar S, Lambert D, Kopmann A, Kunka N, Dick G, Ramatschi M, Wickert J, Kottmeier C (2013) Kitcube—a mobile observation platform for convection studies deployed during HyMeX. *Meteorol Z* 22(6):633–647
- Kiemle C, Ehret G, Giez A, Davis KJ, Lenschow DH, Oncley SP (1997) Estimation of boundary layer humidity fluxes and statistics from airborne differential absorption lidar (DIAL). *J Geophys Res* 102(D24):29189–29203
- Lenschow DH, Mann J, Kristensen L (1994) How long is long enough when measuring fluxes and other turbulence statistics? *J Atmos Ocean Technol* 11:661–673
- Lenschow DH, Wulfmeyer V, Senff C (2000) Measuring second-through fourth-order moments in noisy data. *J Atmos Oceanic Tech* 17(10):1330–1347
- Lenschow DH, Lothon M, Mayor SD, Sullivan PP, Canut G (2012) A comparison of higher-order vertical velocity moments in the convective boundary layer from lidar with in situ measurements and large-eddy simulation. *Bound-Layer Meteorol* 143:107–123
- Mahrt L (1976) Mixed layer moisture structure. *Mon Weather Rev* 104:1403–1407
- Mahrt L (1991) Boundary-layer moisture regimes. *Q J R Meteorol Soc* 117:151–176
- Moene AF, Michels BI, Holtslag AAM (2006) Scaling variances of scalars in a convective boundary layer under different entrainment regimes. *Bound-Layer Meteorol* 120:257–274
- Moeng CH, Arakawa A (2012) Representation of boundary layer moisture transport in cloud-resolving models. *Mon Weather Rev* 140:3682–3698

- Moeng CH, Wyngaard JC (1984) Statistics of conservative scalars in the convective boundary layer. *J Atmos Sci* 41:3161–3169
- Moeng CH, Wyngaard JC (1989) Evaluation of turbulent transport and dissipation closures in second order modelling. *J Atmos Sci* 46:2311–2330
- Monin AS, Yaglom AM (1971) *Statistical fluid mechanics*, vol 1. MIT Press, Cambridge 782 pp
- Pal S, Behrendt A, Wulfmeyer V (2010) Elastic-backscatter-lidar-based characterization of the convective boundary layer and investigation of related statistics. *Ann Geophys* 28:825–847
- Richard E, Buzzi A, Zängl G (2007) Quantitative precipitation forecasting in the Alps: the advances achieved by the Mesoscale Alpine Programme. *Q J R Meteorol Soc* 133:831–846
- Savitzky A, Golay MJE (1964) Smoothing and differentiation of data by simplified least squares procedures. *Anal Chem* 36:1627–1639
- Sorbjan Z (1996) Effects caused by varying the strength of the capping inversion based on a large eddy simulation model of the shear-free convective boundary layer. *J Atmos Sci* 53(14):2015–2024
- Sorbjan Z (1999) Similarity of scalar fields in the convective boundary layer. *J Atmos Sci* 56:2212–2221
- Sorbjan Z (2005) Statistics of scalar fields in the atmospheric boundary layer based on large-eddy simulations. Part I: Free convection. *Bound-Layer Meteorol* 116:467–486
- Sorbjan Z (2006) Statistics of scalar fields in the atmospheric boundary layer based on large-eddy simulations. Part II: Forced convection. *Bound-Layer Meteorol* 119:57–79
- Stevens B, Bony S (2013) What are climate models missing? *Science* 340:1053–1054
- Stevens B, Lenschow DH (2001) Observations, experiments and large-eddy simulations. *Bull Am Meteorol Soc* 82(2):283–294
- Stull RB (1988) *An introduction to boundary layer meteorology*. Kluwer Academic Publisher, Dordrecht, 688 pp
- Sullivan PP, Moeng CH, Stevens B, Lenschow DH, Mayor SD (1998) Structure of the entrainment zone capping the convective atmospheric boundary layer. *J Atmos Sci* 55:3042–3064
- Sullivan PP, Patton EG (2011) The effect of mesh resolution on convective boundary layer statistics and structures generated by large-eddy simulation. *J Atmos Sci* 68:2395–2415
- Späth F, Behrendt A, Muppa SK, Metzendorf S, Riede A, Wulfmeyer V (2015) Water vapor heterogeneities analysis with a scanning differential absorption lidar. In: preparation 2015
- Taylor GI (1938) The spectrum of turbulence. *Proc R Soc* 67:16–20
- Träumner K, Damian Th, Stawiarski Ch, Wieser, A (2014) Turbulent structures and coherence in the atmospheric surface layer. *Bound-Layer Meteorol* doi:[10.1007/s10546-014-9967-6](https://doi.org/10.1007/s10546-014-9967-6)
- Turner DD, Ferrare RA, Wulfmeyer V, Scarino AJ (2014) Aircraft evaluation of ground based Raman lidar water vapor turbulence profiles in convective mixed layers. *J Atmos Ocean Tech* 31:1078–1088
- Van Heerwaarden CC, Vila J, Moene AF, Holtslag AAM (2009) Interactions between dryair entrainment, surface evaporation and convective boundary-layer development. *Q J R Meteorol Soc* 135:1277–1291
- Wagner G, Behrendt A, Wulfmeyer V, Späth F, Schiller M (2013) High-power Ti:sapphire laser at 820 nm for scanning ground-based water-vapor differential absorption lidar. *Appl Opt* 52(11):2454–2469
- Weckwerth T (2000) The effect of small-scale moisture variability on thunderstorm initiation. *Mon Weather Rev* 128:4017–4030
- Weckwerth T, Wilson JW, Wakimoto RM (1996) Thermodynamic variability within the convective boundary layer due to horizontal convective rolls. *Mon Weather Rev* 124:769–784
- Weckwerth T, Parsons DB, Koch SE, Moore JA, LeMone MA, Demoz BB, Flamant C, Geerts B, Wang J, Feltz WF (2004) An overview of the International H₂O Project (IHOP_2002) and some preliminary highlights. *Bull Am Meteorol Soc* 85:253–277
- Wulfmeyer V (1999a) Investigation of turbulent processes in the lower troposphere with water vapor DIAL and radar-RASS. *J Atmos Sci* 56:1055–1076
- Wulfmeyer V (1999b) Investigations of humidity skewness and variance profiles in the convective boundary layer and comparison of the latter with large eddy simulation results. *J Atmos Sci* 56:1077–1087
- Wulfmeyer V, Bösenberg J (1998) Ground-based differential absorption lidar for water-vapor profiling: assessment of accuracy, resolution, and meteorological applications. *Appl Opt* 37:3825–3844
- Wulfmeyer V, Pal S, Turner DD, Wagner E (2010) Can water vapour Raman Lidar resolve profiles of turbulent variables in the convective boundary layer? *Bound-Layer Meteorol* 136:253–284
- Wulfmeyer V, Behrendt A, Kottmeier C, Corsmeier U, Barthlott C, Craig GC, Hagen M, Althausen D, Aoshima F, Arpagaus M, Bauer H-S, Bennett L, Blyth A, Brandau C, Champollion C, Crewell S, Dick G, Di Girolamo P, Dorminger M, Dufournet Y, Eigenmann R, Engelmann R, Flamant C, Foken T, Gorgas T, Grzeschik M, Handwerker J, Hauck C, Höller H, Junkermann W, Kalthoff N, Kiemle C, Klink S, König M, Krauss L, Long CN, Madonna F, Mobbs S, Neiningen B, Pal S, Peters G, Pigeon G, Richard E, Rotach MW, Russchenberg H, Schwitalla T, Smith V, Steinacker R, Trentmann J, Turner DD, van Baelen J, Vogt S, Volkert H, Weckwerth T, Wernli H, Wieser A, Wirth M (2011) The convective and orographically

- induced precipitation study (COPS): the scientific strategy, the field phase, and first highlights. *Q J R Meteorol Soc* 137:3–30
- Wulfmeyer V, Behrendt A, Sorbjan Z, Turner DD, Hardesty RM (2015) Determination of convective boundary layer entrainment fluxes, dissipation rates, and the molecular destruction of variances: theoretical description and a strategy for its confirmation with a novel lidar system synergy. *J Atmos Sci* (under review)
- Wyngaard J, Brost RA (1984) Top-down and bottom-up diffusion of a scalar in the convective boundary layer. *J Atmos Sci* 41:102–112
- Zhou B, Simon JS, Chow FK (2014) The convective boundary layer in the terra incognita. *J Atmos Sci* 71:2545–2563
- Zhu P, Albrecht B (2002) A theoretical and observational analysis on the formation of fair-weather cumuli. *J Atmos Sci* 59:1983–2005

Determination of Convective Boundary Layer Entrainment Fluxes, Dissipation Rates, and the Molecular Destruction of Variances: Theoretical Description and a Strategy for Its Confirmation with a Novel Lidar System Synergy

VOLKER WULFMEYER

*Institute of Physics and Meteorology, University of Hohenheim, Stuttgart, Germany, and
Cooperative Institute for Research in Environmental Sciences, Boulder, Colorado*

SHRAVAN KUMAR MUPPA, ANDREAS BEHRENDT, EVA HAMMANN, AND FLORIAN SPÄTH

Institute of Physics and Meteorology, University of Hohenheim, Stuttgart, Germany

ZBIGNIEW SORBJAN

Physics Department, Marquette University, Milwaukee, Wisconsin

DAVID D. TURNER

NOAA/National Severe Storms Laboratory, Norman, Oklahoma

R. MICHAEL HARDESTY

NOAA/Earth System Research Laboratory, Boulder, Colorado

(Manuscript received 22 December 2014, in final form 20 October 2015)

ABSTRACT

Atmospheric variables in the convective boundary layer (CBL), which are critical for turbulence parameterizations in weather and climate models, are assessed. These include entrainment fluxes, higher-order moments of humidity, potential temperature, and vertical wind, as well as dissipation rates. Theoretical relationships between the integral scales, gradients, and higher-order moments of atmospheric variables, fluxes, and dissipation rates are developed mainly focusing on the entrainment layer (EL) at the top of the CBL. These equations form the starting point for tests of and new approaches in CBL turbulence parameterizations. For the investigation of these relationships, an observational approach using a synergy of ground-based water vapor, temperature, and wind lidar systems is proposed. These systems measure instantaneous vertical profiles with high temporal and spatial resolution throughout the CBL including the EL. The resolution of these systems permits the simultaneous measurement of gradients and fluctuations of these atmospheric variables. For accurate analyses of the gradients and the shapes of turbulence profiles, the lidar system performances are very important. It is shown that each lidar profile can be characterized very well with respect to bias and system noise and that the constant bias has negligible effect on the measurement of turbulent fluctuations. It is demonstrated how different gradient relationships can be measured and tested with the proposed lidar synergy within operational measurements or new field campaigns. Particularly, a novel approach is introduced for measuring the rate of destruction of humidity and temperature variances, which is an important component of the variance budget equations.

 Denotes Open Access content.

Corresponding author address: Volker Wulfmeyer, Institute of Physics and Meteorology, University of Hohenheim, Garbenstraße 30, 70599 Stuttgart, Germany.
E-mail: volker.wulfmeyer@uni-hohenheim.de

DOI: 10.1175/JAS-D-14-0392.1

© 2016 American Meteorological Society

1. Introduction

The turbulent transport of heat, matter, and momentum in the convective boundary layer (CBL) is essential for many key processes in the atmosphere. It determines the horizontal and vertical distribution of scalars such as humidity and other constituents as well as the vertical

stability. Particularly critical are the entrainment fluxes at the CBL top, as they influence the 3D fields of water vapor, temperature, and horizontal wind in the lower troposphere in both vertical directions: above the CBL by entrainment processes and from the CBL top down to the surface and the soil–vegetation layers by its coupling with the surface fluxes and the closure of the surface energy balance. The resulting 3D fields characterize the preconvective environment and influence thunderstorm initiation as well as the development of clouds and precipitation.

Generally, the grid increments of state-of-the-art weather forecast and climate models are too large to resolve small-scale boundary layer turbulence. Consequently, turbulence parameterizations (TP) are essential components of almost all weather and climate models. To a great extent, the TP determines the quality of the simulation of land surface–atmosphere feedback (e.g., Milovac et al. 2014). A particular weakness of the models is the parameterization of entrainment fluxes, which is required for a high quality of simulations on all time scales. On short time scales, an incorrect simulation of entrainment leads to erroneous evolutions of CBL moisture and temperature as well as the convective available potential energy and convective inhibition, which results in poor skill of predicting convection initiation. On longer time scales, incorrect entrainment fluxes cause errors in the vertical distribution of water vapor with negative consequences for the simulation of climate statistics with respect to radiative transfer and the evolution of clouds and precipitation. This concerns reanalyses, regional dynamical downscaling, and global climate change projections. The high sensitivity of NWP model forecast quality on the CBL TP was demonstrated by, for example, Hong et al. (2006), Hill and Lackmann (2009), and Xie et al. (2012) and with respect to the performance of regional climate models by, for example, Dethloff et al. (2001), Park and Bretherton (2009), and Samuelsson et al. (2011).

Models for entrainment fluxes were derived in various publications (Van Zanten et al. 1999; Fedorovich et al. 2004), and relationships useful for applications in NWP models were proposed (Noh et al. 2003). For instance, in the nonlocal Yonsei University (YSU) TP (Hong et al. 2006), the water vapor entrainment flux is the product of an entrainment velocity and the moisture jump at the CBL top. The entrainment velocity is estimated by assuming a constant ratio between the surface and the entrainment heat fluxes of -0.15 and by diagnosing the temperature jump at the CBL top. However, it is unclear whether this constant ratio holds in a real atmospheric boundary layer where gravity waves and wind shear are expected to have a great influence on entrainment fluxes (Wulfmeyer 1999a; Conzemius and Fedorovich 2006).

Particularly, it is expected that the temperature flux ratio decreases to approximately -0.3 during shear convection and even more during forced convection with dramatic consequences on moistening or drying conditions (Sorbjan 2005, 2006).

Sorbjan (2001, 2005, 2006) developed CBL scaling laws for deriving profiles of fluxes and higher-order moments of atmospheric variables. These scaling approaches relate fluxes and higher-order moments of atmospheric variables to their gradients in the entrainment layer (EL). Furthermore, these relationships include dependencies of fluxes and variances on the gradient Richardson number so that the influence of wind shear can also be included. If these relationships are valid, simple tests of existing TPs will be possible.

Advanced CBL TPs with refined representation of entrainment may be derived and incorporated in mesoscale models. This will be possible for hierarchies of model simulations from relatively coarse grid increments to the gray zone (e.g., Saito et al. 2013) where turbulent fluctuations become resolved. Gray-zone experiments are a very important area of research, as both regional climate models and NWP models will reach the corresponding grid increments on the order of 1 km within the next years. Therefore, the representation of land–atmosphere feedback of this new model generation has to be studied in great detail and to be optimized, including a realistic simulation of clouds and precipitation.

A prerequisite of the application of new scaling relationships is their verification. This can be realized by performing large-eddy simulations (LESs) and the confirmation of their results by dedicated observations. Since the 1970s, LES has been used for studying the CBL under various conditions (Deardorff 1970). Advances in computing power and model developments enable the resolution of turbulence above the surface layer throughout the CBL including the EL. Most of the runs have been performed under strong convective conditions with homogeneous surface heat fluxes (Wyngaard and Brost 1984). The results were used for deriving parameterizations of fluxes and variances (Moeng and Sullivan 1994; Ayotte et al. 1996) and their dependence on varying strengths of the inversion (Sorbjan 1996). Detailed studies of entrainment processes were presented by Sullivan et al. (1998) and Kim et al. (2003). First studies are available considering the heterogeneity of surface fluxes (Maronga and Raasch 2013). The similarity relationships derived in Sorbjan (2005, 2006) were tested by only a few dedicated LESs so that it is still not clear whether these relationships are generally applicable.

However, it must be considered that most of the LES results introduced above were based on periodic

boundary conditions, homogeneous land surface conditions, and specific assumptions of the interaction of the free troposphere (damping layers) with the CBL. Effects of land surface heterogeneity, interaction of gravity waves with CBL turbulence, wind shear in the EL, inversion strengths, and large-scale forcing have often not been considered in detail. Only a few studies considering realistic heterogeneous surface were performed (e.g., Hechtel et al. 1990; Maronga and Raasch 2013) and these were used primarily to study the surface energy balance closure problem (Kanda et al. 2004). Thus, more realistic LES studies are still required, for example, by nesting them in mesoscale environments or by gray-zone experiments of limited area or even with global models.

Further progress has recently been achieved by the direct numerical simulation (DNS) of entrainment processes (e.g., Waggy et al. 2013; Garcia and Mellado 2014). These results have been applied to derive further insight in the dependence of entrainment velocities, variances, and fluxes as well as eddy diffusivity on scaling variables. Similar to LES, additional studies are required to study the validity of DNS results in inhomogeneous terrain and in dependence of the mesoscale environment.

Models are only as good as the data used for their verification. The only way to confirm similarity relationships, LES, and DNS of turbulent transport and exchange processes are observations with sufficient resolution and accuracy. This verification should be performed under a range of different meteorological conditions, both at the surface and throughout the mixed layer (ML) and the EL. The observations should provide not only measurements of profiles and gradients of atmospheric variables but also their turbulent fluctuations. Reaching the CBL top is possible with aircraft in situ or remote sensing instrumentation as well as ground-based, vertically steering, or scanning lidar or clear-air radar systems. Unfortunately, dedicated observations for studying LES and TPs are relatively sparse. Still, to date, most of the studies were performed using aircraft in situ turbulence sensors (e.g., Lenschow et al. 1994). Here, it is very challenging to derive instantaneous profiles of turbulent quantities owing to sampling issues and complex flight patterns with the operation of in situ sensors only. Furthermore, it is difficult to measure the distance between the flight lag and the CBL depth z_i , which is important to parameterize variables as functions of z/z_i (e.g., Turner et al. 2014a). Aircraft equipped with lidar systems flying close to the CBL top can deliver both vertical profiles and measurements of the spatial inhomogeneities (Crum and Stull 1987; Crum et al. 1987; Kiemle et al. 1997; Couvreux et al. 2005). However, aircraft campaigns are

expensive and relatively sparse so that it is difficult to relate the results to a variety of meteorological conditions. Mounting in situ sensors on tethered balloons may be another option but it is challenging to reach the CBL top, which can typically range up to 2000 m or more in some locations.

Therefore, for turbulence studies, it is worthwhile to apply a synergy of in situ measurements with airborne and ground-based remote sensing. Passive remote sensing systems such as Fourier-transform infrared (FTIR) (Turner and Löhnert 2014) spectroscopy and microwave radiometers (MWRs) (Löhnert et al. 2009) demonstrated great potential for ABL profiling. However, the vertical resolution of the retrievals, which are based on the inversion of the radiative transfer equation, is limited by the width of weighting functions to 500 m or more in the EL so that gradients of humidity and temperature are mostly averaged out (Wulfmeyer et al. 2015a). Furthermore, the retrievals are generally too noisy for resolving turbulent fluctuations (Kalthoff et al. 2013).

Clear-air radars observe either the refractive index structure parameter or reflectivity from insects (Emeis 2011). These features can be used to retrieve line-of-sight wind velocities or vertical wind speed. Clear-air radar does not provide direct measurements of wind speed because, in the case of structure parameter measurements, the first moment of the Doppler spectrum is influenced by covariances between reflectivity and radial velocity fluctuations (Muschinski and Sullivan 2013). Nevertheless, volume imaging of wind fields is possible with a resolution of a few seconds (e.g., Mead et al. 1998). In the case of insect backscatter, it is questionable whether these can be considered as tracers for atmospheric motion. Therefore, cloud radar signals are usually not evaluated with respect to wind speed in the clear CBL but in clouds.

The relation between the refractive index structure parameter and temperature and moisture gradients can also be applied for retrieving temperature and moisture profiles (Tsuda et al. 2001). However, this method relies on additional reference measurements of humidity and knowledge of the sign of the refractive index gradient so that its accuracy is limited and routine application is difficult. For temperature profiling, the radar acoustic sounding system (RASS) has been developed (e.g., Matuura et al. 1986). These systems measure the propagation speed of sound so that it is possible to retrieve the virtual temperature profile. This technique is limited by the altitude coverage when high horizontal winds carry the sound waves outside of the radar beam. Nevertheless, in the CBL, measurements of temperature profiles with turbulence resolution have been demonstrated (Angevine et al. 1993; Wulfmeyer 1999a).

Lidar systems measure range-resolved signals, which are directly related to atmospheric dynamics and thermodynamics. Thus, these have a great potential for deriving gradients and turbulent fluctuations of humidity, temperature, and wind, simultaneously. For decades, Doppler lidar (DL) systems, which measure the Doppler shift of aerosol particle backscatter by heterodyne detection, have been used for the profiling of higher-order turbulent moments of vertical wind and turbulent kinetic energy dissipation rate (Frehlich et al. 1998; Lenschow et al. 2000; Frehlich and Cornman 2002; Wulfmeyer and Janjić 2005; Hogan et al. 2009; Lathon et al. 2009; Tucker et al. 2009; Ansmann et al. 2010; Träumner et al. 2011; Lenschow et al. 2012). The routine operation of Doppler lidar systems is now possible, as these systems are commercially available and affordable from various companies.

With respect to water vapor profiling, two different lidar options are available. These are water vapor differential absorption lidar (WVDIAL) or water vapor Raman lidar (WVRL), which both can measure profiles and gradients of absolute humidity or mixing ratio as well as turbulent moments in the CBL (Wulfmeyer 1999b; Wulfmeyer et al. 2010; Turner et al. 2014a,b; Muppa et al. 2015). Combinations of these systems have been applied for ground-based profiling of the latent heat flux (Senff et al. 1994; Wulfmeyer 1999a; Giez et al. 1999; Linné et al. 2007; Behrendt et al. 2011) and higher-order moments (Wulfmeyer 1999b; Lenschow et al. 2000). The high accuracies and turbulence resolutions of WVDIAL and Doppler lidar from aircraft have also been used for latent heat flux profiling (Kiemle et al. 2007, 2011) and for detailed comparisons with LES (Couvreur et al. 2005, 2007). Particularly exciting is the fact that recently temperature rotational Raman lidar (TRRL) reached the resolution needed for temperature turbulence profiling as well (Hammann et al. 2015; Behrendt et al. 2015).

In this work, we are focusing on the capabilities and performances of ground-based lidar systems of this kind because these have the advantage that they can provide continuous profiling of mean profiles, gradients, and turbulence profiles improving sampling statistics during similar meteorological conditions. These systems are becoming available in different climate regimes: at the Atmospheric Radiation Measurement (ARM) Program Southern Great Plains site in Oklahoma, United States; in tropical regions such as the ARM site in Darwin, Australia (www.arm.gov/sites; operated from December 2010 until December 2014; Ackerman and Stokes 2003; Mather and Voyles 2013); and in the midlatitudes at various observatories such as Lindenberg, Germany, and Cabauw, the Netherlands; as well as during field campaigns such as the

Convective and Orographically-induced Precipitation Study (COPS) (Wulfmeyer et al. 2008, 2011) (www.uni-hohenheim.de/cops), the High Definition Clouds and Precipitation [HD(CP)²] Observational Prototype Experiment (HOPE) (<https://hdcp2.zmaw.de>), and the recent Surface Atmospheric Boundary Layer Exchange (SABLE) campaign (Wulfmeyer et al. 2015b).

We demonstrate that this novel synergy of lidar systems consisting of DL, WVDIAL/WVRL, and TRRL provides a complete dataset of gradients and turbulent moments for the verification of LES and similarity relationships. We focus on ground-based observations, as it is possible to deploy these lidar systems very close to each other for simultaneous measurements of covariances between different atmospheric variables. Furthermore, measurements can be collected under a variety of different conditions producing robust statistics of turbulent quantities in an affordable manner.

This study is organized as follows: In section 2, we derive an advanced set of scaling relationships in the CBL. Particularly, we derive relationships of momentum, latent heat, and sensible heat fluxes as well as higher-order moments to mean wind, temperature, and moisture gradients with particular emphasis on the EL. Furthermore, new equations for relating integral scales to turbulent quantities are derived. Particularly, what is to our knowledge for the first time, a novel technique for measuring the molecular destruction rates of water vapor and temperature variances is developed that are important components of the variance budget equations.

In section 3, we analyze the capabilities of DL, WVDIAL, WVRL, and TRRL for profiling vertical wind, water vapor, and temperature as well as their higher-order moments. We show how the lidar measurements can be combined for deriving fluxes and higher-order moments using measurements of vertical gradients of mean profiles. The results demonstrate that the proposed lidar synergy is necessary but also sufficient for providing a complete set of measurements for studying and verifying the proposed similarity relationships. It is also shown that these synergetic lidar measurements open up new possibilities for thorough comparisons with LES and detailed studies of TPs.

In section 4, we present first results using WVDIAL and TRRL for studying turbulence profiles up to the third order and their relationship to water vapor and temperature gradients as well as entrainment fluxes. We also get first insight into molecular destruction rates.

In section 5, the results are summarized. A series of new field campaigns in different climate regions is proposed as contributions to studies of land-atmosphere

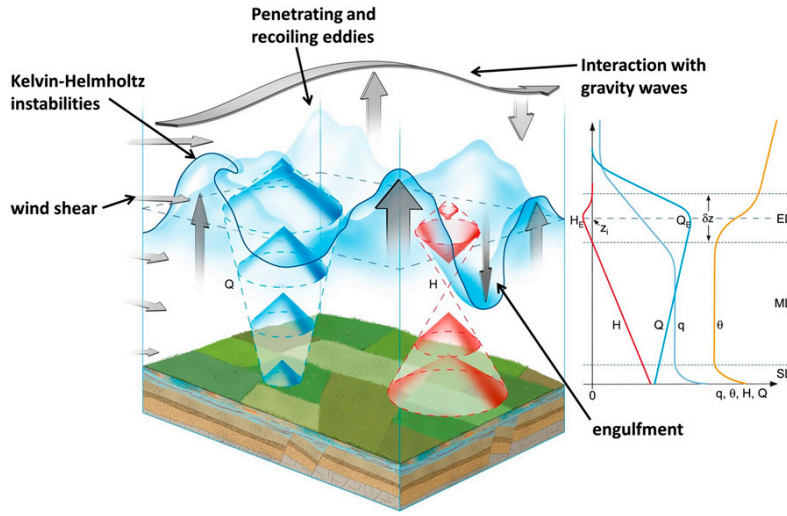


FIG. 1. The convective boundary layer: vertical structure and key processes. The cones on the left side of the figure indicate the mean direction (arrows) and the mean strength (diameters) of either the sensible heat (red) or the latent heat (blue) fluxes.

interaction as well as theories and parameterizations of turbulence in the CBL. In the appendix, the sensitivity of the results on systematic and noise errors is investigated and it is confirmed that the current state-of-the-art lidar systems are able to measure profiles and moments with high accuracy and resolution.

2. Convective boundary layer structure and entrainment

a. Vertical structure

The vertical structure and the turbulent activity of the CBL is depicted in Fig. 1. In a horizontally homogeneous, quasi-stationary, and well-mixed CBL it is expected that the mean potential temperature θ profile can be characterized by a negative gradient in the surface layer (SL), a constant in the ML, and an increase in the EL due to the temperature inversion.

Here, we define the entrainment zone as the region, in which a nonturbulent fluid from the free troposphere is mixed into the CBL and remains part of the CBL afterward. This can occur far downward in the CBL by engulfment, as often observed by remote sensing systems. In contrast, the EL or the interfacial layer is the region around the inversion at the CBL top, which can be used to locate the instantaneous and mean gradients as well as the mean entrainment flux (LeMone 2002).

In the SL, the mean specific humidity q profile should have a negative gradient as well, as long as significant

evapotranspiration is present, a slight negative gradient in the ML, and a stronger negative gradient in the EL. Well-mixed conditions are usually achieved after threefold to fourfold eddy turnover time or the CBL time scale $t^* \approx z_i/w_*$, where z_i is the mean CBL depth and w_* the convective velocity scale:

$$w_* = \left(\frac{G}{\bar{\theta}_v} z_i H_{v,0} \right)^{1/3}. \quad (1)$$

Here, G is the acceleration due to gravity, $\bar{\theta}_v$ is the mean virtual potential temperature in the CBL, and $H_{v,0}$ is surface buoyancy flux. Typical values of w_* in a well-developed CBL range between approximately 1 and 2 m s⁻¹.

In the absence of significant horizontal advection, the evolutions of θ and q are driven by the vertical divergences of the sensible and latent heat flux profiles (H and Q), respectively. Their absolute mean values and directions (the spectra and sizes are not shown) are indicated in Fig. 1 by the diameters and the directions of the cones, respectively. Whereas $H(z)$ must have a negative slope reaching a negative value in the EL, $Q(z)$ can have a negative or positive slope depending on whether the difference between the entrainment flux Q_E and the surface flux Q_0 is negative or positive. In any case, as long as there is a negative slope of q in the EL, then $Q_E > 0$. The understanding and the parameterization of these flux divergences—also for momentum—is the essence of TPs, which are fundamental for weather and climate modeling.

In the SL, the vertical stability can be characterized by the bulk Richardson number,

$$\text{Ri}_b = \frac{G}{\theta_a} z \frac{\theta_{va} - \theta_{vg}}{U_{\text{SL}}^2}, \quad (2)$$

where θ_a is the potential temperature in the surface layer; z is height above the displacement height in the canopy or in other land cover; θ_{va} and θ_{vg} are the virtual potential temperatures of the air and the land surface, respectively; and U_{SL} is the horizontal wind speed in the SL at height z . The depth of the SL can be defined by the extent to which the vertical change of fluxes is less than 10%. Over a homogeneous surface, the resulting vertical profiles of wind, temperature, and humidity can be described by the Monin–Obukhov similarity theory (MOST), which relates their gradients to surface fluxes and stability functions given for different ranges of Ri_b (Grachev et al. 2000; Poulos et al. 2002; Jiménez et al. 2012). The study and measurements of these relationships in the surface layer is possible by using scanning lidar systems and eddy covariance instrumentation and is subject of future publications.

In the ML, θ is nearly constant with height, indicating a well-mixed boundary layer. Vertical flux profiles are evolving in time and are well defined for a specific domain and time average. This can be studied by deriving integral length and temporal scales for the higher moments of the atmospheric variables and their covariances, which can be related to their sampling errors (Lenschow et al. 1994). Typically, 30–60-min averaging time is needed for deriving profiles of turbulent quantities with low noise and acceptable sampling errors on the order of 10%–20%. However, this averaging time may increase further at lower horizontal wind speed U . The amount and the gradient of q are strongly dependent on the ratio between the fluxes in the SL and the EL. As it is particularly challenging and crucial to derive entrainment fluxes, we will focus on vertical exchange processes in the EL.

b. The entrainment layer

The EL separates the ML from the free troposphere by a temperature inversion. The strength of this inversion and the entrainment flux are the result of a variety of interacting processes. These are indicated in Fig. 1 and are mainly due to four effects: 1) the engulfment of air from the free troposphere mixed downward in the turbulent CBL, 2) instabilities induced by wind shear at the EL interface such as Kelvin–Helmholtz and Holmboe waves, 3) penetrating and recoiling convective eddies, and 4) the propagation and excitation of wave modes such as gravity waves and their interaction with the turbulent eddies.

Consequently, various local and nonlocal processes are contributing to the fluxes, which are neither well understood nor accurately parameterized in state-of-the-art mesoscale models. Therefore, sophisticated theoretical concepts are necessary to understand the turbulent variables in the EL. These concepts have to be verified by new combinations of measurements.

1) HIGHER-ORDER MOMENTS AND ENTRAINMENT FLUXES

It can be expected that the flux Q through an interface such as the EL is related to the mean gradient of the variable of interest q so that

$$\mathbf{Q} = -\frac{1}{R} \nabla q, \quad (3)$$

where R is the resistance of the interface. This relationship from stochastic physics is not only used for studying turbulent transport in the atmosphere but also water transport in the soil or fluxes at the land surface (Zehe et al. 2014). The challenge is to relate in a comprehensive and physical way the resistance R to parameters that are expected to influence the entrainment fluxes. Thus, it is desirable to derive a closed set of scaling variables in the EL so that their gradients can be related to fluxes and higher-order turbulent moments. A corresponding set of equations was proposed by Sorbjan (1996, 2001, 2005, 2006) and reads

$$S_w = w_*, \quad (4)$$

$$S_L = \frac{w_*}{N_E}, \quad (5)$$

$$S_\theta = S_L \gamma_E = w_* \frac{\gamma_E}{N_E}, \quad \text{and} \quad (6)$$

$$S_q = S_L g_E = w_* \frac{g_E}{N_E}, \quad (7)$$

where S_w , S_L , S_θ , and S_q are the scaling variables for vertical velocity w statistics, the EL length scale L , the potential temperature θ , and the specific humidity q . The index E denotes that all variables and gradients are taken in the EL. The gradients of θ and q in the EL are γ_E and g_E , respectively. Alternatively, it may be reasonable to replace w_* by the standard deviation of the vertical velocity fluctuations $\sqrt{w'^2_E}$, which is easy to do in all following scaling relationships. For now, we stick with the hypothesis that w_* is the appropriate EL scaling variable.

The Brunt–Väisälä frequency N_E depends on the inversion strength in the EL according to

$$N_E = \sqrt{\beta_E \gamma_E}, \quad (8)$$

with the buoyancy parameter $\beta := G/\theta$.

This scaling [Eqs. (4)–(7)] is based on the following assumptions: 1) the turbulent fluctuations of the vertical wind in the EL scale with the buoyant forcing from the land surface and the CBL depth but not with the wind shear, 2) the time scale of fluctuations of atmospheric variables is the inverse of the Brunt–Väisälä frequency, 3) the most important scaling variable for temperature fluctuations is the mean potential temperature gradient at z_i , 4) the most important scaling variable for moisture fluctuations is its mean moisture gradient at z_i , and 5) despite the complex and different physical processes leading to local transport as depicted in Fig. 1, mean but not local gradients remain the most important scaling variables determining the entrainment flux averaged in time or in space over a homogeneous region.

Based on Eqs. (4)–(7), relationships for entrainment fluxes and higher-order moments can be derived. Entrainment fluxes for momentum $M_{u,v,E}$, temperature H_E , and moisture Q_E can be written by the combination of the scaling variables as

$$\begin{aligned} M_{u,v,E} &= -C_M S_L^2 s_{u,v,E} f_M(\text{Ri}_E) \\ &= -C_M \left(\frac{w_*}{N_E} \right)^2 s_E s_{u,v,E} f_M(\text{Ri}_E) \equiv -\frac{1}{R_{M,E}} s_{u,v,E}, \end{aligned} \quad (9)$$

$$\begin{aligned} H_E &= -C_H S_w S_\theta f_H(\text{Ri}_E) \\ &= -C_H w_*^2 \frac{\gamma_E}{N_E} f_H(\text{Ri}_E) \equiv -\frac{1}{R_{H,E}} \gamma_E, \end{aligned} \quad \text{and} \quad (10)$$

$$\begin{aligned} Q_E &= -C_Q S_w S_q f_Q(\text{Ri}_E) \\ &= -C_Q w_*^2 \frac{g_E}{N_E} f_Q(\text{Ri}_E) \equiv -\frac{1}{R_{Q,E}} g_E, \end{aligned} \quad (11)$$

where $M_{u,v,E}$ denotes the momentum fluxes in two horizontal wind directions described by the indices u and v . The constants C_M , C_H , and C_Q are positive and s_E is the wind shear in the EL such that

$$s_E^2 = \left(\frac{du}{dz} \Big|_E \right)^2 + \left(\frac{dv}{dz} \Big|_E \right)^2 =: (s_{u,E})^2 + (s_{v,E})^2. \quad (12)$$

By comparing Eqs. (9)–(11) with Eq. (3), indeed resistances with respect to each turbulent flux can be defined. Particularly, we expect that the resistances are functions of the gradient Richardson number

$$\text{Ri}_E = \frac{N_E^2}{s_E^2}, \quad (13)$$

which is conceptually similar to Eq. (2). In shearless conditions (free-convection limit) $s_E \rightarrow 0$; thus, $\text{Ri}_E \rightarrow \infty$. In this case, the functions $f_{M,H,Q}$ should reach the constant

value $\lim_{\text{Ri}_E \rightarrow \infty} f_{M,H,Q} = 1$. It may be worthwhile to absorb the constants C_M , C_H , and C_Q in these functions.

For the momentum flux M_E , Sorbjan (2009) analyzed LES datasets and found $C_M \cong 0.2$ and

$$f_M(\text{Ri}_E) = 1 - \frac{1}{\text{Ri}_E}, \quad (14)$$

which is proposed for $\text{Ri}_E > 1$.

For the interfacial heat and humidity fluxes, Sorbjan (2005, 2006) estimated $C_H \cong 0.012$ and $C_Q \cong 0.025$ as well as the dependence of the fluxes on Ri_E by LES and achieved

$$f_{H,Q}(\text{Ri}_E) = \frac{1 + c_{H,Q}/\text{Ri}_E}{\sqrt{1 + 1/\text{Ri}_E}}, \quad (15)$$

where the coefficients $c_{H,Q}$ were assessed to be $c_H \cong c_Q \cong 8$.

In an analogous way, second-order moments of the vertical wind, temperature, and humidity fluctuations can be arranged as follows:

$$\overline{w^2}_E = C_{w^2} S_w^2 f_{w^2}(\text{Ri}_E) = C_{w^2} w_*^2 f_{w^2}(\text{Ri}_E), \quad (16)$$

$$\overline{\theta^2}_E = C_{\theta^2} S_\theta^2 f_{\theta^2}(\text{Ri}_E) = C_{\theta^2} w_*^2 \left(\frac{\gamma_E}{N_E} \right)^2 f_{\theta^2}(\text{Ri}_E), \quad \text{and} \quad (17)$$

$$\overline{q^2}_E = C_{q^2} S_q^2 f_{q^2}(\text{Ri}_E) = C_{q^2} w_*^2 \left(\frac{g_E}{N_E} \right)^2 f_{q^2}(\text{Ri}_E). \quad (18)$$

In the case of EL temperature and humidity variances, Sorbjan (2006) suggested $C_{\theta^2} \cong 0.04$ and $C_{q^2} \cong 0.175$ as well as a functional dependence on Ri_E of the form

$$f_{\theta^2,q^2}(\text{Ri}_E) = \frac{1 + c_{\theta^2,q^2}/\text{Ri}_E}{1 + 1/\text{Ri}_E}. \quad (19)$$

The coefficients c_{θ^2} and c_{q^2} have still to be estimated. For vertical wind, both the function $f_{w^2}(\text{Ri}_E)$ and the coefficient C_{w^2} need to be determined as well.

Figure 2 presents the dependence of the functions f_M , $f_{H,Q}$, and f_{θ^2,q^2} on Ri_E for typical ranges of the proposed constants. The function f_M shows a strong nonlinear behavior for $\text{Ri}_E < 10$ and the momentum flux decreases between $1 < \text{Ri}_E < 10$ by more than an order of magnitude. The other functions show basically three regimes, which may be related to different entrainment processes. In the first regime for $\text{Ri}_E \leq 0.1$, the function f_{θ^2,q^2} is leveling off and approaches the constant value c_{θ^2,q^2} . This may be the range where entrainment is mainly determined by the engulfment of overturning eddies. In contrast, $f_{H,Q}$ is not converging to a limited value but to ∞ for $\text{Ri}_E \rightarrow 0$. It is very important to test this different

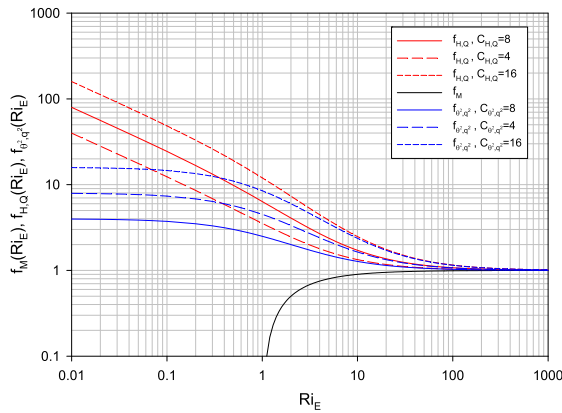


FIG. 2. The functions f_M , $f_{H,Q}$, and f_{θ^2,q^2} for scaling fluxes and variance in dependence of Ri_E . The functions $f_{H,Q}$ and f_{θ^2,q^2} are presented around constants derived by LES.

behavior of the flux and variance scaling functions by additional LES and observations. In the transition regime from $0.1 < Ri_E < 10$, different processes may be responsible for the strength of entrainment simultaneously. Finally, for $Ri_E > 10$, both functions $f_{H,Q}$ and f_{θ^2,q^2} are converging to unity and entrainment may mainly be determined by Kelvin–Helmholtz instabilities and interaction with gravity waves. Please note that these results depend on the grid resolution of the corresponding LES. Further refinements are required by LES with increased grid resolution or DNS. It is also important to explore the difference in scaling using Ri_E , which is proposed here and the bulk Richardson number, which was used, for example, in Sullivan et al. (1998) and Trümner et al. (2011).

A similar approach as for the variances may be used to describe the third moments of w' , θ' , and q' in the EL:

$$\overline{w'^3} = C_{w^3} S_{w^3}^3 f_{w^3}(Ri_E) = C_{w^3} w_*^3 f_{w^3}(Ri_E), \quad (20)$$

$$\overline{\theta'^3} = C_{\theta^3} S_{\theta^3}^3 f_{\theta^3}(Ri_E) = C_{\theta^3} w_*^3 \left(\frac{\gamma_E}{N_E} \right)^3 f_{\theta^3}(Ri_E), \quad \text{and} \quad (21)$$

$$\overline{q'^3} = C_{q^3} S_{q^3}^3 f_{q^3}(Ri_E) = C_{q^3} w_*^3 \left(\frac{g_E}{N_E} \right)^3 f_{q^3}(Ri_E). \quad (22)$$

However, this hypothesis would need to be tested extensively to ensure that the magnitude of the third moments is indeed proportional to the cubes of the gradients for θ and q at z_i as well as to determine the dependence on Ri_E and the coefficients C_{w^3} , C_{θ^3} , and C_{q^3} .

2) DETERMINATION OF INTEGRAL SCALES AS WELL AS DISSIPATION AND DESTRUCTION RATES

We start with the evaluation of stationary turbulence. This is the case if the time series of the fluctuating variable $q(t)$ can be separated into

$$q(t) = q'(t) + \overline{q(t)}, \quad (23)$$

where $\overline{q(t)}$ is a slowly varying component, which can be derived by low-pass filtering or subtracting a linear trend, and $\overline{q'(t)} = 0$. Of course, this analysis can be performed at each height level in the CBL including the EL; however, for the sake of simplicity we omit an index for the height level in the following. The autocovariance function A of this time series is defined as

$$A_q(t_1, t_2) \equiv \overline{[q(t_1) - \overline{q(t_1)}][q(t_2) - \overline{q(t_2)}]}. \quad (24)$$

If the time series $q(t)$ is stationary then

$$A_q(t_1, t_2) = A_q(t_1 - t_2) = A_q(t_2 - t_1) = A_q(\tau) \quad (25)$$

with $|A_q(\tau)| \leq A_q(0)$.

The structure function D of a variable q is defined according to

$$D_q(t_1, t_2) = \overline{[q(t_1) - q(t_2)]^2} \quad \text{or} \\ D_q(\tau) = \overline{[q(t + \tau) - q(t)]^2}. \quad (26)$$

If the time series is stationary, it is easy to show

$$D_q(\tau) = 2[A_q(0) - A_q(\tau)] \quad \text{and} \\ A_q(\tau) = A_q(0) - 0.5D_q(\tau). \quad (27)$$

In the spatial domain, the structure function reads

$$D_q(\mathbf{r}_1, \mathbf{r}_2) = \overline{[q(\mathbf{r}_1) - q(\mathbf{r}_2)]^2} \quad (28)$$

and if the field is locally homogeneous and isotropic then

$$D_q(\mathbf{r}_1, \mathbf{r}) = \overline{[q(\mathbf{r}_1 + \mathbf{r}) - q(\mathbf{r}_1)]^2} \equiv D_q(r) \quad (29)$$

and the relations

$$D_q(r) = 2A_q(0) - 2A_q(r) \quad \text{and} \\ A_q(r) = A_q(0) - 0.5D_q(r) \quad (30)$$

hold.

In the following, we assume that either by high-resolution modeling or measurements, the inertial subrange is resolved for a sufficient short lag of the time series. The inertial subrange lies in between the inner and outer scales of turbulence where it is assumed locally homogeneous and isotropic. Now, we can analyze these equations with respect to the time series of vertical wind, humidity, and temperature at different heights. It was shown in Tatarski (1961) and Monin and Yaglom (1975) that

$$D(r) = C^2 r^{2/3} \quad (31)$$

with the structure parameters C^2 for vertical wind velocity

$$C_w^2 \cong C_K \varepsilon^{2/3}, \quad (32)$$

humidity

$$C_q^2 \cong a_q^2 \frac{\bar{N}_q}{\varepsilon^{1/3}}, \quad (33)$$

and potential temperature

$$C_\theta^2 \cong a_\theta^2 \frac{\bar{N}_\theta}{\varepsilon^{1/3}}, \quad (34)$$

where ε is the turbulent kinetic energy (TKE) dissipation rate, and \bar{N}_q and \bar{N}_θ are the destruction rates of humidity and potential temperature variances due to molecular processes, respectively. The constants in Eqs. (32)–(34) are considered universal in the inertial subrange. The Kolmogorov constant $C_K \cong 2$ and the constants a_q^2 and a_θ^2 are expected to be in the range 2.8–3.2 (Stull 1988).

Consequently, one way of determining dissipation and destruction rates is to start with the autocovariance function A in the time domain and to assume Taylor's hypothesis of frozen turbulence in the inertial subrange. Then,

$$A_w(\tau) = \overline{w^2} - \varepsilon^{2/3} U^{2/3} \tau^{2/3}, \quad (35)$$

$$A_q(\tau) = \overline{q^2} - 0.5 a_q^2 \frac{\bar{N}_q}{\varepsilon^{1/3}} U^{2/3} \tau^{2/3}, \quad \text{and} \quad (36)$$

$$A_\theta(\tau) = \overline{\theta^2} - 0.5 a_\theta^2 \frac{\bar{N}_\theta}{\varepsilon^{1/3}} U^{2/3} \tau^{2/3}. \quad (37)$$

Using these equations, the atmospheric variance, the dissipation and destruction rates, and the integral scales can be determined, respectively, if the autocorrelation functions and the horizontal wind profile $U(z)$ are known.

This can be shown as follows: all autocovariance functions have the form

$$A(\tau) = \nu_a - k \tau^{2/3}, \quad (38)$$

insofar that distortions by mesoscale variability in the inertial subrange can be neglected. In the following, we assume that this is the case, which can be tested by studying the shape of A for $\tau < \mathcal{T}$, where \mathcal{T} is the integral time scale. If the shapes of the data and the fit agree well, the extrapolation of the structure function fit to the autocovariance data to lag zero yields the atmospheric variance ν_a and the coefficient of the structure function k . This technique separates the atmospheric and the noise variance at lag 0, which is necessary as the latter can often not be neglected [see also the appendix and Eq. (A9)].

The autocorrelation function AC is defined as

$$\text{AC}(\tau) = 1 - \frac{k}{\nu_a} \tau^{2/3}. \quad (39)$$

The root of this equation is

$$\tau_0 = \left(\frac{\nu_a}{k} \right)^{3/2} \quad (40)$$

so that the respective integral time scale can be estimated according to

$$\mathcal{T} = \int_0^{\tau_0} \text{AC}(\tau) d\tau = \int_0^{\tau_0} \left(1 - \frac{k}{\nu_a} \tau^{2/3} \right) d\tau, \quad (41)$$

which yields

$$\mathcal{T} = \frac{2}{5} \left(\frac{\nu_a}{k} \right)^{3/2}. \quad (42)$$

Please note that this integration is an approximation of the integral scale of the turbulence fluctuations because we do not integrate to infinity but to the first zero crossing of $\text{AC}(\tau)$. However, this turned out as a good compromise for separating turbulent fluctuations from mesoscale variability and for getting robust results under the presence of significant system noise (Lenschow et al. 2000; Wulfmeyer et al. 2010; Behrendt et al. 2015).

If the shape of AC is mainly controlled by homogeneous and isotropic turbulence, the ratio between the root and the integral scale gives an estimate of how many lags should be used for the interpolation of the structure function. One natural choice is to take approximately $2\mathcal{T}/\Delta t$ lags, where Δt is the resolution of the time series. If the shape of AC is contaminated by mesoscale variability, then an iteration between the fit of the structure function and the determination of the integral scale may be necessary, resulting in a reduction of the number of lags.

The integration of AC yields the dependence of \mathcal{T} or the integral length scales $\mathcal{R} \cong U\mathcal{T}$ on atmospheric variables:

$$\mathcal{T}_w = \frac{2}{5} \left(\sqrt{\overline{w^2}} \right)^3 \frac{1}{\varepsilon U}, \quad \mathcal{R}_w = \frac{2}{5} \left(\sqrt{\overline{w^2}} \right)^3 \frac{1}{\varepsilon}, \quad (43)$$

$$\mathcal{T}_q = \frac{2\sqrt{8}}{5a_q^3} \left(\sqrt{\overline{q^2}} \right)^3 \sqrt{\frac{\varepsilon}{\bar{N}_q^3}} \frac{1}{U},$$

$$\mathcal{R}_q = \frac{2\sqrt{8}}{5a_q^3} \left(\sqrt{\overline{q^2}} \right)^3 \sqrt{\frac{\varepsilon}{\bar{N}_q^3}}, \quad \text{and} \quad (44)$$

$$\mathcal{T}_\theta = \frac{2\sqrt{8}}{5a_\theta^3} \left(\sqrt{\overline{\theta^2}} \right)^3 \sqrt{\frac{\varepsilon}{\bar{N}_\theta^3}} \frac{1}{U}, \quad \mathcal{R}_\theta = \frac{2\sqrt{8}}{5a_\theta^3} \left(\sqrt{\overline{\theta^2}} \right)^3 \sqrt{\frac{\varepsilon}{\bar{N}_\theta^3}}. \quad (45)$$

For the vertical wind, its integral time scale is inversely proportional to the dissipation rate and proportional to the 3/2 power of the variance. It can be expected that variance and dissipation are related variables (larger variance leading to larger dissipation), which can be investigated now with our methodology.

In contrast, the integral scales for humidity and potential temperature are proportional to the square root of the TKE dissipation rate and inversely proportional to the 3/2 power of their destruction rates, respectively. The dependence on the variance profiles is the same as for vertical wind. In the future, it will be very interesting to compare the behavior of molecular destruction and TKE dissipation rates and their dependence on various atmospheric conditions. The results can be used for studying the processes controlling their height dependence.

This can be realized in the following way. Combining the fit of the AC functions or the resulting integral scales with the coefficients of the structure functions permits the direct estimation of dissipation rates. For example, for vertical velocity

$$k_w = \varepsilon^{2/3} U^{2/3} \quad \text{and} \quad (46)$$

$$\varepsilon = \frac{k_w^{3/2}}{U} \quad (47)$$

$$= \frac{2}{5} \frac{(\sqrt{w^2})^3}{U \mathcal{T}_w} = \frac{2}{5} \frac{(\sqrt{w^2})^3}{\mathcal{R}_w}. \quad (48)$$

As the integral scale for vertical wind generally varies less than a factor of 2 with height in the mixed layer and the EL (Lenschow et al. 2000; Lothon et al. 2006), the shape of the ε profile is mainly determined by the profile of the vertical velocity variance.

Correspondingly, for humidity

$$k_q = \frac{1}{2} a_q^2 \frac{\bar{N}_q}{\varepsilon^{1/3}} U^{2/3}, \quad (49)$$

elimination of U with Eq. (47)

$$\frac{k_q}{k_w} = \frac{1}{2} a_q^2 \frac{\bar{N}_q}{\varepsilon}, \quad (50)$$

or elimination of ε with Eq. (47)

$$k_q = \frac{1}{2} a_q^2 \frac{\bar{N}_q}{\sqrt{k_w}} U, \quad (51)$$

thus

$$\bar{N}_q = \frac{2k_q \sqrt{k_w}}{a_q^2} \frac{1}{U}, \quad (52)$$

or using Eqs. (43) and (44)

$$\bar{N}_q = \frac{4}{5} \frac{\bar{q}^2 \sqrt{w^2}}{a_q^2 \mathcal{T}_q^{2/3} \mathcal{T}_w^{1/3} U} = \frac{4}{5} \frac{\bar{q}^2 \sqrt{w^2}}{a_q^2 \mathcal{R}_q^{2/3} \mathcal{R}_w^{1/3}}. \quad (53)$$

In an analogous way for potential temperature

$$k_\theta = \frac{1}{2} a_\theta^2 \frac{\bar{N}_\theta}{\varepsilon^{1/3}} U^{2/3}, \quad (54)$$

$$\frac{k_\theta}{k_w} = \frac{1}{2} a_\theta^2 \frac{\bar{N}_\theta}{\varepsilon}, \quad (55)$$

$$\bar{N}_\theta = \frac{2k_\theta \sqrt{k_w}}{a_\theta^2} \frac{1}{U}, \quad (56)$$

or using Eqs. (43) and (45)

$$\bar{N}_\theta = \frac{4}{5} \frac{\bar{\theta}^2 \sqrt{w^2}}{a_\theta^2 \mathcal{T}_\theta^{2/3} \mathcal{T}_w^{1/3} U} = \frac{4}{5} \frac{\bar{\theta}^2 \sqrt{w^2}}{a_\theta^2 \mathcal{R}_\theta^{2/3} \mathcal{R}_w^{1/3}}. \quad (57)$$

Using Eqs. (49) and (54) we achieve

$$\frac{k_q}{k_\theta} \simeq \frac{\bar{N}_q}{\bar{N}_\theta}. \quad (58)$$

Obviously, LES and DNS output or simultaneous measurements of wind, humidity, and potential temperature profiles at high temporal and spatial resolution permit the estimation of the ratio of dissipation rates [Eqs. (50) and (55)] as well as their absolute values [Eqs. (47) and (48), Eqs. (52) and (53), and Eqs. (56) and (57)] provided that accurate measurements of horizontal wind are available. Of course, these equations are only applicable if the conditions of locally homogeneous and isotropic turbulence as well as Taylor's hypothesis are valid.

3) DISCUSSION

For deriving quantitative results, it is essential that all the turbulent quantities introduced above are estimated as accurate and as general as possible. This may be accomplished with turbulence theory, by dedicated LES and DNS studies, and by measurements. As we are not aware of a turbulence theory that permits the derivation of the unknown resistances and dissipation/destruction rates, these relationships need to be tested considering different heterogeneous land surface forcings, stabilities in EL, wind shear, and gravity wave conditions. Furthermore, it is necessary to explore dependencies of fluxes and higher-order moments on different definitions of the Richardson number in the EL and to refine the functional dependence of fluxes and variances on the Richardson number. From the modeling perspective, this requires a chain of mesoscale model simulations

down to the gray zone or the LES scale in order to imbed the model domain with turbulence resolution in a realistic synoptic and mesoscale environment. It is worthwhile to note that the relationships introduced in sections 2b(1) and 2b(2) also provide essential components of CBL energy and water budgets. For instance, dissipation and molecular destruction rates as well as flux divergences are part of these budgets.

Either using idealistic LES and DNS or gray-zone simulations, the results have to be verified by observations. Gradients play an important role in the magnitude of the variances and fluxes, so accurate profiles of horizontal wind, humidity, and potential temperature in the ML, the EL, and the lower free troposphere are critical (Sorbjan 2009). Here, we are focusing on turbulent processes around the EL. So far, particularly in this region, field experiments have not provided suitable datasets that are capable to confirm the complete set of relationships between gradients, variances, fluxes, and dissipation/destruction rates. In the following, we demonstrate that this can be accomplished with a new synergy of lidar systems.

3. Lidar synergy for studying entrainment fluxes as well as dissipation and variance destruction rates

a. Basic observational requirements

To study the relationships between fluxes and gradients [Eqs. (9)–(11)], variances and gradients [Eqs. (16)–(18)], and even higher-order moments [Eqs. (20)–(22)], it is necessary that four conditions are fulfilled: 1) wind, temperature, and humidity profiles must be measured simultaneously with small and height-independent bias in the ML, the EL, and the lower free troposphere; 2) the vertical resolution of the measurements must be high enough to resolve the gradients in the profiles, particularly in the EL; 3) the temporal resolutions of the measurements must be high enough to resolve turbulent fluctuations; and 4) the precision of the measurements must be high enough so that vertical structures in the turbulence profiles can be resolved.

Currently, it is hardly possible to realize this with airborne in situ or remote sensing measurements. Research aircraft with in situ sensors provide measurements of the required variables but only at a specific height level. Therefore, it is difficult to derive a comprehensive dataset of gradient, variance, and flux profiles under different meteorological conditions especially at a range of heights in the ML and the EL. The horizontal and vertical structure of the CBL can be studied by lidar systems deployed on aircraft but these campaigns are sparse and expensive. Another option is a combination of ground-based scanning lidar systems but their development and

application is still at its infancy. The height of meteorological towers is generally too low to reach the daytime EL, except special meteorological conditions over land (Zhou et al. 1985), so that these structures also do not come into consideration for deriving comprehensive statistics. Tethered balloons with a combination of in situ sensors may be an option but it will be difficult to get vertical profiles and to reach the CBL top, especially in continental CBLs that can be 2 km deep or more.

Passive infrared and microwave spectrometers may be an approach for retrieving temperature and humidity profiles; however, it has been shown that their temporal and vertical resolution is neither capable of resolving gradients nor turbulent fluctuations in the EL (Wulfmeyer et al. 2015a). In the following, we demonstrate that a synergy of active lidar remote sensing systems with the required vertical and temporal resolutions should be able to provide the desired data.

b. Properties and performance of lidar systems

Recent advances in lidar technology permitted the development of three types of lidar systems, which can measure wind, humidity, and temperature profiles with high resolution and accuracy. The DL can measure either vertical wind profiles in the vertical steering mode or horizontal wind profiles in the velocity azimuth display (VAD or scanning in azimuth at a fixed off-zenith elevation) mode. The signal-to-noise ratio (SNR) of the line-of-sight wind measurements is high enough to reach resolutions of 1 s and 30 m with noise errors on the order of 0.1 m s^{-1} . Systematic errors in line-of-sight (LOS) wind measurements are typically on the order of a few centimeters per second. This performance has been demonstrated for decades using research systems like the high-spectral-resolution Doppler lidar (HRDL) of the National Oceanic and Atmospheric Administration (NOAA) (Lenschow et al. 2000; Wulfmeyer and Janjić 2005; Lothon et al. 2009; Lenschow et al. 2012). Furthermore, horizontal wind profiles can be measured by VAD scans. A recent breakthrough in the development of compact, efficient, and eye-safe laser transmitters such as Er-doped fiber lasers permitted the development of very compact, all-solid-state systems, which are now commercially available from different companies (e.g., Philippov et al. 2004; Kameyama et al. 2007).

With respect to water vapor profiling, two methods are available: WVDIAL and WVRL. WVRLs measure profiles of water vapor mixing ratio m . As mixing ratio m can be readily converted to specific humidity q in the CBL by standard pressure and temperature profiles, in the following, we consider only q as the measured variable.

Operational WVRLs have been installed at only a few sites such as the ARM Program Southern Great Plains (SGP) WVRL (Turner et al. 2002). The design and installation of WVRL systems is usually the result of a special project. Extensive research led to a routine technique for the calibration of mixing ratio measurements, which is necessary for WVRL, with an accuracy of approximately 5% (Turner and Goldsmith 1999; Ferrare et al. 2006). Optimization of daytime performance, which is particularly critical for Raman lidar, was mainly achieved with the SGP Raman lidar and has not been accomplished at all sites. Typically, in the daytime, the noise error is less than 1 g kg^{-1} up to the CBL top using a combination of temporal and vertical resolutions of 10 s and 75 m, respectively. For the SGP WVRL, Wulfmeyer et al. (2010) and Turner et al. (2014a,b) demonstrated that this performance is sufficient for measuring profiles of higher-order moments of mixing ratio in the CBL. These higher-order moments derived from noisy lidar observations have also been validated with in situ measurements (Turner et al. 2014a). Furthermore, ARM has operated a nearly identical Raman lidar at Darwin, Australia, which provides a tropical dataset to complement the SGP midlatitude one.

The WVDIAL technique measures the absolute humidity ρ as a function of range. Similar to WVRL, it is straightforward to convert ρ in q with high accuracy by standard pressure and temperature profiles so that we continue to consider q as the measured variable. The technologically more demanding WVDIAL technique is less mature. To the best of our knowledge, just one ground-based system exists worldwide at the Institute of Physics and Meteorology (IPM) of the University of Hohenheim (UHOH) that has daytime turbulence resolution. Currently, this system has the highest temporal and spatial resolution of ground-based water vapor remote sensing systems (Behrendt et al. 2009; Wulfmeyer et al. 2015a). As DIAL does not need a calibration with respect to system constants, a very high accuracy of absolute humidity measurements is achieved. Recently, Späth et al. (2014) demonstrated by theoretical considerations and comparisons with soundings a systematic error of 2%. Because of the high signal-to-noise-ratio of the backscatter signals during daytime, the noise error is about an order of magnitude lower than WVRL using the same combination of vertical and temporal resolutions (Wulfmeyer et al. 2015a). Therefore, WVDIAL is an excellent instrument for measuring water vapor profiles, gradients, and higher-order moments (Muppa et al. 2015).

The TRRL technique is currently the only remote sensing technique that permits the profiling of temperature, its higher-order turbulent moments, and its gradient

in the lower troposphere with high vertical resolution (Wulfmeyer et al. 2015a). Because of a recent breakthrough in system design and performance at IPM, Hammann et al. (2015) demonstrated that it is now possible to determine the strength of the inversion layer during daytime. Comparisons with soundings, which are necessary for the calibration of TRRL, revealed a systematic error of less than 1 K. The noise error of temperature profiles is less than 2 K using resolutions of 10 s and 100 m up to 2 km, which permitted the first profiling of higher-order moments of temperature (Behrendt et al. 2015). Noise error propagation [see Eq. (A14)] explains that it is still possible to extract accurate atmospheric variance measurements at this noise level and that these measurements are particularly significant in the EL. Therefore, the TRRL method is now suited to provide the temperature measurements necessary for the turbulence studies that are subject of this work. As it is easily possible to convert temperature profiles measured with TRRL into profiles of potential temperature and their fluctuations (Behrendt et al. 2011), we continue to use the variable θ in our considerations. Furthermore, the combination of WVRL, WVDIAL, and TRRL permits a straightforward interchange of the different humidity variables m , ρ , and q . Although none of these systems is commercially available yet, new technologies are emerging having this potential (e.g., Spuler et al. 2015).

A single lidar system does not measure fluxes directly. However, the combination of high-resolution vertical wind measurements by DL or a radar wind profiler with WVDIAL or WVRL and TRRL permits the determination of latent and sensible heat flux profiles with the eddy correlation (EC) technique directly, which was originally pioneered in Senff et al. (1994) and also demonstrated by Wulfmeyer (1999a) and Giez et al. (1999). The confirmation that sensible heat flux profiles can be measured by a DL-TRRL combination was recently provided by Wulfmeyer et al. (2015b).

Furthermore, the instantaneous CBL height $z_i(t)$ and correspondingly the mean z_i during the averaging period can be measured very accurately (e.g., Pal et al. 2010). Different methods using vertical gradients of mean profiles and variance profiles can also be compared. This is important for appropriate CBL scaling and for the localization of the EL.

c. Proposed experimental design

A considerable advantage of the application of the lidar system synergy in the CBL is its capability to profile atmospheric variables, their gradients, turbulent moments, and fluxes simultaneously. The combination of these lidar measurements permits a thorough study of

EL scaling by testing different combinations of the equations above allowing both the general relationships (e.g., is the water vapor variance proportional to the square of the mean gradient?) to be evaluated and estimates of the coefficients to be made.

For instance, the combination of lidar systems permits a complete verification of the set of Eqs. (9)–(11), Eqs. (16)–(18), and even Eqs. (20)–(22). If lidar systems demonstrate that these relationships are valid, their measurements can be used for deriving unique quantitative results with respect to fluxes and higher-order moments, as various constants can be determined by means of comparisons.

We recommend the following combination of lidar instruments:

- One scanning Doppler lidar for determining wind profiles in the CBL and the wind shear in the EL. This lidar would primarily perform VAD scans so that horizontal wind profiles could be derived.
- One vertically pointing Doppler lidar for vertical wind measurements and profiling of its higher-order moments. It may be possible to perform these measurements with a single Doppler lidar by switching between vertical and VAD operation modes, if the SNR is high enough. This would need to be investigated by studying the performance characteristics of the particular DL that would be used.
- One vertically pointing DIAL or WVRL with sufficient resolution measuring profiles of q and g as well as profiles of higher-order moments of q .
- One vertically pointing TRRL with sufficient resolution for measuring θ and γ profiles as well as higher-order moments of θ .

In addition to allowing the equations for fluxes and higher-order moments to be investigated, this combination permits a direct measurement of Ri as well as dissipation and molecular destruction rates.

d. Strategy for investigation of CBL scaling based on lidar synergy

Three important contributions of lidar measurements are possible: 1) the direct measurement and independent development of CBL similarity relationships based on the lidar synergy proposed above, 2) the test of the CBL relationships introduced in section 2b, and 3) use of these measurements for model verification. The direct determination of CBL similarity relationships is being addressed by field campaign data such as HOPE in spring 2013, SABLE in August 2014 in Germany, and at the ARM operational sites at SGP and Darwin, from which measurements of a combination of gradients and higher-order turbulent moments of atmospheric variables are available.

In this case, the following data analysis procedure is suggested:

- 1) Determination of all profiles of mean variables, their gradients, and higher-order moments and their characterization with respect to their errors, as discussed in sections 3c(1) and 3c(2).
- 2) Investigation of integral scales for making sure that the major part of the turbulent fluctuations is resolved.
- 3) Performance of the same procedure for the combined variables such as fluxes and dissipation and molecular destruction rates [sections 2b(1), 2b(2), and 3c(2)].

Using these results, the data can be combined and correlated in different ways in order to search for their relationships.

1) RICHARDSON NUMBER RELATIONSHIPS

For studying the relationships introduced in section 2b, first of all, it is essential to study the Ri_E dependence of variances and third-order moments. For instance, using Eqs. (16)–(18), we get

$$f_{w^2}(Ri_E) = \frac{1}{C_{w^2}} \frac{\overline{w'^2}_E}{w_*^2}, \quad (59)$$

$$f_{\theta^2}(Ri_E) = \frac{1}{C_{\theta^2}} \frac{\overline{\theta'^2}_E}{w_*^2 (\gamma_E/N_E)^2}, \quad \text{and} \quad (60)$$

$$f_{q^2}(Ri_E) = \frac{1}{C_{q^2}} \frac{\overline{q'^2}_E}{w_*^2 (g_E/N_E)^2}. \quad (61)$$

For example, if the relationship for moisture [Eq. (19)] is valid, we find

$$Ri_E = \frac{\frac{1}{C_{q^2}} \frac{\overline{q'^2}_E}{w_*^2 (g_E/N_E)^2} - c_{q^2}}{1 - \frac{1}{C_{q^2}} \frac{\overline{q'^2}_E}{w_*^2 (g_E/N_E)^2}}. \quad (62)$$

This equation makes a direct measurement of Ri_E possible merely based on a combination of temperature and water vapor lidar systems. This same approach allows for determining the values of the coefficients C_{q^2} and c_{q^2} as measurements of Ri_E will be available directly from the combination of DL and TRRL [Eq. (13)]. Naturally, many cases would be needed to develop uncertainty estimates for these coefficients and to see if these coefficients have any dependence on the meteorological regime. An analogous equation can be derived for Ri_E in dependence of temperature variance and gradients.

2) HIGHER-ORDER MOMENT RELATIONSHIPS

By the combination of gradient and variance measurements as well as the knowledge of Ri_E , Eqs. (16)–(18) can be studied. First attempts have already been performed by Wulfmeyer et al. (2010) and Turner et al. (2014b). However, for these studies neither wind nor temperature profiles were available yet, so further refinements and the use of more expanded datasets are necessary.

The question arises whether measurements of higher-order moments are helpful to get additional insight regarding turbulence in the EL. These lidar studies may lead to a refinement of the similarity relationships. For instance, focusing on humidity, if Eqs. (18) and (22) are valid, the skewness \mathcal{S}_q in the EL should be negative because

$$\mathcal{S}_q := \frac{\overline{q^3}_E}{(\overline{q^2}_E)^{3/2}} \quad (63)$$

$$= \frac{C_{q^3} w_*^3 (g_E/N_E)^3 f_{q^3}(\text{Ri})}{[C_{q^2} w_*^2 (g_E/N_E)^2 f_{q^2}(\text{Ri})]^{3/2}} \quad (64)$$

$$= -\frac{C_{q^3}}{C_{q^2}^{3/2}} \frac{f_{q^3}(\text{Ri})}{[f_{q^2}(\text{Ri})]^{3/2}} \quad (65)$$

$$\cong -\frac{C_{q^3}}{C_{q^2}^{3/2}}, \quad (66)$$

where the last equation holds in the case of free convection. Under these conditions, the dependence on gradients is eliminated because the relationships are self-similar. Obviously, the similarity relationships propose a negative \mathcal{S}_q in the EL. However, we already know from our measurements that this is not correct but \mathcal{S}_q changes sign from negative to positive in the EL typically just below z_i (Wulfmeyer 1999a; Lenschow et al. 2000; Wulfmeyer et al. 2010; Turner et al. 2014b). The reason for this discrepancy is likely the inappropriate expansion of the scaling relationship for the variance [Eq. (18)] to the third-order moment [Eq. (22)]. This is a first interesting test of the similarity relationships demonstrating the potential of the lidar observations. Additionally, if the coefficients and the dependencies on Ri_E are known, Eq. (65) provides another estimate of Ri_E , which may be useful for studying the consistency of the set of equations.

For vertical wind, it is straightforward to see that the relationships prescribe that $\mathcal{S}_w > 0$. Indeed, this can be confirmed by most measurements (Lenschow et al. 2000, 2012). However, while \mathcal{S}_w remains positive in the EL, there seems to be a negative slope leading to a reduction in the EL, which is not predicted. Thus, a very important topic will be the study of the behavior of third-order moments in the EL of the CBL.

3) FLUX RELATIONSHIPS

Particularly interesting is the application of EL scaling in a way that a minimum set of lidar systems can be applied for deriving fluxes taking advantage of their measurements of higher-order moments. There is indeed an interesting potential because, for example, the combination of Eq. (11) and the square root of Eq. (18) yields

$$Q_E = \frac{C_Q}{\sqrt{C_{q^2}}} w_* \sqrt{q^2_E} \frac{1 + c_Q/Ri_E}{\sqrt{1 + c_{q^2}/Ri_E}} \quad (67)$$

$$= \frac{0.025}{\sqrt{0.175}} w_* \sqrt{q^2_E} \frac{1 + 8/Ri_E}{\sqrt{1 + c_{q^2}/Ri_E}} \quad (68)$$

$$= 0.06 w_* \sqrt{q^2_E} \frac{1 + 8/Ri_E}{\sqrt{1 + c_{q^2}/Ri_E}} \quad (69)$$

$$\cong 0.06 w_* \sqrt{q^2_E}, \quad (70)$$

where the Eq. (70) holds in the case of free convection. In the case of significant wind shear, Eq. (67) and the studies of Ri_E in section 3d(1) or Eq. (62) can be combined so that it may be possible to use a WVDIAL and a TRRL for the direct determination of entrainment moisture fluxes.

Another possibility is to relate the flux with variance and gradients by eliminating w_* :

$$Q_E = -\frac{C_Q}{C_{q^2}} \frac{N_E}{g_E} \overline{q^2_E} \frac{1 + c_Q/Ri_E}{1 + c_{q^2}/Ri_E} \sqrt{1 + \frac{1}{Ri_E}}, \quad (71)$$

$$Q_E \cong -\frac{C_Q}{C_{q^2}} \frac{N_E}{g_E} \overline{q^2_E} \sqrt{1 + \frac{1}{Ri_E}}, \quad \text{and} \quad (72)$$

$$Q_E \approx -\frac{C_Q}{C_{q^2}} \frac{N_E}{g_E} \overline{q^2_E} \cong -0.14 \frac{N_E}{g_E} \overline{q^2_E}, \quad (73)$$

again where the last equation is proposed to be valid in the free convection limit. Comparing Eqs. (71)–(73) with the surface latent heat flux, it can be determined whether the CBL is drying or moistening, as long as moisture advection can be neglected. Obviously, the CBL is moistening if the ratio $V = Q_E/Q_0 < 1$, which translates to

$$V = \frac{Q_E}{Q_0} = 0.06 \frac{w_* \sqrt{q^2_E}}{Q_0} \frac{1 + 8/Ri_E}{\sqrt{1 + c_{q^2}/Ri_E}} \quad (74)$$

$$= 0.06 \frac{\sqrt{q^2_E}}{q_*} \frac{1 + 8/Ri_E}{\sqrt{1 + c_{q^2}/Ri_E}} \quad (75)$$

$$\cong 0.06 \frac{\sqrt{q^2_E}}{q_*}, \quad (76)$$

with the last equation holding in the case of free convection.

Of course, if the relationships for Q_E are verified, they can also be used for determining the flux divergence in the CBL, which is extremely important for CBL TP. Assuming a linear flux profile, the flux divergence is simply

$$\frac{\partial}{\partial z} \overline{w'q'} = \frac{Q_E - Q_0}{z_i} \quad (77)$$

$$\simeq \frac{0.06 \sqrt{q'^2_E w_*} - Q_0}{z_i}. \quad (78)$$

Obviously, a couple of comprehensive relationships can be derived, which are worth an extensive evaluation.

In an additional step, it is also possible to investigate the closure of the budget equations for mean variables, as demonstrated in Senff et al. (1994), Wulfmeyer (1999a,b), as well as for higher-order moments and fluxes.

4) DISSIPATION AND MOLECULAR DESTRUCTION RATES

The lidar measurements allow the profiling of the integral scales throughout the CBL including the EL. If the major part of the turbulent fluctuations is resolved, the parameters of the structure function can be determined. Therefore, we are proposing here a new technique for the combination DL, TRRL, and WVDIAL or WVRL in order to determine TKE dissipation rates as well as the destruction rates of temperature and humidity variances based on Eqs. (43)–(45), Eqs. (47) and (48), Eq. (52) and (53), and Eqs. (56) and (57).

4. First results using WVDIAL and TRRL

a. Dataset

We present data collected during intensive observations period (IOP) 5 of HOPE, which was performed in spring 2013 close to the city of Jülich, Germany. IOP5 was executed on 20 April 2013. We focus on a dataset collected with the IPM WVDIAL and the TRRL between 1130 and 1230 UTC. The lidar systems were located at site close to the village of Hambach near Research Centre Jülich at 50°53'50.56"N, 6°27'50.39"E and 110 m above sea level.

During IOP5, the HOPE domain was under the influence of a high pressure system over the Baltic Sea and a cold front over the Alps to the southeast. The local conditions were measured by a weather and energy balance closure station a few meters from the site. The surface pressure at the measurement site was $p_0 \simeq 1020$ hPa. The horizontal wind speed at 5-m height was 1.5 m s^{-1} from northeast turning to eastern directions at the CBL top, as

revealed by a radio sounding launched at the measurement site at 1300 UTC. The surface temperature was low with 284 K. Because of the large-scale conditions, rather dry air was advected into the region resulting in a surface specific humidity of merely 3.4 g kg^{-1} corresponding to a relative humidity (rh) of approximately 43%. Further details concerning the meteorological conditions are found in Muppa et al. (2015).

Except for a few cirrus clouds, the atmosphere was cloud free and contained only a few aerosol layers in the free troposphere. The surface heating was significant resulting in sensible heat flux of 247 W m^{-2} , whereas the evapotranspiration was modest with 89 W m^{-2} . The friction velocity was $u_* \simeq 0.7 \text{ m s}^{-1}$, corresponding to a Monin–Obukhov length of $L \simeq -126 \text{ m}$.

b. Results derived by lidar synergy

We are focusing on the synergy of the IPM WVDIAL and the TRRL systems. Doppler lidar data had to be excluded because the vertical velocity variance and skewness, as well as the horizontal winds, have not been processed in detail yet. Therefore, a full analysis of fluxes and variances, and their relationships with gradients and dependences on Ri_E , is not possible. In any event, a full exploitation of all equations presented in sections 2 and 3 is beyond the scope of this work and subject of future activities.

However, even without the knowledge of Ri_E , a large number of relations could be studied for the first time here. This is due to the fact that the WVDIAL and TRRL measurements are providing mean profiles and their vertical gradients of specific humidity and potential temperature, variance profiles, and insight into structure coefficients in the same vertical air column, simultaneously. For this study, both the WVDIAL and the TRRL data were processed with a temporal resolution of 10 s and vertical resolutions of 100 m allowing for a consistent analysis of gradients and turbulent moments. Additionally, the TRRL data were corrected with respect to systematic errors induced by incomplete overlap between laser transmitter and field of view of the telescope up to 800 m with a time-independent correction function (Hammann et al. 2015). Afterward, the WVDIAL absolute humidity measurements and the TRRL temperature measurements were transformed into specific humidity and potential temperature using a hydrostatic pressure profile.

The mean specific humidity, potential temperature, and relative humidity profiles and their gradients during the measurement period are presented in Fig. 3 (top). The system noise errors and the estimate of the mean CBL depth z_i are also indicated. As mentioned above, the specific humidity in the ML was rather low with

3 g kg^{-1} . Toward the entrainment layer already a strong decrease of the specific humidity was observed decreasing further to 0.1 g kg^{-1} in the lower free troposphere. This resulted in a strong reduction of rh around the EL as well. The potential temperature profile shown in Fig. 3 shows a well-mixed CBL (as also confirmed by soundings) up to 1000 m with a mean $\theta \approx 282.5 \text{ K}$. The moisture decrease above and the large vertical extent of the region with increasing potential temperature likely indicates an entrainment drying CBL.

During the time period of interest, the CBL was well developed and reached a quasi-stationary depth, as confirmed by the lidar backscatter profiles (not shown). Whereas many different definitions of z_i are available (e.g., Cohn and Angevine 2000; Pal et al. 2010) and some uncertainties remain, we could take advantage of the synergy of our measurements. For this purpose, we evaluated the gradients of the lidar backscatter signals, the minimum of the mean water vapor gradient, and the maximum of the potential temperature gradient in the EL as well as the locations of the maxima of the variance profiles. This resulted in $z_i \approx 1280 \text{ m}$ with a standard deviation of 60 m derived from the instantaneous $z_i(t)$ values of the backscatter gradients. The latter value multiplied by 2 can be considered as an estimate of the mean EL thickness and resulted in $\Delta_{EL} \approx 120 \text{ m}$. This result of z_i was consistent within 20 m with the radio sounding launched at 1300 UTC.

Using the estimate of z_i , we derived a vertical velocity scale of $w_* \approx 2 \text{ m s}^{-1}$, a convective time scale of $t_* \approx 10.7 \text{ min}$, a humidity scale of $q_* \approx 0.015 \text{ g kg}^{-1}$, and a potential temperature scale of $\theta_* \approx 0.1 \text{ K}$. Furthermore, we estimated the corresponding temperature gradient by taking the range $z_i - \Delta_{EL}/2$, $z_i + \Delta_{EL}/2$, which yielded $\gamma_E \approx 0.02 \text{ K m}^{-1}$ or a temperature jump of approximately 2 K in the EL. This resulted in a Brunt–Vaisala frequency of $N_E \approx 0.026 \text{ Hz}$ and a local Richardson number $Ri_l = \Delta\theta/\theta_* \approx 20$. As shown in Fig. 3, the minimum specific humidity gradient in the EL was approximately $-0.012 \text{ g kg}^{-1} \text{ m}^{-1}$ and the averaged gradient in the EL yielded $g_E \approx -0.01 \text{ g kg}^{-1} \text{ m}^{-1}$.

By means of the analyses described in section b of the appendix (see also Lenschow et al. 2000; Wulfmeyer et al. 2010), we derived profiles of the integral scales, variances, and third-order moments of potential temperature and specific humidity. In all these figures, black error bars indicate noise errors and the colored error bars the sampling errors.

Figure 4 presents the profiles of the integral scales \mathcal{T}_θ (top panel) and \mathcal{T}_q (bottom panel). In these panels, we also compared their determination by a numerical integration from lag 0 to the first zero crossing of the autocovariance function with the theoretical result given in

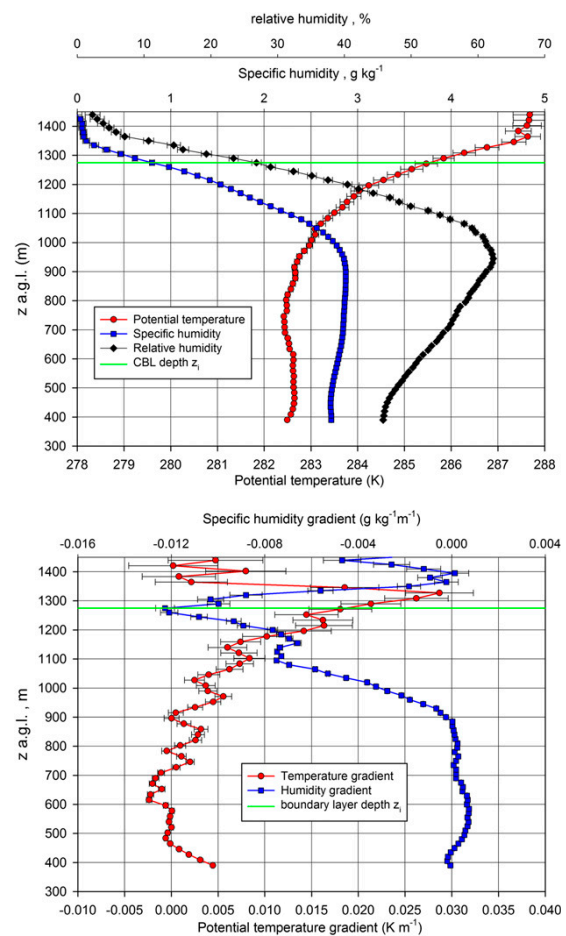


FIG. 3. (top) Mean profiles of specific humidity and potential temperature during IOP5 (1130–1230 UTC). (bottom) Corresponding vertical gradient profiles. The error bars due to system noise and the estimate of z_i are also indicated.

Eq. (42). The outliers in the numerical integration are due to systematic errors, if very low variance levels are determined by the extrapolation of the autocovariance function, as in the numerical integration the autocorrelation function must be used [see Eq. (41) and Fig. A1]. We recommend the use of Eq. (42) because it gives more robust results at low variance levels and compares very well with the numerical integration otherwise.

For potential temperature, a rather constant profile in the CBL was determined with $\mathcal{T}_\theta \approx 50 \text{ s}$. In contrast, \mathcal{T}_q showed a reduction from the ML to the EL from approximately 150 to 50 s. In both profiles, fine structures appear, which are not fully understood yet. Currently, we suppose that these are due to sampling statistics. These results also confirm that the resolution of the lidar profiles was high enough to resolve the temperature and

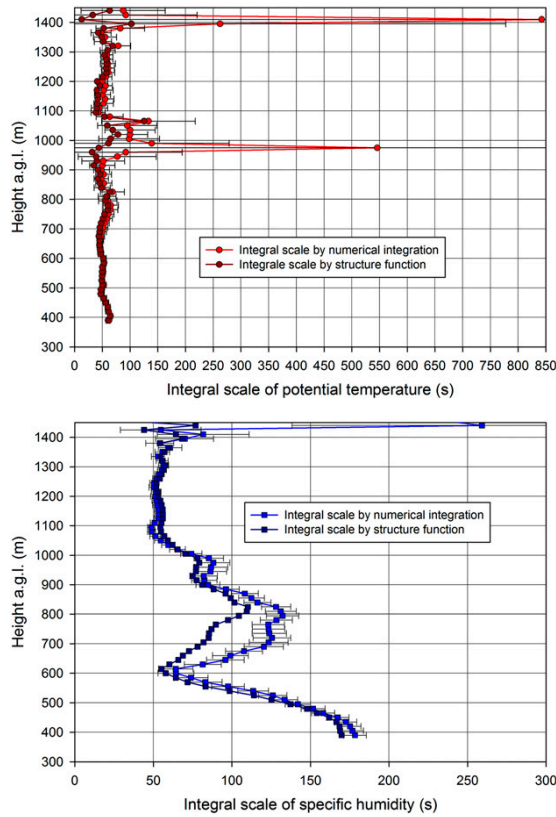


FIG. 4. (top) Potential temperature integral scale derived using the integration of the autocovariance function to the first zero crossing or using the new Eq. (42). (bottom) As in (top), but for specific humidity.

humidity fluctuations into the inertial subrange even in the EL.

The potential temperature and specific humidity variance profiles are depicted in Fig. 5. To demonstrate the high SNR of the measurements, the profiles are plotted on a logarithmic scale. Again, some fine structures in the profiles are found, which may be due to sampling statistics or a too-strong noise correction at low variance level. Otherwise, the potential temperature variance profiles show a nearly constant variance of 0.07 K^2 in the ML and the expected peak in the EL with an amount of 0.5 K^2 . In contrast, the specific humidity variance profile is generally increasing from very low levels by an order of magnitude to $0.1 \text{ g}^2 \text{ kg}^{-2}$ in the ML. In the EL, the typical peak is reached with a value of $0.5 \text{ g}^2 \text{ kg}^{-2}$. It is likely a coincidence in this case that the absolute values of potential temperature and specific humidity variances in the EL are similar.

Profiles of the third-order moments are presented in Fig. 6. In the ML, both profiles indicate a symmetric

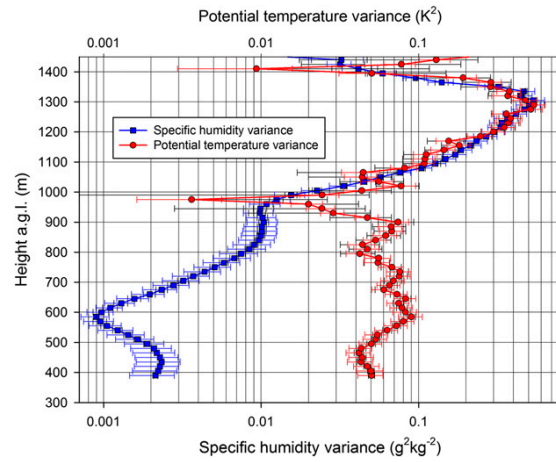


FIG. 5. The specific humidity and potential temperature variance profiles. The error bars in the same color as the plots are the sampling errors and the black error bars are the noise errors.

distribution of the fluctuations. However, in the EL, below z_i the third-order moment turns positive for the potential temperature and negative for the specific humidity fluctuations. Close to z_i , the moments show a zero crossing and are changing sign above, which is clearly visible in the specific humidity but less pronounced in potential temperature, however, likely as a result of a larger noise level in the latter.

c. Discussion

The results presented in Figs. 3–6 can be used to evaluate several relationships proposed in this work. The necessity to derive improved relationships for exchange and turbulent processes in the EL becomes already evident by noting that the standard potential temperature and specific humidity scales derived in section 4b cannot explain the observed variances in this layer.

The main weakness in our study is the lack of knowledge of Ri_E . However, the local $\text{Ri}_l \simeq 20$ and the lack of strong shear in the radiosonde data indicate that the case was not too far from the free-convection limit. Therefore, in the following, we disregard any Ri_E dependencies. Furthermore, we assume that w_* is a reasonable scaling variance for the vertical wind fluctuations even in the EL.

Considering these uncertainties, we start with an evaluation of the variances in the EL. Using Eqs. (17) and (18) and the proposed coefficients C_{θ^2} and C_{q^2} , we get estimates of $\overline{\theta^2} \approx 0.1 \text{ K}^2$ and $\overline{q^2} \approx 0.1 \text{ g}^2 \text{ kg}^{-2}$. Thus, we achieved an underestimation of the variances in the EL by a factor of 5. Obviously, at least one of the assumptions, the validity of the free convection limit, the scaling with w_* , or the values of the constants derived by LES were not valid.

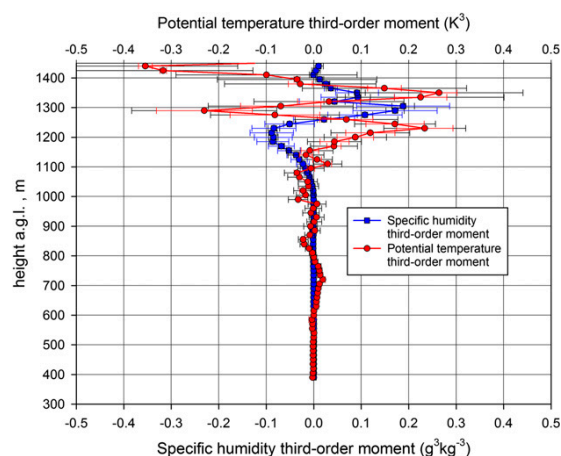


FIG. 6. The specific humidity and potential temperature third-order-moment profiles. The same convention for the colors and error bars is used as in Fig. 5.

We also tested Eqs. (70) and (73) for the water vapor entrainment flux Q_E . Using Eq. (70) we achieved $Q_E \approx 210 \text{ W m}^{-2}$ and using Eq. (73) we got $Q_E \approx 450 \text{ W m}^{-2}$. In both cases, an entrainment drying CBL was confirmed [see also Eq. (76)]. However, because of the strong drying at the CBL top (see Fig. 3), the latter value was likely closer to reality. This indicates that we may have to go away from the scaling using w_* in the EL and it is better to use potential temperature and specific humidity gradients.

Using Fig. 6, we can evaluate also the scaling proposed in Eqs. (21), (22), and (66). It turns out that the gradient scaling does not work in the case of third-order moments because the third-order moment changes sign in the EL leading to a complex structure of the profiles. With respect to water vapor, this structure was also found in other lidar measurements (Wulfmeyer 1999b; Wulfmeyer et al. 2010; Turner et al. 2014b) so that this seems to be common in the CBL. With respect to temperature, we are confirming this complex structure for the second time using active remote sensing—the first time it was shown using TRRL measurement by Behrendt et al. (2015) albeit with different values of the negative and positive maxima. Couvreur et al. (2007) detected and analyzed this structure by LES. They argued that this behavior is due to the deformation of eddies in the region of the inversion causing different updraft and recoiling structures. In the future, further insight in and quantification of the behavior of third-order moments should be collected by additional observations and dedicated LES and DNS runs by analyzing the third-order moment budgets.

The use of Eq. (39) in combination with Eq. (A9) also allowed us to get some insight in the profiles of the structure function coefficients k_q and k_θ . Figure 7 presents the results. In the top panel, except at very low variance levels, we found a striking linear relationship between these coefficients and the corresponding variances with a very similar slope for specific humidity and potential temperature. By a linear fit, we found $\overline{q'^2} \approx 26.5 \text{ s}^{2/3} k_q$ and $\overline{\theta'^2} \approx 26.2 \text{ s}^{2/3} k_\theta$. Furthermore, we studied the ratio k_q/k_θ between these coefficients, which corresponds to the ratio of the molecular destruction rates of humidity and temperature variances. The results are presented in the bottom panel of Fig. 7. Except some outliers due to low SNR and taking a ratio of noisy signals, in the ML, the destruction rate is much smaller for humidity than for temperature. However, in the EL, the ratio reaches approximately the same value of 1 so that the destruction rates are becoming similar.

Despite some missing information, we demonstrated first results comparing profiles of gradients, variances, and the coefficient of the structure function from the ML through the EL in a quasi-stationary CBL. Whereas the variances in the EL were underestimated by the gradient function relationships in comparison to the measurements, reasonable results were achieved for the water vapor entrainment flux. The structure of the third-order moments in the EL is more complex than can be described by gradient relationships. Interesting results were found with respect to the behavior of the structure function coefficients showing a different ratio of molecular destruction rates in the ML and the EL. In the future, it is essential that these studies are extended by simultaneous measurements of wind profiles and vertical velocity statistics because the dependence of the relationships on the functions $f(Ri_E)$ for variances and fluxes as well as the validity of scaling with the convective velocity scale have to be investigated. For this purpose, continuous measurements of the daily cycle of the CBL during field campaigns and/or observatories with sufficient equipment of lidar systems are necessary. Furthermore, the dependence of the results on the resolution of the lidar systems and of dedicated LES runs needs to be explored.

5. Summary and outlook

In this work, we presented methodologies for improving the representation of turbulent transport processes and entrainment in weather and climate models for advanced simulations of water and energy cycles. Usually, turbulent transport processes are represented by the turbulence parameterization (TP), as long as the model grid increment is approximately 1 km or more.

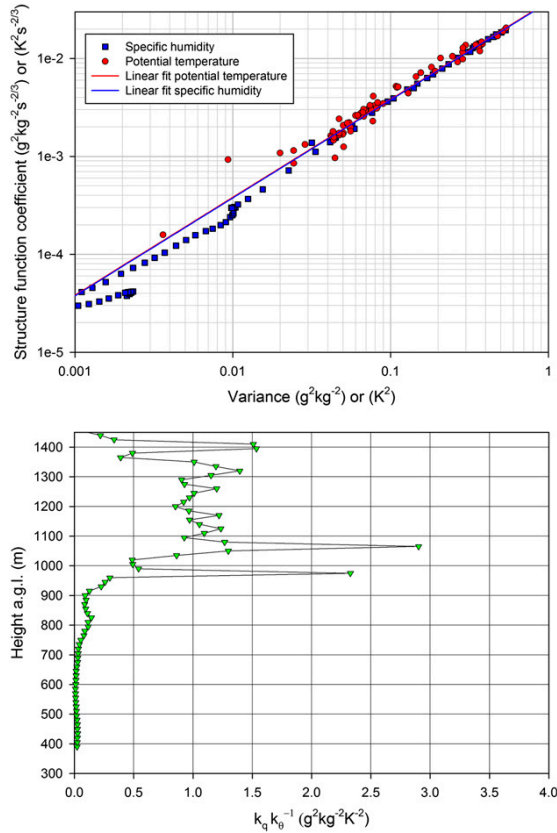


FIG. 7. (top) Relation between variances and structure function coefficients for potential temperature and specific humidity. Additionally, the results of a linear fit are shown. (bottom) The ratio between the coefficient in dependence of height.

However, it is controversial at what grid increment the turbulence should be explicitly simulated without any TP so that the model is running in the large-eddy simulation (LES) mode. Because over many regions of Earth, convection initiation in the daytime is critical for the formation of clouds and precipitation, we are focusing on the investigation of turbulence in the daytime atmospheric convective boundary layer (CBL) with low cloud coverage.

Studies of turbulent transport processes and entrainment can be performed either by LES or high-resolution observations. LES has been used for the investigation of turbulence for a long time, and many aspects of TPs have been derived from the corresponding results. However, it should not be forgotten that a detailed simulation of land surface–atmosphere exchange and feedback requires a realistic representation of the heterogeneity of the land surface with respect to soil properties, land cover, and orography. Furthermore, it is fundamental to

include the simulation of gravity waves at the CBL top, as these are contributing to the strength of entrainment. Only a few LES studies—if any—have been performed that fulfill these requirements. Therefore, strong efforts are still needed to improve LES by imbedding the simulations in a realistic large-scale environment. The latter is leading to the so-called gray-zone experiments where a chain of models resolving down to the LES scale can be compared with respect to their performance in a realistic synoptic setting. In any case, model simulations either in the form of gray-zone experiments or more idealistic LES must be verified with respect to their performance. Furthermore, any TPs require physically based relationships concerning entrainment processes, which must be verified by observations.

We present a new approach for the understanding and simulation of entrainment in the EL at the top of the CBL. After a discussion of the vertical structure of the CBL, EL scaling variables are introduced, which can be combined to derive a series of equations for determining variances and fluxes. These are related to gradients of wind, temperature, and humidity in the EL. It is also shown that the vertical exchange through the EL should contain a functional dependence of the gradient Richardson number Ri_E . Suggestions for these relationships are made. Furthermore, the autocovariance functions of the variables are considered, which can be modeled in the inertial subrange with the structure function for stationary and homogeneous turbulent processes. Physical relationships between the integral temporal and spatial scales and the turbulent quantities are derived, which can be tested by observations. New equations are introduced for profiling the TKE dissipation rate as well as the molecular destruction rates of humidity and temperature variances.

The verification of the relationships requires the measurements of wind, temperature, and humidity profiles as well as their gradients in the CBL including the EL. It is necessary that the corresponding instruments resolve their fluctuations for determining profiles of higher-order moments and of fluxes simultaneously.

We demonstrate that these verification efforts can be realized by a new synergy of DL for profiling the vertical and horizontal wind, WVDIAL or WVRL for humidity profiling, and TRRL for temperature profiling. This combination of instruments is essential but also sufficient for a complete analysis of the similarity relationships. A thorough analysis of the new generation of WVRL, WVDIAL, and TRRL lidar systems, where the last two of them have been developed at the IPM of the UHOH, demonstrates that these systems are capable of fulfilling the measurement needs. A detailed analysis of systematic and noise errors of mean profiles, their

gradients, higher-order moments, fluxes, and dissipation and molecular destruction rates is presented, which can be used to confirm the sufficient performance of these lidar systems.

A straightforward strategy of using the data from these lidar systems is developed. After all profiles of interest are determined and their error bars are characterized, the results can be combined in different ways. For instance, the data can be used for determining Ri_E to study the functional dependence of Ri_E influencing variance and flux profiles. A series of equations is derived to investigate variance- and third-order moment-gradient relationships, flux-variance relationships, and flux-gradient relationships.

We demonstrate that the DL-WVDIAL/WVRL-TRRL synergy has at least three functions: 1) a complete set of equations can be tested for deriving variances and fluxes by gradient relationships; 2) LES can be verified in great detail by studying profiles of second-, third-, and fourth-order moments; and 3) new relationships for fluxes and variances can be derived forming the basis for budget analyses and new TPs.

First tests of these relationships were presented using a dataset from HOPE. Simultaneous measurements of mean profiles and gradients of potential temperature as well as specific humidity and their variances are shown and analyzed. We showed that the similarity relationships underestimate the measured variance, if the free-convection limit was present and the constants previously derived by LES are valid. Furthermore, we assumed that the convective velocity scale is an appropriate scaling variable. The application of a gradient-variance similarity relationship for the entrainment water vapor flux gave reasonable results and indicated an entrainment-drying CBL during the measurement period. The variances were proportional to the fit coefficients of the structure function and the molecular destruction rates of potential temperature and specific humidity variances became similar in the EL. In the future, measurements of additional scaling variables using DL have to be added to refine these studies.

So far, this combination of measurements has only been realized during the HOPE and SABLE field campaigns. Further datasets are available from observatories such as the ARM SGP and Darwin sites but may require some redesign and improvement of instrument equipment and performance there. We propose to perform dedicated field campaigns for studying the proposed relationships and to extend current observatories to fulfill the required measurement needs. Ideally, the operation of this basic synergy of active instruments should be supported by airborne in situ as well as passive and active remote sensing measurements

using a combination of lidar and radar systems extending the measurements in clouds. These efforts should be accompanied by gray-zone simulations down to the LES or even the DNS scale. The relationships and equations in this work as well as simulations of the same scales will enable us to reach a new level of detail and accuracy for testing and developing advanced TPs in the CBL.

Acknowledgments. This work was supported by the Cooperative Institute for Environmental Studies (CIRES) in Boulder, Colorado, by a Visiting Fellow Award for the first author. Furthermore, this study was performed within the German Science Foundation (DFG) Research Unit FOR1695 “Regional Climate Change” and the Federal Ministry of Education and Research (BMBF) program High Definition Clouds and Precipitation (HD(CP)²). This research was also supported by the National Severe Storms Laboratory (NSSL) in Norman, Oklahoma, and the U.S. Department of Energy (DOE) Atmospheric System Research (ASR) via Grant DE-SC0006898.

APPENDIX

Error Analysis of Lidar Profiles

a. Systematic errors

For all lidar systems introduced above, stable system performance has been demonstrated so that any systematic errors should be constant in time during turbulence measurements. The corresponding errors of wind, humidity, and temperature profiles can be taken from the specifications summarized in [section 3b](#). As the height dependence of these errors is very low as well, their effect on gradients can be neglected. It is interesting to investigate the effect of systematic errors on turbulent quantities as well. If the systematic error is just a constant offset, it does not have an influence on the fluctuations so that this effect can be neglected. However, in many lidar systems and other calibrated observing systems, systematic deviations from the mean can be caused by errors in a calibration constant. In this case, the error of the fluctuations can be analyzed as follows using q as an example. If q_T and q_M are the true and the measured values then

$$q_T(t) = q_M(t) + Fq_M(t), \quad (\text{A1})$$

where F is the relative systematic error of the measurement of q_M . Then

$$q'_T(t) = q_T(t) - \bar{q}_T \quad \text{and} \quad (\text{A2})$$

$$q'_M(t) = q_M(t) - \bar{q}_M. \quad (\text{A3})$$

Thus, the systematic error $\Delta q'_M$ in the measurement of the fluctuations of q reads

$$\Delta q'_M(t) = q'_T(t) - q'_M(t) = q_T(t) - \bar{q}_T - [q_M(t) - \bar{q}_M]. \quad (\text{A4})$$

Using Eq. (A1), it follows

$$\Delta q'_M(t) = q_M(t) + Fq_M(t) - \bar{q}_M - F\bar{q}_M - q_M(t) + \bar{q}_M \quad (\text{A5})$$

$$= Fq_M(t) - F\bar{q}_M = F[q_M(t) - \bar{q}_M] \quad (\text{A6})$$

$$= Fq'_M(t). \quad (\text{A7})$$

Applying Eq. (A7) to the derivation of variances, we get

$$\overline{q'^2_M} = (1 + F)^2 \overline{q'^2_T} \simeq (1 + 2F) \overline{q'^2_T}, \quad (\text{A8})$$

where $\overline{q'^2_M}$ is the variance measured including the systematic effect by F , for example, by an inaccurate calibration. Basically, the systematic error doubles, if variances are considered. As F is constant in time and just a few percent for all lidar systems (DL, WVDIAL, WVRL, and TRRL) considered here, systematic errors in the measurements of fluctuations can be neglected.

b. Sampling and noise errors

Error bars due to sampling and noise statistics have to be derived and considered for all profiles in order to specify the significance of the results. Sampling errors are critical for ground-based measurements owing to the considerable integration time to collect turbulent fluctuations with high statistical certainty. Sampling errors can be reduced by performing many measurements under similar meteorological conditions or by the design and operation of ground-based networks. Sampling errors were derived for all kinds of turbulent profiles and specified in [Lenschow et al. \(1994, 2000\)](#); therefore, they are not repeated here.

For all lidar-derived profiles, noise error bars have also to be specified, as their propagation into turbulence profiles is still significant. It is the strength of the lidar technique that these error bars can be derived for each turbulence profile under the current meteorological conditions without any additional assumptions. A very convenient and robust technique for determining noise error profiles was introduced in [Lenschow et al. \(2000\)](#) and applied there to DL and WVDIAL measurements. [Wulfmeyer et al. \(2010\)](#) extended this technique to WVRL and [Behrendt et al. \(2015\)](#) to TRRL turbulence measurements.

This technique is based on the extrapolations of the measured autocovariance functions to lag 0 by the structure functions given in Eqs. (35)–(37). We assume

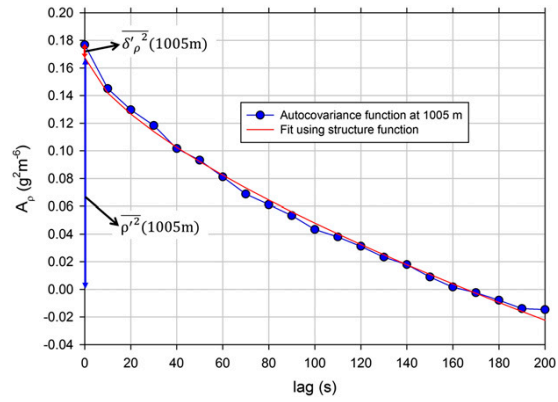


FIG. A1. Separation of atmospheric and noise variance by the fit of the structure function to the autocovariance function A_p for absolute humidity measured with the IPM WVDIAL.

that the noise errors between different lags are uncorrelated, which is the case for all lidar systems of interest here. It follows, for example, for specific or absolute humidity ρ measurements at lag 0:

$$A_q(0) = \overline{q'^2} + \delta^2 \quad \text{or} \quad A_\rho(0) = \overline{\rho'^2} + \delta_\rho^2, \quad (\text{A9})$$

where δ^2 and δ_ρ^2 are the specific or absolute humidity system noise variances at the corresponding temporal and range resolutions. [Figure A1](#) demonstrates this technique for a WVDIAL absolute humidity measurement performed during the SABLE campaign at 1100–1200 UTC 21 August 2014 at a height of 1005 m using a temporal resolution of 10 s. Clearly the noise and the atmospheric variances can be separated. The turbulence is well resolved, as observed by the good fit to the structure function, and the noise contribution is very small. The fit results in $\overline{\rho'^2} \simeq 0.17 \text{ g}^2 \text{ m}^{-6}$ and a noise variance of $\delta_\rho^2 \simeq 0.01 \text{ g}^2 \text{ m}^{-6}$, which corresponds to a noise error standard deviation of just $\delta_\rho \simeq 0.1 \text{ g m}^{-3}$.

Extended studies of this technique (e.g., [Turner et al. 2014b](#)) demonstrated that this separation is routinely possible at all height levels, at much higher noise levels, and even in the presence of clouds. As it was not explicitly mentioned in [Lenschow et al. \(2000\)](#), we are deriving here the error propagation for noise errors of gradients of humidity and temperature profiles as well as for errors of third- and forth-order moments of atmospheric variables. Noise errors of fluxes as well as dissipation and molecular destruction rates are also considered.

1) GRADIENTS

Gradients of humidity and temperature are derived from absolute humidity or mixing ratio profiles (WVDIAL or WVRL) or from temperature profiles (TRRL). In contrast

to radio soundings, the representativeness is improved by continuous measurements of profiles of the variable of interest with a temporal resolution of 1–10 s and averaging them over time periods of 30–120 min, typically. The gradient, for example, for humidity, can be approximated by calculating the differential quotient

$$g(\bar{z}) = \frac{q(z + \Delta z) - q(z)}{\Delta z}, \quad (\text{A10})$$

where Δz is the range resolution of the lidar measurement and the gradient is located at \bar{z} , the mean value between z and $z + \Delta z$. After determination of the noise variance δ^2 at each vertical bin of humidity profile, the error σ_g of the gradient reads

$$\sigma_g \simeq \sqrt{\frac{\delta^2}{N}} \frac{\sqrt{2}}{\Delta z}, \quad (\text{A11})$$

considering that the noise errors at the range bins $z + \Delta z$ and z are nearly the same and statistically independent. Here, N is the number of samples during the averaging time for the determination of the gradient and turbulent quantities.

2) HIGHER-ORDER MOMENTS

Using the error propagation for the fluctuation q' of water vapor, higher-order moment profiles can be characterized with respect to noise errors. For instance, for the noise error σ_{q^2} of the variance we consider that noise errors are independent in each sample q'_i of the fluctuations and achieve by error propagation

$$\sigma_{q^2}^2 \simeq \frac{1}{N^2} \sum_i \left[\frac{\partial}{\partial q'_i} (q'_i)^2 \right]^2 \delta_i^2 \simeq \frac{4}{N^2} \sum_i (q'_i)^2 \delta_i^2 \simeq \frac{4}{N} \overline{q^2} \delta^2. \quad (\text{A12})$$

Thus,

$$\sigma_{q^2} \simeq 2\sqrt{\overline{q^2}} \sqrt{\frac{\delta^2}{N}} \quad \text{and} \quad (\text{A13})$$

$$\sigma_{q^2} \simeq 2\overline{q^2} \sqrt{\frac{\delta^2}{q^2 N}}. \quad (\text{A14})$$

Applying these equations to the example from Fig. A1, which used a time resolution of 10 s and an averaging time of 1 h ($N = 360$), we get an absolute error of $\sigma_{q^2} \simeq 0.004 \text{ g}^2 \text{ m}^{-6}$ and a relative error of $\sigma_{q^2}/\overline{q^2} \simeq 3\%$, which is quite acceptable and demonstrates the low noise of the IPM WVDIAL.

Applying the same principle of Eq. (A12) to higher-order moments, we get for the noise error σ_{q^3} of the third-order moment

$$\sigma_{q^3} \simeq 3\sqrt{\overline{q^4} \frac{\delta^2}{N}} \simeq 3\sqrt{3} \overline{q^2} \sqrt{\frac{\delta^2}{N}}. \quad (\text{A15})$$

We applied the Isserlis theorem to the fourth-order moment as $\overline{q^4} \simeq 3\overline{q^2}^2$ assuming that higher-order moments do not deviate too much from a Gaussian distribution.

Then, Eq. (A15) can also be written in the following forms:

$$\sigma_{q^3} \simeq \frac{3}{2} \sqrt{3} \sqrt{\overline{q^2}} \sigma_{q^2} \quad (\text{A16})$$

or

$$\frac{\sigma_{q^3}}{\overline{q^3}} \simeq 3\sqrt{3} \frac{1}{\mathcal{S}_q} \sqrt{\frac{\delta^2}{\overline{q^2} N}} \quad (\text{A17})$$

by introducing the skewness \mathcal{S}_q of the time series.

The noise error of the fourth-order moment is calculated accordingly and we derive

$$\sigma_{q^4} \simeq 4\sqrt{\overline{q^6}} \sqrt{\frac{\delta^2}{N}} \simeq 4\sqrt{15} \overline{q^2} \sqrt{\frac{\delta^2}{N}} \quad (\text{A18})$$

again using an Isserlis theorem but here for $\overline{q^6} \simeq 15\overline{q^2}^3$. Analogous to the third-order moment we get the following relationships:

$$\sigma_{q^4} \simeq \frac{\sqrt{15}}{2} \overline{q^2} \sigma_{q^2} \quad (\text{A19})$$

or

$$\frac{\sigma_{q^4}}{\overline{q^4}} \simeq 4\sqrt{15} \frac{1}{\mathcal{K}} \sqrt{\frac{\delta^2}{\overline{q^2} N}} \quad (\text{A20})$$

with the kurtosis \mathcal{K} of the time series. Obviously, the noise errors of the n th moment scale approximately with

$$\sigma_{q^n} \propto \sqrt{\overline{q^2}}^{(n-2)} \sigma_{q^2} \quad \text{for } n \in \mathbb{N} \geq 2. \quad (\text{A21})$$

Using these relationships, a full error propagation is possible for all vertical profiles of higher-order moments and their vertical gradients so that errors can be derived for all variables presented in the equations above. The errors scale with the standard deviation of noise during the averaging time. Consequently, as long as no nonlinearities occur in the derivation of fluctuations, it is better to maximize the time resolution so that the atmospheric variability is resolved as far as possible into the inertial subrange. Furthermore, the noise errors of the turbulent moments scale with powers of

atmospheric variances so that the noise errors remain small in the EL.

3) FLUXES

It is also important to study noise errors in fluxes. Here, we achieve

$$\sigma_{w'q'} \simeq \sqrt{q'^2 \frac{\delta_w^2}{N} + w'^2 \frac{\delta_q^2}{N}} \quad (\text{A22})$$

$$\simeq \sqrt{q'^2 w'^2} \sqrt{\frac{\delta_w^2}{N w'^2} + \frac{\delta_q^2}{N q'^2}} \quad (\text{A23})$$

$$\simeq \frac{1}{r} q' w' \sqrt{\frac{\delta_w^2}{N w'^2} + \frac{\delta_q^2}{N q'^2}} \\ = \frac{1}{r} q' w' \sqrt{\left(\frac{\delta_w^2}{w'^2} + \frac{\delta_q^2}{q'^2} \right) \frac{1}{N}}, \quad (\text{A24})$$

where r is the correlation coefficient between vertical wind and water vapor fluctuations. The same equations hold for sensible heat fluxes replacing q' by θ' . Here, for low noise in the flux profiles, a large correlation coefficient and low relative noise error with respect to the atmospheric variances are important.

4) DISSIPATION AND MOLECULAR DESTRUCTION RATES

Finally, we derive the noise error for the dissipation rates based on Eqs. (47), (52), and (56). We achieve

$$\sigma_\varepsilon \simeq \varepsilon \sqrt{\frac{9}{4} \left(\frac{\sigma_{k_w}}{k_w} \right)^2 + \left(\frac{\sigma_U}{U} \right)^2}, \quad (\text{A25})$$

$$\sigma_{N_\theta} \simeq \bar{N}_\theta \sqrt{\left(\frac{\sigma_{k_\theta}}{k_\theta} \right)^2 + \frac{1}{4} \left(\frac{\sigma_{k_w}}{k_w} \right)^2 + \left(\frac{\sigma_U}{U} \right)^2}, \quad \text{and} \quad (\text{A26})$$

$$\sigma_{N_q} \simeq \bar{N}_q \sqrt{\left(\frac{\sigma_{k_q}}{k_q} \right)^2 + \frac{1}{4} \left(\frac{\sigma_{k_w}}{k_w} \right)^2 + \left(\frac{\sigma_U}{U} \right)^2}. \quad (\text{A27})$$

In this case, σ_{k_w} , σ_{k_θ} , and σ_{k_q} are the errors in the determination of the fit coefficients to the structure function by the regression analysis, and σ_U is an error estimate for the horizontal wind profile.

REFERENCES

- Ackerman, T. P., and G. M. Stokes, 2003: The Atmospheric Radiation Measurement Program—To predict reliably what increased greenhouse gases will do to global climate, we have to understand the crucial role of clouds. *Phys. Today*, **56**, 38–46, doi:10.1063/1.1554135.
- Angevine, W., S. Avery, and G. Kok, 1993: Virtual heat flux measurements from a boundary-layer profiler-RASS compared to aircraft measurements. *J. Appl. Meteor.*, **32**, 1901–1907, doi:10.1175/1520-0450(1993)032<1901:VHFMFA>2.0.CO;2.
- Ansmann, A., J. Fruntke, and R. Engelmann, 2010: Updraft and downdraft characterization with Doppler lidar: Cloud-free versus cumuli-topped mixed layer. *Atmos. Chem. Phys.*, **10**, 7845–7858, doi:10.5194/acp-10-7845-2010.
- Ayotte, K. W., and Coauthors, 1996: An evaluation of neutral and convective planetary boundary-layer parameterizations relative to large eddy simulations. *Bound.-Layer Meteor.*, **79**, 131–175, doi:10.1007/BF00120078.
- Behrendt, A., V. Wulfmeyer, A. Riede, G. Wagner, S. Pal, H. Bauer, M. Radlach, and F. Späth, 2009: Three-dimensional observations of atmospheric humidity with a scanning differential absorption Lidar. *Remote Sensing of Clouds and the Atmosphere XIV*, R. H. Picard, K. Schäfer, and A. Comeron et al., Eds., International Society for Optical Engineering (SPIE Proceedings, Vol. 7475), 74750L, doi:10.1117/12.835143.
- , and Coauthors, 2011: Observation of convection initiation processes with a suite of state-of-the-art research instruments during COPS IOP 8b. *Quart. J. Roy. Meteor. Soc.*, **137**, 81–100, doi:10.1002/qj.758.
- , E. Hammann, S. K. Muppa, S. Pal, and V. Wulfmeyer, 2015: Profiles of second- to forth-order moments of turbulent temperature fluctuations in the convective boundary layer: First measurements with rotational Raman lidar. *Atmos. Chem. Phys.*, **15**, 5485–5500, doi:10.5194/acp-15-5485-2015.
- Cohn, S., and W. Angevine, 2000: Boundary layer height and entrainment zone thickness measured by lidars and wind-profiling radars. *J. Appl. Meteor.*, **39**, 1233–1247, doi:10.1175/1520-0450(2000)039<1233:BLHAEZ>2.0.CO;2.
- Conzemius, R. J., and E. Fedorovich, 2006: Dynamics of sheared convective boundary layer entrainment. Part I: Methodological background and large-eddy simulations. *J. Atmos. Sci.*, **63**, 1151–1178, doi:10.1175/JAS3691.1.
- Couvreur, F., F. Guichard, J.-L. Redelsperger, C. Kiemle, V. Masson, J.-P. Lafore, and C. Flamant, 2005: Water-vapour variability within a convective boundary-layer assessed by large-eddy simulations and IHOP_2002 observations. *Quart. J. Roy. Meteor. Soc.*, **131**, 2665–2693, doi:10.1256/qj.04.167.
- , —, V. Masson, and J.-L. Redelsperger, 2007: Negative water vapour skewness and dry tongues in the convective boundary layer: Observations and large-eddy simulation budget analysis. *Bound.-Layer Meteor.*, **123**, 269–294, doi:10.1007/s10546-006-9140-y.
- Crum, T., and R. Stull, 1987: Field measurements of the amount of surface layer air versus height in the entrainment zone. *J. Atmos. Sci.*, **44**, 2743–2753, doi:10.1175/1520-0469(1987)044<2743:FMOTAO>2.0.CO;2.
- , —, and E. Eloranta, 1987: Coincident lidar and aircraft observations of entrainment into thermals and mixed layers. *J. Climate Appl. Meteor.*, **26**, 774–788, doi:10.1175/1520-0450(1987)026<0774:CLAAOO>2.0.CO;2.
- Deardorff, J., 1970: A three-dimensional numerical investigation of the idealized planetary boundary layer. *Geophys. Fluid Dyn.*, **1**, 377–410, doi:10.1080/03091927009365780.
- Dethloff, K., C. Abegg, A. Rinke, I. Hebestadt, and V. F. Romanov, 2001: Sensitivity of Arctic climate simulations to different boundary-layer parameterizations in a regional climate model. *Tellus*, **53A**, 1–26, doi:10.1034/j.1600-0870.2001.01073.x.
- Emeis, S., 2011: *Surface-Based Remote Sensing of the Atmospheric Boundary Layer*. Atmospheric and Oceanographic Sciences Library, Vol. 40, Springer, 174 pp.

- Fedorovich, E., R. Conzemius, and D. Mironov, 2004: Convective entrainment into a shear-free, linearly stratified atmosphere: Bulk models reevaluated through large eddy simulations. *J. Atmos. Sci.*, **61**, 281–295, doi:10.1175/1520-0469(2004)061<0281:CEIASL>2.0.CO;2.
- Ferrare, R., and Coauthors, 2006: Evaluation of daytime measurements of aerosols and water vapor made by an operational Raman lidar over the Southern Great Plains. *J. Geophys. Res.*, **111**, D05S08, doi:10.1029/2005JD005836.
- Frehlich, R., and L. Cornman, 2002: Estimating spatial velocity statistics with coherent Doppler lidar. *J. Atmos. Oceanic Technol.*, **19**, 355–366, doi:10.1175/1520-0426-19.3.355.
- , S. M. Hannon, and S. W. Henderson, 1998: Coherent Doppler lidar measurements of wind field statistics. *Bound.-Layer Meteor.*, **86**, 233–256, doi:10.1023/A:1000676021745.
- Garcia, J. R., and J. P. Mellado, 2014: The two-layer structure of the entrainment zone in the convective boundary layer. *J. Atmos. Sci.*, **71**, 1935–1955, doi:10.1175/JAS-D-13-0148.1.
- Giez, A., G. Ehret, R. L. Schwiesow, K. J. Davis, and D. H. Lenschow, 1999: Water vapor flux measurements from ground-based vertically pointed water vapor differential absorption and Doppler lidars. *J. Atmos. Oceanic Technol.*, **16**, 237–250, doi:10.1175/1520-0426(1999)016<0237:WVFMFG>2.0.CO;2.
- Grachev, A. A., C. W. Fairall, and E. F. Bradley, 2000: Convective profile constants revisited. *Bound.-Layer Meteor.*, **94**, 495–515, doi:10.1023/A:1002452529672.
- Hammann, E., A. Behrendt, F. Le Mounier, and V. Wulfmeyer, 2015: Temperature profiling of the atmospheric boundary layer with rotational Raman lidar during the HD(CP)² Observational Prototype Experiment. *Atmos. Chem. Phys.*, **15**, 2867–2881, doi:10.5194/acp-15-2867-2015.
- Hechtel, L., C.-H. Moeng, and R. Stull, 1990: Temperature profiling of the atmospheric boundary layer with rotational Raman lidar during the HD(CP)² Observational Prototype Experiment. *J. Atmos. Sci.*, **47**, 1721–1741, doi:10.1175/1520-0469(1990)047<1721:TEONSF>2.0.CO;2.
- Hill, K. A., and G. M. Lackmann, 2009: Analysis of idealized tropical cyclone simulations using the Weather Research and Forecasting Model: Sensitivity to turbulence parameterization and grid spacing. *Mon. Wea. Rev.*, **137**, 745–765, doi:10.1175/2008MWR2220.1.
- Hogan, R. J., A. L. M. Grant, A. J. Illingworth, G. N. Pearson, and E. J. O'Connor, 2009: Vertical velocity variance and skewness in clear and cloud-topped boundary layers as revealed by Doppler lidar. *Quart. J. Roy. Meteor. Soc.*, **135**, 635–643, doi:10.1002/qj.413.
- Hong, S.-Y., Y. Noh, and J. Dudhia, 2006: A new vertical diffusion package with an explicit treatment of entrainment processes. *Mon. Wea. Rev.*, **134**, 2318–2341, doi:10.1175/MWR3199.1.
- Jiménez, P. A., J. Dudhia, J. F. González-Rouco, J. Navarro, J. P. Montávez, and E. García-Bustamante, 2012: A revised scheme for the WRF surface layer formulation. *Mon. Wea. Rev.*, **140**, 898–918, doi:10.1175/MWR-D-11-00056.1.
- Kalthoff, N., and Coauthors, 2013: Dry and moist convection in the boundary layer over the Black Forest—A combined analysis of in situ and remote sensing data. *Meteor. Z.*, **22**, 445–461, doi:10.1127/0941-2948/2013/0417.
- Kameyama, S., T. Ando, K. Asaka, Y. Hirano, and S. Wadaka, 2007: Compact all-fiber pulsed coherent Doppler lidar system for wind sensing. *Appl. Opt.*, **46**, 1953–1962, doi:10.1364/AO.46.001953.
- Kanda, M., A. Inagaki, M. O. Letzel, S. Raasch, and T. Watanabe, 2004: LES study of the energy imbalance problem with eddy covariance fluxes. *Bound.-Layer Meteor.*, **110**, 381–404, doi:10.1023/B:BOUN.0000007225.45548.7a.
- Kiemle, C., G. Ehret, A. Giez, K. Davis, D. Lenschow, and S. P. Oncley, 1997: Estimation of boundary layer humidity fluxes and statistics from airborne differential absorption lidar (DIAL). *J. Geophys. Res.*, **102**, 29 189–29 203, doi:10.1029/97JD01112.
- , and Coauthors, 2007: Latent heat flux profiles from collocated airborne water vapor and wind lidars during IHOP_2002. *J. Atmos. Oceanic Technol.*, **24**, 627–639, doi:10.1175/JTECH1997.1.
- , M. Wirth, A. Fix, S. Rahm, U. Corsmeier, and P. Di Girolamo, 2011: Latent heat flux measurements over complex terrain by airborne water vapour and wind lidars. *Quart. J. Roy. Meteor. Soc.*, **137**, 190–203, doi:10.1002/qj.757.
- Kim, S.-W., S.-U. Park, and C.-H. Moeng, 2003: Entrainment processes in the convective boundary layer with varying wind shear. *Bound.-Layer Meteor.*, **108**, 221–245, doi:10.1023/A:1024170229293.
- LeMone, M., 2002: Convective boundary layer. *Encyclopedia of Atmospheric Sciences*, 1st ed. J. Holton and J. Curry, Eds., Academic Press, 250–257.
- Lenschow, D. H., J. Mann, and L. Kristensen, 1994: How long is long enough when measuring fluxes and other turbulence statistics? *J. Atmos. Oceanic Technol.*, **11**, 661–673, doi:10.1175/1520-0426(1994)011<0661:HLILEW>2.0.CO;2.
- , V. Wulfmeyer, and C. Senff, 2000: Measuring second-through fourth-order moments in noisy data. *J. Atmos. Oceanic Technol.*, **17**, 1330–1347, doi:10.1175/1520-0426(2000)017<1330:MSTFOM>2.0.CO;2.
- , M. Lothon, S. D. Mayor, P. P. Sullivan, and G. Canut, 2012: A comparison of higher-order vertical velocity moments in the convective boundary layer from lidar with in situ measurements and large-eddy simulation. *Bound.-Layer Meteor.*, **143**, 107–123, doi:10.1007/s10546-011-9615-3.
- Linné, H., B. Hennemuth, J. Bösenberg, and K. Ertel, 2007: Water vapour flux profiles in the convective boundary layer. *Theor. Appl. Climatol.*, **87**, 201–211, doi:10.1007/s00704-005-0191-7.
- Löhnert, U., D. D. Turner, and S. Crewell, 2009: Ground-based temperature and humidity profiling using spectral infrared and microwave observations. Part I: Simulated retrieval performance in clear-sky conditions. *J. Appl. Meteor. Climatol.*, **48**, 1017–1032, doi:10.1175/2008JAMC2060.1.
- Lothon, M., D. H. Lenschow, and S. D. Mayor, 2006: Coherence and scale of vertical velocity in the convective boundary layer from a Doppler lidar. *Bound.-Layer Meteor.*, **121**, 521–536, doi:10.1007/s10546-006-9077-1.
- , —, and —, 2009: Doppler lidar measurements of vertical velocity spectra in the convective planetary boundary layer. *Bound.-Layer Meteor.*, **132**, 205–226, doi:10.1007/s10546-009-9398-y.
- Maronga, B., and S. Raasch, 2013: Large-eddy simulations of surface heterogeneity effects on the convective boundary layer during the LITFASS-2003 experiment. *Bound.-Layer Meteor.*, **146**, 17–44, doi:10.1007/s10546-012-9748-z.
- Mather, J. H., and J. W. Voyles, 2013: The ARM Climate Research Facility: A review of structure and capabilities. *Bull. Amer. Meteor. Soc.*, **94**, 377–392, doi:10.1175/BAMS-D-11-00218.1.
- Matuura, M., Y. Masuda, H. Inuki, S. Kato, S. Fukao, T. Sato, and T. Tsuda, 1986: Radio acoustic measurement of temperature profile in the troposphere and stratosphere. *Nature*, **323**, 426–428, doi:10.1038/323426a0.
- Mead, J., G. Hopcraft, S. Frasier, B. Pollard, C. Cherry, D. Schaubert, and R. McIntosh, 1998: A volume-imaging radar wind profiler for atmospheric boundary layer turbulence studies.

- J. Atmos. Oceanic Technol.*, **15**, 849–859, doi:10.1175/1520-0426(1998)015<0849:AVIRWP>2.0.CO;2.
- Milovac, J., K. Warrach-Sagi, J. Ingwersen, A. Behrendt, F. Späth, V. Wulfmeyer, and H. D. Wizemann, 2014: Sensitivity of the WRF model to boundary layer and land surface parameterizations: Comparisons with differential absorption lidar and eddy covariance measurements. *21st Symp. on Boundary Layers and Turbulence*, Leeds, United Kingdom, Amer. Meteor. Soc., 26. [Available online at <https://ams.confex.com/ams/21BLT/webprogram/Paper248146.html>.]
- Moeng, C.-H., and P. P. Sullivan, 1994: A comparison of shear- and buoyancy-driven planetary boundary layer flows. *J. Atmos. Sci.*, **51**, 999–1022, doi:10.1175/1520-0469(1994)051<0999:ACOSAB>2.0.CO;2.
- Monin, A. S., and A. Yaglom, 1975: *Statistical Fluid Mechanics*. Vol. 2, *Mechanics of Turbulence*, MIT Press, 896 pp.
- Muppa, S. K., A. Behrendt, F. Späth, V. Wulfmeyer, S. Metzendorf, and A. Riede, 2015: Turbulent humidity fluctuations in the convective boundary layer: Case studies using water vapour differential absorption lidar measurements. *Bound.-Layer Meteor.*, doi:10.1007/s10546-015-0078-9, in press.
- Muschinski, A., and P. Sullivan, 2013: Using large-eddy simulation to investigate intermittency fluxes of clear-air radar reflectivity in the atmospheric boundary layer. *Proc. Antennas and Propagation Society Int. Symp. (APSURSI)*, Orlando, FL, IEEE, 2321–2322, doi:10.1109/APS.2013.6711819.
- Noh, Y., W. G. Cheon, S. Y. Hong, and S. Raasch, 2003: Improvement of the K-profile model for the planetary boundary layer based on large eddy simulation data. *Bound.-Layer Meteor.*, **107**, 401–427, doi:10.1023/A:1022146015946.
- Pal, S., A. Behrendt, and V. Wulfmeyer, 2010: Elastic-backscatter-lidar-based characterization of the convective boundary layer and investigation of related statistics. *Ann. Geophys.*, **28**, 825–847, doi:10.5194/angeo-28-825-2010.
- Park, S., and C. S. Bretherton, 2009: The University of Washington shallow convection and moist turbulence schemes and their impact on climate simulations with the Community Atmosphere Model. *J. Climate*, **22**, 3449–3469, doi:10.1175/2008JCLI2557.1.
- Philippov, V., C. Codemard, Y. Jeong, C. Alegria, J. K. Sahu, J. Nilsson, and G. N. Pearson, 2004: High-energy in-fibre pulse amplification for coherent lidar applications. *Opt. Lett.*, **29**, 2590–2592, doi:10.1364/OL.29.002590.
- Poulos, G. S., and Coauthors, 2002: CASES-99: A comprehensive investigation of the stable nocturnal boundary layer. *Bull. Amer. Meteor. Soc.*, **83**, 555–581, doi:10.1175/1520-0477(2002)083<0555:CACIOT>2.3.CO;2.
- Saito, K., and Coauthors, 2013: Super high-resolution mesoscale weather prediction. *J. Phys.: Conf. Ser.*, **454**, 012073, doi:10.1088/1742-6596/454/1/012073.
- Samuelsson, P., and Coauthors, 2011: The Rossby Centre Regional Climate model RCA3: Model description and performance. *Tellus*, **63A**, 4–23, doi:10.1111/j.1600-0870.2010.00478.x.
- Senff, C., J. Bösenberg, and G. Peters, 1994: Measurement of water vapor flux profiles in the convective boundary layer with lidar and radar-RASS. *J. Atmos. Oceanic Technol.*, **11**, 85–93, doi:10.1175/1520-0426(1994)011<0085:MOWVFP>2.0.CO;2.
- Sorbian, Z., 1996: Effects caused by varying the strength of the capping inversion based on a large eddy simulation model of the shear-free convective boundary layer. *J. Atmos. Sci.*, **53**, 2015–2024, doi:10.1175/1520-0469(1996)053<2015:ECBVT>2.0.CO;2.
- , 2001: An evaluation of local similarity on the top of the mixed layer based on large-eddy simulations. *Bound.-Layer Meteor.*, **101**, 183–207, doi:10.1023/A:1019260632125.
- , 2005: Statistics of scalar fields in the atmospheric boundary layer based on large-eddy simulations. Part I: Free convection. *Bound.-Layer Meteor.*, **116**, 467–486, doi:10.1007/s10546-005-0907-3.
- , 2006: Statistics of scalar fields in the atmospheric boundary layer based on large-eddy simulations. Part II: Forced convection. *Bound.-Layer Meteor.*, **119**, 57–79, doi:10.1007/s10546-005-9014-8.
- , 2009: Improving non-local parameterization of the convective boundary layer. *Bound.-Layer Meteor.*, **130**, 57–69, doi:10.1007/s10546-008-9331-9.
- Späth, F., A. Behrendt, S. K. Muppa, S. Metzendorf, A. Riede, and V. Wulfmeyer, 2014: High-resolution atmospheric water-vapor measurements with a scanning differential absorption lidar. *Atmos. Chem. Phys. Discuss.*, **14**, 29 057–29 099, doi:10.5194/acpd-14-29057-2014.
- Spuler, S. M., K. S. Repasky, B. Morley, D. Moen, M. Hayman, and A. R. Nehrir, 2015: Field-deployable diode-laser-based differential absorption lidar (DIAL) for profiling water vapor. *Atmos. Meas. Tech.*, **8**, 1073–1087, doi:10.5194/amt-8-1073-2015.
- Stull, R. B., 1988: *An Introduction to Boundary Layer Meteorology*. Atmospheric and Oceanographic Sciences Library, Vol. 13, Springer, 670 pp.
- Sullivan, P. P., C.-H. Moeng, B. Stevens, D. H. Lenschow, and S. D. Mayor, 1998: Structure of the entrainment zone capping the convective atmospheric boundary layer. *J. Atmos. Sci.*, **55**, 3042–3064, doi:10.1175/1520-0469(1998)055<3042:SOTEZC>2.0.CO;2.
- Tatarski, V. I., 1961: *Wave Propagation in a Turbulent Medium*. McGraw-Hill, 285 pp.
- Träumner, K., C. Kottmeier, U. Corsmeier, and A. Wieser, 2011: Convective boundary-layer entrainment: Short review and progress using Doppler lidar. *Bound.-Layer Meteor.*, **141**, 369–391, doi:10.1007/s10546-011-9657-6.
- Tsuda, T., M. Miyamoto, and J. Furumoto, 2001: Estimation of a humidity profile using turbulence echo characteristics. *J. Atmos. Oceanic Technol.*, **18**, 1214–1222, doi:10.1175/1520-0426(2001)018<1214:EOAHPU>2.0.CO;2.
- Tucker, S. C., W. A. Brewer, R. M. Banta, C. Senff, S. P. Sandberg, D. C. Law, A. M. Weickmann, and R. M. Hardesty, 2009: Doppler lidar estimation of mixing height using turbulence, shear, and aerosol profiles. *J. Atmos. Oceanic Technol.*, **26**, 673–688, doi:10.1175/2008JTECHA1157.1.
- Turner, D. D., and J. E. M. Goldsmith, 1999: Twenty-four-hour Raman lidar water vapor measurements during the Atmospheric Radiation Measurement Program's 1996 and 1997 water vapor intensive observation periods. *J. Atmos. Oceanic Technol.*, **16**, 1062–1076, doi:10.1175/1520-0426(1999)016<1062:TFHRLW>2.0.CO;2.
- , and U. Löhnert, 2014: Information content and uncertainties in thermodynamic profiles and liquid cloud properties retrieved from the ground-based Atmospheric Emitted Radiance Interferometer (AERI). *J. Appl. Meteor. Climatol.*, **53**, 752–771, doi:10.1175/JAMC-D-13-0126.1.
- , R. A. Ferrare, L. A. Heilman Brasseur, W. F. Feltz, and T. P. Tooman, 2002: Automated retrievals of water vapor and aerosol profiles over Oklahoma from an operational Raman lidar. *J. Atmos. Oceanic Technol.*, **19**, 37–50, doi:10.1175/1520-0426(2002)019<0037:AROWVA>2.0.CO;2.
- , V. Wulfmeyer, and A. J. Scarino, 2014a: Aircraft evaluation of ground-based Raman lidar water vapor turbulence profiles in convective mixed layers. *J. Atmos. Oceanic Technol.*, **31**, 1078–1088, doi:10.1175/JTECH-D-13-00075.1.
- , V. Wulfmeyer, L. K. Berg, and J. H. Schween, 2014b: Water vapor turbulence profiles in stationary continental convective

- mixed layers. *J. Geophys. Res. Atmos.*, **119**, 11 151–11 165, doi:10.1002/2014JD022202.
- Van Zanten, M. C., P. G. Duynkerke, and J. W. M. Cuijpers, 1999: Entrainment parameterization in convective boundary layers. *J. Atmos. Sci.*, **56**, 813–828, doi:10.1175/1520-0469(1999)056<0813:EPICBL>2.0.CO;2.
- Waggy, S. B., S. Biringen, and P. Sullivan, 2013: Direct numerical simulation of top-down and bottom-up diffusion in the convective boundary layer. *J. Fluid Mech.*, **724**, 581–606, doi:10.1017/jfm.2013.130.
- Wulfmeyer, V., 1999a: Investigation of turbulent processes in the lower troposphere with water vapor DIAL and radar-RASS. *J. Atmos. Sci.*, **56**, 1055–1076, doi:10.1175/1520-0469(1999)056<1055:IOTPIT>2.0.CO;2.
- , 1999b: Investigations of humidity skewness and variance profiles in the convective boundary layer and comparison of the latter with large eddy simulation results. *J. Atmos. Sci.*, **56**, 1077–1087, doi:10.1175/1520-0469(1999)056<1077:IOHSAV>2.0.CO;2.
- , and T. Janjić, 2005: Twenty-four-hour observations of the marine boundary layer using shipborne NOAA high-resolution Doppler lidar. *J. Appl. Meteor.*, **44**, 1723–1744, doi:10.1175/JAM2296.1.
- , and Coauthors, 2008: The Convective and Orographically Induced Precipitation Study: A research and development project of the World Weather Research Program for improving quantitative precipitation forecasting in low-mountain regions. *Bull. Amer. Meteor. Soc.*, **89**, 1477–1486, doi:10.1175/2008BAMS2367.1.
- , S. Pal, D. D. Turner, and E. Wagner, 2010: Can water vapour Raman lidar resolve profiles of turbulent variables in the convective boundary layer? *Bound.-Layer Meteor.*, **136**, 253–284, doi:10.1007/s10546-010-9494-z.
- , and Coauthors, 2011: The Convective and Orographically-induced Precipitation Study (COPS): The scientific strategy, the field phase, and first highlights. *Quart. J. Roy. Meteor. Soc.*, **137**, 3–30, doi:10.1002/qj.752.
- , and Coauthors, 2015a: A review of the remote sensing of lower tropospheric thermodynamic profiles and its indispensable role for the understanding and the simulation of water and energy cycles. *Rev. Geophys.*, **53**, 819–895, doi:10.1002/2014RG000476.
- , and Coauthors, 2015b: New concepts for studying land-surface-atmosphere feedback based on a new lidar synergy and grey zone simulations. *Geophysical Research Abstracts*, Vol. 17, Abstract EGU2015-5054. [Available online at <http://meetingorganizer.copernicus.org/EGU2015/EGU2015-5054.pdf>.]
- Wyngaard, J. C., and R. A. Brost, 1984: Top-down and bottom-up diffusion of a scalar in the convective boundary layer. *J. Atmos. Sci.*, **41**, 102–112, doi:10.1175/1520-0469(1984)041<0102:TDABUD>2.0.CO;2.
- Xie, B., J. C. H. Fung, A. Chan, and A. Lau, 2012: Evaluation of nonlocal and local planetary boundary layer schemes in the WRF model. *J. Geophys. Res.*, **117**, D12103, doi:10.1029/2011JD017080.
- Zehe, E., and Coauthors, 2014: From response units to functional units: A thermodynamic reinterpretation of the HRU concept to link spatial organization and functioning of intermediate scale catchments. *Hydrol. Earth Syst. Sci.*, **18**, 4635–4655, doi:10.5194/hess-18-4635-2014.
- Zhou, M. Y., D. H. Lenschow, B. B. Stankov, J. C. Kaimal, and J. E. Gaynor, 1985: Wave and turbulence structure in a shallow baroclinic convective boundary layer and overlying inversion. *J. Atmos. Sci.*, **42**, 47–57, doi:10.1175/1520-0469(1985)042<0047:WATSIA>2.0.CO;2.

5 Summary

This thesis includes six publications concerning the UHOH DIAL. In this context, the DIAL concept was introduced and I investigated the wavelength sensitivity of the RD effect with the conclusion that on the slope of an absorption line the RD effect can be significantly reduced or even vanishes completely. Tuning the online wavelength to the slope requires a high wavelengths stability of the laser transmitter. Advancements in the development of the transmitter setup, especially in the development of a new seeder system are presented and allow selecting a wavelength on the slope. The new seed lasers were DFB lasers which provide a frequency stability of 6.3 MHz and a linewidth of less than 4.7 MHz. The new seed laser system includes also a new concept of a fast optical switch to toggle between the online and offline laser beam injected into the Ti:sapphire resonator. This new concept is based on an EOD and allows switching with a response time of less than 10 μ s. The crosstalk between the channels is 33 dB which results in a spectral purity of 99.95 %. Hence, the requirements for high accuracy DIAL measurements are fulfilled. The achieved frequency stability enables also the adaptation of the absorption cross-section value depending on the ambient atmospheric conditions by tuning the laser wavelength along the slope of an absorption line.

An overview of the setup of the UHOH DIAL system is given which was designed for observations of the humidity in the lower troposphere. With the improvements of the laser transmitter, the first scanning measurements with a WVDIAL were performed. I developed new analysis tools with a new approach for error estimations as well as adequate visualization procedures for 2-D–3-D data sets. Within two field experiments three scanning modes were realized. In 2013 during HOPE, RHI scanning measurements in two different directions were made. The noise estimation results in 6 % within the ABL with a strong increase at the top of the ABL. The first volume scan was realized during SABLE 2014. The captured 3-D humidity field allowed to relate structures of the humidity layers to the surface elevation with a small hill nearby. The instrumental noise within the measurement range stayed below 0.5 g m⁻³ or below 7 %. Low elevation scanning measurements revealed for one hour mean values lower humidity above grassland than above a maize field and than above a forest. The uncertainties were constant over the measured height range between 20 and 140 m and reads < 0.3 g m⁻³ or < 0.3 % at 400 m distance and < 0.9 g m⁻³ or < 1 % at 1200 m distance.

Furthermore, applications of WV data measured with DIAL are presented. There was an evaluation of different WRF model setups of which simulation output profiles were compared with mean profiles of scanning DIAL data from the FLUXPAT campaign 2009 regarding moisture content, PBL evolution and PBLH.

High-resolution vertical pointing DIAL measurements were used to derive higher-order

moments up to the fourth-order as well as skewness and kurtosis. These were investigated for two cases of HOPE. These profiles were again used to investigate relationships with simultaneously performed temperature and wind lidar measurements. It was demonstrated that the synergy of these measurements can be used for investigations of new turbulence parameterizations and for model validation.

6 Outlook

The ongoing laser transmitter improvements will provide higher output power. With around 10 W instead of 6.75 W the vision of Wulfmeyer and Walther (2001a,b) will be realized and will allow for increasing the measurement range, shortening the integration time, and reducing the uncertainties. More laser power would also be beneficial for scanning with higher scan speed, e.g., to sample the same volume more often or with smaller increments. Even with the currently used optical fiber, which limits the transmitted laser power for scanning measurements, the setup could be extended by combining both setup configurations for scanning and vertical observations at the same time. This would mean to have the second detection channel with the small receiving telescope recording also during scanning operation for simultaneous vertical profiling of the atmosphere. For transmitting laser pulses vertically, I suggest to replace the high-reflexion flip mirror (HRFM, see Fig. 5) by a beam splitter and transmit the excess laser power via a free beam into the atmosphere. This would provide simultaneous data sets of vertical and scanning measurements.

Scanning DIAL measurements of the ABL humidity field demonstrated new possibilities for future research. More measurements will allow to continue the investigation of the humidity fields over different kinds of vegetation, over more surface characteristics and under different meteorological influences. The low elevation scanning measurements can be combined with simultaneous captured temperature and wind velocity observations to test the Monin-Obukhov similarity relationships.

New data sets will also help to improve our knowledge and understanding of the exchange processes of the LA system, of turbulent transport, of entrainment fluxes, and of higher-order moments. Model evaluation studies regarding representation of feedback processes and ABL turbulence parameterizations can be performed based on high-resolution observations. Furthermore, the use of WVDIAL data for data assimilation and its impact can be investigated. Finally, this will lead to an improved model performance in weather forecasts and will reduce the uncertainties of climate projections.

Abbreviations

2-D	2-dimensional
3-D	3-dimensional
ABL	atmospheric boundary layer
APD	avalanche photo diode
BE	beam expander
BR	beam reducer
BSM	beam-steering mirror
CBL	convective boundary layer
CO₂	carbon dioxide
COPS	Convective and Orographically-induced Precipitation Study
DFB	distributed feedback
DIAL	differential absorption lidar
ECDL	external cavity diode laser
EOD	electro-optic deflector
FC	fiber coupler
FWHM	full width at half maximum
HD(CP)²	High Definition of Clouds and Precipitation for advancing Climate Prediction
HITRAN	High-resolution TRANsmission molecular absorption database
HOPE	HD(CP) ² Observational Prototype Experiment
HR	high-reflection mirror
HRFM	high-reflection flip mirror
IF	interference filter
IPCC	Intergovernmental Panel on Climate Change

IPM	Institute of Physics and Meteorology
IR	infrared
IWV	integrated water vapor
LA	land-atmosphere
LES	large eddy simulation
MOST	Monin-Obukhov similarity theory
MWR	microwave radiometer
NASA	National Aeronautics and Space Administration
PD	photo diode
PM	primary mirror
RHI	range-height indicator
RRL	rotational Raman lidar
RD	Rayleigh-Doppler
SABLE	Surface Atmosphere Boundary Layer Exchange
SM	secondary mirror
SNR	signal-to-noise ratio
TM	transmitting telescope mirror
TR32	Transregio 32
UHOH	University of Hohenheim
UV	ultraviolet
WV	water vapor
WVDIAL	water vapor DIAL
WVRL	WV Raman lidar

References

- Ansmann, A.: Errors in ground-based water-vapor DIAL measurements due to Doppler-broadened Rayleigh backscattering, *Appl. Opt.*, 24, 3476–3480, doi:10.1364/AO.24.003476, 1985.
- Ansmann, A. and Bösenberg, J.: Correction scheme for spectral broadening by Rayleigh scattering in differential absorption lidar measurements of water vapor in the troposphere, *Appl. Opt.*, 26, 3026–3029, doi:10.1364/AO.26.003026, 1987.
- Barnes, J., Barnes, N., Wang, L., and Edwards, W.: Injection seeding. II. $\text{Ti:Al}_2\text{O}_3$ experiments, *IEEE J. Quantum Electron.*, 29, 2684–2692, doi:10.1109/3.250391, 1993.
- Barnes, N. and Barnes, J.: Injection seeding. I. Theory, *IEEE J. Quantum Electron.*, 29, 2670–2683, doi:10.1109/3.250390, 1993.
- Behrendt, A., Nakamura, T., Onishi, M., Baumgart, R., and Tsuda, T.: Combined Raman lidar for the measurement of atmospheric temperature, water vapor, particle extinction coefficient, and particle backscatter coefficient, *Appl. Opt.*, 41, 7657–7666, doi:10.1364/AO.41.007657, 2002.
- Behrendt, A., Wulfmeyer, V., Riede, A., Wagner, G., Pal, S., Bauer, H., Radlach, M., and Späth, F.: 3-Dimensional observations of atmospheric humidity with a scanning differential absorption Lidar, in: *Society of Photo-Optical Instrumentation Engineers (SPIE) Conference Series*, vol. 7475, doi:10.1117/12.835143, 2009.
- Behrendt, A., Pal, S., Aoshima, F., Bender, M., Blyth, A., Corsmeier, U., Cuesta, J., Dick, G., Dorninger, M., Flamant, C., Girolamo, P. D., Gorgas, T., Huang, Y., Kalthoff, N., Khodayar, S., Mannstein, H., Träumner, K., Wieser, A., and Wulfmeyer, V.: Observation of convection initiation processes with a suite of state-of-the-art research instruments during COPS IOP 8b, *Q. J. R. Meteorolog. Soc.*, 137, 81–100, doi:10.1002/qj.758, 2011.
- Behrendt, A., Wulfmeyer, V., Hammann, E., Muppa, S., and Pal, S.: Profiles of second to fourth- order moments of turbulent temperature fluctuations in the convective boundary layer: first measurements with rotational Raman lidar, *Atmos. Chem. Phys.*, 15, 5485–5500, doi:10.5194/acp-15-5485-2015, 2015.
- Bhawar, R., Girolamo, P. D., Summa, D., Flamant, C., Althausen, D., Behrendt, A., Kiemle, C., Bosser, P., Cacciani, M., Champollion, C., Iorio, T. D., Engelmann, R., Herold, C., Müller, D., Pal, S., Wirth, M., and Wulfmeyer, V.: The water vapour intercomparison effort in the framework of the Convective and Orographically-induced

References

- Precipitation Study: airborne-to-ground-based and airborne-to-airborne lidar systems, *Q. J. R. Meteorolog. Soc.*, 137, 325–348, doi:10.1002/qj.697, 2011.
- Blumberg, W. G., Turner, D. D., Löhnert, U., and Castleberry, S.: Ground-Based Temperature and Humidity Profiling Using Spectral Infrared and Microwave Observations. Part II: Actual Retrieval Performance in Clear-Sky and Cloudy Conditions, *J. Appl. Meteor. Climatol.*, 54, 2305–2319, doi:10.1175/jamc-d-15-0005.1, 2015.
- Bösenberg, J.: Ground-based differential absorption lidar for water-vapor and temperature profiling: methodology, *Appl. Opt.*, 37, 3845–3860, doi:10.1364/ao.37.003845, 1998.
- Browell, E. V., Wilkerson, T. D., and McIlrath, T. J.: Water vapor differential absorption lidar development and evaluation, *Appl. Opt.*, 18, 3474–3483, doi:10.1364/ao.18.003474, 1979.
- Browell, E. V., Carter, A. F., Shipley, S. T., Allen, R. J., Butler, C. F., Mayo, M. N., Siviter, J. H., and Hall, W. M.: NASA multipurpose airborne DIAL system and measurements of ozone and aerosol profiles, *Appl. Opt.*, 22, 522–534, doi:10.1364/ao.22.000522, 1983.
- Bucholtz, A.: Rayleigh-scattering calculations for the terrestrial atmosphere, *Appl. Opt.*, 34, 2765–2773, doi:10.1364/ao.34.002765, 1995.
- Eichinger, W.: Estimation of spatially distributed latent heat flux over complex terrain from a Raman lidar, *Agric. For. Meteorol.*, 105, 145–159, doi:10.1016/s0168-1923(00)00183-0, 2000.
- Eichinger, W. E., Cooper, D. I., Forman, P. R., Griegos, J., Osborn, M. A., Richter, D., Tellier, L. L., and Thornton, R.: The Development of a Scanning Raman Water Vapor Lidar for Boundary Layer and Tropospheric Observations, *J. Atmos. Oceanic Technol.*, 16, 1753–1766, doi:10.1175/1520-0426(1999)016<1753:tdoasr>2.0.co;2, 1999.
- Fernald, F. G.: Analysis of atmospheric lidar observations: some comments, *Appl. Opt.*, 23, 652–653, doi:10.1364/ao.23.000652, 1984.
- Findell, K. L. and Eltahir, E. A. B.: Atmospheric Controls on Soil Moisture–Boundary Layer Interactions. Part II: Feedbacks within the Continental United States, *J. Hydrometeorol.*, 4, 570–583, doi:10.1175/1525-7541(2003)004<0570:acosml>2.0.CO;2, 2003.
- Froidevaux, M., Higgins, C. W., Simeonov, V., Ristori, P., Pardyjak, E., Serikov, I., Calhoun, R., van den Bergh, H., and Parlange, M. B.: A Raman lidar to measure

- water vapor in the atmospheric boundary layer, *Adv. Water Resour.*, 51, 345–356, doi:10.1016/j.advwatres.2012.04.008, 2013.
- Goldsmith, J. E. M., Blair, F. H., Bisson, S. E., and Turner, D. D.: Turn-key Raman lidar for profiling atmospheric water vapor, clouds, and aerosols, *Appl. Opt.*, 37, 4979–4990, doi:10.1364/ao.37.004979, 1998.
- Hammann, E.: High-resolution temperature and humidity profiling of the atmospheric boundary layer with scanning rotational Raman lidar, Doctoral thesis, Universität Hohenheim, in review, 2016.
- Hammann, E., Behrendt, A., Le Mounier, F., and Wulfmeyer, V.: Temperature Profiling of the Atmospheric Boundary Layer with Rotational Raman Lidar during the HD(CP)² Observational Prototype Experiment, *Atmos. Chem. Phys.*, 15, 2867–2881, doi:10.5194/acp-15-2867-2015, 2015.
- Hong, S.-Y.: Stable Boundary Layer Mixing in a Vertical Diffusion Scheme, the Korea Meteor. Soc., Fall conference, Seoul, Korea, Oct. 25-26., 2007.
- Hong, S.-Y., Noh, Y., and Dudhia, J.: A New Vertical Diffusion Package with an Explicit Treatment of Entrainment Processes, *Mon. Wea. Rev.*, 134, 2318–2341, doi: 10.1175/mwr3199.1, 2006.
- Khalesifard, H. R., Fix, A., Ehret, G., Schiller, M., and Wulfmeyer, V.: Fast-switching system for injection seeding of a high-power Ti:sapphire laser, *Rev. Sci. Instrum.*, 80, 073 110, doi:10.1063/1.3184011, 2009.
- Koch, G. J., Barnes, B. W., Petros, M., Beyon, J. Y., Amzajerjian, F., Yu, J., Davis, R. E., Ismail, S., Vay, S., Kavaya, M. J., and Singh, U. N.: Coherent differential absorption lidar measurements of CO₂, *Appl. Opt.*, 43, 5092–5099, doi: 10.1364/ao.43.005092, 2004.
- Koster, R. D., Sud, Y. C., Guo, Z., Dirmeyer, P. A., Bonan, G., Oleson, K. W., Chan, E., Versegny, D., Cox, P., Davies, H., Kowalczyk, E., Gordon, C. T., Kanae, S., Lawrence, D., Liu, P., Mocko, D., Lu, C.-H., Mitchell, K., Malyshev, S., McAvaney, B., Oki, T., Yamada, T., Pitman, A., Taylor, C. M., Vasic, R., and Xue, Y.: GLACE: The Global Land–Atmosphere Coupling Experiment. Part I: Overview, *J. Hydrometeorol.*, 7, 590–610, doi:10.1175/jhm510.1, 2006.
- Kotlarski, S., Keuler, K., Christensen, O. B., Colette, A., Déqué, M., Gobiet, A., Goergen, K., Jacob, D., Lüthi, D., van Meijgaard, E., Nikulin, G., Schär, C., Teichmann,

- C., Vautard, R., Warrach-Sagi, K., and Wulfmeyer, V.: Regional climate modeling on European scales: a joint standard evaluation of the EURO-CORDEX RCM ensemble, *Geosci. Model Dev.*, 7, 1297–1333, doi:10.5194/gmd-7-1297-2014, 2014.
- Löhnert, U., Turner, D. D., and Crewell, S.: Ground-Based Temperature and Humidity Profiling Using Spectral Infrared and Microwave Observations. Part I: Simulated Retrieval Performance in Clear-Sky Conditions, *J. Appl. Meteor. Climatol.*, 48, 1017–1032, doi:10.1175/2008jamc2060.1, 2009.
- Matsuda, M.: Development of a scanning Raman lidar for observing the spatiotemporal distribution of water vapor, Master Thesis, Bulletin of Research Institute for Sustainable Humansphere, Kyoto University, Japan, 9, 42, URL <http://hdl.handle.net/2433/185648>, 2013.
- Melfi, S. H.: OBSERVATION OF RAMAN SCATTERING BY WATER VAPOR IN THE ATMOSPHERE, *Appl. Phys. Lett.*, 15, 295–297, doi:10.1063/1.1653005, 1969.
- Mellor, G. L. and Yamada, T.: Development of a turbulence closure model for geophysical fluid problems, *Rev. Geophys.*, 20, 851–875, doi:10.1029/rg020i004p00851, 1982.
- Metzendorf, S., Wulfmeyer, V., Behrendt, A., Späth, F., and Riede, A.: Frequency-Agile Ti:Sapphire Laser System with High Power and High Pulse Energy for Spectroscopic Applications, in: Conference on Lasers and Electro-Optics (CLEO/Europe), Munich, Germany, 21–25 June, 2015.
- Milovac, J., Warrach-Sagi, K., Behrendt, A., Späth, F., Ingwersen, J., and Wulfmeyer, V.: Investigation of PBL schemes combining the WRF model simulations with scanning water vapor differential absorption lidar measurements, *J. Geophys. Res. Atmos.*, 121, 624–649, doi:10.1002/2015jd023927, 2016.
- Monin, A. and Obukhov, A.: Basic laws of turbulent mixing in the surface layer of the atmosphere, *Tr. Akad. Nauk SSSR Geophys. Inst.*, 24, 163–187, URL http://www.mcnaughty.com/keith/papers/Monin_and_Obukhov_1954.pdf, 1954.
- Muppa, S. K., Behrendt, A., Späth, F., Wulfmeyer, V., Metzendorf, S., and Riede, A.: Turbulent Humidity Fluctuations in the Convective Boundary Layer: Case Studies Using Water Vapour Differential Absorption Lidar Measurements, *Boundary-Layer Meteorol.*, 158, 43–66, doi:10.1007/s10546-015-0078-9, 2016.
- NASA: US Standard Atmosphere, US Government Printing Office, Washington, DC, 1976.

- Ostermeyer, M., Kappe, P., Menzel, R., and Wulfmeyer, V.: Diode-pumped Nd:YAG master oscillator power amplifier with high pulse energy, excellent beam quality, and frequency-stabilized master oscillator as a basis for a next-generation lidar system, *Appl. Opt.*, 44, 582–590, doi:10.1364/ao.44.000582, 2005.
- Pal, S., Behrendt, A., and Wulfmeyer, V.: Elastic-backscatter-lidar-based characterization of the convective boundary layer and investigation of related statistics, *Ann. Geophys.*, 28, 825–847, doi:10.5194/angeo-28-825-2010, 2010.
- Radlach, M., Behrendt, A., and Wulfmeyer, V.: Scanning rotational Raman lidar at 355 nm for the measurement of tropospheric temperature fields, *Atmos. Chem. Phys.*, 8, 159–169, doi:10.5194/acp-8-159-2008, 2008.
- Rothman, L., Gordon, I., Babikov, Y., Barbe, A., Benner, D. C., Bernath, P., Birk, M., Bizzocchi, L., Boudon, V., Brown, L., Campargue, A., Chance, K., Cohen, E., Coudert, L., Devi, V., Drouin, B., Fayt, A., Flaud, J.-M., Gamache, R., Harrison, J., Hartmann, J.-M., Hill, C., Hodges, J., Jacquemart, D., Jolly, A., Lamouroux, J., Roy, R. L., Li, G., Long, D., Lyulin, O., Mackie, C., Massie, S., Mikhailenko, S., Müller, H., Naumenko, O., Nikitin, A., Orphal, J., Perevalov, V., Perrin, A., Polovtseva, E., Richard, C., Smith, M., Starikova, E., Sung, K., Tashkun, S., Tennyson, J., Toon, G., Tyuterev, V., and Wagner, G.: The HITRAN2012 molecular spectroscopic database, *J. Quant. Spectrosc. Ra.*, 130, 4–50, doi:10.1016/j.jqsrt.2013.07.002, 2013.
- Santanello, J. A., Peters-Lidard, C. D., Kennedy, A., and Kumar, S. V.: Diagnosing the Nature of Land–Atmosphere Coupling: A Case Study of Dry/Wet Extremes in the U.S. Southern Great Plains, *J. Hydrometeorol.*, 14, 3–24, doi:10.1175/jhm-d-12-023.1, 2013.
- Schiller, M.: A high-power laser transmitter for ground-based and airborne water-vapor measurements in troposphere, Doctoral thesis, Universität Hohenheim, 2008.
- Schotland, R. M.: Some observations of the vertical profile of water vapor by means of a ground based optical radar, in: *Proceedings of the Fourth Symposium on Remote Sensing of Environment*, pp. 273–283, U. Michigan, Ann Arbor, 1966.
- Schotland, R. M.: Errors in the Lidar Measurement of Atmospheric Gases by Differential Absorption, *J. Appl. Meteorol.*, 13, 71–77, doi:10.1175/1520-0450(1974)013<0071:eitlmo>2.0.CO;2, 1974.
- Seneviratne, S. I., Corti, T., Davin, E. L., Hirschi, M., Jaeger, E. B., Lehner, I., Orlowsky, B., and Teuling, A. J.: Investigating soil moisture–climate inter-

- actions in a changing climate: A review, *Earth-Sci. Rev.*, 99, 125–161, doi:10.1016/j.earscirev.2010.02.004, 2010.
- Späth, F., Metzendorf, S., Behrendt, A., Wizemann, H.-D., Wagner, G., and Wulfmeyer, V.: Online/offline injection seeding system with high frequency-stability and low crosstalk for water vapor DIAL, *Opt. Commun.*, 309, 37–43, doi:10.1016/j.optcom.2013.07.003, 2013.
- Späth, F., Behrendt, A., Muppa, S. K., Metzendorf, S., Riede, A., and Wulfmeyer, V.: 3-D water vapor field in the atmospheric boundary layer observed with scanning differential absorption lidar, *Atmos. Meas. Tech.*, 9, 1701–1720, doi:10.5194/amt-9-1701-2016, 2016.
- van Heerwaarden, C. C., de Arellano, J. V.-G., Moene, A. F., and Holtslag, A. A. M.: Interactions between dry-air entrainment, surface evaporation and convective boundary-layer development, *Q. J. R. Meteorolog. Soc.*, 135, 1277–1291, doi:10.1002/qj.431, 2009.
- Wagner, G., Behrendt, A., Wulfmeyer, V., Späth, F., and Schiller, M.: High-power Ti:sapphire laser at 820 nm for scanning ground-based water-vapor differential absorption lidar, *Appl. Opt.*, 52, 2454–2469, doi:10.1364/ao.52.002454, 2013.
- Warrach-Sagi, K., Schwitalla, T., Wulfmeyer, V., and Bauer, H.-S.: Evaluation of a climate simulation in Europe based on the WRF–NOAH model system: precipitation in Germany, *Clim. Dyn.*, 41, 755–774, doi:10.1007/s00382-013-1727-7, 2013.
- Whiteman, D. N., Melfi, S. H., and Ferrare, R. A.: Raman lidar system for the measurement of water vapor and aerosols in the Earth’s atmosphere, *Appl. Opt.*, 31, 3068–3082, doi:10.1364/ao.31.003068, 1992.
- Whiteman, D. N., Demoz, B., Rush, K., Schwemmer, G., Gentry, B., Girolamo, P. D., Comer, J., Veselovskii, I., Evans, K., Melfi, S. H., Wang, Z., Cadirola, M., Mielke, B., Venable, D., and Hove, T. V.: Raman Lidar Measurements during the International H₂O Project. Part I: Instrumentation and Analysis Techniques, *J. Atmos. Oceanic Technol.*, 23, 157–169, doi:10.1175/jtech1838.1, 2006.
- Wulfmeyer, V.: Ground-based differential absorption lidar for water-vapor and temperature profiling: development and specifications of a high-performance laser transmitter, *Appl. Opt.*, 37, 3804–3824, doi:10.1364/ao.37.003804, 1998.
- Wulfmeyer, V. and Bösenberg, J.: Single-mode operation of an injection-seeded alexandrite ring laser for application in water-vapor and temperature differential absorption lidar, *Opt. Lett.*, 21, 1150–1152, doi:10.1364/ol.21.001150, 1996.

- Wulfmeyer, V. and Walther, C.: Future performance of ground-based and airborne water-vapor differential absorption lidar I Overview and theory, *Appl. Opt.*, 40, 5304–5320, doi:10.1364/ao.40.005304, 2001a.
- Wulfmeyer, V. and Walther, C.: Future performance of ground-based and airborne water-vapor differential absorption lidar II Simulations of the precision of a near-infrared, high-power system, *Appl. Opt.*, 40, 5321–5336, doi:10.1364/ao.40.005321, 2001b.
- Wulfmeyer, V., Behrendt, A., Bauer, H.-S., Kottmeier, C., Corsmeier, U., Blyth, A., Craig, G., Schumann, U., Hagen, M., Crewell, S., Girolamo, P. D., Flamant, C., Miller, M., Montani, A., Mobbs, S., Richard, E., Rotach, M. W., Arpagaus, M., Russchenberg, H., Schlüssel, P., König, M., Gärtner, V., Steinacker, R., Dorninger, M., Turner, D. D., Weckwerth, T., Hense, A., and Simmer, C.: RESEARCH CAMPAIGN: The Convective and Orographically Induced Precipitation Study, *Bull. Am. Meteorol. Soc.*, 89, 1477–1486, doi:10.1175/2008bams2367.1, 2008.
- Wulfmeyer, V., Behrendt, A., Kottmeier, C., Corsmeier, U., Barthlott, C., Craig, G. C., Hagen, M., Althausen, D., Aoshima, F., Arpagaus, M., Bauer, H.-S., Bennett, L., Blyth, A., Brandau, C., Champollion, C., Crewell, S., Dick, G., Girolamo, P. D., Dorninger, M., Dufournet, Y., Eigenmann, R., Engelmann, R., Flamant, C., Foken, T., Gorgas, T., Grzeschik, M., Handwerker, J., Hauck, C., Höller, H., Junkermann, W., Kalthoff, N., Kiemle, C., Klink, S., König, M., Krauss, L., Long, C. N., Madonna, F., Mobbs, S., Neininger, B., Pal, S., Peters, G., Pigeon, G., Richard, E., Rotach, M. W., Russchenberg, H., Schwitalla, T., Smith, V., Steinacker, R., Trentmann, J., Turner, D. D., van Baelen, J., Vogt, S., Volkert, H., Weckwerth, T., Wernli, H., Wieser, A., and Wirth, M.: The Convective and Orographically-induced Precipitation Study (COPS): the scientific strategy, the field phase, and research highlights, *Q. J. R. Meteorolog. Soc.*, 137, 3–30, doi:10.1002/qj.752, 2011.
- Wulfmeyer, V., Hardesty, R. M., Turner, D. D., Behrendt, A., Cadeddu, M. P., Girolamo, P. D., Schlüssel, P., Baelen, J. V., and Zus, F.: A review of the remote sensing of lower tropospheric thermodynamic profiles and its indispensable role for the understanding and the simulation of water and energy cycles, *Rev. Geophys.*, 53, 819–895, doi:10.1002/2014rg000476, 2015.
- Wulfmeyer, V., Muppa, S. K., Behrendt, A., Hammann, E., Späth, F., Sorbjan, Z., Turner, D. D., and Hardesty, R. M.: Determination of Convective Boundary Layer Entrainment Fluxes, Dissipation Rates, and the Molecular Destruction of Variances: Theoretical Description and a Strategy for Its Confirmation with a Novel Lidar System Synergy, *J. Atmos. Sci.*, 73, 667–692, doi:10.1175/jas-d-14-0392.1, 2016.

Curriculum Vitae

Personal Data

Name: **Florian Heiko Späth**
Address: Wilhelmstr. 1, 73779 Deizisau, Germany
Birth: 12th August 1983 in Esslingen am Neckar
Citizenship: German
eMail: f.spaeth@uni-hohenheim.de

Eudcation

since 07/2011 Doctoral student
Institute of Physics and Meteorology, University of Hohenheim

since 05/2010 Scientist
Institute of Physics and Meteorology, University of Hohenheim

10/2004 - 03/2010 Study of Physics (Diploma degree)
University of Stuttgart

2000 - 2003 Abitur at Friedrich-Ebert-School, Esslingen am Neckar

1994 - 2000 Realschule Plochingen

1990 - 1994 Grund- und Hauptschule Deizisau

Publications

Späth, F., Metzendorf, S., Behrendt, A., Wizemann, H.-D., Wagner, G., and Wulfmeyer, V.: Online/offline injection seeding system with high frequency-stability and low crosstalk for water vapor DIAL, *Opt. Commun.*, 309, 37–43, doi:10.1016/j.optcom.2013.07.003, 2013.

Späth, F., Behrendt, A., Muppa, S. K., Metzendorf, S., Riede, A., and Wulfmeyer, V.: 3-D water vapor field in the atmospheric boundary layer observed with scanning differential absorption lidar, *Atmos. Meas. Tech.*, 9, 1701–1720, doi:10.5194/amt-9-1701-2016, 2016.

Behrendt, A., Wulfmeyer, V., Riede, A., Wagner, G., Pal, S., Bauer, H., Radlach, M., and **Späth, F.**: 3-Dimensional observations of atmospheric humidity with a scanning differential absorption Lidar, in: Society of Photo-Optical Instrumentation Engineers (SPIE) Conference Series, vol. 7475, doi:10.1117/12.835143, 2009.

Wagner, G., Behrendt, A., Wulfmeyer, V., **Späth, F.**, and Schiller, M.: High-power Ti:sapphire laser at 820 nm for scanning ground-based water-vapor differential absorption lidar, *Appl. Opt.*, 52, 2454–2469, doi:10.1364/ao.52.002454, 2013.

Milovac, J., Warrach-Sagi, K., Behrendt, A., **Späth, F.**, Ingwersen, J., and Wulfmeyer, V.: Investigation of PBL schemes combining the WRF model simulations with scanning water vapor differential absorption lidar measurements, *J. Geophys. Res. Atmos.*, 121, 624–649, doi:10.1002/2015jd023927, 2016.

Muppa, S. K., Behrendt, A., **Späth, F.**, Wulfmeyer, V., Metzendorf, S., and Riede, A.: Turbulent Humidity Fluctuations in the Convective Boundary Layer: Case Studies Using Water Vapour Differential Absorption Lidar Measurements, *Boundary-Layer Meteorol.*, 158, 43–66, doi:10.1007/s10546-015-0078-9, 2016.

Wulfmeyer, V., Muppa, S. K., Behrendt, A., Hammann, E., **Späth, F.**, Sorbjan, Z., Turner, D. D., and Hardesty, R. M.: Determination of Convective Boundary Layer Entrainment Fluxes, Dissipation Rates, and the Molecular Destruction of Variances: Theoretical Description and a Strategy for Its Confirmation with a Novel Lidar System Synergy, *J. Atmos. Sci.*, 73, 667–692, doi:10.1175/jas-d-14-0392.1, 2016.

Conference Contributions

F. Späth, S. Metzendorf, A. Behrendt, V. Wulfmeyer: "Fast and Stable Online-Offline Switch of the UHOH Water Vapor DIAL", 26th International Laser Radar Conference, 25-29 June, Proto Heli, Greece, 2012.

F. Späth, A. Behrendt, V. Wulfmeyer: "Data Analysis of 3-Dimensional Water Vapor Fields Measured with the UHOH DIAL System", 26th International Laser Radar Conference, 25-29 June, Proto Heli, Greece, 2012.

F. Späth, M.B. Verdejo, A. Behrendt, J.H. Schween, S. Steinke, S. Crewell, V. Wulfmeyer: "Heterogeneity of Water Vapor in the Boundary Layer Determined with a DIAL and a MWR", International Symposium: Patterns in Soil-Vegetation-Atmosphere Systems: Monitoring, Modelling & Data Assimilation, 11-14 March, Bonn, Germany, 2013.

F. Späth, S.K. Muppa, S. Metzendorf, A. Riede, A. Behrendt, V. Wulfmeyer : "Overview of the UHOH Water Vapor DIAL Measurements: Vertical profiles and fields of moisture and aerosols during HOPE", DPG-Frühjahrstagung (Spring Meeting), 17-21 March, Berlin, Germany, 2014.

F. Späth, E. Hammann, S.K. Muppa, S. Metzendorf, A. Riede, A. Behrendt, V. Wulfmeyer : "Scanning lidar measurements of water vapor and temperature in the atmospheric boundary layer", DPG-Frühjahrstagung (Spring Meeting), 23-27 March, Heidelberg, Germany, 2015.

F. Späth, S.K. Muppa, A. Behrendt, S. Metzendorf, A. Riede, V. Wulfmeyer : "3D Water Vapor Measurements in the Boundary Layer with the UHOH Scanning Differential Absorption Lidar", 27th International Laser Radar Conference, 06-10 July, New York, United States, 2015.

F. Späth, A. Behrendt, V. Wulfmeyer: "Sensitivity of the Rayleigh-Doppler Effect with Respect to Wavelength and Backscatter Coefficient", 27th International Laser Radar Conference, 06-10 July, New York, United States, 2015.

Eidesstattliche Versicherung

Eidesstattliche Versicherung gemäß §7 Absatz 7 der Promotionsordnung der Universität Hohenheim zum Dr. rer. nat.

1. Bei der eingereichten Dissertation zum Thema handelt es sich um meine eigenständig erbrachte Leistung.
2. Ich habe nur die angegebenen Quellen und Hilfsmittel benutzt und mich keiner unzulässigen Hilfe Dritter bedient. Insbesondere habe ich wörtlich oder sinngemäß aus anderen Werken übernommene Inhalte als solche kenntlich gemacht.
3. Ich habe nicht die Hilfe einer kommerziellen Promotionsvermittlung oder -beratung in Anspruch genommen.
4. Die Bedeutung der eidesstattlichen Versicherung und der strafrechtlichen Folgen einer unrichtigen oder unvollständigen eidesstattlichen Versicherung sind mir bekannt.

Die Richtigkeit der vorstehenden Erklärung bestätige ich: Ich versichere an Eides Statt, dass ich nach bestem Wissen die reine Wahrheit erklärt und nichts verschwiegen habe.

Stuttgart-Hohenheim, 28.04.2016

Ort und Datum

Unterschrift

Acknowledgment

At the end of this work there is the point to thank different persons who made this doctoral thesis possible:

First, I would like to thank Professor Dr. Volker Wulfmeyer for the opportunity to write my dissertation at the Institute of Physics and Meteorology on this pioneering topic and to be my advisor. Your knowledge and experience in working with DIAL was very helpful and valuable in the discussions we had. I also acknowledge for all the possibilities to get in contact with the scientific community at conferences and meetings.

For the readiness to be reviewers of my thesis I thank Prof. Christoph Kottmeier and Prof. Andreas Fangmeier as well as the dean of the faculty Prof. Heinz Breer.

Many thanks belong also to my co-advisor Dr. Andreas Behrendt, the head of the working group remote sensing. I am very grateful for the fruitful discussions and all your helpful support whenever a scientific questions came up. Your constructive criticism for the successful finalization of publications and this thesis I appreciate very much.

A special thanks goes to my colleagues of the working group remote sensing, by name Dr. Eva Hammann, Simon Metzendorf, Dr. Shravan Muppa, Dr. Andrea Riede. It was a pleasure to operate our complex DIAL system with you in the best manner of teamwork. I really enjoyed our campaign life when we moved out with our instruments into the fields. With your collaboration it was possible to achieve the first 3-dimensional water vapor observations with a DIAL.

Mein Dank geht auch an die restlichen Mitglieder des IPM für ihre offene und hilfbereite Zusammenarbeit. Es war stets eine angenehme Arbeitsumgebung ohne die manch langer Tag im Büro nicht möglich gewesen wäre. Zudem erinnere ich mich gerne an unsere diversen Diskussionen in Mittags- und Kaffeepause.

An dieser Stelle möchte ich mich auch bei meinen Freunden für ihre Rücksichtnahme bedanken, wenn ich mal wieder anderweitig beschäftigt war. Ich habe dennoch jede freie Zeit mit euch sehr genossen, egal ob mit euch im Verein beim Kajakfahren, im Unisport beim Volleyball spielen, bei der Organisation verschiedenster Veranstaltungen oder auch einfach mal Abends beim gemütlichen zusammensitzen. Danke für die Gelegenheiten, die ihr mir geben habt, um mich von der Doktorarbeit abzulenken und meinen Kopf wieder frei zu bekommen. Das hat mir besonders in den stressigen Phasen sehr geholfen.

And last but not least,...

Abschließend einen ganz besonderen Dank an meine Familie, die mich während der gesamten Zeit der Doktorarbeit unterstützten und in den stressigen Zeiten den Rücken frei gehalten haben. Es war immer schön euer Interesse an meiner Arbeit zu sehen, auch wenn ihr nicht immer mit allem was ich euch erzählt habe was anfangen konntet. Ohne diesen Rückhalt wäre es mit Sicherheit ein ganzes Stück schwerer gewesen.

Allen ein herzliches Dankeschön!